Isogeometric Analysis of Shells

Ralph Echter
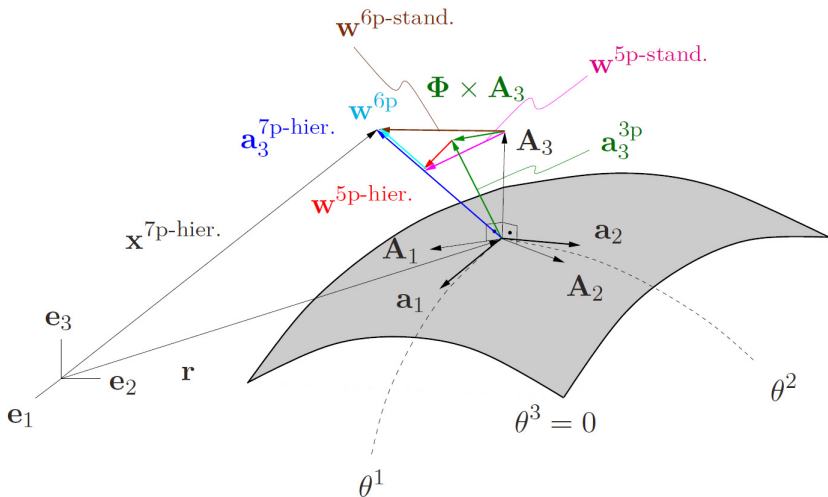
$$\mathbf{x}^{7\text{p-hier.}} = \underbrace{\underbrace{\underbrace{\underbrace{\mathbf{r} + \theta^3\left(\mathbf{A}_3 + \mathbf{\Phi} \times \mathbf{A}_3\right)}_{3\text{p}} + \theta^3\,\mathbf{w}^{5\text{p-hier.}}}_{5\text{p-hier.}} + \theta^3\,\mathbf{w}^{6\text{p}}}_{6\text{p-hier.}} + \left(\theta^3\right)^2\mathbf{w}^{7\text{p}}}_{7\text{p-hier.}}$$

Isogeometric Analysis of Shells

von

Ralph Echter

Isogeometric Analysis
of Shells

Von der Fakultät Bau- und Umweltingenieurwissenschaften
der Universität Stuttgart zur Erlangung der Würde eines
Doktor-Ingenieurs (Dr.-Ing.) genehmigte Abhandlung

vorgelegt von

Ralph Echter

aus Aichach

Hauptberichter:	Prof. Dr.-Ing. habil. Manfred Bischoff, Stuttgart
Mitberichter:	Prof. Dr.-Ing. Kai-Uwe Bletzinger, München
Mitberichter:	Prof. Robert L. Taylor, Berkeley
Tag der mündlichen Prüfung:	04. Oktober 2013

Institut für Baustatik und Baudynamik der Universität Stuttgart

2013

Kurzfassung

Die vorliegende Arbeit befasst sich mit der Entwicklung einer hierarchischen Familie von Schalenmodellen und deren Diskretisierung basierend auf NURBS (Non-Uniform Rational B-Splines) Funktionen für die numerische Analyse von Schalenstrukturen.

Als mechanisches Basismodell wird eine mittelflächenparametrisierte 3-Parameter-Formulierung mit Kirchhoff-Lovescher Schalenkinematik verwendet. Diese eignet sich im Besonderen für die Modellierung von dünnen Schalen, deren Deformationsverhalten maßgebend durch Biege- und Membranverformungen bestimmt wird. Einflüsse aus Querschubverformungen und Dickenänderungen der Schale werden folglich nicht berücksichtigt. Für die Beschreibung der Kinematik genügen somit drei unabhängige Parameter, welche bei diesem Modell den drei Verschiebungskomponenten eines Materialpunktes der Mittelfläche entsprechen. Es werden keine zusätzlichen Rotationsfreiheitsgrade eingeführt, so dass die Schalenformulierung rotationsfrei ist.

Die verwendeten kinematischen Gleichungen beruhen auf der Annahme kleiner Verformungen. Zudem werden die Materialeigenschaften als linear-elastisch und isotrop definiert und über das Hookesche Konstitutivgesetz eine lineare, algebraische Beziehung zwischen den auftretenden Spannungen und Verzerrungen beschrieben. Für die asymptotische Korrektheit des Modells wird in den Materialgleichungen die Spannungsannahme $\sigma^{33} = 0$ zur Elimination von ε_{33} mit Hilfe statischer Kondensation verwendet. Die auf A.E.H. Love beruhende Hypothese, die Krümmungsanteile über die Dicke der Schale zu vernachlässigen, wird nicht berücksichtigt. Biege- und Membrananteile sind somit infolge der Nebendiagonalblöcke in der Materialmatrix gekoppelt. Desweiteren erfolgt keine Vorabintegration der konstitutiven Gleichungen, wodurch die auftretenden statischen und kinematischen Variablen in den Schalengleichungen den Spannungen und Verzerrungen und nicht deren Resultierenden entsprechen.

Mit zunehmender Schalendicke ist der Einfluss von Querschubdeformationen auf die Gesamtverformungen und damit auf die gesamte Verzerrungsenergie des Systems als wesentliche zusätzliche Größe zu beachten. Für das in dieser Arbeit entwickelte Schalenmodell mit Reissner-Mindlin-Kinematik, werden die Annahmen der kirchhoff-loveschen Schalenkinematik durch Einführen zusätzlicher, von den Verschiebungsableitungen unabhängigen Parametern erweitert. Das Einbringen dieser Parameter in die kinematischen Gleichungen erfolgt durch einen hierarchischen Differenzvektor und ermöglicht somit die Abbildung von Querschubeffekten. Aufgrund der Inextensibilitätsbedingung für den Schalendirektor in der aktuellen Konfiguration ist lediglich die Einführung von zwei zusätzlichen Parametern nötig. Um zu gewährleisten, dass die Reissner-Mindlin-Schale in Dickenrichtung während der Deformation weder gestaucht noch gedehnt wird, werden die Komponenten des Differenzvektors als Funktion der Basisvektoren der Schalenmittelfläche in der Referenzkonfiguration beschrieben.

Für die Berücksichtigung der Dickenänderung der Schale wird in dieser Arbeit zudem ein 7-Parameter-Schalenmodell entwickelt, welches einer Erweiterung des Reissner-Mindlin-Modells mit fünf Parametern entspricht. Das 7-Parameter-Modell ermöglicht eine Dehnbarkeit des Schalendirektors und besitzt sowohl konstante, als auch lineare Spannungs-

und Verzerrungskomponenten über die Schalendicke. Zudem entfällt die Notwendigkeit der Modifikation der Konstitutivgesetze. Dreidimensionale Materialgesetze können direkt verwendet werden.

Die wesentliche Neuerung und Innovation in dieser Arbeit ist die hierarchische Parametrisierung der Familie von 3-, 5- und 7-Parameter-Schalenmodellen, welche signifikante Vorteile im Hinblick auf Modelladaptivität und Elementtechnologie mit sich bringt. Üblicherweise wird bei schubweichen Reissner-Mindlin-Schalenelementen der Differenzvektor auf den Direktor der unverformten Konfiguration addiert. Dies führt zu geringeren Kontinuitätsanforderungen an die verwendeten Funktionsräume gegenüber jenen von Kirchhoff-Love-Schalenelementen. Im Fall einer reinen Verschiebungsformulierung tritt gleichzeitig Querschublocking auf, was in mehreren numerischen Beispielen verifiziert wird. Neben dieser in der Arbeit angewendeten Standardvorgehensweise wird eine hierarchische Parametrisierung des Reissner-Mindlin-Schalenmodells entwickelt. Eine vektorielle Größe, die physikalisch nur dem Schubanteil entspricht wird dabei auf die gedrehte Normale des Kirchhoff-Love-Modells addiert. Die kinematischen Gleichungen nach Kirchhoff-Love werden somit lediglich um den Schub erweitert, ohne dass eine komplette Neuformulierung, wie bei der nicht-hierarchischen Reissner-Mindlin-Schale, erforderlich ist.

Beide genannten Parametrisierungen beschreiben dasselbe Schalenmodell. Der hierarchische Ansatz folgt im Wesentlichen den Ausführungen von BAŞAR AND KRÄTZIG (1985) und wird für Reissner-Mindlin-Schalenelemente in ähnlicher Form in LONG ET AL. (2012) angewendet. Die ursprüngliche Absicht in BAŞAR AND KRÄTZIG (1985) war, über eine hierarchische Parametrisierung der Gesamtverformung mit unabhängigen Biege- und Schubanteilen aus Reissner-Mindlin-Schalenmodellen durch Vernachlässigen des Schubvektors Kirchhoff-Love-Theorien zu generieren. Im Hinblick auf das diskretisierte Modell führt die hierarchische Parametrisierung dazu, dass Reissner-Mindlin-Schalenelemente bereits bei einer reinen Verschiebungsformulierung durch die Entkopplung von Biege- und Schubdeformationen kein Querschublocking aufweisen.

Die hierarchische 7-Parameter-Formulierung stellt eine Erweiterung der hierarchischen 5-Parameter-Variante dar. Für die Berücksichtigung der Dickenänderung, sowie konstanter und linearer Normalverzerrungen in Dickenrichtung, wird das Reissner-Mindlin-Modell um einen sechsten und siebten Verschiebungsparameter angereichert, was zu einem quadratischen Verschiebungsverlauf über die Dicke führt. Durch systematisches Deaktivieren der sechsten und siebten Verschiebungsparameter kann andererseits aus der Kinematik des hierarchischen 7-Parameter-Modells jene der hierarchischen Reissner-Mindlin-Formulierung generiert werden. Wird darüber hinaus zusätzlich der hierarchische Differenzvektor entfernt, erhält man die kinematischen Schalengleichungen nach Kirchhoff-Love. Dies ermöglicht das gleichzeitige Verwenden aller drei Elementtypen innerhalb eines Finite-Elemente-Netzes je nach Bedarf und stellt somit eine ideale Grundlage für Modelladaptivität dar. In numerischen Experimenten kann zudem gezeigt werden, dass für die hierarchischen 7-Parameter-Schalenelemente dieser Arbeit, im Gegensatz zu den nicht-hierarchischen Schalenelementen, bei einer reinen Verschiebungsformulierung neben Querschublocking auch Krümmungs-Dicken-Locking automatisch vermieden wird.

Im Gegensatz zu den verminderten Kontinuitätsanforderungen an die Verschiebungs-funktionen der nicht-hierarchischen 5- und 7-Parameter-Schalenformulierungen, müssen alle hierarchischen Varianten die Anforderungen der schubstarren Kirchhoff-Love-Schale erfüllen, welches das Basismodell der hierarchischen Formulierungen ist. Ansatzfunktionen mit C^1-Kontinuität lassen sich jedoch ohne großen Aufwand mit den in dieser Arbeit verwendeten höher-kontinuierlichen NURBS Funktionen definieren. NURBS sind der im Bereich des CAD am weitesten verbreitete Funktionstyp und werden hier als Ansatzfunktionen der isogeometrischen Methode nach HUGHES ET AL. (2005) und COTTRELL ET AL. (2009) verwendet. Neben dem Erfüllen der Kontinuitätsanforderungen entsprechend dem Schalenmodell, erlaubt die Anwendung von NURBS mit höherer Kontinuität zudem eine eindeutige und punktweise exakte Definition des Schalendirektors im gesamten Gebiet.

In numerischen Experimenten wird der Einfluss von NURBS Diskretisierungen mit höherer Ordnung und Kontinuität auf die Genauigkeit der diskreten Lösungsfunktionen untersucht. Die dabei ermittelten Berechnungsergebnisse weisen gegenüber den C^0-kontinuierlichen Lösungen geringere Fehler auf. Des Weiteren werden die bei verschiebungsbasierten isogeometrischen finiten Schalenelementen am häufigsten vorkommenden Lockingphänomene einzeln untersucht. Neben dem bereits erwähnten Querschublocking und Krümmungs-Dicken-Locking, tritt bei allen entwickelten Elementformulierungen Membranlocking auf. Um dies zu vermeiden, werden zwei neue Strategien entwickelt, welche sich für NURBS Diskretisierungen mit beliebiger Kontinuität und Polynomordnung eignen. Zum einen wird die auf BLETZINGER ET AL. (2000) beruhende DSG-Methode für den Membrananteil der NURBS-basierten Schalenelemente weiterentwickelt, um sowohl Membran- als auch in-plane Schublocking zu vermeiden. Das zweite Verfahren basiert auf einem gemischten Verschiebungs-Spannungs-Ansatz auf Grundlage des Hellinger-Reissner-Zweifeldfunktionals. Die mit beiden Methoden modifizierten Kirchhoff-Love- und hierarchischen 5- und 7-Parameter-Schalenelemente sind völlig frei von geometrischen Lockingeffekten. Infolge kontinuierlicher Verzerrungs- und Spannungsfunktionen kann die NURBS-DSG-Methode zur Kopplung von Freiheitsgraden führen, was die Recheneffizienz negativ beeinflusst.

In mehreren Benchmarkbeispielen wird die Leistungsfähigkeit der neu entwickelten hierarchischen Schalenelemente gezeigt. Die Ergebnisse der Verschiebungsformulierungen stimmen dabei gut mit den Berechnungsergebnissen aus der Literatur überein, siehe zum Beispiel KIENDL ET AL. (2009). Durch das zusätzliche Beseitigen von Membranlocking kann zudem ein deutlich schnelleres Konvergenzverhalten der numerischen Schalenlösungen zu den Referenzergebnissen erzielt werden. Für komplexe Geometrien, welche die Definition mehrerer NURBS Flächenpatches erfordern, wird zur Kopplung von Patchen die in KIENDL ET AL. (2010) entwickelte "bending strip"-Methode verwendet. Bezüglich geeigneter Steifigkeitsparameter der bending strips wird auf die Auswertungen in KIENDL (2011) zurückgegriffen.

Bei der isogeometrischen Analyse von stark gekrümmten beziehungsweise dicken Schalenstrukturen lassen sich deutliche Unterschiede in den Berechnungsergebnissen der verwendeten Schalenmodelle (3-, 5- und 7-Parameter) feststellen. Der Einfluss aus Querschub und mechanischen Effekten höherer Ordnung nimmt jedoch mit zunehmender

Schlankheit der Schale schnell ab. Im Hinblick auf modelladaptive Diskretisierungen werden außerdem bei den hierarchischen Reissner-Mindlin-Schalenelementen jene Freiheitsgrade deaktiviert, welche zum Schubvektor gehören. Die dabei erhaltenen Berechnungsergebnisse stimmen exakt mit denen der schubstarren 3-Parameter-Schalenelemente überein.

Abstract

The present work addresses the development of a hierarchic family of shell models and accompanying discretization schemes with NURBS (Non-Uniform Rational B-Splines) functions that are suitable for the analysis of both thick and thin shell structures.

The hierarchy in the shell mechanics is based on a minimalistic 3-parameter formulation, which mechanically corresponds to the shear-rigid Kirchhoff-Love shell model. It is particularly suitable for modeling thin structures with predominantly membrane and bending action. Transverse shear effects and extensibility of the shell in thickness direction are not accounted for. The assumed linear kinematics of the thin shell can be described with three independent parameters, which correspond to the mid-surface displacement components of a material point. No rotations are defined as additional degrees of freedom such that the formulation is rotation-free.

Linear-elastic and isotropic material properties are assumed. For asymptotic correctness of the model the constitutive law is modified by implementing the stress condition $\sigma^{33} = 0$ to eliminate ε_{33} via static condensation. Additionally, Love's first approximation, neglecting contributions with regard to curvature in thickness direction of the shell is not considered. Consequently, membrane and bending action are coupled due to nonzero off-diagonal blocks in the constitutive matrix. No pre-integration of the material law is performed. The static and kinematic variables of the shell equations are therefore stresses and strains.

With increasing thickness of the structure, transverse shear effects become more pronounced, thus significantly contributing to the total strain energy of the system. For the Reissner-Mindlin shell model developed in this work, the Kirchhoff-Love assumption is relaxed by introducing additional parameters, which do not depend on the gradient of the mid-surface displacement field and thus allow for extra transverse shear effects. These parameters are introduced via a hierarchic difference vector. The inextensibility of the director in the deformed configuration reduces the number of additionally required parameters to two. In the geometrically linear case, the inextensibility constraint is constructed by expressing the components of difference vector with respect to the in-plane base vectors of the reference shell mid-surface.

In order to account for changes in thickness direction additionally, a 7-parameter shell formulation is derived, which represents an extension of the Reissner-Mindlin-type model with five parameters. The 7-parameter shell model incorporates extensibility of the director in thickness direction and enables the application of three-dimensional constitutive laws without the need of modifications.

The main innovation of this thesis is based on the hierarchic parametrization of the family of 3-, 5- and 7-parameter shell formulations, which results in significant benefits both with regard to model-adaptivity and finite element technology. The common approach in FEA consists of adding a difference vector on the director of the undeformed configuration. As a result, continuity requirements on the applied function spaces are reduced. It represents the first Reissner-Mindlin-type shell formulation to be used in this work. Equal-order interpolation of both the mid-surface displacement field and the

difference vector, however, results in transverse shear locking which is verified in several numerical plate bending experiments. Alternatively, a hierarchic parametrization is derived for the Reissner-Mindlin model that imposes a shear vector on the rotated director of the 3-parameter Kirchhoff-Love formulation. The procedure of adding the extra parameters is defined so that the kinematic equations of the basic Kirchhoff-Love model are gradually enhanced to obtain the shear flexible 5-parameter model, without the need of a complete new description of the shell kinematics.

Although exactly representing the same shell model, with regard to finite element discretization, the hierarchic parametrization of the current director avoids transverse shear locking already in a pure displacement formulation. The ansatz to split the total deformation of the Reissner-Mindlin shell model into independent components related to bending and shear in principal follows BAŞAR AND KRÄTZIG (1985) and was used in a similar way for shear-deformable subdivision-based shell finite elements in LONG ET AL. (2012). In BAŞAR AND KRÄTZIG (1985) the authors applied the decomposition of the rotation of the shell director into the contribution of the deformed shell normal (Kirchhoff-Love) and rotations related to shear. This allows to derive Kirchhoff-Love theories from shear deformation formulations by simply removing the transverse shear contribution. For FEA, this approach, moreover, offers the significant advantage of an independent parametrization of the transverse shear and consequently avoids incompatibilities of the discrete function spaces in the corresponding kinematic equations. For a decreasing shell thickness the solution asymptotically converges to the Kirchhoff-Love solution, whereas removal of the shear vector directly recovers the 3-parameter Kirchhoff-Love model.

The hierarchic 7-parameter shell formulation represents an extension of the hierarchic 5-parameter Reissner-Mindlin shell model. In order to account for extensibility of the director and linear transverse normal strains, the kinematics of the Reissner-Mindlin formulation is enriched with a 6th and 7th displacement parameter, which ultimately yields linear and quadric displacement contributions across the thickness. By switching off the linear and quadratic displacement contributions in thickness direction, the kinematics of the hierarchic 5-parameter Reissner-Mindlin model can be obtained, whereas further elimination of the difference vector yields the kinematic equations of the 3-parameter Kirchhoff-Love shell. This consequently allows for a straightforward combination of these three element types within one mesh and thus serves as an ideal basis for a model adaptive approach. Numerical experiments in this thesis demonstrate that besides transverse shear locking also curvature thickness locking is by default avoided in pure displacement-based 7-parameter shell finite elements due to the concept of a hierarchic parametrization. The non-hierarchic 7-parameter shell elements with pure displacement formulation and difference vector to be imposed on the director of the undeformed configuration are sensitive to both transverse shear and curvature thickness locking on the contrary.

The continuity requirements on the displacement functions for the proposed hierarchic 5- and 7-parameter shell models are identical to those of the 3-parameter Kirchhoff-Love formulation, i.e. C^1. The demand for shape functions with square integrable partial derivatives of order two, however, can be naturally satisfied with the higher-continuity

NURBS discretizations used in this work. NURBS which represent the standard functions of computer-aided engineering design are applied as shape functions in an isoparametric finite element concept following the isogeometric method of Hughes and coworkers (HUGHES ET AL. (2005), COTTRELL ET AL. (2009)). Their higher continuity property additionally enables a pointwise exact definition of the shell director in the entire patch domain.

The effect of higher-order and higher-continuity NURBS discretizations on the accuracy of the discrete solution functions is investigated and analyzed in several numerical experiments. Computational results of higher-continuity NURBS are provided to demonstrate the superior accuracy compared to C^0-continuous discretizations. Additionally, analysis of the most prominent locking effects that may show up for the displacement-based isogeometric shell finite elements reveals that the in-plane part of all shell elements developed in this thesis is, in general, considerably prone to locking. Therefore, two new strategies to remove geometric locking effects from higher-order and higher-continuity NURBS discretizations were developed and applied to the membrane part of the shell elements to cure locking: First, the DSG approach of BLETZINGER ET AL. (2000) was successfully transferred to higher-order and higher-continuity NURBS discretizations in order to remove membrane and in-plane shear locking. Second, a mixed displacement-stress formulation which is based on a two-field Hellinger-Reissner variational principle with independent displacement and stress fields is applied to the in-plane strain components of the shell elements. The modified isogeometric Kirchhoff-Love and hierarchic 5- and 7-parameter shell formulations are completely free from geometric locking. Higher-continuity NURBS shape functions to be used for the discretization of the displacement fields in general result in continuous strain and stress distributions which in the case of the NURBS-DSG method may result in a coupling of degrees of freedom that compromises computational efficiency.

In several benchmark problems the performance of the newly developed hierarchic shell elements is proven. For the displacement-based element formulations the numerical results conform well with the results from literature like for example from KIENDL ET AL. (2009). Modification of the membrane part with the mixed displacement-stress ansatz successfully removes locking and leads to significantly faster convergence of the investigated results to the reference solutions. For multipatch analysis, the penalty-type bending strip method of KIENDL ET AL. (2010) is used to connect NURBS surface patches with slope continuity in a weak sense. Appropriate stiffness parameters for the bending strips are defined according to KIENDL (2011).

The isogeometric analysis of highly-curved respectively thick shell structures reveals significant differences in the system response for the three different shell models (3-, 5- and 7-parameter). Simultaneously, a fast diminution of the influence of both transverse shear and higher-order mechanical effects on the investigated displacement results can be observed. For model adaptivity, analysis of the same problem setup is performed with hierarchic 5-parameter Reissner-Mindlin shell elements by systematically deactivating those degrees of freedom related to the shear vector. The computational results obtained, perfectly match the 3-parameter Kirchhoff-Love solution.

Abstract

Danksagung

Die vorliegende Arbeit entstand in der Zeit von 2007 bis 2013 während meiner Tätigkeit als wissenschaftlicher Mitarbeiter am Institut für Baustatik und Baudynamik der Universität Stuttgart. In dieser Zeit durfte ich an diesem renommierten Institut in einem hervorragenden Umfeld arbeiten.

Meinem Doktorvater Herrn Professor Manfred Bischoff möchte ich an dieser Stelle außerordentlich herzlich für die Möglichkeiten danken, die er mir an seinem Institut eröffnet hat. Er hat eine Atmosphäre geschaffen, in der ich mich stets sehr wohl gefühlt und gerne gearbeitet habe. Von seiner fachlichen Kompetenz, seinem Vertrauen und Rückhalt, sowie der stetigen Förderung meiner wissenschaftlichen Arbeit habe ich nicht nur wissenschaftlich sehr profitieren können. Auch seine menschliche Größe und sein Charakter sind beispielhaft und waren für mich persönlich eine Bereicherung für die ich sehr dankbar bin.

Herrn Professor Robert L. Taylor und Herrn Professor Kai-Uwe Bletzinger danke ich für die Übernahme des Mitberichts, die gründliche Durchsicht des Manuskripts sowie ihre Kommentare und Verbesserungsvorschläge. Ihr Interesse an meiner Arbeit ist mir eine große Ehre und hat mich sehr gefreut.

Mein herzlicher Dank gilt auch Herrn Professor Ekkehard Ramm für die motivierenden fachlichen Diskussionen und Anregungen zu meiner Arbeit und die persönlichen privaten Gespräche abseits wissenschaftlicher Themen. Vielen Dank dafür.

Meinen Kollegen danke ich für das freundschaftliche und angenehme Arbeitsklima, die fachlichen Diskussionen, die große Hilfsbereitschaft jederzeit und vor allem für die guten privaten Gespräche und schönen gemeinsamen Unternehmungen. Ein großer Dank an Johannes Irslinger, der mir stets mit guten fachlichen Ratschlägen zur Seite stand und große Teile meiner Doktorarbeit Korrektur las.

Von ganzen Herzen danke ich meinen lieben Eltern und meiner lieben Britta für ihr Vertrauen, ihre Unterstützung, ihre liebevolle Art und die vielen schönen Momente im privaten Umfeld.

Stuttgart, im Dezember 2013   Ralph Echter

Contents

Contents

List of Figures

List of Tables

Nomenclature

The symbols and abbreviations which are frequently used within this thesis are explained in the following enumeration. Quantities which occur rarely throughout the text are introduced in the corresponding context.

Vectors, matrices and second-order tensors are labeled with bold Greek or Latin letters. Scalar quantities are defined in standard notation. For higher-order tensorial quantities, capital blackboard bold letters are employed. Einstein summation convention is used for the spatial components of quantities with small Latin indices (i, j, k, l) running from 1 to 3 and Greek indices (α, β) taking on values 1 or 2. All other sums in this thesis are explicitly defined by the summation symbol $\sum$. For the notation to be used for the tensorial equations, in particular the definitions of contraction, dyadic product, product rule, divergence theorem and partial integration, the reader is referred to Appendix A.1.

Abbreviations

1D	One dimensional
2D	Two dimensional
3D	Three dimensional
3p, 5p, 7p	3-, 5-, 7-parameters
ANS	Assumed Natural Strain
B-splines	Basis splines
CAD	Computer-Aided Design
CAM	Computer-Aided Modeling
CG	Conjugate gradient

d.o.f.	Degree of freedom
DSG	Discrete Strain Gap
ex	Exact
ext	External
EAS	Enhanced Assumed Strain
FEA	Finite element analysis
Gp	Greville points, Marsden-Schoenberg points
hier.	Shell models with difference vector imposed on rotated director
HR	Hellinger-Reissner
IGA	Isogeometric Analysis
int	Internal
lin	Linear, linearized
mixed	Mixed $\mathbf{u}$-$\boldsymbol{\sigma}$-approach
NURBS	Non-Uniform Rational Basis Splines
PK2	Second Piola-Kirchhoff stress tensor
Pvw	Principle of virtual work
inf, sup	Infimum, supremum
stand.	Shell models with difference vector imposed on undeformed director
BB, LBB	Babuška-Brezzi condition, Ladyzhenskaya-Babuška-Brezzi condition

Mathematical symbols

$\| \bullet \|$	Euclidean norm
$\frac{\partial(\bullet)}{\partial k}, (\bullet)_{,k}$	Partial derivative of $(\bullet)$ with respect to argument k
$\times$	Cross product
$\otimes$	Tensor product
$\mathrm{d}(\bullet)$	Infinitesimal element (line, area, volume)
$\det(\bullet)$	Determinant of $(\bullet)$
$\mathrm{div}(\bullet)$	Divergence of $(\bullet)$
$\mathrm{grad}(\bullet)$	Gradient of $(\bullet)$
$\mathrm{tr}(\bullet)$	Trace of $(\bullet)$
$(\bullet)^{\mathrm{T}}$	Transpose of $(\bullet)$
$(\bullet)^{-1}$	Inverse of $(\bullet)$
$(\bullet \cdot \bullet)$	Single contraction of two vectors, tensor and vector
$(\bullet : \bullet)$	Double contraction of two tensors
$\cup$	Union of sets
$\cap$	Intersection of sets
$\varnothing$	Empty set
$\forall$	For all
$\delta(\bullet)$	Variation of $(\bullet)$, virtual quantity

$\delta_i{}^j$	Kronecker delta in mixed-variant form
$\in$	Element of
$\sqrt{(\bullet)}$	Square root of $(\bullet)$
$\mathbb{A}$	Assembly operator

Latin letters

$\mathbf{0}$	Origin of Cartesian basis
$\mathbf{A}_i, \mathbf{A}^i$	Co-, contravariant base vectors of shell mid-surface, reference configuration
$\mathbf{a}_i, \mathbf{a}^i$	Co-, contravariant base vectors of shell mid-surface, current configuration
$\overline{\mathbf{b}}$	Body force per unit volume
$b(\bullet, \bullet)$	Bilinear form, e.g. to express deformation energy
$\mathcal{B}$	Material body
$\partial \mathcal{B}$	Boundary of $\mathcal{B}$
$\mathbf{B}$	Strain-displacement matrix
$\mathbf{B}_p$	Set of univariate B-spline basis functions of order p
$\mathbf{B}_p^{(b)}$	B-th derivative of $\mathbf{B}_p$
$\hat{\mathbf{B}}_p$	Set of "linked" B-spline basis functions of order p
$cn^{\text{cont.}}, cn$	Constraint ratio of continuous and discrete model
$\mathbb{C}, C^{ijkl}$	Fourth order material tensor, contravariant coefficients
C^p	Continuity of order p of NURBS basis
$\mathbf{C}(\xi), \mathbf{C}^w(\xi)$	NURBS curve object, weighted B-spline curve object
$\mathbf{d}$	Vector of discrete control point displacements
$(\bullet)^{\text{h}}$	Discrete form of quantity $(\bullet)$
$e_{u^{\text{h}}}$	Relative error in displacements
$\|e_u\|_{L^2}$	Exact error in displacements in L^2-norm
E	Young's modulus
$\mathbf{e}_i$	Covariant Cartesian base vectors
$\mathbf{E}, E_{ij}$	Nonlinear Green-Lagrange strain tensor, covariant coefficients
$\mathbf{f}$	Discrete force vector
$F(\bullet), f(\bullet),$	Linear forms, e.g. to express work of body forces
$\mathbf{F}$	Material deformation gradient
$\mathbf{G}_i, \mathbf{G}^i$	Co-, contravariant base vectors of body, reference configuration
$\mathbf{G}$	Metric tensor
G_{ij}, G^{ij}	Co-, contravariant metric coefficients of body, reference configuration
$\mathbf{g}_i, \mathbf{g}^i$	Co-, contravariant base vectors of body, current configuration
g_{ij}, g^{ij}	Co-, contravariant metric coefficients of body, current configuration
$\mathbf{L}$	Material gradient of $\mathbf{F}$
$\mathcal{H}^n$	Sobolev space of functions with square integrable derivatives up to order n

$\mathbf{I}$	Identity tensor
J	Jacobian
K	Bulk modulus
$\mathbf{K}$	Stiffness matrix
L^2	Sobolev space of square-integrable functions
$\mathcal{M}$	Material points
$\mathbf{M}_{r,s}$	Set of bivariate NURBS basis functions for membrane stress fields
$\mathbf{n}$	Normal vector of current configuration
$\mathbf{N}_p$	Set of univariate NURBS basis functions of order p
$\mathbf{N}_{p,q}$	Set of bivariate NURBS basis functions of order p and q
$\mathcal{P}$	Spatial point
$\mathbf{P}$	Set of control points of NURBS curve and surface objects
p, q	Polynomial degree of basis functions in ξ- and η-direction
$\mathbb{R}^n$	Euclidean space of dimension n
$\mathbf{R}$	Position vector of shell mid-surface, reference configuration
$\mathbf{r}$	Position vector of shell mid-surface, current configuration
$\mathbf{S}, S^{ij}$	Second Piola-Kirchhoff stress tensor, contravariant coefficients
$\mathbf{S}(\xi, \eta)$	NURBS surface object
t	Time, thickness in reference configuration
$\mathbf{t}$	Traction vector
$\overline{\mathbf{t}}$	Prescribed tractions
$\mathbf{T}$	Transformation matrix of stress components
$\mathbf{u}$	Displacement vector
$\overline{\mathbf{u}}$	Prescribed displacements
$\mathcal{U}$	Function space with continuous functions of $\mathcal{H}^1$
$\mathbf{v}$	Mid-surface displacement vector
$\mathcal{W}^{\mathrm{int}}(\mathbf{E})$	Strain energy density function
x, y, z	Global Cartesian coordinates
$\mathbf{X}$	Position vector of body, reference configuration
$\mathbf{x}$	Position vector of body, current configuration
$\{w_i\}$	Set of weights, homogenous coordinates of control points
W	Weighting function
$\mathbf{w}^{\mathrm{5p-stand.}}$	Difference vector of 5p shell imposed on undeformed director
$\mathbf{w}^{\mathrm{5p-hier.}}$	Difference vector of 5p shell imposed on rotated director
$\mathbf{w}^{\mathrm{6p}}$	Linear displacement field across the thickness of 7p shells
$\mathbf{w}^{\mathrm{7p}}$	Quadratic displacement field across the thickness of 7p shells

Greek letters

γ	Shear angle
γ_i	Coefficients of knot refinement, respectively order elevation
θ^i	Curvilinear convective coordinates
ξ, η, ζ	Parametric coordinates
κ	Curvature
λ, μ	Lamé constants
ν	Poisson's ratio
$\boldsymbol{\varepsilon}, \varepsilon_{ij}$	Linearized Green-Lagrange strain tensor, covariant coefficients
$\boldsymbol{\Xi}, \mathbf{H}$	Knot vectors
ξ_i, η_i	Knot values of vectors $\boldsymbol{\Xi}, \mathbf{H}$
π	Circle number
$\Pi^{\text{int}}(\boldsymbol{\varepsilon}(\mathbf{u}))$	Internal potential energy, strain energy
$\Pi^{\text{ext}}(\mathbf{u})$	External potential energy
$\delta\Pi_{\text{Pvw}}$	Principle of virtual work
$\delta\Pi_{\text{HR}}$	Principle of Hellinger-Reissner
ρ	Mass density of body
$\boldsymbol{\sigma}, \sigma^{ij}$	Cauchy stress tensor, contravariant coefficients (curvilinear)
$\overline{\sigma}^{ij}$	Contravariant coefficients (local Cartesian)
τ, τ^{-1}	Mapping function, homeomorphism and inverse
$\boldsymbol{\Upsilon}$	Mapping from reference to current configuration
φ	Cross sectional rotation of Timoshenko beam
$\boldsymbol{\Phi}, \varphi_\alpha$	Rotation vector of director $\mathbf{A}_3$ and rotation angles
$\boldsymbol{\omega}$	Vector of stress parameters
Ω	Spatial domain, configuration
Ω_0	Reference, initial configuration
Ω_t	Current, deformed configuration
$\partial\Omega$	Boundary of Ω
$\partial\Omega_\sigma$	Neumann traction boundary of Ω
$\partial\Omega_u$	Dirichlet displacement boundary of Ω
$\tilde{\Omega}_{\text{e}}$	Spatial element domain
$\tilde{\Omega}_{\text{pa}}$	Parametric patch domain
Ω_{pa}	Spatial patch domain

1

Introduction

1.1 Motivation

Curved thin-walled structures represent a fundamental construction element in both nature and technology. Examples range from eggshells, cell walls or the leaves of plants to shell structures in engineering, such as in the automotive industry, aircraft construction, aerospace technology or civil engineering.

Figure 1.1: Shells in nature and technology (WIKIPEDIA (2013a), WIKIPEDIA (2013b), WIKIPEDIA (2013c)).

Shell structures are three-dimensional continua, with one dimension being significantly smaller than the remaining two. Due to curvature, shells are able to carry transverse load with membrane action and thus make optimal use of the material. This ultimately yields highly optimized and efficient structures that may be built very slender with excellent load-carrying capacity. Exploitation of this property, however, brings in significant sensitivities to imperfections with respect to both geometry and loading. Small changes in the input parameters of shell design and type of loading may result in large changes of the system response.

Since the 18th century, large efforts have been made to properly describe the load-carrying behavior of shells. Initially, descriptive-mechanical considerations were replaced more and more by mathematical and theoretical analysis. Nowadays, in particular numerical methods are applied for the analysis of shells. Within the finite element method to be used in this thesis, one of the first elements with Kirchhoff-Love kinematics was the SHEBA element of ARGYRIS AND SCHARPF (1968). The continuity requirements on the displacements were accounted for by using polynomial shape functions of fifth-order, which consequently led to a complex element formulation. Yet another early Kirchhoff-Love-type finite element is the Bogner-Fox-Schmit (BFS) plate element that is based on higher-order Hermitian shape functions (BOGNER ET AL. (1960)). For unstructured meshes that are based on local polynomials, displacements and their derivatives as nodal degrees of freedom, the required C^1-continuity of the basis functions cannot be satisfied at inter-element boundaries (ZIENKIEWICZ AND TAYLOR (2005)). If independent shear deformations according to REISSNER (1945) and MINDLIN (1951) are additionally accounted for in the shell kinematics, the continuity requirements on the applied shape functions reduce to C^0. This ansatz leads to first-order theories, which enable the application of shape functions with square integrable first-order partial derivatives. The advantage of lower continuity basis functions is compromised, however, by the existence of serious ill-conditioning in discrete constrained problems, which arise from the mismatch of function spaces to be used for the interpolation of the primary field variables while the underlying mathematical problem is well-posed.

The idea to break up the established use of low-order and low-continuity polynomial bases in finite element analysis is not entirely new. Higher-order and higher-continuity splines have already been used as element shape functions since at least the 1970s. In SWARTZ AND WENDROFF (1974), spline-based element formulations were compared to finite difference methods for time dependent problems. PRENTER (1975) presented variational methods and numerical schemes for finite element and collocation methods on the basis of spline spaces. Elastic composite plate structures were analyzed in CHUNG-TZE (1979) by using cubic B-splines as a finite element basis. The author identified improved accuracy compared to conventional finite element discretizations and savings in both memory requirements and computational costs. B-spline-based finite elements for the analysis of shells of revolution were developed in FAN AND LUAH (1990). Although several publications on spline finite elements have been published for more than 40 years, the seminal paper of Hughes and coworkers on isogeometric analysis (IGA) (HUGHES ET AL. (2005)) was probably the first to cast the idea of integrating popular methods of CAD and analysis into a uniform and consistent concept. The application of the significantly richer functions of CAD to FEA improves the accuracy of discrete solutions, compared to standard C^0-continuous discretizations, which was first documented for structural and fluid mechanics problems in HUGHES ET AL. (2005), COTTRELL ET AL. (2006) and COTTRELL ET AL. (2007). With regard to shell analysis, these func-

tions offer completely new capabilities and potential. The higher-continuity property of NURBS to be used in this thesis allows for the straightforward formulation of Kirchhoff-Love shell elements, and enables the pointwise exact definition of the shell director in the entire domain, which consequently annihilates the aforementioned problems of constructing elements with higher-order derivatives.

Cirak and coworkers derived shell finite elements with Kirchhoff-Love kinematics based on CAD-exact smooth C^1-continuous subdivision surfaces for the analysis of thin and moderately thick shell structures (CIRAK ET AL. (2000)). The main drawback of subdivision techniques, which originate from the animation industry, is their lack of compatibility with NURBS that on their part represent the standard tool in engineering design. In LONG ET AL. (2012), a further subdivision discretization scheme was developed. The formulation accounts for both Reissner-Mindlin and Kirchhoff-Love kinematics by introducing a shear vector that is superimposed on the deformed shell normal vector to model the structural behavior of thick shells. An independent parametrization of the mid-surface displacements and the shear vector avoids incompatibilities in the discrete model a priori and thus transverse shear locking. Removing the entire shear vector recovers the Kirchhoff-Love shell kinematics.

The first NURBS-based isogeometric shell element with nonlinear Kirchhoff-Love kinematics was presented in KIENDL ET AL. (2009). The element formulation is rotation-free and thus based on mid-surface displacement degrees of freedom only. Modeling of clamped edges and symmetry boundary conditions is performed by constraining those displacement degrees of freedom of the adjacent rows of control points, which are required to fix the tangent. No finite element technology is introduced in the shell formulation to avoid membrane locking. The shell element retains a pure displacement ansatz. In multipatch FEA, the authors suggest the application of constraint equations for the control points along common edges in order to preserve the higher continuity at patch interfaces. The subsequent paper, KIENDL ET AL. (2010), alternatively introduced a penalty-type method denoted as "bending strip" to couple multiple NURBS surface patches in a weak sense for thin shell analysis.

An isogeometric NURBS-based Reissner-Mindlin shell was presented in BENSON ET AL. (2010), which, compared to the ansatz of Kiendl, additionally accounts for transverse shear effects and is thus more convenient for thick shell analysis. The formulation is based on the concept of degeneration. Again, no modification of the pure displacement ansatz is performed, so that the shell element is prone to both transverse shear and membrane locking. In the shell kinematics, the director vectors are not constructed exactly from the surface tangent space, but are computed approximately by closest point projections onto the shell surface. The directors thus may deviate significantly from the orientation of the shell normal. BENSON ET AL. (2011) therefore introduced a "lifting operator". By solving a linear equation system, this operator satisfies the condition that the exact normals to be computed at the integration points by the cross product

of the in-plane tangent vectors coincide with the values at the integration points to be obtained from the interpolation of the control point directors. This approach, however, is confined to Kirchhoff-Love-type shell elements.

DORNISCH ET AL. (2013) derived an isogeometric Reissner-Mindlin shell with exactly calculated director vectors. The element formulation utilizes additional rotational degrees of freedom and allows for both geometric and material nonlinearities. It is derived from continuum theory. The authors established exact nodal basis systems for every control point for both the interpolation of the director and the correct definition of the rotation axes related to the rotational degrees of freedom. In a preprocessing step, an equation system has to be solved for every patch in order to ensure orthonormality of the interpolated basis system at quadrature points and a correct orientation of both the director and the rotation axes. This strategy appears to have similarities to the "lifting operator"-approach of BENSON ET AL. (2011). Like the isogeometric shell of BENSON ET AL. (2010), the Reissner-Mindlin shell of Dornisch and coworkers retains a pure displacement ansatz and is therefore sensitive to locking.

An isogeometric shell formulation denoted as "blended shell theory" was defined in BENSON ET AL. (2013). The ansatz essentially combines the developments of BENSON ET AL. (2010) and BENSON ET AL. (2011) as linking together the shell theories of Kirchhoff-Love and Reissner-Mindlin by a linear combination of the kinematics of both models. The main intention is to use the Kirchhoff-Love model in regions which are dominated by membrane and bending action, whereas Reissner-Mindlin kinematics are accounted for in areas where transverse shear has a significant influence, i.e. in non-smooth domains of low continuity, such as folds, intersections or boundaries. The crucial point of the blended shell is based on the definition of the director. Whereas for the Kirchhoff-Love ansatz the constraint of the deformed director to remain normal to the mid-surface is imposed, the Reissner-Mindlin shell additionally accounts for independent rotations to model transverse shear effects. The idea of applying the Reissner-Mindlin model to regions of high curvature and using Kirchoff-Love elsewhere yields significant savings of degrees of freedom and consequently computational efficiency. In the blended shell element of BENSON ET AL. (2013) again no action is taken to avoid both geometric and material-based locking effects.

1.2 Scope and objective

In this thesis, a new hierarchic family of 3-, 5- and 7-parameter shell models and their discrete formulations are developed.

The expression "hierarchic" on the one hand implies a hierarchy in the mechanical model. The main innovation of the term "hierarchic" to be used in this work, however, is re-

lated to a hierarchic parametrization of the family of shell formulations with regard to model-adaptivity. Based on a minimalistic ansatz with three independent parameters which mechanically represents the Kirchhoff-Love shell kinematics suitable for modeling thin structures with predominantly membrane and bending action, additional degrees of freedom can be activated systematically to improve the approximation quality of the shell model. The procedure of adding the extra parameters is defined so that the kinematic equations of this basic formulation can be gradually enhanced to generate the shear flexible 5-parameter model, also known as Reissner-Mindlin kinematics, which is more accurate for describing the structural behavior of thick shells. In order to account for higher-order and three-dimensional effects, ultimately a 7-parameter shell is derived from the 5-parameter formulation, without the need of a completely new description of the shell kinematics.

The idea to split the entire director deformation of shear deformable structures into individual components related to bending and shear is quite natural and was frequently used in classical theories on beams, plates and shells for more than fifty years. In BAŞAR AND KRÄTZIG (1985), although not the first textbook on this topic, this split of the entire rotation of the shell director in a contribution with respect to the deformed shell normal (Kirchhoff-Love) and an additional rotation related to shear is described in an illustrative manner. The original motivation was to derive Kirchhoff-Love theories from shear deformation formulations by simply removing the transverse shear contribution. This approach, moreover, offers the possibility of an independent parametrization of the shear in finite element analysis and consequently avoids incompatibilities of the discrete function spaces in the kinematic equations for the transverse shear and thus shear locking in a pure displacement ansatz. For the 3D shell with 7 parameters, the hierarchic concept additionally removes curvature thickness locking, which will be demonstrated in more detail in Chapter 5. For reasons of comparison, 5- and 7-parameter shells with non-hierarchic, but conventional parametrization are derived, where the difference vectors are imposed on the undeformed director.

The shell models of this thesis are mainly based on the concept of degeneration to be specified in more detail in Section 4.1.3. The discretization of the shell equations follows the isogeometric approach of HUGHES ET AL. (2005) by using NURBS shape functions for both the geometry and the solution fields. Despite the CAD exact geometry representation in the analysis environment, the aforementioned higher-order and higher-continuity properties of NURBS enable the straightforward definition of Kirchhoff-Love shell elements with higher-order derivatives of the displacement field, and in addition, a pointwise exact shell director in the whole patch domain. Whereas the conventional parametrization of Reissner-Mindlin kinematics only requires C^0-continuous functions for the well-posedness of the underlying mechanical problem, the hierarchic shear-deformable 5- and 7-parameter shells require at least C^1-continuous functions due to the 3-parameter Kirchhoff-Love-type base model.

The new possibilities and advantages in finite element analysis with higher-order and higher-continuity NURBS discretizations with regard to finite element technology and, especially in the context of eliminating locking imply considerably higher complexity. Higher-continuity discretizations of primary solution variables result in derived quantities, such as stresses and strains, which are again continuous and thus require unlocking procedures that take into account information on patch level rather than on element level. The strategies developed in Chapter 6 completely remove geometric locking effects from the in-plane part of the hierarchic shell elements with pure displacement ansatz and thus yield locking-free isogeometric shell formulations.

1.3 Overview

This introduction concludes with an outline of the individual chapters in order to provide an overview of the subsequent matters and the structural setup of this thesis.

In Chapter 2, the governing equations of differential geometry and non-polar continuum mechanics of solids are presented, which yield a set of coupled partial differential equations. The strong form of the field equations of solid continua are subsequently reformulated by means of variational methods. For the formulation of displacement-based isogeometric shell finite elements, the principle of virtual work is used, whereas the two-field Hellinger-Reissner principle forms the variational basis for a mixed displacement-stress formulation to remove locking.

Chapter 3 introduces the topic of NURBS, which represent the standard function type used in engineering design and which, for analysis, will be applied to both shell geometry representations and discretizations of the solution functions. Therefore, the concepts of knot vectors, patches, control polygons and projective geometry are introduced. Furthermore, several strategies for a systematic modification of the NURBS basis and thus the geometric object are presented. These are also utilized to control the discrete solution spaces of physical quantities.

By taking into account the derivations of Chapter 2 for solid continua, a new hierarchic family of 3-, 5- and 7-parameter shell models is developed in Chapter 4; see also ECHTER ET AL. (2013). Starting from a basic shell model with three independent parameters which mechanically represents the Kirchhoff-Love kinematics, additional parameters are systematically added to improve the approximation quality of the shells. The procedure of adding the extra degrees of freedom is performed so that the kinematic equations of the basic model are gradually enhanced to generate the 5- and 7-parameter models, without the need of a completely new description of the shell kinematics. Additionally, 5- and 7-parameter shell models with non-hierarchic difference vector formulation are established for reasons of comparison.

Chapter 5 covers the discrete formulation of the shell equations of Chapter 4 by using the NURBS function definitions of Chapter 3 in an isogeometric concept. The resulting algebraic equations represent pure displacement formulations. Besides investigating the effect of higher-order and higher-continuity NURBS discretizations on the accuracy of the discrete solution functions, a systematic analysis with regard to locking of the displacement-based NURBS shell elements of this thesis is carried out.

The numerical experiments of Chapter 5 reveal that, along with an improved accuracy of the higher-continuity NURBS shell discretizations, the membrane part of the hierarchic shell elements with pure displacement ansatz is considerably prone to locking. Therefore, in Chapter 6, two methods are developed which successfully remove geometric locking from the in-plane part of the shell finite elements of this work for both higher-order and higher-continuity NURBS discretizations (ECHTER AND BISCHOFF (2010), ECHTER ET AL. (2013)). The first approach generalizes the discrete strain gap (DSG) method of KOSCHNICK ET AL. (2002) and BISCHOFF ET AL. (2003) to higher-continuity NURBS, whereas the second ansatz relies on a mixed displacement-stress formulation based on a two-field Hellinger-Reissner variational principle. The resulting hierarchic NURBS shell elements with modification of the membrane part are completely free from any geometric locking effects.

In Chapter 7, more complex numerical examples with multiple NURBS patches are analyzed in order to investigate the efficiency of the new isogeometric shell element formulations.

Chapter 8 provides a summary of the developments in the thesis along with conclusions and indications of future work.

In Appendix A.1, further mathematical background on vector and tensor algebra fundamentals is presented.

2

Continuum Mechanics, Differential Geometry

In this chapter, the governing equations of differential geometry and non-polar continuum mechanics of three-dimensional solids are presented to an extent required within this thesis and to establish a uniform notation. The balance laws used in this work are confined to mechanical problems and serve as a basis for the material-independent formulation of the deformation processes of solids.

First, the fundamentals of elementary differential geometry required to describe geometric configurations of deformable solid bodies in space are introduced. Without considering microscopic physical effects, the principal equations of motion and deformation, i.e. the kinematics of continuous solid media are defined in material (Lagrangian) description.

Based on the concepts of configuration and motion of continuous bodies, appropriate strain measures and strain-displacement relations are established as one of the field equations of continuum mechanics.

The interaction of material within a body during deformation results in the notion of a stress state. By applying Cauchy's stress theorem, surface tractions are uniquely related to second-order stress tensor fields. Additionally, relevant alternative stress tensors are defined.

From the momentum balance laws and Cauchy's stress theorem, the equilibrium equations of elastostatics as the second field equation are subsequently derived.

The third functional field equation of continuum mechanics to be introduced is the constitutive law in order to sufficiently describe the response of a material and to specify the stress-strain relationship.

Finally, the governing equations which consist of kinematics, equilibrium and material

law are reformulated by means of variational and energy principles. They serve as a basis for the development of numerical approximation and discretization methods as the finite element method to be used within this thesis.

A more comprehensive treatment of the basics of both differential geometry and continuum mechanics for solids and structures is covered, for instance, in HSIUNG (1981), KREYSZIG (1991), CIARLET (2006), MARSDEN AND HUGHES (1983), CIARLET (1988), ALTENBACH AND ALTENBACH (1994), STEIN AND BARTHOLD (1996), HOLZAPFEL (2000), ZIENKIEWICZ ET AL. (2005).

2.1 Elementary differential geometry

Differential geometry which relates the mathematical branches of analysis and geometry enables an elegant analytic investigation of the geometric properties of point sets by using methods of infinitesimal, i.e. differential and integral calculus.

For all quantities and relations introduced to describe the configuration and motion of a material body $\mathcal{B}$ in 3D Euclidean space $\mathbb{R}^3$, the concept of classical differential geometry is applied. A material body $\mathcal{B}$ in continuum mechanics corresponds to a contiguous set of material points $\mathcal{M}$. Its boundary is denoted with $\partial \mathcal{B}$.

An orientation in space $\mathbb{R}^3$ is defined with the introduction of a fixed orthogonal Cartesian coordinate system. Its orthonormal basis $\mathbf{e}_i$ is pointing in the direction of the coordinate axes and the reference point $\mathbf{0}$ is coincident with the origin of the Cartesian basis. Thus the position of every spatial point $\mathcal{P}$ relative to the origin $\mathbf{0}$ is uniquely associated with a position vector $\mathbf{X}$ as the linear combination of material convective coordinates X^i and base vectors $\mathbf{e}_i$, as shown in Figure 2.1. In this work, Latin indices run from 1 to 3 and Greek indices take on the values 1 or 2.

$$\mathbf{X} = X^i \, \mathbf{e}_i, \quad \text{with} \quad \mathbf{e}_i = \mathbf{e}^i, \, \|\mathbf{e}_i\| = 1 \tag{2.1}$$

The symbol $\|(\bullet)\|$ in Equation (2.1) denotes the Euclidean norm of $(\bullet)$ in $\mathbb{R}^3$. Consequently a bijective, i.e. continuous and invertible map τ, which in mathematical literature is frequently denoted as homeomorphism, may be defined. It uniquely associates to every material point $\mathcal{M} \in \mathcal{B}$ for every point in time a corresponding point $\mathcal{P}$ in Euclidean space $\mathbb{R}^3$ labeled with a position vector $\mathbf{X}$. For a fixed moment in time, the mapping τ of $\mathcal{B}$ to its image Ω in $\mathbb{R}^3$ represents a configuration which is specified in Equation (2.2)

$$\tau : \begin{cases} \mathcal{B} \to \Omega \subset \mathbb{R}^3 \\ \mathcal{M} \mapsto \mathbf{X} = \tau \, (\mathcal{M}) \, . \end{cases} \tag{2.2}$$

The inverse mapping of spatial points of $\mathbb{R}^3$ to the material points $\mathcal{M} \in \mathcal{B}$ exists as well and is denoted with τ^{-1}. Moreover, convective curvilinear coordinates are introduced in order to adequately describe the geometry and kinematics of the curved structural objects in this thesis. Therefore each point $\mathcal{P} \in \mathbb{R}^3$ can be uniquely identified by the co-ordinates θ^i. The position vector $\mathbf{X}$, which in Equation (2.1) is related to the Cartesian basis $\mathbf{e}_i$ in curvilinear convective coordinates reads

$$\mathbf{X} = \mathbf{X}\left(\theta^i\right). \tag{2.3}$$

The partial derivative of $\mathbf{X}$ with respect to θ^i yields the covariant base vectors $\mathbf{G}_i$, which represent tangents to the coordinate lines θ^i and in contrast to $\mathbf{e}_i$, are in general not orthonormal. The expression $(\bullet)_{,k}$ corresponds to the partial derivative of a quantity $(\bullet)$ with respect to the argument k.

$$\mathbf{G}_i = \mathbf{X}_{,i} = \frac{\partial \mathbf{X}}{\partial \theta^i} = \frac{\partial X^j}{\partial \theta^i}\,\mathbf{e}_j \tag{2.4}$$

The base vectors $\mathbf{G}_i$ define a tangent vector space at every point $\mathcal{P}$ and enable the derivation of important local geometric properties to be specified later in this section.
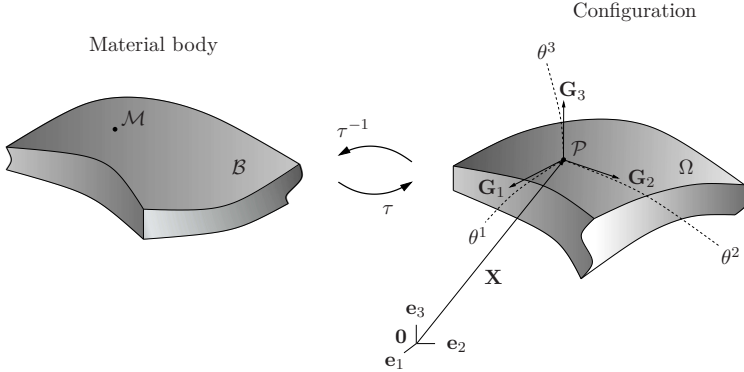
Figure 2.1: Mapping τ of material points $\mathcal{M}$ to spatial points $\mathcal{P}$.

The contravariant base vectors $\mathbf{G}^i$ may be consequently derived by

$$\mathbf{G}^i = \frac{\partial \theta^i}{\partial X^j}\,\mathbf{e}^j, \quad \mathbf{G}_i \cdot \mathbf{G}^j = \delta_i{}^j. \tag{2.5}$$

They represent a dual basis to $\mathbf{G}_i$. The Kronecker delta $\delta_i{}^j$ takes the value of one if $i = j$ and is zero otherwise.

With the co- and contravariant base vectors at hand, the components of the metric tensor $\mathbf{G}$ can be directly computed according to Equation (2.6)

$$\mathbf{G} = \mathbf{G}^i \cdot \mathbf{G}^j \, \mathbf{G}_i \otimes \mathbf{G}_j = G^{ij} \, \mathbf{G}_i \otimes \mathbf{G}_j = G_{ij} \, \mathbf{G}^i \otimes \mathbf{G}^j \,. \tag{2.6}$$

Thus, important local geometric quantities with regard to the metric of the body, such as distances between points, lengths or angles between tangent vectors, or the size of differential line, area or volume segments may be derived.

The symbol ($\otimes$) in Equation (2.6) represents the tensor product of the respective base vectors in either covariant or contravariant form. The contravariant components of the metric tensor are obtained by the inverse of G_{ij}. They enable the calculation of the contravariant base vectors $\mathbf{G}^i$, which also lie in the tangent space that is spanned by the covariant basis.

$$\mathbf{G}^i = G^{ij} \, \mathbf{G}_j \tag{2.7}$$

The kinematic equations of the isogeometric shell models of Chapter 4 only require the definition of the metric tensor $\mathbf{G}$ without explicitly using curvature tensor properties associated with the second fundamental form of differential geometry, which will therefore be omitted in the subsequent derivations. For more information on curvature characteristics of curves and surfaces references Klingbeil (1966), Başar and Krätzig (1985) and Ciarlet (2006) are recommended.

2.2 Deformation, strain measures

2.2.1 Deformation and motion

In Section 2.1, the definition of a configuration of a body was introduced. For describing the motion and deformation of a body, several configurations for different moments in time have to be defined. The configuration Ω_0 of Euclidean space $\mathbb{R}^3$ at time $t = 0$ is denoted as reference or initial configuration and represents an undeformed, unloaded and unstressed state of the body, although in principle other choices are possible as well. Each material point is uniquely identified with a position vector $\mathbf{X}$ which represents its spatial position at $t = 0$. For all quantities of the reference configuration, capital letters are used.

The spatial domain occupied by $\mathcal{B}$ during motion, that is for time $t > 0$, is denoted as current or deformed configuration Ω_t. Material points in the current configuration Ω_t are identified with position vectors $\mathbf{x}$. Quantities of the deformed configuration are

labeled with lowercase letters. The mappings for both configurations read

$$
\begin{aligned}
\tau_{t_0} &= \tau\left(\mathcal{P}, t=0\right) &=: \mathbf{X}\,, \\
\tau_t &= \tau\left(\mathcal{P}, t>0\right) &=: \mathbf{x}\,.
\end{aligned}
\tag{2.8}
$$

$\boldsymbol{\Upsilon}$ in Equation (2.9) defines the mapping between the reference and current configuration and may be interpreted as a deformation process. In Lagrangian formulation, it is described with the material coordinates X^i of the material points of the reference configuration.

$$
\mathbf{x} = \boldsymbol{\Upsilon}_t\left(\mathbf{X}\right) = \boldsymbol{\Upsilon}\left(\mathbf{X}, t\right) = \left[\tau_t \circ \tau_{t_0}^{-1}\right]\left(\mathbf{X}\right)
\tag{2.9}
$$

The symbol $(\circ)$ in Equation (2.9) represents a superposition of the mappings τ_t and $\tau_{t_0}^{-1}$. The configurations and motion of a continuum body are illustrated in Figure 2.2.
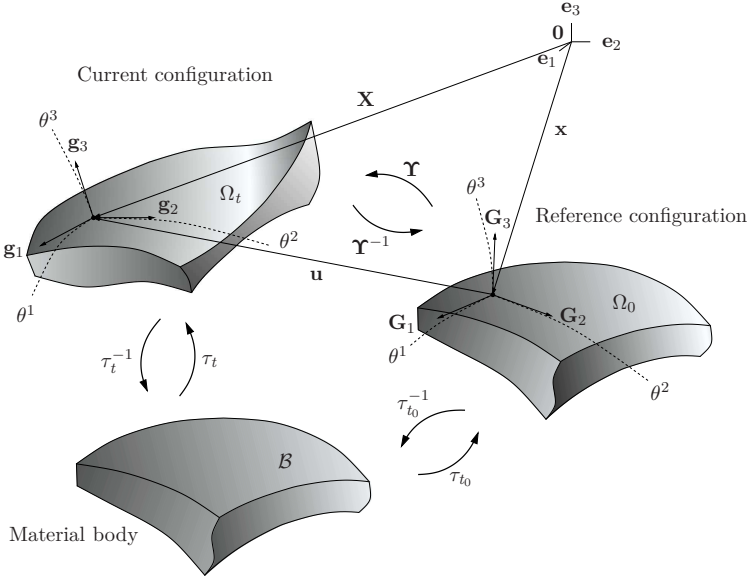
Figure 2.2: Motion of the material body.

By partial derivation of $\mathbf{x}$ with respect to the curvilinear coordinates θ^i, the covariant base vectors $\mathbf{g}_i$ of the current configuration are obtained. The computation of both

13

the contravariant base vectors $\mathbf{g}^i$ and metric of the deformed configuration is performed analogously to the procedure described in Section 2.1

$$\mathbf{g}_i = \frac{\partial \mathbf{x}}{\partial \theta^i}, \quad \mathbf{g}^i = \frac{\partial \theta^i}{\partial \mathbf{x}}.$$ (2.10)

The material deformation gradient $\mathbf{F}$ is introduced to define the relative spatial position of two neighboring material points after deformation in dependence of their relative initial position. It represents an unsymmetric tensor of second-order and is used in Equation (2.11) for the linear geometric mapping of an infinitesimal line element $\mathrm{d}\mathbf{X}$ of the reference configuration to an infinitesimal line element $\mathrm{d}\mathbf{x}$ of the current configuration

$$\mathrm{d}\mathbf{x} = \mathbf{F} \cdot \mathrm{d}\mathbf{X}.$$ (2.11)

In Equation (2.12), the tangent vectors of the deformed configuration are computed from the tangent vectors of the undeformed state by means of $\mathbf{F}$

$$\begin{aligned} \mathbf{g}_i &= \frac{\partial \mathbf{x}}{\partial \theta^i} = \frac{\partial \mathbf{x}}{\partial \mathbf{X}} \cdot \frac{\partial \mathbf{X}}{\partial \theta^i} = \mathbf{F} \cdot \mathbf{G}_i, \\ \mathbf{g}^i &= \mathbf{F}^{-\mathrm{T}} \cdot \mathbf{G}^i. \end{aligned}$$ (2.12)

In order to ensure the connectivity of adjacent material points of $\mathcal{B}$ during deformation, the mapping from the reference to the current configuration has to be bijective, which is equivalent to satisfying the condition $\det(\mathbf{F}) \neq 0$. This also requires that the inverse mapping of Equation (2.11), i.e. $\mathrm{d}\mathbf{X} = \mathbf{F}^{-1} \cdot \mathrm{d}\mathbf{x}$ and thus $\mathbf{F}^{-1}$ has to exist. In order to physically avoid self-penetration of material, the Jacobian determinant of $\mathbf{F}$ must also only take on positive values, i.e. $\det(\mathbf{F}) > 0$.

Additionally, the displacement field $\mathbf{u}$ will be introduced as the difference vector of the position vectors of the deformed and reference configuration, which in Lagrangian formulation is a function of the reference position $\mathbf{X}$ and time t. All subsequent derivations are restricted to both static behavior and linear elasticity such that the parameter time t can be disregarded in the following definitions of the description of motion. The displacement field $\mathbf{u}$ is consequently determined by

$$\mathbf{u} = \mathbf{x} - \mathbf{X}.$$ (2.13)

Equation (2.13) allows for an alternative definition of the deformation gradient $\mathbf{F}$ as the sum of the displacement gradient tensor $\mathbf{L} = \text{grad}\,\mathbf{u}$ and the identity tensor $\mathbf{I}$, which is used in Section 2.2.2 in the derivation of adequate strain measures.

As $\mathbf{F}$ uniquely describes the deformation process of a body, it represents a valid strain measure for constitutive equations in general. Several disadvantages, however, such as the inability to exactly represent rigid body modes without strains, unsymmetry and dependency on orientation, limit its applicability as an adequate strain measure in continuum mechanics. Therefore, in Section 2.2.2 alternative strain measures are derived, which are used in Chapter 4 to describe the strain-displacement relationships of the hierarchic family of shell models.

2.2.2 Strain measures

Nonlinear continuum mechanics in general utilizes a multitude of different strain and strain rate quantities in order to properly describe the kinematics of continuous bodies. As linear kinematics are assumed within this thesis, however, only the linearized Green-Lagrange strain tensor $\boldsymbol{\varepsilon}$ will be derived from the more general geometric nonlinear Green-Lagrange strain measure $\mathbf{E}$.

The second order tensor $\mathbf{E}$, in contrast to the aforementioned material deformation gradient $\mathbf{F}$, is invariant with regard to arbitrary rigid body motions and is symmetric. Its derivation can be directly related to the deformation behavior of the body. For this, $\mathbf{E}$ is defined by the difference of the squares of differential line segments ds and dS of the deformed and undeformed configurations Ω_t and Ω_0 respectively.

$$
\begin{aligned}
(\text{ds})^2 - (\text{dS})^2 &= \text{d}\mathbf{x} \cdot \text{d}\mathbf{x} - \text{d}\mathbf{X} \cdot \text{d}\mathbf{X} = (\mathbf{F} \cdot \text{d}\mathbf{X}) \cdot (\mathbf{F} \cdot \text{d}\mathbf{X}) - \text{d}\mathbf{X} \cdot \mathbf{I} \cdot \text{d}\mathbf{X} \\
&= \text{d}\mathbf{X} \cdot \underbrace{(\mathbf{F}^{\text{T}} \cdot \mathbf{F} - \mathbf{I})}_{2\,\mathbf{E}} \cdot \text{d}\mathbf{X}
\end{aligned}
\tag{2.14}
$$

Alternatively, $\mathbf{E}$ may be formulated in curvilinear convective coordinates as the difference of the metric tensors of both configurations or by means of the material displacement gradient $\mathbf{L}$ as follows (STEIN AND BARTHOLD (1996), WRIGGERS (2001), BELYTSCHKO ET AL. (2008))

$$
\begin{aligned}
\mathbf{E} &= \frac{1}{2}\left(g_{ij} - G_{ij}\right)\mathbf{G}^i \otimes \mathbf{G}^j, \\
\mathbf{E} &= \frac{1}{2}\left(\mathbf{L} + \mathbf{L}^{\text{T}} + \mathbf{L}^{\text{T}} \cdot \mathbf{L}\right).
\end{aligned}
\tag{2.15}
$$

For small displacements, rotations and strains, the linearized form of $\mathbf{E}$ can be straight-forwardly derived from the last definition in Equation (2.15) by omitting the quadratic contribution $\mathbf{L}^{\mathrm{T}} \cdot \mathbf{L}$. In curvilinear convective coordinates, the linearized Green-Lagrange strain tensor $\boldsymbol{\varepsilon}$ and its coefficients ε_{ij} read

$$\boldsymbol{\varepsilon} = \frac{1}{2}\left(\mathbf{L} + \mathbf{L}^{\mathrm{T}}\right) = \underbrace{\frac{1}{2}\left(\mathbf{u}_{,i} \cdot \mathbf{G}_j + \mathbf{u}_{,j} \cdot \mathbf{G}_i\right)}_{\varepsilon_{ij}} \mathbf{G}^i \otimes \mathbf{G}^j. \tag{2.16}$$

2.3 Concept of stress, static equilibrium

This section is related to the concepts of stress and static equilibrium for linear elastic continuous bodies.

2.3.1 Stress measures

The concept of stress is defined by means of the Eulerian method of sections and the Cauchy stress theorem, which establishes a linear relationship between the traction vector $\mathbf{t}$ and the normal vector $\mathbf{n}$ of a differential surface element of the current configuration with a second-order tensor field $\boldsymbol{\sigma}$, denoted as Cauchy stress tensor

$$\mathbf{t} = \boldsymbol{\sigma} \cdot \mathbf{n}. \tag{2.17}$$

The reference of both the normal and the traction vector with regard to the current configuration in Equation (2.17) associates the spatial tensor $\boldsymbol{\sigma}$ with the notion of a true or physical stress tensor. Symmetry of $\boldsymbol{\sigma}$, i.e. $\boldsymbol{\sigma} = \boldsymbol{\sigma}^{\mathrm{T}}$, can be derived from the balance of angular momentum. The Cauchy stress tensor represents an objective, frame-invariant stress measure, which is therefore suitable to be used in constitutive relations.

$$\boldsymbol{\sigma} = \sigma^{ij} \mathbf{g}_i \otimes \mathbf{g}_j \tag{2.18}$$

In the continuum mechanics of solids, several formulations of stress tensors rely on material (Lagrangian) coordinates and a description of quantities related to the reference configuration. The second Piola-Kirchhoff (PK2) stress tensor $\mathbf{S}$, which represents the work conjugate of the previously introduced Green-Lagrange strain tensor $\mathbf{E}$, is entirely defined in the undeformed material configuration. It can be derived from the Cauchy

stress tensor by the so-called Piola transformation, a pull-back operation from the deformed into the reference configuration by means of the material deformation gradient $\mathbf{F}$ and its Jacobian determinant. $\mathbf{S}$, like the Cauchy stress tensor, is symmetric and materially objective

$$
\begin{aligned}
\mathbf{S} &= S^{ij}\,\mathbf{G}_i \otimes \mathbf{G}_j\,, \\
\mathbf{S} &= \det\left(\mathbf{F}\right) \mathbf{F}^{-1} \cdot \boldsymbol{\sigma} \cdot \mathbf{F}^{-\mathrm{T}}\,.
\end{aligned}
\tag{2.19}
$$

Computation of the Cauchy stress tensor from the PK2 tensor can be performed, on the other hand, by the push-forward of $\mathbf{S}$ to the current, deformed configuration.

For small deformations and strains, the differences among the presented stress tensors are negligible. The material deformation gradient $\mathbf{F}$ becomes approximately the identity tensor $\mathbf{I}$, i.e. $\mathbf{F} \approx \mathbf{I}$. By applying these results to Equation (2.19), one obtains

$$
\mathbf{S}^{\mathrm{lin}} \approx \det\left(\mathbf{I}\right) \mathbf{I}^{-1} \cdot \boldsymbol{\sigma}^{\mathrm{lin}} \cdot \mathbf{I}^{-\mathrm{T}} = \boldsymbol{\sigma}^{\mathrm{lin}}\,.
\tag{2.20}
$$

Further, more detailed information with regard to different stress measures, their transformations and specific properties are provided, for instance, in references BAŞAR AND WEICHERT (2000), ZIENKIEWICZ AND TAYLOR (2005), BELYTSCHKO ET AL. (2008) or BONET AND WOOD (2008).

2.3.2 Equilibrium equations

From the balance of linear momentum the strong form of static equilibrium can be derived if inertia effects are neglected. The balance law states that the change in time of the linear momentum during deformation of a body is equal to the sum of all external volume forces and surface tractions acting on that body. The Cauchy equilibrium equation ultimately reads

$$
\mathrm{div}\left(\boldsymbol{\sigma}^{\mathrm{lin}}\right) + \rho\,\overline{\mathbf{b}} = \mathbf{0}\,.
\tag{2.21}
$$

ρ in Equation (2.21) represents the density of the body, which in linear elastostatics is identical for both the reference and current configuration and $\rho\,\overline{\mathbf{b}}$ equals the body force per unit volume, which is assumed to be a prescribed, i.e. known quantity.

2.4 Linear elastic constitutive law

Up to now, the equations and relations referring to the kinematics, concept of stress and static equilibrium of solid continua are independent of material-specific properties and thus do not suffice to completely describe the response of a continuous body with respect to an applied loading.

Therefore, constitutive laws have to be defined, which represent the third and last functional field equation of the mechanical boundary value problem under consideration. The focus of this work lies on the development of efficient isogeometric shell element formulations. Only small displacements are accounted for in the kinematics. For simplicity but without loss of generality the most basic constitutive model for homogeneous, elastic and isotropic materials defined by Hooke's law is applied. Hooke's law may be derived directly from the Saint-Venant-Kirchhoff material, which is valid for large displacements but small strains. Consequently, an algebraic, linear relation between the stresses $\boldsymbol{\sigma}^{\mathrm{lin}}$ and strains $\boldsymbol{\varepsilon}$ can be established.

$$\boldsymbol{\sigma}^{\mathrm{lin}} = \lambda \operatorname{tr}(\boldsymbol{\varepsilon}) \, \mathbf{I} + 2\,\mu\,\boldsymbol{\varepsilon} = \mathbb{C} : \boldsymbol{\varepsilon} \tag{2.22}$$

$(\bullet : \bullet)$ in Equation (2.22) represents a double contraction of the two tensors $\mathbb{C}$ and $\boldsymbol{\varepsilon}$. The parameters λ and μ are denoted as Lamé constants. They are related to the more engineering material constants, Young's modulus E and Poisson's ratio ν, via

$$\lambda = \frac{\nu\,E}{(1+\nu)\,(1-2\,\nu)}, \quad \mu = \frac{E}{2\,(1+\nu)}\,. \tag{2.23}$$

The fourth order material tensor $\mathbb{C}$ may be formally obtained by partial derivation of the strain energy density function $\mathcal{W}^{\mathrm{int}}(\boldsymbol{\varepsilon})$ as follows: $\mathbb{C} = \frac{\partial^2 \mathcal{W}^{\mathrm{int}}(\boldsymbol{\varepsilon})}{\partial \boldsymbol{\varepsilon}\, \partial \boldsymbol{\varepsilon}}$. It is defined in Equation (2.24) in convective curvilinear coordinates and will be used for the shell models of Chapter 4.

$$\mathbb{C} = C^{ijkl}\,\mathbf{G}_i \otimes \mathbf{G}_j \otimes \mathbf{G}_k \otimes \mathbf{G}_l\,, \quad C^{ijkl} = \lambda\,G^{ij}\,G^{kl} + \mu\left(G^{ik}\,G^{jl} + G^{il}\,G^{jk}\right) \tag{2.24}$$

2.5 Variational principles

The field equations derived in Sections 2.2 to 2.4 consist of local geometric relations, equilibrium and the constitutive law according to Equations (2.16), (2.21) and (2.22). They represent a system of coupled differential equations and describe the governing

relations of the boundary value problem of linear elastostatics in strong form, which are summarized here for convenience.

$$
\begin{aligned}
\text{Kinematics :} \quad &\boldsymbol{\varepsilon} = \frac{1}{2}\left(\mathbf{u}_{,i}\cdot\mathbf{G}_j + \mathbf{u}_{,j}\cdot\mathbf{G}_i\right)\mathbf{G}^i\otimes\mathbf{G}^j \quad &&\text{in } \Omega \\
\text{Equilibrium :} \quad &\operatorname{div}\left(\boldsymbol{\sigma}^{\mathrm{lin}}\right) + \rho\,\overline{\mathbf{b}} = \mathbf{0} \quad &&\text{in } \Omega \\
\text{Material :} \quad &\boldsymbol{\sigma}^{\mathrm{lin}} = \mathbb{C}:\boldsymbol{\varepsilon} \quad &&\text{in } \Omega
\end{aligned}
\tag{2.25}
$$

In order to obtain a unique solution for the mechanical boundary value problem, both geometric and static boundary conditions have to be defined. The spatial domain occupied by the boundary of the body $\partial\Omega$ is separated into a portion $\partial\Omega_u$ of prescribed displacements $\overline{\mathbf{u}}$ and a portion $\partial\Omega_\sigma$ of prescribed tractions $\overline{\mathbf{t}}$. For the boundary of the body $\partial\Omega$, the following convention holds

$$
\partial\Omega_u \cup \partial\Omega_\sigma = \partial\Omega, \quad \partial\Omega_u \cap \partial\Omega_\sigma = \varnothing. \tag{2.26}
$$

The prescribed Neumann and Dirichlet boundary conditions for the static linear elastic boundary value problem of continuum mechanics read

$$
\begin{aligned}
\text{Neumann boundary conditions :} \quad &\boldsymbol{\sigma}^{\mathrm{lin}}\cdot\mathbf{n} = \overline{\mathbf{t}} \quad &&\text{on } \partial\Omega_\sigma\,, \\
\text{Dirichlet boundary conditions :} \quad &\mathbf{u} = \overline{\mathbf{u}} \quad &&\text{on } \partial\Omega_u\,.
\end{aligned}
\tag{2.27}
$$

Finding closed form analytic solutions for the presented set of coupled partial differential equations is restricted to only a small number of linear elastic problems by a proper choice of admissible stress or displacement functions. Examples of mechanical problems for which analytical solutions are available are, among others, the Saint-Venant torsion of prismatic beams or the elastic half-space.

Therefore, mathematical expressions that are equivalent to the strong form of the partial differential equations of linear elasticity will be formulated by means of variational methods. These serve as a basis to establish computer-based discretization techniques such as the finite element method used within this thesis in order to derive approximate sets of algebraic equations to be solved numerically.

The first variational form introduced herein is the principle of virtual work. It will be used to define isogeometric shell finite elements with pure displacement ansatz in Chapters 4 and 5. For constrained problems, however, unphysical locking effects show up in the single-field displacement models such that alternatively a mixed formulation based on a two-field Hellinger-Reissner variational principle will be provided (ODEN AND REDDY (1976), PARK AND FELIPPA (1998), PARK AND FELIPPA (2000), PIAN AND WU (2006), BISCHOFF (2011b)).

2.5.1 Principle of virtual work

The principle of virtual work represents a variational formulation, which is equivalent to the momentum balance equations and Neumann boundary conditions. It can be derived from the principle of minimum potential energy Π which consists of both strain energy $\Pi^{\text{int}}(\boldsymbol{\varepsilon}(\mathbf{u}))$ and external energy contributions $\Pi^{\text{ext}}(\mathbf{u})$. Π represents a functional, i.e. a function of a function that is mapped onto the space of real numbers.

Implicit inclusion of the material law with the stress-strain relationship and subsequent introduction of the kinematic equations, yields Π as a functional of the displacement field $\mathbf{u}$ only. From all possible displacements, the one which minimizes $\Pi(\mathbf{u})$ satisfies equilibrium and thus provides the solution to the single-field variational problem. The minimum condition requires that the first variation $\delta\Pi(\mathbf{u})$, with respect to the displacements becomes zero, which yields the virtual work principle $\delta\Pi_{\text{Pvw}} = 0$.

The equilibrium and Neumann boundary conditions are called Euler-Lagrange equations, which are satisfied weakly in an integral sense. The subsidiary material and kinematic equations, as well as the Dirichlet boundary conditions are satisfied strongly. The principle of virtual work may also be derived from the strong form of the differential equations with the method of weighted residuals. In contrast to the aforementioned procedure, this ansatz does not require the existence of a potential and is therefore also valid for problems with friction, non-conservative loads or material inelasticity.

The way to proceed starts with formulating the differential equations of static equilibrium and force boundary terms as a weighted residuum. Therefore, these equations are multiplied with an arbitrary vector-valued test function denoted with $\delta\mathbf{u}$. Energetically, the test function $\delta\mathbf{u}$ may be interpreted as a virtual displacement function. It has to be kinematically admissible, i.e. has to vanish on $\partial\Omega_u$ where $\overline{\mathbf{u}}$ is prescribed. Finally, the residual equations are integrated over the domain of the body. Integration by parts and insertion of both the kinematic and material equations again yields the principle of virtual work as a single-field functional, which is equivalent to the formulation derived from the principle of minimum potential energy

$$
\begin{aligned}
\delta\Pi_{\text{Pvw}}\left(\mathbf{u},\,\delta\mathbf{u}\right) & = \delta\Pi^{\text{int}}\left(\mathbf{u},\,\delta\mathbf{u}\right) + \delta\Pi^{\text{ext}}\left(\mathbf{u},\,\delta\mathbf{u}\right) \\
& = \int_{\Omega} \boldsymbol{\sigma}^{\text{lin}} : \operatorname{grad}\delta\mathbf{u}\,\mathrm{d}\Omega - \int_{\Omega} \rho\,\overline{\mathbf{b}}\cdot\delta\mathbf{u}\,\mathrm{d}\Omega - \int_{\partial\Omega_{\sigma}} \overline{\mathbf{t}}\cdot\delta\mathbf{u}\,\partial\Omega_{\sigma} = 0\,.
\end{aligned}
$$

$$(2.28)$$

Functional analysis requirements on virtual work principle

In this section, basic definitions and requirements from the mathematical field of functional analysis are provided for the theoretical analysis of the variational forms introduced in this chapter to describe the elliptic boundary value problem of linear elasticity.

The way of argumentation only provides basic necessary fundamentals without giving mathematically complete and rigorous proofs or derivations. For a thorough treatment of this topic with regard to the finite element analysis, the reader is referred to MARSDEN AND HUGHES (1983), REDDY (1998), HUGHES (2000), BRAESS (2003), HÖLLIG (2003), BRENNER AND SCOTT (2008).

Due to the existence of first derivatives in Equation (2.28), the variational index of the weak form is equal to one. Therefore, an admissible function space $\mathcal{U}$ has to be defined, which comprises the set of all functions $\mathbf{u}$ with square integrable first derivatives and satisfaction of the Dirichlet boundary conditions

$$\mathcal{U} = \left\{ \mathbf{u} \in \mathcal{H}^1, \mathbf{u} = \overline{\mathbf{u}} \text{ on } \partial\Omega_u \right\} . \tag{2.29}$$

$\mathcal{H}^n$ in general represents a Sobolev space as a set of all functions with square integrable derivatives up to order n. The variations $\delta\mathbf{u}$ have to vanish on $\partial\Omega_u$ as mentioned previously. Therefore, the admissible function space of $\delta\mathbf{u}$ is defined as

$$\mathcal{U}^0 = \left\{ \delta\mathbf{u} \in \mathcal{H}^1_0, \delta\mathbf{u} = \mathbf{0} \text{ on } \partial\Omega_u \right\} . \tag{2.30}$$

For simplifying subsequent writing, a mathematical notation of the energy contributions of the principle of virtual work is applied. The internal energy of Equation (2.28) may be formally expressed by a symmetric, bilinear form $b(\mathbf{u}, \delta\mathbf{u})$, which implies linearity in each variable and represents a bilinear mapping of vector valued functions onto the space of real numbers $\mathbb{R}$. The external virtual energy, which consists of the virtual work of body forces $\rho\,\overline{\mathbf{b}}$ and surface tractions $\overline{\mathbf{t}}$, may be described by linear forms $f(\delta\mathbf{u})$ and $F(\delta\mathbf{u})$ respectively. In particular, the bilinear and linear functionals of the principle of virtual work read

$$
\begin{aligned}
b(\mathbf{u}, \delta\mathbf{u}) \quad &:= \int\limits_{\Omega} \boldsymbol{\sigma}^{\text{lin}} : \text{grad}\,\delta\mathbf{u}\,\mathrm{d}\Omega = \int\limits_{\Omega} \boldsymbol{\varepsilon}(\mathbf{u}) : \mathbb{C} : \text{grad}\,\delta\mathbf{u}\,\mathrm{d}\Omega\,, \\
f(\delta\mathbf{u}) \quad &:= \int\limits_{\Omega} \rho\,\overline{\mathbf{b}} \cdot \delta\mathbf{u}\,\mathrm{d}\Omega\,, \\
F(\delta\mathbf{u}) \quad &:= \int\limits_{\partial\Omega_\sigma} \overline{\mathbf{t}} \cdot \delta\mathbf{u}\,\partial\Omega_\sigma\,,
\end{aligned}
\tag{2.31}
$$

such that the virtual work principle $\delta\Pi_{\text{Pvw}}$ can be rewritten in the following mathematical notation

$$b(\mathbf{u}, \delta\mathbf{u}) - f(\delta\mathbf{u}) - F(\delta\mathbf{u}) = 0 \qquad \forall\,\delta\mathbf{u} \in \mathcal{U}^0\,. \tag{2.32}$$

Endowing the Sobolev spaces $\mathcal{H}^n$ with an inner product yields inner product spaces which finally enable the definition of a norm $\|\bullet\|_{\mathcal{H}^n}$. With normed spaces, magnitudes of functions are measurable and thus evaluations of the approximation quality on the basis of the selected function spaces are possible. Additionally, information with regard to convergence and rates of convergence may be established. Bounded Sobolev spaces $\mathcal{H}^n$ with associated norm $\|\bullet\|_{\mathcal{H}^n}$ are denoted as Hilbert spaces.

With these definitions at hand, boundedness and ellipticity of bilinear forms $b(\cdot, \cdot)$ on Hilbert spaces can be deduced, which enable the derivation of the main existence theorem of functional analysis for elliptic variational forms: the Lax-Milgram-Theorem. It states that every problem which can be formulated with a continuous (bounded) and coercive (elliptic) bilinear functional has a unique solution $\mathbf{u}$. The symmetry of the bilinear form in linear elasticity furthermore characterizes the solution $\mathbf{u}$ as the minimum of a quadratic functional, i.e. the elastic potential energy.

A bilinear functional is bounded above and continuous if there is a constant $0 < c < \infty$ such that

$$|b(\mathbf{u}, \delta\mathbf{u})| \leq c\, \|\mathbf{u}\|\, \|\delta\mathbf{u}\| \qquad \forall\, \mathbf{u} \in \mathcal{U},\ \delta\mathbf{u} \in \mathcal{U}^0. \tag{2.33}$$

In addition, the ellipticity of a bilinear form is established, if for a constant $0 < \overline{c} < \infty$

$$|b(\mathbf{u}, \mathbf{u})| \geq \overline{c}\, \|\mathbf{u}\|^2 \qquad \forall\, \mathbf{u} \in \mathcal{U}. \tag{2.34}$$

Satisfaction of Equation (2.33) reveals that the application of $|b(\mathbf{u}, \delta\mathbf{u})|$ does not produce results which rise beyond the limits of the associated norms with regard to $\mathbf{u}$ and $\delta\mathbf{u}$. The ellipticity condition $b(\mathbf{u}, \mathbf{u})$ ensures the definition of a lower bound on the functional such that stability of the solution is satisfied with the existence of Equation (2.34) and boundedness of the linear forms $f(\delta\mathbf{u})$ and $F(\delta\mathbf{u})$. Stability therefore requires from the solution $\mathbf{u}$ to be stable with regard to variations of the applied external load.

The necessary conditions for obtaining a unique and stable solution of the continuous single-field virtual work functional now have been established. These conditions can be directly transferred to the discrete functionals defined in Chapter 5 of this thesis where NURBS functions are used as both trial and test functions in an isoparametric finite element concept.

2.5.2 Principle of Hellinger-Reissner

Single-field finite element formulations on the basis of the principle of virtual work may lead to significant numerical difficulties, particularly for constraint problems such as incompressible or nearly incompressible material behavior or the Kirchhoff constraint in plate and shell structures, which in literature is frequently denoted as locking.

In order to remove membrane locking from the displacement-based isogeometric shell elements derived in Chapters 4 and 5, a mixed formulation based on the Hellinger-Reissner principle (HELLINGER (1914), REISSNER (1950)) will be employed. This ansatz moreover removes both in-plane shear locking and volumetric locking which is, however, not investigated in more detail for the shell analyses of this thesis. For the mixed formulation the relations in the constrained kinematic equations are alleviated in the variational functional by expressing them weakly. The two-field functional uses both displacements and stresses as independent field variables and may be derived either by the method of weighted residuals or from the principle of minimum complementary energy.

In the weighted residual approach, in addition to the principle of virtual work, the kinematic equations of the strong form are also multiplied with test functions $\delta\boldsymbol{\sigma}$ and integrated over the domain of the body. Applying integration by parts and subsequently inserting the material equations yields the principle of Hellinger-Reissner $\delta\Pi_{\mathrm{HR}}$. The Euler-Lagrange equations consist of equilibrium, kinematics and both Neumann and Dirichlet boundary conditions. The only strong condition is the material law.

$$
\begin{aligned}
\delta\Pi_{\mathrm{HR}}\left(\mathbf{u},\,\boldsymbol{\sigma},\,\delta\mathbf{u},\,\delta\boldsymbol{\sigma}\right) = \ & -\int_{\Omega}\boldsymbol{\sigma}^{\mathrm{lin}} : \operatorname{grad}\delta\mathbf{u}\ \mathrm{d}\Omega + \int_{\Omega}\rho\,\overline{\mathbf{b}}\cdot\delta\mathbf{u}\ \mathrm{d}\Omega \\
& + \int_{\Omega}\left(\mathbb{C}^{-1} :\, \boldsymbol{\sigma}^{\mathrm{lin}}\right) : \delta\boldsymbol{\sigma}\ \mathrm{d}\Omega - \int_{\Omega}\operatorname{grad}\mathbf{u} : \delta\boldsymbol{\sigma}\ \mathrm{d}\Omega \\
& + \int_{\partial\Omega_{\sigma}}\overline{\mathbf{t}}\cdot\delta\mathbf{u}\ \partial\Omega_{\sigma} + \int_{\partial\Omega_{u}}\left(\mathbf{u}-\overline{\mathbf{u}}\right)\cdot\delta\boldsymbol{\sigma}\cdot\mathbf{n}\ \partial\Omega_{u} = 0
\end{aligned}
\tag{2.35}
$$

Alternatively, the Hellinger-Reissner functional can be derived from the principle of minimum complementary energy which represents a functional of stresses only and is equivalent to the kinematic and Dirichlet equations. This approach employs Lagrangian multipliers to add both the equilibrium and Neumann boundary conditions to the complementary energy expression. The Lagrange multipliers show up as additional free variables in the equation system. The minimization problem thus becomes a stationary problem (saddle point problem).

For more detailed information on the derivation of the two-field Hellinger-Reissner principle in addition to the references presented within this section see, for instance, ANDELFINGER (1991), ANDELFINGER AND RAMM (1993), HAUSSER (1996), BRAESS (2003), PIAN AND WU (2006).

Functional analysis requirements on Hellinger-Reissner principle

The Dirichlet boundary conditions in the Hellinger-Reissner principle $\delta\Pi_{\mathrm{HR}}$ represent Euler-Lagrange equations such that displacement functions do not have to satisfy com-

patibility across element boundaries in the discrete model. Due to first derivatives in Equation (2.35) continuous functions of space $\mathcal{H}^1$ are generally used which satisfy the geometric boundary conditions. Consequently, the displacement boundary term $(\mathbf{u} - \overline{\mathbf{u}})$ vanishes in the functional. For the stresses, on the other hand, no derivatives show up in $\delta\Pi_{\mathrm{HR}}$ such that the function space for the stresses may be of $\mathcal{H}^0$, which contains the set of all functions that are square integrable. The mathematically oriented writing of the Hellinger-Reissner functional, following the notation introduced for the virtual work principle, is defined as follows

$$-\overline{b}\left(\boldsymbol{\sigma}, \delta\mathbf{u}\right) + f\left(\delta\mathbf{u}\right) + \tilde{b}\left(\boldsymbol{\sigma}, \delta\boldsymbol{\sigma}\right) - b\left(\mathbf{u}, \delta\boldsymbol{\sigma}\right) + F\left(\delta\mathbf{u}\right) = 0\,. \tag{2.36}$$

The bilinear forms of Equation (2.36) are listed in more detail in Equation (2.37). The linear forms are equal to the ones defined for the virtual work functional of Equation (2.31)

$$
\begin{aligned}
\overline{b}\left(\boldsymbol{\sigma}, \delta\mathbf{u}\right) &:= \int_{\Omega} \boldsymbol{\sigma}^{\mathrm{lin}} : \operatorname{grad}\delta\mathbf{u}\,\mathrm{d}\Omega\,, \\
b\left(\mathbf{u}, \delta\boldsymbol{\sigma}\right) &:= \int_{\Omega} \operatorname{grad}\mathbf{u} : \delta\boldsymbol{\sigma}\,\mathrm{d}\Omega\,, \\
\tilde{b}\left(\boldsymbol{\sigma}, \delta\boldsymbol{\sigma}\right) &:= \int_{\Omega} \left(\mathbb{C}^{-1} : \boldsymbol{\sigma}^{\mathrm{lin}}\right) : \delta\boldsymbol{\sigma}\,\mathrm{d}\Omega\,.
\end{aligned}
\tag{2.37}
$$

Compared to single field variational principles, the extremum property is lost for multi-field principles where the initial minimization problem becomes a saddle point problem. The two-field Hellinger-Reissner principle, according to Equation (2.35), is convex with regard to the primary variable $\mathbf{u}$ and concave with regard to the secondary variable $\boldsymbol{\sigma}$. In order to ensure uniqueness of the solution, the functional $\delta\Pi_{\mathrm{HR}}$ has to be bounded (continuous), convex and elliptic (coercive) with regard to the field $\mathbf{u}$ and additionally negative coercive and concave for $\boldsymbol{\sigma}$.

Boundedness above with regard to both variables $\mathbf{u}$ and $\boldsymbol{\sigma}$ is ensured, if the continuity condition according Equation (2.33) is satisfied for the bilinear forms of $\delta\Pi_{\mathrm{HR}}$.

The definition of a lower bound for functionals with different arguments such as the Hellinger-Reissner two-field principle according to the ellipticity condition of Equation (2.34) is too rigorous as pairs of functions $\mathbf{u}$ and $\boldsymbol{\sigma}$ may exist which are orthogonal with respect to the multi-field functional. In order to ensure stability of the continuous problem, a less restrictive condition suffices. It states that ellipticity, according to Equation (2.34), only has to be satisfied for at least one $\boldsymbol{\sigma}$ with regard to arbitrary functions $\mathbf{u}$ in contrast to the requirement of satisfying coercivity for all pairs of $\boldsymbol{\sigma}$ and $\mathbf{u}$.

For the stresses, ellipticity has to be satisfied in the same way as defined for the single-

field functional with Equation (2.34), however on a bounded subspace consisting of all stress functions which are orthogonal to $\mathbf{u}$ in the bilinear form $b\left(\mathbf{u}, \delta\boldsymbol{\sigma}\right)$. In order to establish coercivity of the functional with respect to $\mathbf{u}$, the bilinear form $\overline{b}\left(\boldsymbol{\sigma}, \delta\mathbf{u}\right)$ has to satisfy the inf-sup condition, that is

$$\inf_{\|\mathbf{u}\|} \sup_{\|\boldsymbol{\sigma}\|} \frac{\left|\overline{b}\left(\boldsymbol{\sigma}, \delta\mathbf{u}\right)\right|}{\|\boldsymbol{\sigma}\|\,\|\mathbf{u}\|} \geq c > 0\,. \tag{2.38}$$

The inf-sup condition of Equation (2.38) is frequently referred to as the Babuška-Brezzi (BB) condition or Ladyzhenskaya-Babuška-Brezzi (LBB) condition, respectively, according to the scientific contributions of Ladyzhenskaya and Ural'tseva (1968), Babuška and Aziz (1972) and Brezzi (1974) in which the existence and stability conditions of the mixed formulations with saddle point structure were first analyzed.

For the derivation of locking-free NURBS-based shell finite elements in Chapter 6, appropriate choices of discrete function spaces for both the displacements and stresses will be discussed. On the one hand, orthogonality of stress functions and displacements has to be avoided in order to prevent zero energy deformation modes. On the other hand, the definition of too many stress parameters which cannot be properly balanced by the existing strain modes, yields parasitic unphysical energy contributions that have to be precluded as well.

3

NURBS-based Geometry Modeling

In this chapter, the basic definitions and properties of NURBS basis functions and NURBS geometric objects will be explained using, essentially, the references PIEGL AND TILLER (1997), ROGERS (2001), FARIN (2002), FARIN ET AL. (2002) and COTTRELL ET AL. (2009).

NURBS, up to now, represent the standard format in the field of computer-aided design (CAD) and computer-aided modeling (CAM), which are used for the numerical description of the continua, defined in Chapter 2. The analysis-suitable discretization with NURBS functions will be used in Chapter 5 and the following within an isoparametric finite element environment for the derivation of a hierarchic family of isogeometric shell finite elements, thus combining engineering design and finite element analysis (FEA).

This idea goes back to Hughes and coworkers (HUGHES ET AL. (2005)), who presented a seminal paper on the integration of analysis-suitable CAD representation techniques into the FEA framework, which they denoted *Isogeometric Analysis* (IGA). Their main motivation was to bring together more closely the branches of FEA and CAD by directly embedding the CAD geometry into analysis and adopting the significantly richer CAD function spaces to FEA.

With regard to the development of isogeometric shell finite element formulations in Chapters 4 to 6 which represents the main topic of this thesis, special focus is laid on the higher-order and higher-continuity properties of the NURBS basis, rather than a detailed investigation of combining CAD and FEA. The higher continuity enables a straightforward formulation of Kirchhoff-Love shell models with a variational index of two and additionally a unique and continuous representation of the shell normal in the entire patch domain. In the context of isogeometric shell analysis, these advantages have been utilized first in KIENDL ET AL. (2009).

Chapter 3 begins with a short historical view on the development of CAD-based mod-

eling, particularly focusing on NURBS. The mathematical description of geometric objects in engineering design most frequently relies on parametric representations, the basic properties of which are outlined in Section 3.2. The derivation of NURBS basis functions requires the definition of knot vectors, which determine the main properties of the basis functions and subdivide the geometry into elements. Based on these results, NURBS curves and surfaces are defined in Section 3.4 by using the concepts of homogeneous coordinates and projective geometry. Subsequently, several methods for a systematic modification of the NURBS basis and thus the geometric object are presented, which, from the CAD perspective, increase the geometric flexibility and, for analysis, additionally, enable the discrete solution spaces of physical quantities to be controlled. Details of connecting several NURBS surface patches are described in Section 3.6.

3.1 Developments in CAD modeling

The roots of systematic drafting techniques can be found in the Renaissance era, where Italian naval architects made use of conic sections as mathematical design and drawing tools in ship building. The term "spline" originates from thin wooden strips which were bent into the smoothly curved shape of the ship body by means of a fixed set of leaden pins.

In aircraft construction, the demand for higher-continuous curve and surface descriptions became of great importance since the beginning of the twentieth century. In 1944, Liming first used mathematical formulations with conic sections for the design of aircraft fuselages, which he adopted to existing design drawings by the variation of function coefficients.

With the beginning of mass production in the automotive industry in the 1950s, the demand for computer-compatible design methods arose. Fundamental contributions on the uniform parametric description of curves and surfaces with Bernstein polynomials which enabled a fast and intuitive engineering design with particular geometric significance are the works of the French engineer Bézier at Renault and the French mathematician de Casteljau at Citroën (BÉZIER (1968), DE CASTELJAU (1963)). Geometric objects were defined as linear combinations of control points and Bernstein functions. Shape modifications were no longer applied directly to the geometry, but to the control polygon, without the need to change the properties of the basis functions.

The main drawback of Bernstein polynomials, due to their global support, was resolved with the development of B-splines (RIESENFELD (1972)). These functions represent piecewise polynomials with compact support and thus enable local shape modification. The recursion formulae by Cox and de Boor (COX (1972), DE BOOR (1972)) established stable numerical schemes for computing functions of higher order.

A generalization of B-splines to piecewise rational functions denoted as NURBS was first addressed in the doctoral thesis of VERSPRILLE (1975). NURBS enable an exact formulation of rational conic sections which are frequently used in engineering applications. Nowadays, they represent the basic technology in free-form design in commercial CAD systems, such as CATIA or RHINO and data exchange standards, as for example IGES, STEP or PHIGS. NURBS may be regarded as a superset of B-splines, which themselves represent a superset of Bézier functions.

Apart from NURBS, a variety of alternative analysis-suitable CAD function types exist. Since a comprehensive treatment is beyond the scope of this thesis, only two further established methods are briefly described.

The first approach represents finite element formulations with subdivision techniques that have been successfully applied to the analysis of thin and moderately thick shell structures by Cirak and coworkers (CIRAK ET AL. (2000), CIRAK AND ORTIZ (2001), LONG ET AL. (2012)). Smooth C^1-continuous subdivision surfaces are generated from the limit of a recursive computation, which is based on the triangulation of nodal point sets with Loop's subdivision scheme (LOOP (1987)). Subdivision techniques are most frequently used in the animation industry. Due to their lack of compatibility with NURBS, they are not widely adopted in engineering design.

Secondly, T-splines become of great importance in IGA, as they represent a generalization of NURBS, by using the concept of hanging nodes known from classical FEA. Thus, T-junctions and unstructured discretizations of the domain are possible and the tensor product constraint of NURBS discretizations is removed. T-splines are NURBS-compatible and carry over most of their basic properties. Additional benefits of analysis-suitable T-splines are, among others, local refinement capabilities and the watertight merging of geometric domains. The drawback of trimmed NURBS surfaces may be solved by using untrimmed T-splines. Details of trimmed NURBS surfaces are investigated, for instance, in KIM ET AL. (2009) and SCHMIDT ET AL. (2012). The application of T-splines in the isogeometric analysis of solids and fluids has been successfully carried out in BAZILEVS ET AL. (2010), DÖRFEL ET AL. (2010), LI ET AL. (2012) and SCOTT ET AL. (2012).

For more details with regard to subdivision techniques and T-splines which are not considered within this thesis, the aforementioned citations and references therein are recommended.

3.2 Parametric geometry representation

In Section 3.1, the concepts of parameter space, knot vector, basis function and control polygon have been briefly mentioned. Now, these topics are investigated in detail as they

provide the fundamental ingredients for the isogeometric shell analyses with NURBS functions in this work.

3.2.1 Analytic representation forms

The mathematical description of geometric objects is based on either

- explicit,
- implicit or
- parametric formulations

depending on the type of problem under consideration.

In Figure 3.1, the different forms of representation are shown as functions of the Cartesian coordinates x, y and z and independent parameters ξ and η for the example of a spherical surface with unit radius and center to be coincident with the origin of the Cartesian coordinate system.

$$
\begin{aligned}
\text{Explicit :} \quad & z = \pm \sqrt{1 - x^2 - y^2} \\
\text{Implicit :} \quad & x^2 + y^2 + z^2 - 1 = 0 \\
\text{Parametric :} \quad & x(\xi, \eta) = \sin(\xi) \cos(\eta) \\
& y(\xi, \eta) = \sin(\xi) \sin(\eta) \\
& z(\xi, \eta) = \cos(\xi) \\
& 0 \leq \xi \leq \pi \\
& 0 \leq \eta \leq 2\pi
\end{aligned}
$$
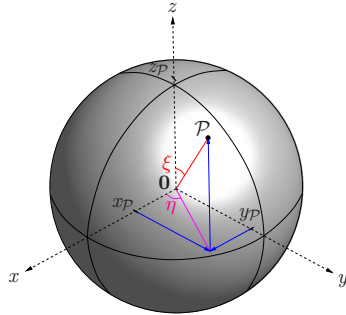
Figure 3.1: Unit sphere – types of representation.

Although the explicit representation of geometric objects is frequently used due to its simplicity, it is rarely applied in CAD, as distinct disadvantages have to be considered. Explicit formulations are axis dependent and thus difficult to transform. The definition of infinite derivatives is impossible for polynomials and multi-valued functions have a complex structure. Finally, a large group of geometric objects cannot be defined uniquely in explicit form, as illustrated in Figure 3.1 in the required distinction of cases.

In the field of CAD, implicit and parametric forms are particularly preferred. Implicit models are also axis dependent; however, multi-valued and closed forms, as well as infinite slopes can be defined precisely. They are well suited for the determination of

intersections and the evaluation of spatial positions on geometric objects.

The main focus within this work is on parametric representation techniques, which are most widely used in the field of CAD. Parametric forms allow for an elegant description of multi-valued and closed form functions and the computation of infinite derivatives. They are axis independent, naturally define bounded domains by the bounds of the parameter space, and in addition to analytical representations, offer a straightforward definition of free-form shapes, as required for modeling car bodies, ship hulls or aircraft wings. Additionally, a large variety of stable and efficient numerical algorithms exist (PIEGL AND TILLER (1997), FARIN (1999), FARIN (2002)).

3.2.2 NURBS parameter space, knot vectors

The modeling of NURBS-based geometry is defined as a linear combination of NURBS basis functions and associated vector-valued coefficients, denoted as control points. The computation of NURBS functions in parametric form requires the definition of a parameter space $\tilde{\Omega}_{\mathrm{pa}}$, which is related to knot vectors. These vectors are defined as a sequence of equal or increasing real numbers, called knots. For a fixed polynomial degree p and number k of basis functions, a knot vector Ξ has the following structure in one dimension

$$\Xi = \{\xi_1, \xi_2, ..., \xi_{k+p+1}\}. \tag{3.1}$$

A normalization of the knot vector domain is irrelevant for the shape of the basis functions, which do not depend on absolute knot values, but on their relative distances, i.e. knot spans. Ξ directly determines the properties of the basis functions and thus the geometric object. Knot spans of nonzero length subdivide the entire geometry into elements.
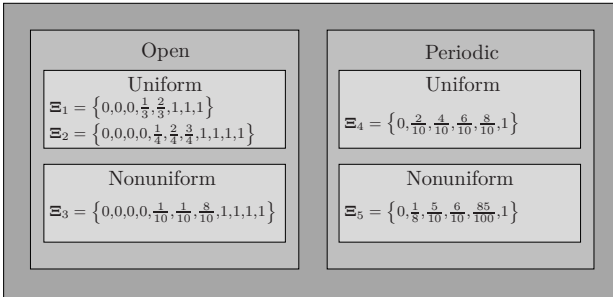
Figure 3.2: Types of knot vectors.

The two main classes of knot vectors are periodic and open, with a further differentiation into the categories uniform and nonuniform, which depends on the arrangement of knot values, as shown in Figure 3.2.

Both open and periodic knot vectors enable the modeling of geometries that are either open or closed. In open knot vectors, the first and last knots have a multiplicity of $p + 1$, with p again defining the polynomial degree of the basis functions. The geometry interpolates the endpoints of the associated control polygon and is furthermore tangential to the first and last segments of the control net. The first plots of NURBS geometries, which illustrate the concept of control polygons more clearly, are provided in Section 3.4. Open knot vectors are most frequently used in computer-aided geometric modeling and will be exclusively used in this work.

The end knots of periodic knot vectors in contrast to open vectors only possess a multiplicity of one. The geometric object does not interpolate the vertices of the control polygon in general.

Uniform knot vectors are characterized by equidistant knot spans, which yield a uniform parametrization of the geometry. Internal knot values may only occur once. Nonuniform knot vectors either possess unequal knot spacings and/or internal knots with multiplicity greater than one. They are well suited for modeling sharp corners and kinks and to adequately resolve domains of high curvature.

The knot vectors Ξ_1 and Ξ_2 in Figure 3.2 are two examples of open and uniform types. Obviously, the first and last knots are repeated p times and internal knot values $(0 < \xi < 1)$ only show up once. Ξ_1 represents a knot vector for computing basis functions up to the polynomial order two, whereas Ξ_2 leads to cubic basis functions.

Ξ_3 is open and nonuniform. Internal knot values are unequally spaced or repeated, which, as previously mentioned, significantly affects the properties of the NURBS basis. Examples of periodic knot vectors are provided with Ξ_4 and Ξ_5, which have the same principal structure as open knot vectors, except for the multiplicities of the first and last knot values.

The NURBS curve and surface objects to be investigated in this work can be described with either one or two parameters, ξ and η. The associated parametric domains are therefore either line segments or rectangles, which are defined by the tensor product of two knot vectors $\boldsymbol{\Xi}$ and $\mathbf{H}$, respectively.

The shell surfaces of Euclidean space $\mathbb{R}^3$ whose topologies are rectangular in the parametric space, only require the definition of one patch. For more complex geometries or the application of different physical models, several patches have to be set up and joined along common interfaces in order to define the complete body. Details of connecting several NURBS surface patches are described in Section 3.6.

3.3 B-spline basis functions

The notion of a knot vector introduced in Section 3.2.2 enables a complete definition of the parameter space of NURBS patches. For the computation of the piecewise rational NURBS basis functions, the derivation of polynomial B-splines which only depend on the knot vector data is required in the first step. As illustrated in the subsequent section, NURBS functions are defined with B-splines and the concepts of homogeneous coordinates and projective geometry.

Higher-dimensional (bivariate and trivariate) NURBS cannot be derived directly from the higher-dimensional B-spline functions; see Section 3.4. Therefore, the subsequent computation of B-spline basis functions is restricted to the one-dimensional case.

Recursive computation

B-spline functions are linearly independent, piecewise polynomials with compact support. On the knot spans $[\xi_i, \xi_{i+1})$, the one-dimensional segments of B-splines are infinitely continuously differentiable, whereas at knot locations the pieces are tied together with reduced continuity. The maximum regularity of B-spline functions is $p - 1$.

Different possibilities of computing the B-spline basis functions exist. Most frequently, the recursive computer-compatible relation of Cox (COX (1972)) and de Boor (DE BOOR (1972)) is used.

Starting from the piecewise constant, one-dimensional functions of parameter ξ,

$$\mathbf{B}_0 = \{B_{i,0}(\xi)\} = \begin{cases} 1 & \text{for } \xi_i \leq \xi < \xi_{i+1} \\ 0 & \text{else}, \end{cases} \tag{3.2}$$

higher-order ($p > 0$) B-spline functions are derived recursively as follows

$$\mathbf{B}_p = \{B_{i,p}(\xi)\} = \frac{\xi - \xi_i}{\xi_{i+p} - \xi_i} B_{i,p-1}(\xi) + \frac{\xi_{i+p+1} - \xi}{\xi_{i+p+1} - \xi_{i+1}} B_{i+1,p-1}(\xi). \tag{3.3}$$

The piecewise constant B-splines $\mathbf{B}_0$ are defined on the entire parametric domain $\tilde{\Omega}_{\mathrm{pa}}$ of $\boldsymbol{\Xi}$, but take on values of one only within the half-open interval $[\xi_i, \xi_{i+1})$ and are zero elsewhere. Higher-order functions are linear combinations of two basis functions of one order lower together with associated coefficients. Equation (3.3) may lead to a quotient of $\frac{0}{0}$, which by definition is set to zero.

In Figure 3.3, the graphical interrelation of the recursive computation is displayed for one-dimensional B-splines up to order four according to PIEGL AND TILLER (1997). The dependency on the parametric coefficients is omitted therein.

$$
\begin{array}{c}
B_{1,0} \\
\quad \diagdown\, B_{1,1} \\
B_{2,0} \qquad\quad \diagdown\, B_{1,2} \\
\quad \diagdown\, B_{2,1} \qquad\quad \diagdown\, B_{1,3} \\
B_{3,0} \qquad\quad \diagdown\, B_{2,2} \qquad\quad \diagdown\, B_{1,4} \\
\quad \diagdown\, B_{3,1} \qquad\quad \diagdown\, B_{2,3} \qquad \vdots \\
B_{4,0} \qquad\quad \diagdown\, B_{3,2} \qquad \vdots \\
\quad \diagdown\, B_{4,1} \qquad \vdots \\
B_{5,0} \qquad \vdots \\
\vdots
\end{array}
$$
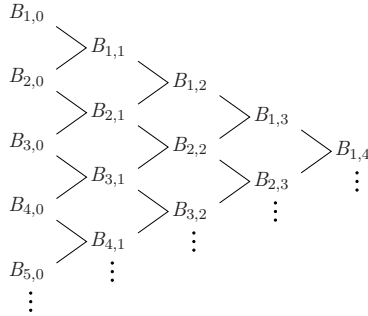
Figure 3.3: Graphical recursive relation – one-dimensional B-spline basis.

Important properties of the B-spline basis functions also with regard to the isogeometric shell analyses of the subsequent chapters are

- Local support: Each B-spline basis function $B_{i,p}(\xi)$ is nonzero only on the knot span $[\xi_i, \xi_{i+p+1})$,

- Local linear independence of B-spline basis functions,

- Positivity: Each B-spline basis function $B_{i,p}(\xi)$ is nonnegative in the entire parametric domain of $\boldsymbol{\Xi}$,

- Partition of unity: The sum of all B-spline basis functions for any parameter ξ is equal to one,

- Extrema: Except piecewise constants, B-spline basis functions $B_{i,p}(\xi)$ have exactly one maximum value.

Uniform B-spline basis

In a first example, uniform B-spline basis functions from zeroth to second order are computed according to Equations (3.2) and (3.3) and displayed in Figure 3.4 for the open uniform knot vector $\boldsymbol{\Xi}_1 = \left\{ 0, 0, 0, \frac{1}{3}, \frac{2}{3}, 1, 1, 1 \right\}$ of Figure 3.2.

The plot clearly illustrates that up to a polynomial order of $p = 1$, the one-dimensional B-spline basis is identical to the conventional Lagrange basis functions. With increasing order, however, both bases differ significantly from each other. Whereas the higher-order B-splines with uniform knot vector have a uniform and homogeneous shape, the structure of Lagrange functions become more and more heterogeneous with increasing polynomial order. Additionally, the support of higher-order B-splines is distributed over several knot spans, whereas the Lagrange basis is confined to one single element.
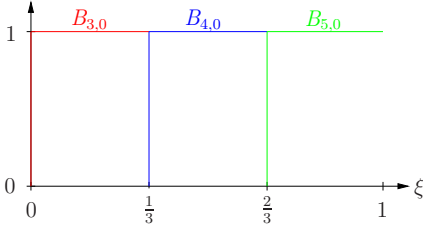
$$
\begin{aligned}
B_{1,0} = B_{2,0} &= 0 & &-\infty < \xi < \infty, \\
B_{3,0} &= 1 & &0 \le \xi < \tfrac{1}{3}, \\
&= 0 & &\text{else}, \\
B_{4,0} &= 1 & &\tfrac{1}{3} \le \xi < \tfrac{2}{3}, \\
&= 0 & &\text{else}, \\
B_{5,0} &= 1 & &\tfrac{2}{3} \le \xi < 1, \\
&= 0 & &\text{else}, \\
B_{6,0} = B_{7,0} &= 0 & &-\infty < \xi < \infty.
\end{aligned}
$$
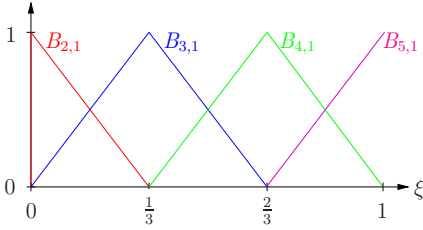
$$
\begin{aligned}
B_{1,1} &= 0 & &-\infty < \xi < \infty, \\
B_{2,1} &= 1 - 3\xi & &0 \le \xi < \tfrac{1}{3}, \\
&= 0 & &\text{else}, \\
B_{3,1} &= 3\xi & &0 \le \xi < \tfrac{1}{3}, \\
&= 2 - 3\xi & &\tfrac{1}{3} \le \xi < \tfrac{2}{3}, \\
&= 0 & &\text{else}, \\
B_{4,1} &= -1 + 3\xi & &\tfrac{1}{3} \le \xi < \tfrac{2}{3}, \\
&= 3 - 3\xi & &\tfrac{2}{3} \le \xi < 1, \\
&= 0 & &\text{else}, \\
B_{5,1} &= -2 + 3\xi & &\tfrac{2}{3} \le \xi < 1, \\
&= 0 & &\text{else}, \\
B_{6,1} &= 0 & &-\infty < \xi < \infty.
\end{aligned}
$$
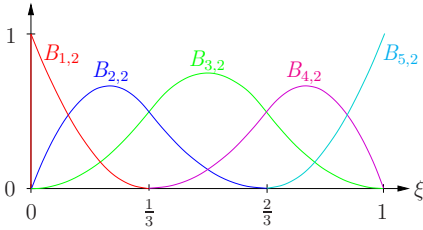
$$
\begin{aligned}
B_{1,2} &= (-1 + 3\xi)^2 & &0 \le \xi < \tfrac{1}{3}, \\
&= 0 & &\text{else}, \\
B_{2,2} &= 6\xi - \tfrac{27}{2}\xi^2 & &0 \le \xi < \tfrac{1}{3}, \\
&= \tfrac{1}{2}(-2 + 3\xi)^2 & &\tfrac{1}{3} \le \xi < \tfrac{2}{3}, \\
&= 0 & &\text{else}, \\
B_{3,2} &= \tfrac{9}{2}\xi^2 & &0 \le \xi < \tfrac{1}{3}, \\
&= -\tfrac{3}{2} + 9\xi - 9\xi^2 & &\tfrac{1}{3} \le \xi < \tfrac{2}{3}, \\
&= \tfrac{9}{2}(-1 + \xi)^2 & &\tfrac{2}{3} \le \xi < 1, \\
&= 0 & &\text{else}, \\
B_{4,2} &= \tfrac{1}{2}(-1 + 3\xi)^2 & &\tfrac{1}{3} \le \xi < \tfrac{2}{3}, \\
&= -\tfrac{15}{2} + 21\xi - \tfrac{27}{2}\xi^2 & &\tfrac{2}{3} \le \xi < 1, \\
&= 0 & &\text{else}, \\
B_{5,2} &= (-2 + 3\xi)^2 & &\tfrac{2}{3} \le \xi < 1, \\
&= 0 & &\text{else}.
\end{aligned}
$$

Figure 3.4: Constant to quadratic uniform B-spline basis of Ξ_1.

The effects of higher-order and higher-continuity NURBS discretizations on the computational results of the developed isogeometric shell finite element formulations will be investigated in detail in Chapter 5 and the following.

The piecewise structure of higher-order B-splines is illustrated in Figure 3.5 for the quadratic B-spline $B_{3,2}$, which was derived in Figure 3.4. The function is composed of three polynomial segments, which are defined on the knot spans $\left[0, \frac{1}{3}\right)$, $\left[\frac{1}{3}, \frac{2}{3}\right)$ and $\left[\frac{2}{3}, 1\right)$. Whereas the polynomials are infinitely continuously differentiable, $B_{3,2}$ represents a $C^{p-m} = C^{2-1} = C^1$-continuous piecewise function due to the existence of the internal knot values $\xi = \frac{1}{3}$ and $\xi = \frac{2}{3}$ with multiplicity $m = 1$.
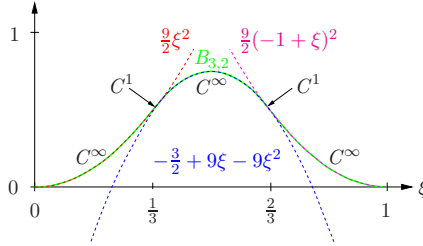
Figure 3.5: Polynomial segments of $B_{3,2}$.

Nonuniform B-spline basis

In contrast to Lagrange polynomials, B-splines and NURBS allow for a systematic control of continuity by repeating existing knots, which is an essential property for the geometric modeling of objects with kinks and sharp bends. Inserting multiple knots additionally reduces the support of the basis. Apart from purely geometric considerations, the control of continuity of the basis functions is fundamental with regard to the analysis of non-smooth problems such as contact, sharp boundary layers in plates and shells or material interfaces, for example.
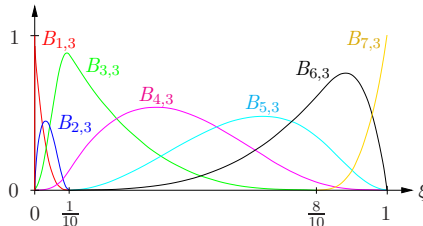
Figure 3.6: Cubic nonuniform B-spline basis $\mathbf{B}_3$ of $\mathbf{\Xi}_3$.

$\mathbf{\Xi}_3$ of Figure 3.2 represents an open nonuniform knot vector for computing B-spline basis functions of order three. Non-uniformity of $\mathbf{\Xi}_3$ is based on both nonuniform knot

spans and the existence of multiple interior knot values at $\xi = \frac{1}{10}$. Therefore, the maximum available continuity of C^2 is reduced to C^1 at $\xi = \frac{1}{10}$. Compared to the uniform quadratic basis of Figure 3.4, the heterogeneous shape of the cubic B-spline functions becomes clearly apparent in Figure 3.6.

Periodic B-spline basis

Finally, periodic uniform linear and quadratic B-spline basis functions are derived from the knot vector $\mathbf{\Xi}_4$ of Figure 3.2 and are displayed in Figure 3.7. All functions are identical and shifted within the parametric domain, which offers efficient computation strategies.

Finite element analysis with periodic B-splines defined on regular parametric domains has been investigated in HÖLLIG (2002), HÖLLIG (2003), among others. Periodic basis functions will not be used in this work. For more details with regard to both CAD and FEA applications, the reader is referred to ROGERS AND ADAMS (1990), PIEGL AND TILLER (1997), FARIN ET AL. (2002), HÖLLIG (2002) and HÖLLIG (2003).
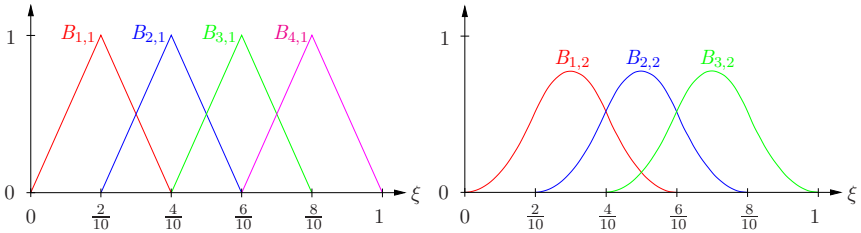
Figure 3.7: Periodic B-spline basis functions $p = 1, 2$ of $\mathbf{\Xi}_4$.

Derivatives of B-spline basis functions

Derivatives of B-spline functions are obtained by formal differentiation. A general formula for computing the b-th derivative of one-dimensional B-spline functions $\mathbf{B}_p(\xi)$ is given as follows

$$\mathbf{B}_p^{(b)} = \left\{ B_{i,p}^{(b)}(\xi) \right\} = p \left(\frac{B_{i,p-1}^{(b-1)}(\xi)}{\xi_{i+p} - \xi_i} - \frac{B_{i+1,p-1}^{(b-1)}(\xi)}{\xi_{i+p+1} - \xi_{i+1}} \right). \tag{3.4}$$

The details of Equation (3.4) are provided, for instance, in PIEGL AND TILLER (1997), as well as strategies for applying the Cox-de Boor recursion formula for a more efficient

computation of B-spline derivatives.

The higher continuity of the basis may result in derived quantities such as strains or stresses in solid FEA, which are again continuous, a fact that does not show up with standard Lagrange discretizations independent of their polynomial order.

The required modifications of conventional methods to unlock element formulations of isogeometric higher-order and higher-continuity shell analysis, which account for continuous strain and stress distributions, are developed in Chapter 6.

3.4 NURBS curves and surfaces

So far, the notion of knot vectors and the computation of one-dimensional polynomial B-spline basis functions have been introduced. For deriving NURBS functions, however, additional geometric information based on the concepts of homogeneous coordinates and projective transformation is required, which is explained within this section.

The geometric definition of NURBS objects in $\mathbb{R}^d$, with "d" representing the spatial dimension, is related to a perspective map of weighted polynomial B-spline data from the projective space $\mathbb{R}^{d+1}$. Therefore, at first B-spline geometries are defined as linear combinations of the basis functions and vector valued coefficients associated with the control points.

B-spline curves in $\mathbb{R}^d$

A B-spline curve $\mathbf{C}(\xi)$ of $\mathbb{R}^d$ with basis of order p is defined as

$$\mathbf{C}(\xi) = \sum_{i=1}^{k+1} B_{i,p}(\xi)\,\mathbf{P}_i. \tag{3.5}$$

$\mathbf{P} = \{\mathbf{P}_i\} \in \mathbb{R}^d$ represent the position vectors to the control points, whose linear interpolation is denoted as control polygon. Every control point is uniquely associated with one basis function. The properties of $\mathbf{C}(\xi)$ directly follow from the properties of the corresponding B-spline basis. The entire curve is composed of individual polynomial segments, which are connected at the knot locations mapped into the spatial domain. B-spline objects are contained in the convex hull of their control polygons, which enables intuitive shape design and results from the non-negativity, partition of unity and local support properties of the B-spline basis. For a polynomial order of one, the geometric object coincides with the control net and will otherwise only be approximated. By changing the spatial location of a point $\mathbf{P}_i$, the curve is affected only in the interval

associated with the knot spans $[\xi_i, \xi_{i+p+1})$ due to the local support property of the B-spline basis. In contrast to Bézier objects, the number of control points $\{\mathbf{P}_i\}$ to be used for the modeling $\mathbf{C}(\xi)$ is independent of the order of the basis.

$$\mathbf{\Xi}_2 = \left\{0, 0, 0, 0, \tfrac{1}{4}, \tfrac{2}{4}, \tfrac{3}{4}, 1, 1, 1, 1\right\}$$

$$\mathbf{P}(x,y) = \{(0,0), (2,0), (1,4), (7,4), (5,-2), (8,-2), (8,2)\}$$

Figure 3.8: B-spline curve $\mathbf{C}_{\mathbf{\Xi}_2}(\xi)$.
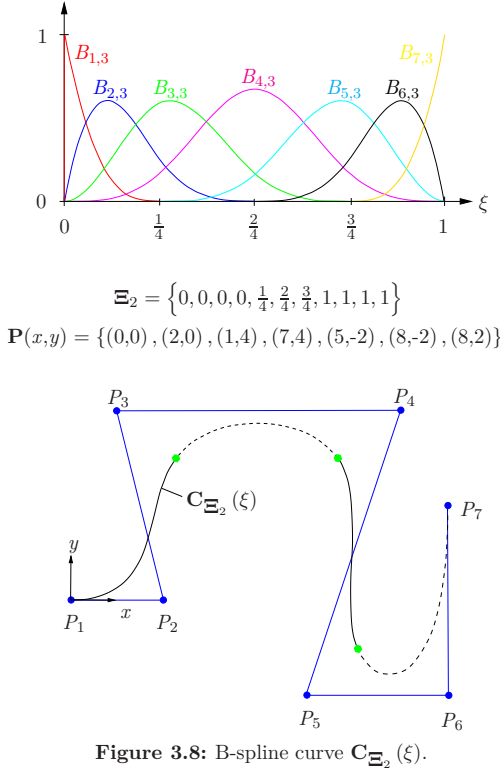
As a first example, the B-spline curve $\mathbf{C}_{\mathbf{\Xi}_2}(\xi) \in \mathbb{R}^2$ is presented in Figure 3.8. The cubic B-spline basis is derived from the open uniform knot vector $\mathbf{\Xi}_2$ of Figure 3.2. The four knot spans $\left[0, \tfrac{1}{4}\right), \left[\tfrac{1}{4}, \tfrac{2}{4}\right), \left[\tfrac{2}{4}, \tfrac{3}{4}\right), \left[\tfrac{3}{4}, 1\right)$ subdivide the object into four elements, which are displayed with different linestyles. The uniform open knot vector defines the maximum continuity of $C^{p-1} = C^2$ of $\mathbf{C}_{\mathbf{\Xi}_2}(\xi)$ and an identical orientation of the curve's end tangents with the end segments of the control mesh. Clearly, the convex hull property and the approximation of the control mesh can be ascertained. With decreasing polynomial order, the curve converges toward the control polygon, whereas increasing the order moves the object further away from the control net, but preserves the convex hull property.

B-spline geometries are invariant with respect to affine transformations, which in general are composed of linear transformations, such as rotations, shearing or scaling and subsequent translation. Affine invariance represents an important property in CAD applications, as modifications of the geometric objects may therefore be directly applied to the control point data.

Compared to classical FEA, in NURBS discretizations, the entire parametric domain $\tilde{\Omega}_{\mathrm{pa}}$ of a patch, which may consist of an arbitrary number of elements, is mapped with one global geometry function into the spatial domain Ω_{pa} (COTTRELL ET AL. (2009), DÖRFEL ET AL. (2010)). See, for instance, Figure 3.12.

Weighted B-splines, projective transformation and NURBS curves

With the definitions of B-spline curve objects at hand, the geometric derivation of NURBS objects on the basis of perspective mappings of the weighted polynomial B-spline data will now be explained. Geometries in the projective space may be described by using the concept of homogeneous coordinates, which are frequently denoted as weights $\{w_i\}$. A weighted polynomial B-spline geometry of $\mathbb{R}^{\mathrm{d}+1}$ is obtained by first multiplying its control point data with the homogeneous coordinates. By means of projective transformation, the weighted geometry of $\mathbb{R}^{\mathrm{d}+1}$ is subsequently mapped onto the projective hyperplane $\mathbb{H} = 1$ of Euclidean space $\mathbb{R}^{\mathrm{d}}$, which may be graphically visualized by straight lines passing from the weighted control points through the origin $\mathbf{0}$ of the coordinate system $\{x, y, z\}$. Due to perspective invariance, the transformation of the entire geometric object is accurately modeled by applying the mapping to the control point data only. In Figure 3.9, the projection of a weighted polynomial B-spline curve $\mathbf{C}^w(\xi) \in \mathbb{R}^3$ onto a rational curve $\mathbf{C}(\xi) \in \mathbb{R}^2$ is schematically shown.

Algebraically, the projection can be determined by the quotient of the weighted B-spline geometry and a scalar weighting function $W(\boldsymbol{\xi})$, which is defined in Equation (3.6) for a NURBS curve. $W(\boldsymbol{\xi})$ represents the sum of all B-spline basis functions of a patch that are multiplied with the control point weights.

$$\mathbf{C}(\xi) = \frac{\mathbf{C}^w(\xi)}{W(\xi)} = \frac{\sum\limits_{i=1}^{k+1} B_{i,p}(\xi) \mathbf{P}_i^w}{\sum\limits_{j=1}^{k+1} B_{j,p}(\xi) w_j} \tag{3.6}$$

The weights directly affect the NURBS geometry. For values $w_i > 1$, the object moves toward the control polygon, whereas for weights smaller than one, the influence of the control point on the geometry decreases. Control points with $w_i = 0$ do not affect the
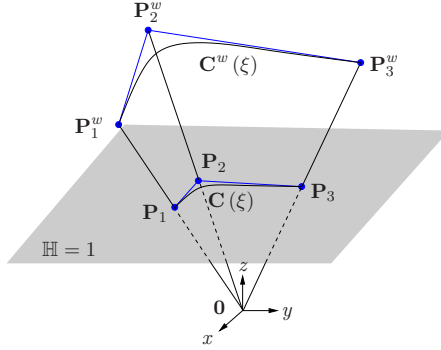
Figure 3.9: Projective transformation – generation of a NURBS curve.

geometric object at all. If all $\{w_i\}$ are equal to one, the NURBS basis simplifies to the polynomial B-spline basis (ROGERS AND ADAMS (1990), PIEGL AND TILLER (1997), FARIN (1999) or FARIN ET AL. (2002)).

Alternatively, the rational NURBS basis of $\mathbb{R}^d$ may be directly determined in $\mathbb{R}^d$: The polynomial B-spline basis is first weighted with the homogeneous coordinates $\{w_i\}$ and subsequently divided by the weighting function $W(\boldsymbol{\xi})$, as shown for the one-dimensional case in Equation (3.7).

$$\mathbf{N}_p = \{N_{i,p}(\xi)\} = \frac{B_{i,p}(\xi)\,w_i}{W(\xi)} = \frac{B_{i,p}(\xi)\,w_i}{\sum\limits_{j=1}^{k+1} B_{j,p}(\xi)\,w_j} \tag{3.7}$$

The NURBS object finally results from the NURBS basis $\mathbf{N}_p$ and the control point data of $\mathbb{R}^d$ as defined in Equation (3.8)

$$\mathbf{C}(\xi) = \sum_{i=1}^{k+1} N_{i,p}(\xi)\,\mathbf{P}_i. \tag{3.8}$$

This algebraic approach, which is identical for curves, surfaces and solid bodies, has the same principal structure as the one introduced for modeling B-spline curve objects according to Equation (3.5). NURBS inherit the essential properties of B-spline basis functions, such as partition of unity, linear independence, local support and positivity. Due to their rational character, they additionally allow for an exact modeling of conic structures and enable a higher geometric flexibility than B-spline discretizations.

NURBS conic sections

Conic sections represent rational functions of second order and may be exactly defined with quadratic NURBS.

For the example of a quadratic circular segment of $\mathbb{R}^2$, the definition of control point positions and their associated weights are briefly explained and shown in Figure 3.10. Circular arcs with sweep angle α less than $180°$ may already be modeled with one quadratic NURBS element, which consequently consists of three basis functions and associated control points. Arcs with $\alpha \geq 180°$ are not frequently used in CAD, as they require the use of negative weights, which leads to an undesired loss of the convex hull property among others (PIEGL AND TILLER (1997)).

The open knot vector for recursively computing the quadratic basis functions has the structure $\Xi = \{0, 0, 0, 1, 1, 1\}$ and results in an interpolation of the control polygon at both ends, i.e. $\mathbf{P}_1$ and $\mathbf{P}_3$ by the curve object $\mathbf{C}(\xi)$ with weights $w_1 = w_3 = 1$. For this simple example, the control polygon only consists of two straight line segments $\overline{\mathbf{P}_1 \mathbf{P}_2}$ and $\overline{\mathbf{P}_2 \mathbf{P}_3}$ of equal length, which simultaneously define the end tangents on the circular arc. A radius of r and a sweep angle of $\alpha = 60°$ are selected, such that the coordinates (x_i, y_i, w_i) of the end control points can be specified by $\mathbf{P}_1 = (0, 0, 1)$ and $\mathbf{P}_3 = (r, 0, 1)$. The intersection of the tangent vectors of the arc yields the position of control point $\mathbf{P}_2$, which is $\left(\frac{r}{2}, \tan 30° \frac{r}{2}, w_2\right)$. For the exact definition of the circular arc with sweep angle α, the weight w_2 has to be equal to half of the cosine of α, which is $w_2 = \cos\frac{60°}{2}$.
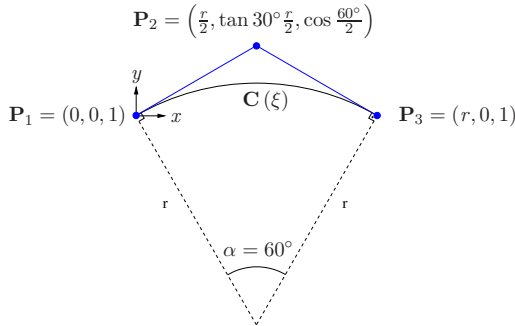
Figure 3.10: Circular arc ($\alpha = 60°$) – quadratic NURBS curve.

The complete circle may now be modeled by combining six of the previously derived circular segments, which are only C^0-continuous at their ends due to the open knot vector property. The entire NURBS object is, however, C^1-continuous, as the tangent vectors of adjoining segments are both collinear and of equal length. With regard to analysis,

C^1-continuity is restricted to the undeformed configuration without the definition of further constraints, as the relocation of control point positions during deformation may change both the orientation and length of adjacent tangent vectors.

Modeling of the NURBS circle with segments of sweep angle $\alpha = 90°$ or sweep angle $\alpha = 120°$ for example yields the weights $w_2 (\alpha = 90°) = \frac{\sqrt{2}}{2}$ and $w_2 (\alpha = 120°) = \frac{1}{2}$ of control point $\mathbf{P}_2$, respectively. In Figure 3.11, two examples of quadratic NURBS circles with three and six segments are shown.
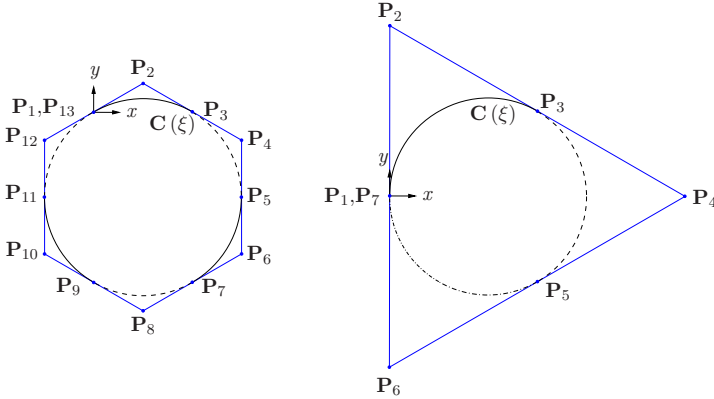
Figure 3.11: Full circles – three and six NURBS segments.

NURBS surfaces

The geometric description of NURBS surface structures of $\mathbb{R}^3$ requires the definition of bivariate NURBS basis functions. Therefore, in addition to the knot vector $\mathbf{\Xi}$, a second knot vector denoted as $\mathbf{H}$ is introduced. Both vectors may have a different parametrization and thus define basis functions of different number, continuity and polynomial order in each parametric direction. In contrast to B-splines, bivariate NURBS are not the result of applying a tensor product scheme to the one-dimensional NURBS basis functions, as is shown in Equation (3.9)

$$\mathbf{N}_{p,q} = \left\{ N_{i,j}^{p,q} (\xi,\eta) \right\} = \frac{B_{i,p} (\xi) \, C_{j,q} (\eta) \, w_{i,j}}{\sum\limits_{\bar{i}=1}^{k+1} \sum\limits_{\bar{j}=1}^{l+1} B_{\bar{i},p} (\xi) \, C_{\bar{j},q} (\eta) \, w_{\bar{i},\bar{j}}} \, . \tag{3.9}$$

The polynomial degree in ξ direction is denoted with p; the one for the η direction with q. $\{B_{i,p} (\xi)\}$ and $\{C_{j,q} (\eta)\}$ represent the univariate polynomial B-spline basis functions

of both parametric directions and $\{w_{i,j}\}$ are the scalar weights. A NURBS surface can be consequently defined as

$$\mathbf{S}\left(\xi,\eta\right) = \sum_{i=1}^{k+1} \sum_{j=1}^{l+1} N_{i,j}^{p,q}\left(\xi,\eta\right) \mathbf{P}_{i,j}, \tag{3.10}$$

where $\{\mathbf{P}_{i,j}\}$ represents the set of control points. From the properties of one-dimensional NURBS, the following main properties of bivariate NURBS basis functions and surfaces can be established: positivity, linear independence, partition of unity, extrema and local support of the basis, as well as affine invariance and convex hull property of the geometric objects.

Construction of bivariate basis:
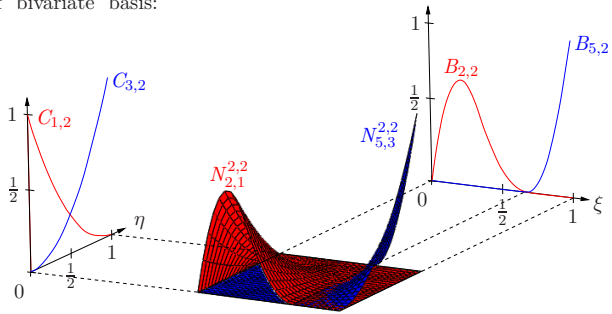
Geometric NURBS mapping:
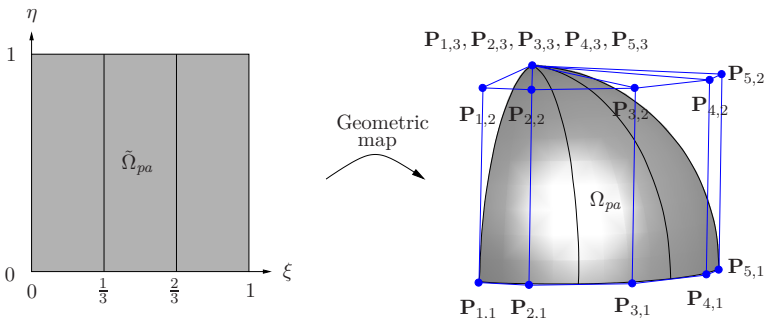
Figure 3.12: Spherical NURBS surface and bivariate basis functions.

In Figure 3.12, the construction of a spherical NURBS surface of $\mathbb{R}^3$ and its required "in-

gredients" are briefly explained. The parametric domain $\tilde{\Omega}_{pa}$ is defined by the two knot vectors $\mathbf{\Xi} = \left\{0, 0, 0, \frac{1}{3}, \frac{2}{3}, 1, 1, 1\right\}$ and $\mathbf{H} = \{0, 0, 0, 1, 1, 1\}$, from which the basis functions can be derived according to Equations (3.2), (3.3) and (3.9). As examples, the two biquadratic NURBS basis functions $N_{2,1}^{2,2}(\xi, \eta)$ and $N_{5,3}^{2,2}(\xi, \eta)$ and the involved one-dimensional B-spline basis functions are shown.

Although the entire object can already be modeled with one element, a refined discretization with three elements in circumferential direction and one element in meridian direction is selected, which illustrates more clearly the tensor product structure of the parametric domain $\tilde{\Omega}_{\mathrm{pa}}$ and the local support properties of the bivariate basis functions $\mathbf{N}_{p,q}$.

The computation of the control point locations and associated weights for conic sections has been briefly explained herein. A systematic modification of NURBS surface objects is identical to NURBS curves. Algorithms for computing the refined control point data are dealt with in more detail in Section 3.5. Therefore, the refined control polygon is only visualized without detailed derivation.

3.5 Algorithms for a systematic modification of NURBS

In this section, three basic algorithms for increasing the geometric flexibility of NURBS-based objects are presented by modifying the properties of the associated basis functions. These techniques, which are frequently denoted as

- knot insertion, knot refinement,
- order elevation, degree elevation and
- k-refinement,

do not only affect the geometric shape, but with regard to analysis and in particular the subsequent derivation of isogeometric shell finite elements, they are also used to control the discrete solution spaces of physical quantities such as the displacements, strains and stresses.

3.5.1 Knot insertion, knot refinement

The insertion of a single knot or several knots simultaneously in a vector $\mathbf{\Xi}$ is commonly denoted as knot insertion or knot refinement and relies on the Oslo algorithm originally developed in COHEN ET AL. (1980). For multivariate NURBS, knots may be inserted independently for the individual parametric directions.

Knot insertion is similar to conventional h-refinement techniques of classical FEA by

subdividing elements into smaller ones. The higher flexibility of knot refinement, however, is related to the potential of additionally inserting existing knots and therefore controlling the continuity and support of the NURBS basis without changing its polynomial degree. The insertion of existing knots does not generate new elements.

The subdivision of the parametric domain and thus the geometric NURBS object into new elements by the insertion of new knots requires the recomputation of both the basis functions and associated control points, such that the object remains geometrically and parametrically unchanged. Equation (3.11) defines the calculation of the new control points $\{\overline{\mathbf{P}}\}$ as a linear combination of the initial data $\{\mathbf{P}\}$ for the one-dimensional case (Piegl and Tiller (1997)). One single knot $\overline{\xi}$ is inserted in between two existing values ξ_a and ξ_{a+1}, where a represents the position in the knot vector. As usual, p is the polynomial degree of the basis. Inserting single knots only requires the computation of p new control points. All other control vertices coincide with the initial configuration

$$\overline{\mathbf{P}}_i = \gamma_i \, \mathbf{P}_i + (1 - \gamma_i) \, \mathbf{P}_{i-1} \,, \quad \text{with}$$

$$\gamma_i = \begin{cases} 1 & i \leq a - p, \\ \dfrac{\overline{\xi} - \xi_i}{\xi_{i+p} - \xi_i} & a - p + 1 \leq i \leq a, \\ 0 & a + 1 \leq i \,. \end{cases} \tag{3.11}$$

In Figure 3.13, knot insertion is applied to the cubic B-spline curve of Figure 3.8. A new knot $\overline{\xi} = \frac{5}{8}$ is therefore inserted into the original vector $\mathbf{\Xi}_2$, which yields the refined knot vector $\overline{\mathbf{\Xi}}_2$. Both the initial and the refined B-spline basis functions are displayed-the former ($\mathbf{B}_3$) with black dashed lines, the latter ($\overline{\mathbf{B}}_3$) in color. The recursive computation of the B-spline basis reveals that the first two and the last functions of $\mathbf{B}_3$ and $\overline{\mathbf{B}}_3$ coincide. The refined basis maintains its polynomial order as well as its continuity. It contains the initial basis as a subset.

The computation of the $p = 3$ new control points follows from Equation (3.11) with the location of the new knot $\overline{\xi} = \frac{5}{8}$ being equal to $a = 6$ in the knot vector.

The figure clearly illustrates that the initial and the refined curves $\mathbf{C}_{\mathbf{\Xi}_2}(\xi)$ and $\overline{\mathbf{C}}_{\mathbf{\Xi}_2}(\xi)$ are geometrically identical. The green dots on the curve objects show the initial split into four elements, whereas the extra turquoise dot represents the additional subdivision of knot span $\left[\frac{2}{4}, \frac{3}{4}\right)$ into two spans. The individual line segments are displayed in alternating solid and dashed line styles.

Knot refinement can be described as a process of sequentially inserting single knots into the vector. Therefore, the refinement algorithms of knot insertion may be used repeatedly without the need of additional means. Nevertheless, significantly more efficient procedures exist, with regard to concurrent insertion of knots, which are not reproduced

$$\Xi_2 = \left\{0,0,0,0,\tfrac{1}{4},\tfrac{2}{4},\tfrac{3}{4},1,1,1,1\right\}$$

$$\overline{\Xi}_2 = \left\{0,0,0,0,\tfrac{1}{4},\tfrac{2}{4},\tfrac{5}{8},\tfrac{3}{4},1,1,1,1\right\}$$

$$\mathbf{P}\left(x,y\right) = \left\{(0,0),(2,0),(1,4),(7,4),(5,-2),(8,-2),(8,2)\right\}$$

$$\gamma_i = \left\{1,1,1,\tfrac{5}{6},\tfrac{1}{2},\tfrac{1}{4},0,0\right\}$$

$$\overline{\mathbf{P}}\left(x,y\right) = \left\{(0,0),(2,0),(1,4),(6,4),(6,1),\left(\tfrac{23}{4},-1\right),(8,-2),(8,2)\right\}$$

Figure 3.13: Knot insertion – B-spline curve $\overline{\mathbf{C}}_{\overline{\Xi}_2}(\xi)$.
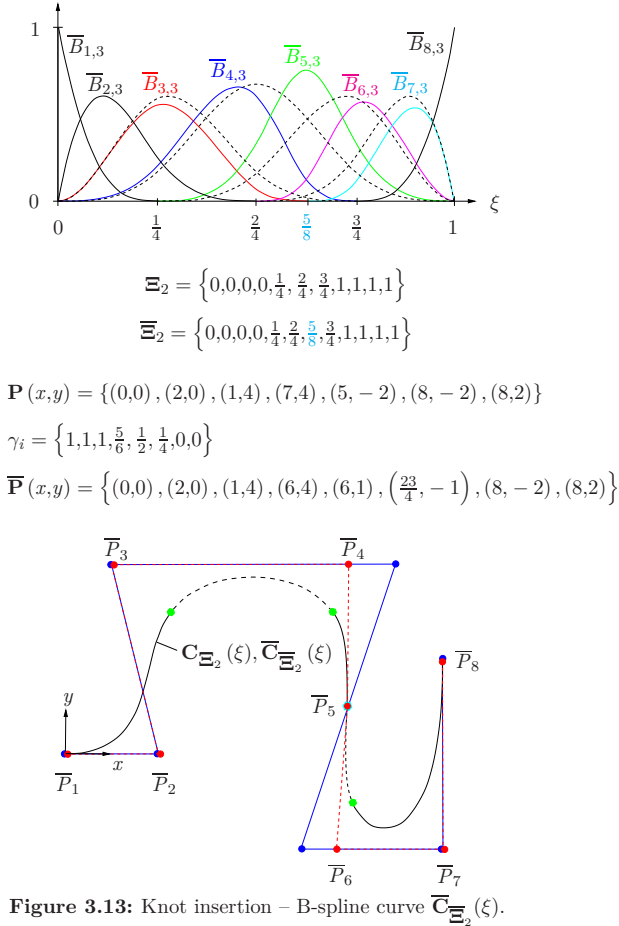
herein and can be found, for instance, in PIEGL AND TILLER (1997).

Due to the tensor product scheme of the parameter space $\tilde{\Omega}_{\mathrm{pa}} = \boldsymbol{\Xi} \otimes \mathbf{H}$ for the modeling of NURBS surfaces, the one-dimensional algorithms can be directly applied to the rows and columns of the control mesh. Standard knot insertion and knot refinement consequently affect the entire patch and thus preclude local refinement.

In Figure 3.14, the spherical biquadratic NURBS surface of Figure 3.12 is reused to present three different levels of mesh refinement due to knot insertion. The spatial domain consists of one single patch Ω_{pa} with rectangular topology and can thus be

modeled with one biquadratic NURBS element, which is shown in the left plot as a linear combination of nine bivariate NURBS basis functions and corresponding control points according to Equation (3.10). The refined models in the center and the right side of the figure both utilize a discretization with three elements in circumferential direction and either one or three elements in meridian direction. The associated knot vectors are additionally displayed.

$$\boldsymbol{\Xi} = \{0,0,0,1,1,1\} \qquad \overline{\boldsymbol{\Xi}} = \left\{0,0,0,\tfrac{1}{3},\tfrac{2}{3},1,1,1\right\} \qquad \overline{\overline{\boldsymbol{\Xi}}} = \left\{0,0,0,\tfrac{1}{3},\tfrac{2}{3},1,1,1\right\}$$

$$\mathbf{H} = \{0,0,0,1,1,1\} \qquad \overline{\mathbf{H}} = \{0,0,0,1,1,1\} \qquad \overline{\overline{\mathbf{H}}} = \left\{0,0,0,\tfrac{1}{3},\tfrac{2}{3},1,1,1\right\}$$
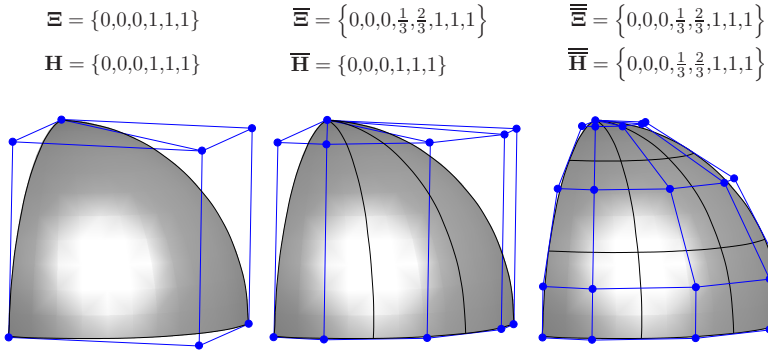
Figure 3.14: Knot refinement – spherical NURBS segments and control polygons.

The topic of local mesh refinement is not covered within this work. Therefore, in the following, some fundamental approaches are only briefly summarized.

In HÖLLIG (2003), a subdivision technique for B-splines referred to as a two-scale relation was presented as a linear combination and averaging approach of B-spline basis functions with the same degree defined on half of the original grid width. Originally, the concept of hierarchical B-spline refinement was introduced in FORSEY AND BARTELS (1988).

Schillinger and coworkers recently employed and further developed the hierarchical adaptive approach for both B-splines and NURBS (SCHILLINGER (2012), SCHILLINGER ET AL. (2012)) in combination with the finite cell method, an embedded domain approach which was developed in PARVIZIAN ET AL. (2007).

In VUONG ET AL. (2011) hierarchical B-splines and NURBS were used as locally refined function spaces to be integrated in the framework of isogeometric analysis and applied to two-dimensional problems.

Bornemann and Cirak presented a hierarchical B-spline finite element concept based on subdivision projection schemes, which enable a straightforward implementation into an existing finite element code architecture (BORNEMANN AND CIRAK (2013)).

3.5.2 Order elevation, degree elevation

The second strategy for increasing the flexibility of NURBS objects is degree elevation or order elevation of the NURBS basis. In this work, the expressions "degree" and "order" have the same meaning, whereas in many textbooks on CAD the term "order" is associated with the degree of polynomial functions plus one.

Due to order elevation, the NURBS object is embedded in a higher-dimensional vector space without changing the geometry and parametrization. This method is similar to p-refinement of conventional FEA (SZABÓ ET AL. (2004)) and identical for the case of C^0-continuity of the basis in the entire domain.

The principle steps of order elevation are briefly outlined in the following. First, the parametric domain $\tilde{\Omega}_{\mathrm{pa}}$ is subdivided into Bézier, i.e. C^0-continuous elements by successively inserting existing internal knot values. Thus, the number of elements remains unchanged. Subsequently, order elevation is performed on each knot span either by one or by several degrees in one step. Finally, redundant multiple knots are removed in order to reconnect the individual knot segments. The polynomial order of the NURBS object is increased, while the continuity of the basis remains unchanged.

In order to preserve the original shape of the geometry, order elevation requires the recomputation of control point locations. For NURBS structures, the new control points $\left\{\overline{\mathbf{P}}\right\}$ are calculated from the original data $\{\mathbf{P}\}$ together with the coefficients γ_i on Bézier segments according to Equation (3.12) for a one-dimensional model with an order elevation by one degree (PIEGL AND TILLER (1997)). More sophisticated and efficient numerical algorithms exist for degree elevation by several orders in one step; they are, however, not reproduced herein as they are very complex. The reader is therefore referred to the textbooks and articles on CAD cited throughout this chapter.

$$
\begin{aligned}
\overline{\mathbf{P}}_i^w &= \left(1 - \gamma_i\right) \mathbf{P}_i^w + \gamma_i \, \mathbf{P}_{i-1}^w, \quad \text{with} \\
\gamma_i &= \frac{i-1}{p+1}, \quad i = 1, \dots, p+2
\end{aligned}
\tag{3.12}
$$

Order elevation by one degree will now be made concrete for the cubic B-spline curve of Figure 3.8, which consists of four elements. The parametric domain $\tilde{\Omega}_{\mathrm{pa}}$ is defined by the open uniform knot vector $\boldsymbol{\Xi}_2$, which yields C^2-continuity. In order to preserve this continuity, the order elevated knot vector must have the following structure: $\overline{\boldsymbol{\Xi}}_2 = \left\{0, 0, 0, 0, 0, \frac{1}{4}, \frac{1}{4}, \frac{2}{4}, \frac{2}{4}, \frac{3}{4}, \frac{3}{4}, 1, 1, 1, 1, 1\right\}$. This enables the computation of the refined basis functions $\mathbf{B}_4$ of order four, as displayed in color in Figure 3.15. The initial cubic basis ($\mathbf{B}_3$) is shown in a black dashed line style.

A detailed presentation of the entire algorithm for computing the new control points, which is nested in the procedure of Bézier segmentation, order elevation and knot re-
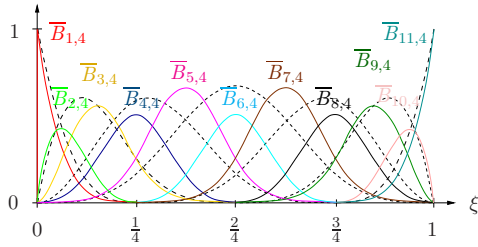
$$\Xi_2 = \left\{0,0,0,0,\tfrac{1}{4},\tfrac{2}{4},\tfrac{3}{4},1,1,1,1\right\}$$

$$\overline{\Xi}_2 = \left\{0,0,0,0,0,\tfrac{1}{4},\tfrac{1}{4},\tfrac{2}{4},\tfrac{2}{4},\tfrac{3}{4},\tfrac{3}{4},1,1,1,1,1\right\}$$

$$\mathbf{P}\,(x,y) = \left\{(0,0),(2,0),(1,4),(7,4),(5,-2),(8,-2),(8,2)\right\}$$

$$\overline{\mathbf{P}}\,(x,y) = \left\{(0,0),(1.5,0),(1.75,1),(1.625,3.5),(4,4),(6.33,3.5),\right.$$

$$\left.(6,1),(5.54,-1.5),(7.25,-2),(8,-1),(8,2)\right\}$$
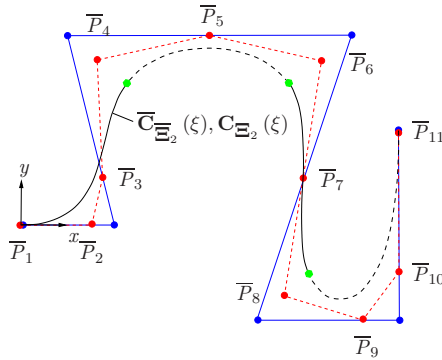
Figure 3.15: Order elevation – B-spline curve $\overline{\mathbf{C}}_{\overline{\Xi}_2}(\xi)$.

moval, is too complex to be reproduced herein. Therefore, only the final result of the new control point data is presented and highlighted in red. The original control mesh is displayed with blue solid lines. The number of elements remains unchanged.

Degree elevation of NURBS surfaces is performed in the same manner, as explained for knot insertion of surface structures in Section 3.5.1 by applying the one-dimensional algorithms to the rows and columns of the control mesh. A large variety of efficient and stable algorithms for order elevation of both NURBS curves and surfaces can be found in the CAD-based literature referred to in this chapter.

3.5.3 K-refinement

The knot refinement and order elevation procedures introduced so far represent powerful computational algorithms in order to enrich and modify the NURBS basis and to increase the flexibility of geometric objects.

A novel refinement strategy denoted as "k-refinement" combines the two aforementioned methods of knot refinement and order elevation, such that the refined NURBS basis is of higher order and higher continuity. It was presented in HUGHES ET AL. (2005) within the establishment of isogeometric analysis.

The modus operandi of k-refinement, in principal, consists of first elevating the degree of the NURBS basis functions up to a desired order, followed by the insertion of distinct, new knot values into the order-elevated knot vector. The maximum possible continuity of the NURBS basis, however, can only be obtained if the NURBS surface topologically corresponds to a rectangle and can thus be modeled with one element. Continuity constraints between elements in the initial configuration of the knot vector will therefore be retained during refinement.

In Figure 3.16, the concept of k-refinement is illustrated for a one-dimensional parametric domain. For simplicity, a discretization with nonrational B-spline basis functions is defined, which only depends on the knot vector. The approach of k-refinement applied to NURBS, however, is identical.

A linear $(p = 1)$ B-spline basis $\mathbf{B}_1(\xi)$ of an open knot vector $\mathbf{\Xi}$ with one single knot span is order-elevated to degree three first and subsequently uniformly refined with five distinct knot values. The new knot vector $\overline{\mathbf{\Xi}}$ now subdivides the domain into six elements. The k-refined cubic B-spline basis $\overline{\mathbf{B}}_3(\xi)$ has a maximum continuity of $C^{p-1} = C^2$.

$$\mathbf{\Xi} = \{0,0,1,1\} \qquad \overline{\mathbf{\Xi}} = \left\{0,0,0,0,\tfrac{1}{6},\tfrac{2}{6},\tfrac{3}{6},\tfrac{4}{6},\tfrac{5}{6},1,1,1,1\right\}$$
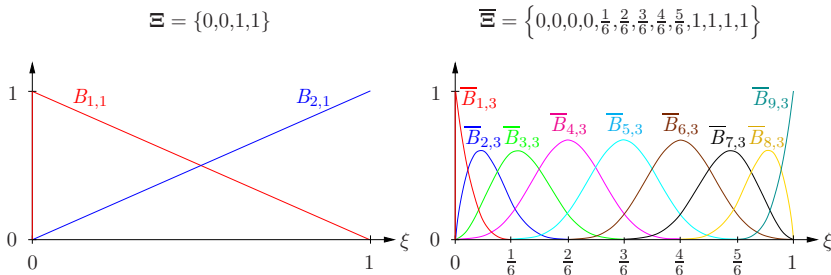
Figure 3.16: K-refinement – one-dimensional B-spline basis.

K-refinement results in a homogeneous shape of the basis functions independent of their polynomial order, which is in clear contrast to higher-order Lagrangian C^0-continuous functions associated with corner and interior nodes. A comparison of the homogeneous structure of maximum-continuity NURBS basis functions of order three to the inhomoge-

neous pattern of cubic Lagrange functions is graphically illustrated for a one-dimensional discretization with ten elements in Figure 5.6.

The superior behavior of k-refined NURBS in the analysis of structural and fluid mechanics problems, compared to conventional h- and p-refinement, has already been established in the first paper on IGA (HUGHES ET AL. (2005)) and has since been confirmed in a multitude of scientific works. For the derivation of NURBS-based shell finite elements with Kirchhoff-Love kinematics, which require functions with square integrable partial derivatives of order two, the formulation of higher, at least C^1-continuous basis functions, is essential. This is shown in Chapters 4 and the following. The effect of higher-continuity k-refined NURBS on the accuracy of discrete solutions in isogeometric shell analysis of smooth structural mechanics problems is investigated in Chapters 5 to 7. An in-depth mathematical treatment of the approximation properties of higher-continuity NURBS due to k-refinement will not be reproduced herein. Complementary literature is e.g. BAZILEVS (2006), COTTRELL ET AL. (2007), HUGHES ET AL. (2008) and EVANS ET AL. (2009).

3.6 Multiple NURBS surface patches

The existence of complex geometries, material interfaces or discontinuities in the thickness function of the shell body, for instance, require the definition of several patches and adequate coupling techniques.

Whereas the continuity within patches may be of higher order, at patch interfaces it is, in general, not greater than C^0 without employing further constraint conditions. In this thesis, only smooth NURBS surface multipatches with compatible parametrization along common interfaces are used. Thus, the control points of common edges spatially coincide. A corresponding example of a cylindrical shell with four NURBS patches is shown in Figure 3.17.

For subsequent FEA, the same degrees of freedom are assigned to spatially coincident control points, which yields a C^0-continuous patch coupling. This, however, is not sufficient for several isogeometric shell formulations of Chapter 4, which are based on Kirchhoff-Love shell kinematics.

In KIENDL ET AL. (2009), the authors derived an isogeometric rotation-free Kirchhoff-Love shell element and also addressed the problem of smooth multipatch coupling. By taking into account the rectangular structure of the NURBS control mesh, they suggest the application of linear constraint equations in master-slave form on patch interfaces with identical parametrization in order to strongly enforce slope continuity. For connecting patches with kinks, the relations to preserve the angle during deformation become nonlinear, which prevent a strong enforcement of the constraint conditions. Kiendl and
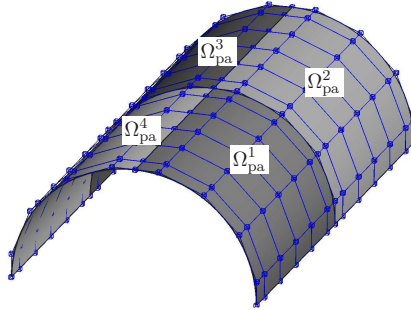
Figure 3.17: Compatible NURBS multipatch – C^0-continuous coupling.

coworkers therefore introduce a penalty-type method denoted as the "bending strip", which weakly imposes the constraint of connecting surface patches with slope continuity (KIENDL ET AL. (2010)).

This approach is used in Chapter 7 for the smooth coupling of compatible NURBS surface patches. It is schematically illustrated in Figure 3.18 for smoothly connecting two compatible NURBS surface patches of a cylindrical shell.

Bending strip (green)

Physical domain $\Omega_{\text{pa, bend.}}$ Parametric domain $\tilde{\Omega}_{\text{pa, bend.}}$
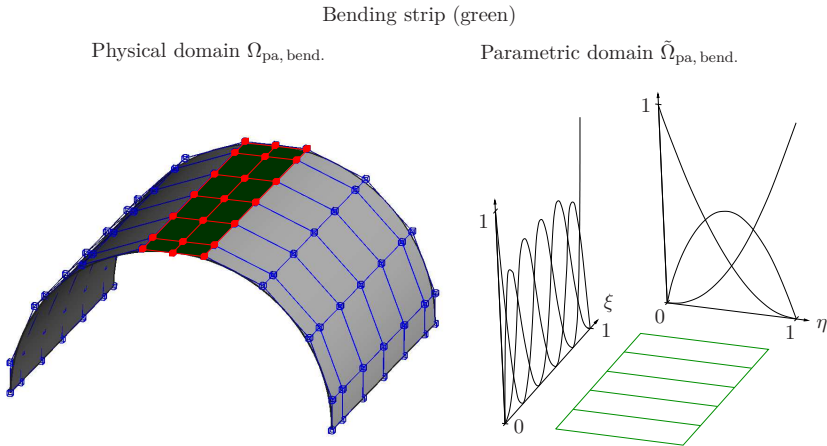
Figure 3.18: Bending strip – weak C^1 NURBS patch coupling.

Each patch is uniformly discretized with a mesh of four elements (six control points) in circumferential and five elements (seven control points) in axial direction by using biquadratic NURBS. This provides a conforming parametrization along the shared edge.

For the definition of the bending strip patch, which in physical space is displayed in dark green, triples of control points along the entire patch interface are used. The associated control mesh is highlighted in red. The bending strip does not possess any mass or stiffness, except a directional user-defined bending stiffness perpendicular to the interface edge. Investigations of reliable bending stiffness values to preserve the included angle during deformation have been performed in KIENDL ET AL. (2010). The parameter space of the bending strip patch is defined by the tensor product of two knot vectors. The triples of control points in transverse direction of the interface require the definition of one element of second order. Along the interface edge, the parametrization, i.e. the knot vector structure of the adjoining NURBS edges, is adopted. This approach slightly differs from the original version, where for simplicity and less computational costs, linear NURBS functions are used along interface edges for the bending strip. The entire bending strip of the cylindrical shell example consequently consists of five elements in axial direction and one element in transverse direction with biquadratic NURBS functions.

In BENSON ET AL. (2013), limitations of the bending strip method are discussed as it precludes, for instance, the evolution of plastification in regions of high stresses such as shell intersections or near boundaries. This restriction, however, is not relevant for the linear elastic analyses of this thesis. In the same article, the authors alternatively propose the use of rigid bodies as generalizations of linear constraint techniques to nonlinear and explicit applications.

For further details on the coupling of patches in IGA, the reader is referred to COTTRELL ET AL. (2007), COTTRELL ET AL. (2009) and KIENDL (2011) in addition to the literature already mentioned.

4

Hierarchic Shell Models

This chapter presents a new hierarchic family of 3-, 5- and 7-parameter shell models (ECHTER ET AL. (2013)), which serve as a basis for the development of isogeometric displacement-based shell finite element formulations in Chapter 5.

The expression "hierarchic", on the one hand, can be related to the *mechanical* shell model. Starting from the basic 3-parameter shell in Section 4.3, which is suitable for modeling thin structures with predominantly membrane and bending action, by additionally accounting for shear flexibility, 5-parameter shell formulations see Section 4.4 are defined that are more convenient for moderately thick shells. The inclusion of extensibility in thickness direction enables, moreover, the derivation of 6- or 7-parameter shell models, which are presented in Section 4.5, and which additionally allow for complete three-dimensional constitutive laws.

The main objective of "hierarchic" in this chapter, however, is related to the hierarchic *parametrization* of the shell models with regard to model adaptivity. On the basis of a minimalistic shell model, which mechanically corresponds to the 3-parameter formulation, additional degrees of freedom will be switched on systematically in order to increase the approximation quality of the shell model. The procedure of adding the extra parameters is defined, such that the kinematic equations of the basic model are gradually enhanced to obtain the 5- and 7-parameter models, which, consequently, does not require a complete reformulation. The hierarchic parametrization of the kinematic equations additionally avoids certain locking effects in the discrete finite element formulations, which are investigated in detail in Chapter 5.

In addition, for reasons of comparison, 5- and 7-parameter shell models with nonhierarchic parametrization are derived. These formulations are specified with the expression "standard" shell models in this thesis.

The hierarchic shells of this chapter are mainly based on the concept of degeneration,

which is specified in detail in Section 4.1.3. Additionally, the following basic assumptions and approximations are accounted for: All proposed concepts are restricted to single layer models with constant thickness, geometrically linear kinematics and homogeneous, linear-elastic and isotropic material properties. No pre-integration of the constitutive law is performed. The static and kinematic variables of the shell equations are therefore stresses and strains.

For further information on classical shell theories and modeling techniques, the reader is referred to FLÜGGE (1962), NAGHDI (1972), BAŞAR AND KRÄTZIG (1985), GREEN AND ZERNA (1992), BISCHOFF ET AL. (2004) and TIMOSHENKO AND WOINOWSKY-KRIEGER (2007) to name but a few.

4.1 Principal strategies for deriving shell models

In this section, principal strategies to derive shell models are briefly summarized, with the concept of degeneration representing the basis for the shell formulations of Sections 4.3 to 4.5 and the shell finite elements of Chapters 5 and 6.

Shells represent curved, thin-walled structures where one dimension is, in general, significantly smaller than the other two. Therefore, physically reasonable assumptions with respect to geometry, kinematics and material law are frequently applied to the governing equations, which consequently yields an approximation of the 3D continuum theory. A quantification of the error for different simplified assumptions in classical shell surface theories has been dealt with in BAŞAR AND KRÄTZIG (1985) and BÜCHTER (1992), among others.

For details on the justification of various rod, plate and shell theories by mathematically proving the asymptotic convergence of their governing equations and solutions to three-dimensional theories in the limit of small parameters, such as the thickness or the curvature, the reader is referred to MORGENSTERN (1959), SANCHEZ-PALENCIA AND VASSILIEV (1992), ARNOLD AND FALK (1996) or ANTMAN (2005), for instance.

The principal strategies to derive shell models are

- the derivation from 3D non-polar continuum mechanics,

- the so-called direct approach (Cosserat surface) or

- the degenerated solid concept.

Classical shell theories are based on shell models obtained via the direct approach or the derivation from three-dimensional continuum mechanics. The degenerated solid concept has its origin in the derivation of shell finite elements. However, it was proved by BÜCHTER (1992) that identical assumptions with regard to geometry, kinematics and material law may finally yield the same element formulations.

4.1.1 Shell models from 3D non-polar continuum mechanics

The main idea of shell models to be derived from 3D non-polar continuum mechanics is the reduction of the mechanical behavior of a continuum to its essentials. Therefore, the behavior in thickness direction of the thin continuum is described independently of the mid-surface parametrization, which finally yields a spatial semi-discretization.

NAGHDI (1972) discretized the thickness direction of a shell continuum by an infinite series of monomials, which recovered the 3D mechanical behavior of the shell without approximation. Instead of monomials, Legendre polynomials could also be used.

For shell models with Kirchhoff-Love or Reissner-Mindlin kinematics, the basic assumptions and simplifications mainly imply the approximation of the shell body by its mid-surface and a linear ansatz across the thickness, the inextensibility of the shell director, the formulation of equilibrium without higher-order contributions and the neglect of transverse normal stresses, which consequently require a modification of the constitutive law to ensure asymptotic correctness (BAŞAR AND KRÄTZIG (1985)).

Alternatively to NAGHDI (1972), multi-layer theories have been developed, which again yield the exact 3D continuum solution in the limit of an infinite number of layers in thickness direction. Multi-layer shell models are not considered herein. The reader is referred to EPSTEIN AND GLOCKNER (1977), GRUTTMANN AND WAGNER (1994), BRAUN (1995) or HÖRMANN (2002), for instance.

Dimensional reduction can be performed by pre-integration of the material law in thickness direction of the shell body, thus associating the kinematic strain with stress resultants, which become functions of the in-plane convective coordinates only. Material pre-integration will, however, not be applied in this work. A more detailed discussion on this topic can be found, for example, in BAŞAR AND KRÄTZIG (1985), BÜCHTER (1992), BISCHOFF (1999) or BISCHOFF ET AL. (2004).

Details with regard to the assumptions to be made for the mechanical behavior of the 3-, 5- and 7-parameter shell models of this thesis are specified in Sections 4.3 to 4.5.

4.1.2 Shell models by direct approach

Instead of reducing a three-dimensional continuum theory to a 2D surface theory by imposing assumptions and approximations on both the kinematics and the material law, as explained in Section 4.1.1, surface-based shell theories may alternatively be derived directly on the basis of two-dimensional directed material continua, i.e. Cosserat-surfaces (DUHEM (1893), COSSERAT AND COSSERAT (1909)).

Each material point of the two-dimensional Cosserat surface, in addition to its position vector, is equipped with extra vectorial quantities denoted as directors. The Cosserat continuum therefore allows for the postulation of quantities, without the need of approx-

imations. Shell models of this type are therefore frequently referred to as geometrically exact (ERICKSEN AND TRUESDELL (1958), GREEN ET AL. (1965), SIMO AND FOX (1989)), although these formulations do not imply any higher accuracy compared to shell models derived from 3D non-polar continuum mechanics.

Despite the elegance of exactly formulating the shell kinematics on a Cosserat-surface, the delicate point of the direct approach is to relate the kinematic to the static variables by a proper choice of material law, which cannot be derived directly and associated to the static and kinematic variables of the three-dimensional continuum. The definition of a constitutive law therefore represents the essential modeling assumption (BAŞAR AND KRÄTZIG (1985)).

4.1.3 Degenerated solid concept

The degenerated solid concept has its origin in the derivation of shell finite elements. Instead of discretizing the shell models obtained in Sections 4.1.1 and 4.1.2, typical shell assumptions are imposed to the thickness direction via a certain choice of shape functions.

The concept in its original form is related to AHMAD ET AL. (1968) and was generalized to geometrical nonlinearities in RAMM (1976). Büchter identifies the equivalence of shell element formulations derived from 3D continuum mechanics and those obtained from degeneration, provided that identical physical and numerical assumptions are made (BÜCHTER (1992), BÜCHTER AND RAMM (1992)).

The imposition of a linear displacement ansatz in thickness direction of the shell body without any further assumptions on both the kinematics and material law, yields a 6-parameter shell model. By application of a difference vector formulation, the resulting independent parameters of the degenerated shell formulation are the three mid-surface displacement components and three difference vector displacement components, which are used to describe the deformation behavior of the shell.

The 3-, 5- and 7-parameter shell models of Sections 4.3 to 4.5, which are mainly based on the concept of degeneration, employ a surface parametrization of the homogeneous shell body. In contrast to conventional concepts of degeneration with Lagrangian basis functions and the application of averaged nodal directors (BÜCHTER (1992), BISCHOFF (1999), BISCHOFF ET AL. (2004)), the formulations of this thesis utilize a unique and continuous director field based on higher-order and higher-continuity NURBS discretizations.

Continuum-based degenerated shell elements, which physically represent 3D solids, have been developed, for instance, in SCHOOP (1986), PARISCH (1995), HAUPTMANN AND SCHWEIZERHOF (1998), KLINKEL ET AL. (2006) and HARTMANN (2007).

4.2 Differential shell geometry and kinematics
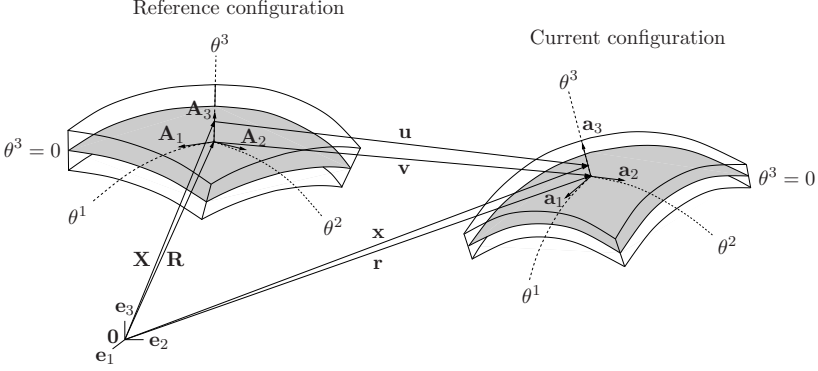
Figure 4.1: Configurations of the shell body.

A convective curvilinear coordinate system is introduced for the parametrization of the 3D shell body. The in-plane coordinates are defined by θ^α; the shell thickness direction by θ^3. Points of the shell mid-surface are specified by $\theta^3 = 0$. Material points of the shell body are thus labeled by the same coordinate triple $\left(\theta^\alpha, \theta^3\right)$ before and after deformation, while their location in space changes, i.e. their position vectors.

According to the conventions of Chapter 2, capital letters are used for quantities in the reference configuration and small letters refer to the current configuration.

For dimensional reduction, the position vectors $\mathbf{X}$ of the shell body in the undeformed configuration are defined as linear functions of θ^3. Thus, both the position vector $\mathbf{R}$ to a point on the shell mid-surface and the director $\mathbf{A}_3$ are only functions of the in-plane coordinates θ^α

$$\mathbf{X}\left(\theta^1, \theta^2, \theta^3\right) = \mathbf{R}\left(\theta^1, \theta^2\right) + \theta^3 \, \mathbf{A}_3\left(\theta^1, \theta^2\right). \tag{4.1}$$

According to Equations (2.4) and (4.1), the covariant base vectors of the shell body are defined by partial differentiation of the position vector $\mathbf{X}$ with respect to the convective coordinates θ^i

$$
\begin{aligned}
\mathbf{G}_\alpha &= \frac{\partial \mathbf{X}}{\partial \theta^\alpha} &&= \mathbf{R}_{,\alpha} + \theta^3 \, \mathbf{A}_{3,\alpha}\,, \\
\mathbf{G}_3 &= \frac{\partial \mathbf{X}}{\partial \theta^3} &&= \mathbf{A}_3\,.
\end{aligned}
\tag{4.2}
$$

For the shell mid-surface, the in-plane covariant base vectors are derived by partial derivation of the position vector $\mathbf{X}$ with respect to the in-plane convective coordinates θ^α as follows

$$\mathbf{A}_\alpha = \frac{\partial \mathbf{X}}{\partial \theta^\alpha} \bigg|_{\theta^3=0} = \mathbf{R}_{,\alpha} \,. \tag{4.3}$$

The third base vector $\mathbf{A}_3$ of the reference configuration, denoted as director, is obtained from the normalized cross product of the in-plane covariant base vectors $\mathbf{A}_\alpha$. It coincides with the normal vector of the undeformed mid-surface

$$\mathbf{A}_3 = \frac{\mathbf{A}_1 \times \mathbf{A}_2}{\|\mathbf{A}_1 \times \mathbf{A}_2\|} \,. \tag{4.4}$$

$\mathbf{A}_3$ may alternatively be derived from the position vector $\mathbf{X}$: $\mathbf{A}_3 = \frac{\partial \mathbf{X}}{\partial \theta^3}$.

4.3 Kirchhoff-Love shell model (3p)

Historically, the first hypothesis on the bending behavior of elastic rods was devised by the Swiss mathematician and physicist J. Bernoulli in 1691, who postulated that the cross section of a beam remains straight and normal to its center line during deformation, which is denoted as normal hypothesis.

The first mathematically correct theory on the structural behavior of plates accounting for Bernoulli's normal hypothesis was derived by G. Kirchhoff in 1850, which states that normals to the mid-surface in the undeformed configuration remain normal and unstretched in the deformed configuration (KIRCHHOFF (1850)).

Based on the work of Kirchhoff for plate problems, A. E. H. Love derived a general theory for both curved and plane surfaces (LOVE (1888)). The normality hypothesis for shell structures is therefore frequently associated with the term Kirchhoff-Love hypothesis.

In the 20th century, a multitude of Kirchhoff-Love type shell theories were developed (REISSNER (1942), GREEN AND ZERNA (1954), WUNDERLICH (1966), KOITER (1960), KOITER (1961)), to name but a few. It lasted, however, until 1963, when the first consistent Kirchhoff-Love type shell theory was derived by NAGHDI (1963).

Kinematics

In this section, the linearized Green-Lagrange strain tensor $\boldsymbol{\varepsilon}^{3\mathrm{p}}$ is derived in curvilinear convective coordinates, as required for the virtual work expression of the Kirchhoff-Love

shell model. The derivation is based on the concept of degeneration discussed in Section 4.1.3, the differential shell geometry and kinematic specifications of Section 4.2 and common assumptions and approximations for thin shells to be established in the following.

The deformation behavior of the thin, elastic and homogeneous shells in this thesis is physically dominated by membrane and bending action. The constraint to be imposed on the director of staying normal to the mid-surface, also in the deformed configuration, yields vanishing transverse shear deformations. Rotations of cross-sectional fibers are therefore not independent, but equal to the gradient of the mid-surface displacement field. Additionally, extensibility of the thin shell in thickness direction and transverse normal strains and stresses are disregarded.

By summarizing these assumptions and simplifications, the kinematics of thin shells with surface parametrization, as displayed in Figure 4.1, can be described with three independent parameters (3-parameter formulation (3p)), which correspond to the mid-surface displacement components v_i of a material point.

The computation of the linearized Green-Lagrange strain tensor with Kirchhoff-Love kinematics requires the specification of several additional variables which have not been introduced so far.

First, the position vector $\mathbf{x}^{3p}$ to an arbitrary material point of the shell body in the deformed configuration is defined as

$$\mathbf{x}^{3p}\left(\theta^1, \theta^2, \theta^3\right) = \mathbf{r}\left(\theta^1, \theta^2\right) + \theta^3\, \mathbf{a}_3^{3p}\left(\theta^1, \theta^2\right). \tag{4.5}$$

The director $\mathbf{a}_3^{3p}$ of the deformed configuration may be derived from a linearized rotation of $\mathbf{A}_3$, as shown in the principal sketch of Figure 4.2 and described for the general case of a linearized vector rotation, for instance, in BELYTSCHKO ET AL. (2008)

$$\mathbf{a}_3^{3p} = \mathbf{A}_3 + \boldsymbol{\Phi} \times \mathbf{A}_3. \tag{4.6}$$

$\boldsymbol{\Phi} \times \mathbf{A}_3$ represents the difference vector between the director of the undeformed configuration $\mathbf{A}_3$ and the rotated director of the current configuration $\mathbf{a}_3^{3p}$. The orthogonality of $\boldsymbol{\Phi} \times \mathbf{A}_3$ to the undeformed director $\mathbf{A}_3$ ensures satisfaction of the inextensibility constraint of the shell in thickness direction during deformation by assuming linearized kinematics.

The rotation of $\mathbf{A}_3$ is defined by the rotation vector $\boldsymbol{\Phi}$, which is a function of $\mathbf{A}_\alpha$ and associated rotation angles φ_α. $\boldsymbol{\Phi}$ represents an element of the tangent space, which is spanned by the in-plane base vectors $\mathbf{A}_\alpha$.
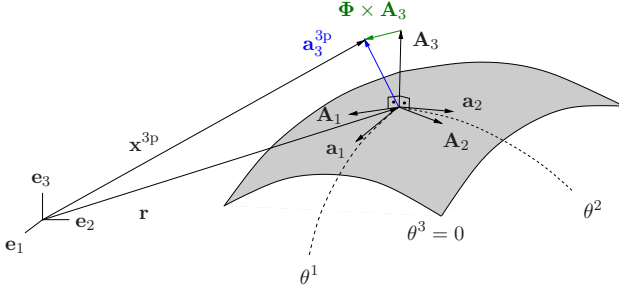
Figure 4.2: Deformed configuration – 3-parameter model.

$$\boldsymbol{\Phi} = \varphi_1 \, \mathbf{A}_1 + \varphi_2 \, \mathbf{A}_2 \tag{4.7}$$

The associated rotation angles φ_α read

$$
\begin{aligned}
\varphi_1 &= \frac{1}{\|\mathbf{A}_1 \times \mathbf{A}_2\|} \left(\mathbf{a}_2 - \mathbf{A}_2 \right) \cdot \mathbf{A}_3 &&= \frac{1}{\|\mathbf{A}_1 \times \mathbf{A}_2\|} \mathbf{v}_{,2} \cdot \mathbf{A}_3 \, , \\
\varphi_2 &= -\frac{1}{\|\mathbf{A}_1 \times \mathbf{A}_2\|} \left(\mathbf{a}_1 - \mathbf{A}_1 \right) \cdot \mathbf{A}_3 &&= -\frac{1}{\|\mathbf{A}_1 \times \mathbf{A}_2\|} \mathbf{v}_{,1} \cdot \mathbf{A}_3 \, .
\end{aligned}
\tag{4.8}
$$

$\mathbf{a}_\alpha$ are the covariant base vectors of the current configuration and $\mathbf{v}_{,\alpha}$ represent the partial derivatives of the mid-surface displacement field $\mathbf{v}$ of the shell with respect to the in-plane convective coordinates θ^α. $\|\mathbf{A}_1 \times \mathbf{A}_2\|$ denotes the Euclidean norm of $\mathbf{A}_1 \times \mathbf{A}_2$. The computation of the rotation angles φ_α is therefore related to the projection of the rotated in-plane base vectors $\mathbf{a}_\alpha$ in the direction of the undeformed normal $\mathbf{A}_3$.

The difference of the position vectors $\mathbf{x}^{3p}$ and $\mathbf{X}$ yields the displacement field $\mathbf{u}^{3p}$ at any point of the shell body. For the 3-parameter Kirchhoff-Love shell model, this results in

$$
\begin{aligned}
\mathbf{u}^{3p} &= \mathbf{x}^{3p} - \mathbf{X} \\
&= \mathbf{r} + \theta^3 \, \mathbf{a}_3^{3p} - \mathbf{R} - \theta^3 \mathbf{A}_3 \\
&= \mathbf{v} + \theta^3 \left(\boldsymbol{\Phi} \times \mathbf{A}_3 \right) .
\end{aligned}
\tag{4.9}
$$

The derivation of the Green-Lagrange strain tensor coefficients ε_{ij}^{3p} requires the partial derivatives of the displacement field $\mathbf{u}^{3p}$ with respect to the convective coordinates θ^i

$$
\begin{aligned}
\mathbf{u}^{3p}_{,\alpha} &= \mathbf{v}_{,\alpha} + \theta^3 \left(\boldsymbol{\Phi}_{,\alpha} \times \mathbf{A}_3 + \boldsymbol{\Phi} \times \mathbf{A}_{3,\alpha} \right) , \\
\mathbf{u}^{3p}_{,3} &= \mathbf{a}_3^{3p} - \mathbf{A}_3 = \boldsymbol{\Phi} \times \mathbf{A}_3 \, .
\end{aligned}
\tag{4.10}
$$

The covariant base vectors of the shell body have already been defined in Equation (4.2). The contravariant form is obtained from Equation (2.7), such that $\boldsymbol{\varepsilon}^{3\mathrm{p}}$ and its coefficients can be finally computed according to Equation (2.16)

$$
\begin{aligned}
\boldsymbol{\varepsilon}^{3\mathrm{p}} \quad &= \varepsilon_{ij}^{3\mathrm{p}}\,\mathbf{G}^{i}\otimes\mathbf{G}^{j}, \\
\text{with} & \\
\varepsilon_{ij}^{3\mathrm{p}} \quad &= \frac{1}{2}\left(\mathbf{u}_{,i}^{3\mathrm{p}}\cdot\mathbf{G}_{j}+\mathbf{u}_{,j}^{3\mathrm{p}}\cdot\mathbf{G}_{i}\right).
\end{aligned}
\tag{4.11}
$$

With the kinematic assumptions made so far, the strain tensor consists of constant, linear and quadratic components. The constant part of $\boldsymbol{\varepsilon}^{3\mathrm{p}}$ represents the membrane strains and the linear contributions are related to changes in curvature, i.e. bending. Quadratic terms in Equation (4.11) will be neglected in accordance with common assumptions of classical shell theories, which in general do not consider higher-order contributions for the stresses and strains or their resultants, respectively.

The choice of working with stresses and strains as kinematic and static variables in this work, however, does not preclude the use of quadratic components in general. The resulting error of neglecting quadratic terms remains acceptably small for thin shells with little curvature according to investigations performed in BAŞAR AND KRÄTZIG (1985) or BÜCHTER (1992), for instance.

The individual strain tensor components for the presented 3-parameter Kirchhoff-Love shell model, which account for both constant and linear contributions, are

$$
\begin{aligned}
\varepsilon_{11}^{3\mathrm{p}} \;&=\; \mathbf{v}_{,1}\cdot\mathbf{A}_{1} \\
&\quad +\theta^{3}\left(\mathbf{v}_{,1}\cdot\mathbf{A}_{3,1}+\boldsymbol{\Phi}_{,1}\times\mathbf{A}_{3}\cdot\mathbf{A}_{1}\right), \\
2\,\varepsilon_{12}^{3\mathrm{p}} \;&=\; \mathbf{v}_{,1}\cdot\mathbf{A}_{2}+\mathbf{v}_{,2}\cdot\mathbf{A}_{1} \\
&\quad +\theta^{3}\left(\mathbf{v}_{,1}\cdot\mathbf{A}_{3,2}+\boldsymbol{\Phi}_{,1}\times\mathbf{A}_{3}\cdot\mathbf{A}_{2}+\mathbf{v}_{,2}\cdot\mathbf{A}_{3,1}+\boldsymbol{\Phi}_{,2}\times\mathbf{A}_{3}\cdot\mathbf{A}_{1}\right), \\
\varepsilon_{22}^{3\mathrm{p}} \;&=\; \mathbf{v}_{,2}\cdot\mathbf{A}_{2} \\
&\quad +\theta^{3}\left(\mathbf{v}_{,2}\cdot\mathbf{A}_{3,2}+\boldsymbol{\Phi}_{,2}\times\mathbf{A}_{3}\cdot\mathbf{A}_{2}\right), \\
\varepsilon_{i3}^{3\mathrm{p}} \;&=\; 0\,.
\end{aligned}
\tag{4.12}
$$

All strain contributions $\boldsymbol{\Phi}\times\mathbf{A}_{3,\alpha}\cdot\mathbf{A}_{\beta}$ in Equation (4.12) vanish: The vectorial quantities obtained from the cross products of $\boldsymbol{\Phi}$ and $\mathbf{A}_{3,\alpha}$ both lie in the tangent space spanned by the vectors $\mathbf{A}_{\alpha}$ and are normal to the mid-surface. By subsequent scalar multiplication with the in-plane base vectors $\mathbf{A}_{\beta}$, the final result becomes zero.

Constitutive law

The linear elastic constitutive law for three-dimensional continua was defined in Section 2.4 according to Equation (2.22). For the shell models of this chapter, the derivation of the material tensor relies on the base vectors of Equation (4.2).

The inextensibility constraint requires zero transverse normal strains, i.e. $\varepsilon_{33}^{3\mathrm{p}} = 0$. Zero transverse normal strains, however, do not automatically ensure zero transverse normal stresses $\sigma^{3\mathrm{p},\,33}$, i.e. for nonzero Poisson's ratio. Asymptotic correctness of the model therefore necessitates the modification of the constitutive law by implementing the stress assumption $\sigma^{3\mathrm{p},\,33} = 0$ to eliminate $\varepsilon_{33}^{3\mathrm{p}}$ via static condensation. Equations with regard to transverse shear are automatically equal to zero and therefore do not have to be considered for the Kirchhoff-Love model. Thus, the modified material tensor $\mathbb{C}^{3\mathrm{p}}$ only relates the in-plane stress components $\sigma^{3\mathrm{p},\,\alpha\beta}$ to the in-plane strain components $\varepsilon_{\alpha\beta}^{3\mathrm{p}}$.

Further details on the definition of the constitutive law for the Kirchhoff-Love shell model can be found, for instance, in BAŞAR AND KRÄTZIG (1985), BISCHOFF ET AL. (2004) or BISCHOFF (2011a).

Love's first approximation, which simplifies the "true" shape of an infinitesimal cross-sectional area element by neglecting contributions with regard to curvature is not considered in the definition of the material tensor $\mathbb{C}^{3\mathrm{p}}$. Consequently, membrane and bending action are coupled due to nonzero off-diagonal blocks in the constitutive matrix.

Numerical integration of the discrete finite element equations is performed with three independent nested loops, two for the in-plane directions (θ^α) and one across the thickness (θ^3).

Internal virtual work

With the strain tensor $\boldsymbol{\varepsilon}^{3\mathrm{p}}$ of Equation (4.12), its first variation and the material tensor $\mathbb{C}^{3\mathrm{p}}$ the internal virtual work of the Kirchhoff-Love shell can be defined

$$\delta\Pi_{\mathrm{Pvw}}^{3\mathrm{p},\,\mathrm{int}} = \int\limits_{\Omega} \delta\left(\boldsymbol{\varepsilon}^{3\mathrm{p}}\right)^{\mathrm{T}} : \mathbb{C}^{3\mathrm{p}} : \boldsymbol{\varepsilon}^{3\mathrm{p}} \, \mathrm{d}\Omega\,. \tag{4.13}$$

With regard to the formulation of Kirchhoff-Love-type shell finite elements in the subsequent chapter, the existence of second derivatives in the kinematics with respect to curvature requires at least C^1-continuity of the displacement field. The satisfaction of this condition is rather challenging when discretizations with standard Lagrange finite element basis functions are applied, but can be naturally satisfied with subdivision techniques or the higher-continuity NURBS discretizations of Chapter 3.

4.4 Reissner-Mindlin shell model (5p)

With increasing thickness of the structure, transverse shear effects become more pronounced, thus significantly contributing to the total strain energy of the system.

For Reissner-Mindlin models, the Kirchhoff-Love kinematics are relaxed by introducing additional rotation parameters for the director, which do not depend on the gradient of the mid-surface displacement field and thus allow for extra transverse shear effects. Instead of applying a rotation tensor for shear deformable plates and shells, a difference vector formulation can be defined, which is the approach to be used in this thesis.

The differentiability requirements on the displacement functions in the energy functional of Reissner-Mindlin models reduce to functions of Sobolev space $\mathcal{H}^1$ with square integrable first derivatives to ensure C^0-continuity. Reissner-Mindlin models are therefore also denoted as first-order shear deformation theories (REDDY (1997)).

Early significant scientific contributions which extended the kinematics of the Kirchhoff theory for plates by additionally accounting for independent transverse shear deformations were developed in REISSNER (1945) and MINDLIN (1951). The corresponding kinematics is therefore commonly denoted as Reissner-Mindlin kinematics.

On basis of the works by Reissner and Mindlin, a multitude of shear deformable shell theories have been developed. See, for instance, the depictions in NAGHDI (1972) and BAŞAR AND KRÄTZIG (1985).

4.4.1 Standard parametrization (5p-stand.)

Kinematics

The inextensibility of the director in the deformed configuration reduces the number of additionally required parameters to two. The difference vector $\mathbf{w}^{\text{5p-stand.}}$, which is a function of in-plane convective coordinates θ^α only, is added to the director of the undeformed configuration as follows

$$\mathbf{a}_3^{\text{5p-stand.}} = \mathbf{A}_3 + \mathbf{w}^{\text{5p-stand.}} . \tag{4.14}$$

In the geometrically linear case, the inextensibility constraint can be constructed by expressing the components of $\mathbf{w}^{\text{5p-stand.}}$ with respect to the covariant base vectors $\mathbf{A}_\alpha$

$$\mathbf{w}^{\text{5p-stand.}} = \breve{w}^1 \mathbf{A}_1 + \breve{w}^2 \mathbf{A}_2 . \tag{4.15}$$

The kinematics of the shell model can be described with five independent parameters (5-parameter formulation (5p)), which correspond to the three mid-surface displacement components v_i and the difference vector components $\breve{w}^\alpha$.

In the following, the linearized Green-Lagrange strain tensor $\boldsymbol{\varepsilon}^{\text{5p-stand.}}$ and its coefficients are briefly derived for the 5-parameter Reissner-Mindlin model with standard difference vector formulation. For more detailed definitions and alternative approaches with rotation tensors, the reader is referred to the textbooks cited at the beginning of this chapter.

The displacement field is obtained from the difference of the position vectors of both configurations

$$\mathbf{u}^{\text{5p-stand.}} = \mathbf{v} + \theta^3 \, \mathbf{w}^{\text{5p-stand.}}\,, \tag{4.16}$$

from which the partial derivatives can be derived as follows

$$
\begin{aligned}
\mathbf{u}_{,\alpha}^{\text{5p-stand.}} &= \mathbf{v}_{,\alpha} + \theta^3 \, \mathbf{w}_{,\alpha}^{\text{5p-stand.}}\,,\\
\mathbf{u}_{,3}^{\text{5p-stand.}} &= \mathbf{a}_3^{\text{5p-stand.}} - \mathbf{A}_3 = \mathbf{w}^{\text{5p-stand.}}\,.
\end{aligned}
\tag{4.17}
$$

By using the base vector definitions of Equations (4.2) and (2.7), the Green-Lagrange strain tensor $\boldsymbol{\varepsilon}^{\text{5p-stand.}}$ and its coefficients are computed

$$
\begin{aligned}
\boldsymbol{\varepsilon}^{\text{5p-stand.}} &= \varepsilon_{ij}^{\text{5p-stand.}} \, \mathbf{G}^i \otimes \mathbf{G}^j\,,\\
\text{with}&\\
\varepsilon_{ij}^{\text{5p-stand.}} &= \frac{1}{2}\left(\mathbf{u}_{,i}^{\text{5p-stand.}} \cdot \mathbf{G}_j + \mathbf{u}_{,j}^{\text{5p-stand.}} \cdot \mathbf{G}_i\right).
\end{aligned}
\tag{4.18}
$$

The strain tensor components with both constant and linear contributions are

$$
\begin{aligned}
\varepsilon_{11}^{\text{5p-stand.}} &= \mathbf{v}_{,1} \cdot \mathbf{A}_1 + \theta^3 \left(\mathbf{v}_{,1} \cdot \mathbf{A}_{3,1} + \mathbf{w}_{,1}^{\text{5p-stand.}} \cdot \mathbf{A}_1\right),\\
2\,\varepsilon_{12}^{\text{5p-stand.}} &= \mathbf{v}_{,1} \cdot \mathbf{A}_2 + \mathbf{v}_{,2} \cdot \mathbf{A}_1\\
&\quad + \theta^3 \left(\mathbf{v}_{,1} \cdot \mathbf{A}_{3,2} + \mathbf{v}_{,2} \cdot \mathbf{A}_{3,1} + \mathbf{w}_{,1}^{\text{5p-stand.}} \cdot \mathbf{A}_2 + \mathbf{w}_{,2}^{\text{5p-stand.}} \cdot \mathbf{A}_1\right),\\
\varepsilon_{22}^{\text{5p-stand.}} &= \mathbf{v}_{,2} \cdot \mathbf{A}_2 + \theta^3 \left(\mathbf{v}_{,2} \cdot \mathbf{A}_{3,2} + \mathbf{w}_{,2}^{\text{5p-stand.}} \cdot \mathbf{A}_2\right),\\
2\,\varepsilon_{13}^{\text{5p-stand.}} &= \mathbf{v}_{,1} \cdot \mathbf{A}_3 + \mathbf{w}^{\text{5p-stand.}} \cdot \mathbf{A}_1\,,\\
2\,\varepsilon_{23}^{\text{5p-stand.}} &= \mathbf{v}_{,2} \cdot \mathbf{A}_3 + \mathbf{w}^{\text{5p-stand.}} \cdot \mathbf{A}_2\,,\\
\varepsilon_{33}^{\text{5p-stand.}} &= 0\,.
\end{aligned}
\tag{4.19}
$$

Constitutive law

The modified constitutive law for 5-parameter Reissner-Mindlin shells accounts for in-extensibility in thickness direction in the same way as the 3-parameter Kirchhoff-Love model. In order to ensure the asymptotic correctness of the formulation, the stress assumption $\sigma^{5p,\,33} = 0$ is introduced in the material equations to eliminate ε_{33}^{5p} by static condensation. Again, Love's first approximation is not accounted for. Due to transverse shear deformations, the modified material tensor $\mathbb{C}^{5p}$ relates the stress components $\sigma^{5p\text{-stand.},\,\alpha i}$ to the strain components $\varepsilon_{\alpha i}^{5p\text{-stand.}}$.

Internal virtual work

Finally, the internal virtual work can be derived by means of the strain tensor definition of Equation (4.18) and the modified material tensor $\mathbb{C}^{5p}$, which is specified in more detail in Başar and Krätzig (1985), Bischoff et al. (2004) and Bischoff (2011a), among others

$$
\delta\Pi_{\text{Pvw}}^{5p\text{-stand.},\,\text{int}} = \int\limits_{\Omega} \delta\left(\boldsymbol{\varepsilon}^{5p\text{-stand.}}\right)^{\text{T}} : \mathbb{C}^{5p} : \boldsymbol{\varepsilon}^{5p\text{-stand.}}\ \mathrm{d}\Omega\,. \tag{4.20}
$$

4.4.2 Hierarchic parametrization (5p-hier.)

The approach of adding a difference vector onto the director of the undeformed configuration is most commonly used in FEA due to reduced continuity requirements on the applied function spaces. In this section, alternatively, a hierarchic Reissner-Mindlin shell model is derived, which imposes the transverse shear on the rotated director of the 3-parameter Kirchhoff-Love model of Section 4.3. Mechanically, both continuous models (5p-stand. and 5p-hier.) yield the same result. With regard to finite element discretization, however, the hierarchic parametrization of the current director will remove certain locking effects to be specified in more detail in Chapter 5.

The continuity requirements on the displacement functions for the proposed hierarchic shell model (5p-hier.) are identical to those of the 3-parameter formulation of the previous section, i.e. C^1, which can, as mentioned before, be naturally satisfied with the higher-continuity NURBS discretizations of Chapter 3.

The idea of splitting the total deformation of the director of shear deformable structures into a component related to bending and an additional independent component due to shear is quite natural and was frequently used in classical theories on beams,

plates and shells for more than fifty years. The textbook BAŞAR AND KRÄTZIG (1985), although not the first scientific work on this topic, describes in an illustrative manner the split of the entire rotation of the shell director in a contribution with respect to the deformed shell normal (Kirchhoff-Love) and an additional rotation related to shear. The original motivation and teaching purpose in BAŞAR AND KRÄTZIG (1985) was to derive Kirchhoff-Love theories from shear deformation theories by simply removing the transverse shear contribution. For FEA, this approach, moreover, offers the possibility of an independent parametrization of the shear deformations. This consequently avoids incompatibilities of the discrete function spaces in the kinematic equations for the transverse shear and thus transverse shear locking.

Kinematics

The imposition of a difference vector $\mathbf{w}^{\text{5p-hier.}}$, which exclusively accounts for shear deformations, on the rotated director $\mathbf{a}_3^{\text{3p}}$ of the Kirchhoff-Love formulation is displayed schematically in Figure 4.3 and defined in Equation (4.21).
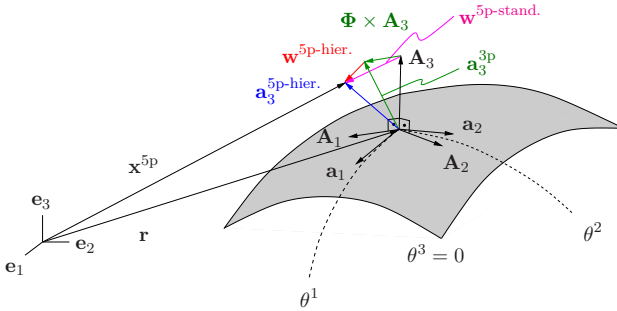
Figure 4.3: Deformed configuration – 5-parameter models.

$$
\mathbf{a}_3^{\text{5p-hier.}} \quad = \quad \underbrace{\mathbf{a}_3^{\text{3p}}}_{\substack{\text{membrane+}\\\text{bending}}} \quad + \quad \underbrace{\mathbf{w}^{\text{5p-hier.}}}_{\substack{\text{transverse}\\\text{shear}}} = \mathbf{a}_3^{\text{5p-stand.}}
$$

(4.21)

The hierarchic difference vector $\mathbf{w}^{\text{5p-hier.}}$ is a function of the in-plane convective coordinates θ^α only, as described for the standard Reissner-Mindlin model. Inextensibility of the director can therefore be again defined by expressing the components of $\mathbf{w}^{\text{5p-hier.}}$ with respect to the covariant base vectors $\mathbf{A}_\alpha$

$$\mathbf{w}^{\text{5p-hier.}} = \tilde{w}^1 \mathbf{A}_1 + \tilde{w}^2 \mathbf{A}_2\,. \tag{4.22}$$

If the vectors $\mathbf{a}_3^{\text{3p}}$ and $\mathbf{a}_3^{\text{5p-hier.}}$ are normalized, their difference $\mathbf{w}^{\text{5p-hier.}}$ exactly corresponds to the shear angle γ. For a shell thickness of t, the hierarchic difference vector is related to the shear angle and half of the shell thickness. For thin shells with $t \to 0$, the solution of the shear-deformable Reissner-Mindlin shell asymptotically converges towards the Kirchhoff-Love solution, whereas the removal of $\mathbf{w}^{\text{5p-hier.}}$ from Equation (4.21) directly leads to the 3-parameter Kirchhoff-Love model. This concept has been applied in a similar way in Long et al. (2012) in the context of smooth subdivision surfaces for accurately modeling both thin and thick shells.

The entire displacement field of the hierarchic Reissner-Mindlin shell consists of contributions of the Kirchhoff-Love model and the hierarchic difference vector $\mathbf{w}^{\text{5p-hier.}}$. Partial derivation of $\mathbf{u}^{\text{5p-hier.}}$, required for computing the Green-Lagrange strain tensor coefficients, yields

$$\begin{aligned}
\mathbf{u}_{,\alpha}^{\text{5p-hier.}} &= \mathbf{u}_{,\alpha}^{\text{3p}} + \theta^3\, \mathbf{w}_{,\alpha}^{\text{5p-hier.}}\,, \\
\mathbf{u}_{,3}^{\text{5p-hier.}} &= \mathbf{u}_{,3}^{\text{3p}} + \mathbf{w}^{\text{5p-hier.}}\,.
\end{aligned} \tag{4.23}$$

With the covariant base vectors of Equation (4.2), the linearized Green-Lagrange strain tensor $\boldsymbol{\varepsilon}^{\text{5p-hier.}}$ is defined

$$\begin{aligned}
\boldsymbol{\varepsilon}^{\text{5p-hier.}} &= \varepsilon_{ij}^{\text{5p-hier.}}\, \mathbf{G}^i \otimes \mathbf{G}^j\,, \\
\text{with} \\
\varepsilon_{ij}^{\text{5p-hier.}} &= \frac{1}{2}\left(\mathbf{u}_{,i}^{\text{5p-hier.}} \cdot \mathbf{G}_j + \mathbf{u}_{,j}^{\text{5p-hier.}} \cdot \mathbf{G}_i\right).
\end{aligned} \tag{4.24}$$

The computation of the strain tensor coefficients follows directly from Equations (4.2), (4.12), (4.22), (4.23) and (4.24), again neglecting quadratic contributions in θ^3

$$\begin{aligned}
\varepsilon_{11}^{\text{5p-hier.}} &= \varepsilon_{11}^{\text{3p}} + \theta^3\left(\mathbf{w}_{,1}^{\text{5p-hier.}} \cdot \mathbf{A}_1\right), \\
2\,\varepsilon_{12}^{\text{5p-hier.}} &= 2\varepsilon_{12}^{\text{3p}} + \theta^3\left(\mathbf{w}_{,1}^{\text{5p-hier.}} \cdot \mathbf{A}_2 + \mathbf{w}_{,2}^{\text{5p-hier.}} \cdot \mathbf{A}_1\right), \\
\varepsilon_{22}^{\text{5p-hier.}} &= \varepsilon_{22}^{\text{3p}} + \theta^3\left(\mathbf{w}_{,2}^{\text{5p-hier.}} \cdot \mathbf{A}_2\right), \\
2\,\varepsilon_{13}^{\text{5p-hier.}} &= \mathbf{w}^{\text{5p-hier.}} \cdot \mathbf{A}_1\,, \\
2\,\varepsilon_{23}^{\text{5p-hier.}} &= \mathbf{w}^{\text{5p-hier.}} \cdot \mathbf{A}_2\,, \\
\varepsilon_{33}^{\text{5p-hier.}} &= 0\,.
\end{aligned} \tag{4.25}$$

Important to notice in Equation (4.25) are the transverse shear strain coefficients $\varepsilon_{\alpha 3}^{\text{5p-hier.}}$, which only consist of the constant components $\mathbf{w}^{\text{5p-hier.}} \cdot \mathbf{A}_\alpha$ through the thickness of the shell. Linear terms do not show up due to the inextensibility constraint.

The discrete hierarchic shell element (5p-hier.) with pure displacement formulation to be derived in Chapter 5 with equal order interpolation of both the mid-surface displacements and the difference vectors will be free from transverse shear locking. The condition of zero transverse shear strains for the case of pure bending can be easily established by setting the hierarchic difference vector to zero.

The standard model of Section 4.4.1, on the other hand, has additional contributions with first derivatives of the mid-surface displacement field $\mathbf{v}$ in the strain tensor coefficients $\varepsilon_{\alpha 3}^{\text{5p-stand.}}$ – see Equation (4.19). This may lead to transverse shear locking in the discrete finite element model with equal order interpolation of both the mid-surface and difference vector displacements. Further details with regard to the discrete shell models and the problem of locking are provided in Chapter 5.

Constitutive law

The constitutive law of the hierarchic 5-parameter shell model is identical to the standard formulation of Section 4.4.1 and will therefore not be repeated here.

Internal virtual work

The internal virtual work of the hierarchic 5-parameter Reissner-Mindlin shell can now be derived with the strain tensor of Equation (4.24) and the modified material tensor $\mathbb{C}^{\text{5p}}$

$$\delta\Pi_{\text{Pvw}}^{\text{5p-hier., int}} = \int\limits_{\Omega} \delta\left(\boldsymbol{\varepsilon}^{\text{5p-hier.}}\right)^{\text{T}} : \mathbb{C}^{\text{5p}} : \boldsymbol{\varepsilon}^{\text{5p-hier.}} \, \mathrm{d}\Omega \,. \tag{4.26}$$

4.5 3D shell model (7p)

For the previously presented thin to moderately thick shell models with three or five parameters, respectively, several simplifications and assumptions on the kinematics in thickness direction of the shell body have been defined, which also require a modification of the material law to ensure an asymptotically correct formulation. For thick shells, however, effects in thickness direction become more and more pronounced and have to be accounted for.

In this section, two 7-parameter shell formulations are derived, which represent an extension of the 5-parameter Reissner-Mindlin models of Section 4.4. The 3D shells incorporate extensibility of the director in thickness direction and enable the application of three-dimensional constitutive laws without the need of modifications.

4.5.1 Standard parametrization (7p-stand.)

Kinematics

The 7-parameter shell formulation with standard parametrization represents an extension of the standard 5-parameter Reissner-Mindlin shell model of Section 4.4.1 and retains a pure displacement formulation. In order to describe the thickness change of the shell based on an extension or shortening of the current director, a 6th displacement parameter $\mathring{w}^{6\mathrm{p}}$ is introduced, which, in accordance with the standard 5-parameter shell (5p-stand.), is defined with respect to the covariant base vectors of the mid-surface and leads to a linear distribution of the transverse displacements in θ^3-direction

$$\mathbf{w}^{6\mathrm{p}} = \mathring{w}^{6\mathrm{p}}\,\mathbf{A}_3\,. \tag{4.27}$$

The introduction of a 7th displacement parameter $\overline{w}^{7\mathrm{p}}$ yields a quadratic distribution of the transverse displacements in θ^3-direction with $(\theta^3)^2\,\mathbf{w}^{7\mathrm{p}} = (\theta^3)^2\,\overline{w}^{7\mathrm{p}}\,\mathbf{A}_3$ and thus linear transverse normal strains ε_{33}. In the 6-parameter model, these linear normal strains in θ^3-direction are not present, which results in an imbalance to the linear stresses σ^{33}. Early 7-parameter shell models with quadratic displacement ansatz in thickness direction have been developed in KÜHHORN AND SCHOOP (1992), SANSOUR (1995) or PARISCH (1995), for instance.

Alternatively, linear strain components may be introduced for the thickness direction of the shell body as 7th parameter and added to the 6-parameter displacement model on the basis of an EAS (enhanced assumed strain) method. The application of enhanced strain components requires the use of multi-field variational functionals for deriving finite element formulations, compared to the aforementioned pure displacement ansatz. Prominent early publications in this field are, among others, SIMO AND RIFAI (1990), BÜCHTER AND RAMM (1992), BISCHOFF AND RAMM (1997), EBERLEIN AND WRIGGERS (1997) or BETSCH ET AL. (1998)).

Coming back to the pure displacement-based 7-parameter shell model, the position vector of the deformed configuration is defined as

$$
\begin{aligned}
\mathbf{x}^{\text{7p-stand.}} &= \mathbf{r} + \theta^3\,\mathbf{a}_3^{\text{5p-stand.}} + \theta^3\,\mathbf{w}^{\text{6p}} + \left(\theta^3\right)^2\mathbf{w}^{\text{7p}} \\
&= \mathbf{r} + \theta^3\,\mathbf{A}_3 + \theta^3\,\mathbf{w}^{\text{5p-stand.}} + \theta^3\left(\mathring{w}^{\text{6p}}\,\mathbf{A}_3\right) + \left(\theta^3\right)^2\left(\overline{w}^{\text{7p}}\,\mathbf{A}_3\right).
\end{aligned}
\tag{4.28}
$$

For reasons of presentation, the dependencies of the variables on the convective coordinates θ^i are omitted.

The director of the deformed configuration $\mathbf{a}_3^{\text{7p-stand.}}$ of the 3D shell model may consequently be derived from Equation (4.28) and reads

$$
\mathbf{a}_3^{\text{7p-stand.}} = \mathbf{A}_3 + \mathbf{w}^{\text{5p-stand.}} + \mathbf{w}^{\text{6p}}.
\tag{4.29}
$$

It has to be mentioned that in Equation (4.29), the quadratic displacements $\left(\theta^3\right)^2\mathbf{w}^{\text{7p}}$ are not included. They are, however, used in Equation (4.30) for the definition of the entire displacement field $\mathbf{u}^{\text{7p-stand.}}$. Transverse shear effects and changes in thickness direction are accounted for with $\mathbf{w}^{\text{5p-stand.}}$ and $\mathbf{w}^{\text{6p}}$, whereas linear transverse normal strains are enabled via $\mathbf{w}^{\text{7p}}$

$$
\mathbf{u}^{\text{7p-stand.}} = \mathbf{u}^{\text{5p-stand.}} + \theta^3\,\mathbf{w}^{\text{6p}} + \left(\theta^3\right)^2\mathbf{w}^{\text{7p}}.
\tag{4.30}
$$

From Equation (4.30), the partial derivatives of $\mathbf{u}^{\text{7p-stand.}}$ with respect to the convective coordinates θ^i can be derived

$$
\begin{aligned}
\mathbf{u}_{,\alpha}^{\text{7p-stand.}} &= \mathbf{u}_{,\alpha}^{\text{5p-stand.}} + \theta^3\left(\mathring{w}_{,\alpha}^{\text{6p}}\,\mathbf{A}_3 + \mathring{w}^{\text{6p}}\,\mathbf{A}_{3,\alpha}\right) + \left(\theta^3\right)^2\left(\overline{w}_{,\alpha}^{\text{7p}}\,\mathbf{A}_3 + \overline{w}^{\text{7p}}\,\mathbf{A}_{3,\alpha}\right), \\
\mathbf{u}_{,3}^{\text{7p-stand.}} &= \mathbf{u}_{,3}^{\text{5p-stand.}} + \left(\mathring{w}^{\text{6p}}\,\mathbf{A}_3\right) + 2\,\theta^3\left(\overline{w}^{\text{7p}}\,\mathbf{A}_3\right).
\end{aligned}
\tag{4.31}
$$

Finally, the linearized Green-Lagrange strain tensor $\boldsymbol{\varepsilon}^{\text{7p-stand.}}$ of the 7-parameter model is established

$$
\begin{aligned}
&\boldsymbol{\varepsilon}^{\text{7p-stand.}} = \varepsilon_{ij}^{\text{7p-stand.}}\,\mathbf{G}^i \otimes \mathbf{G}^j, \\
&\text{with} \\
&\varepsilon_{ij}^{\text{7p-stand.}} = \frac{1}{2}\left(\mathbf{u}_{,i}^{\text{7p-stand.}}\cdot\mathbf{G}_j + \mathbf{u}_{,j}^{\text{7p-stand.}}\cdot\mathbf{G}_i\right).
\end{aligned}
\tag{4.32}
$$

The computation of the strain tensor coefficients follows directly from Equations (4.2), (4.31) and (4.32)

$$
\begin{aligned}
\varepsilon_{11}^{\text{7p-stand.}} &= \varepsilon_{11}^{\text{5p-stand.}} + \theta^3 \left(\mathbf{w}_{,1}^{6p} \cdot \mathbf{A}_1 \right), \\
2\varepsilon_{12}^{\text{7p-stand.}} &= 2\varepsilon_{12}^{\text{5p-stand.}} + \theta^3 \left(\mathbf{w}_{,1}^{6p} \cdot \mathbf{A}_2 + \mathbf{w}_{,2}^{6p} \cdot \mathbf{A}_1 \right), \\
\varepsilon_{22}^{\text{7p-stand.}} &= \varepsilon_{22}^{\text{5p-stand.}} + \theta^3 \left(\mathbf{w}_{,2}^{6p} \cdot \mathbf{A}_2 \right), \\
2\varepsilon_{13}^{\text{7p-stand.}} &= 2\varepsilon_{13}^{\text{5p-stand.}} + \mathbf{w}^{6p} \cdot \mathbf{A}_1 + \theta^3 \left(\mathbf{w}_{,1}^{6p} \cdot \mathbf{A}_3 + \mathbf{w}^{6p} \cdot \mathbf{A}_{3,1} + 2\,\overline{w}^{7p} \underbrace{\mathbf{A}_3 \cdot \mathbf{A}_1}_{=0} \right) \\
2\varepsilon_{23}^{\text{7p-stand.}} &= 2\varepsilon_{23}^{\text{5p-stand.}} + \mathbf{w}^{6p} \cdot \mathbf{A}_2 + \theta^3 \left(\mathbf{w}_{,2}^{6p} \cdot \mathbf{A}_3 + \mathbf{w}^{6p} \cdot \mathbf{A}_{3,2} + 2\,\overline{w}^{7p} \underbrace{\mathbf{A}_3 \cdot \mathbf{A}_2}_{=0} \right) \\
\varepsilon_{33}^{\text{7p-stand.}} &= \mathbf{w}^{6p} \cdot \mathbf{A}_3 + \theta^3 \left(2\,\mathbf{w}^{7p} \cdot \mathbf{A}_3 \right).
\end{aligned}
\tag{4.33}
$$

In Equation (4.33), the quadratic contributions in θ^3-direction are again neglected according to the assumptions of classical shell theories, where higher-order contributions for the stresses and strains or their resultants, respectively, are not accounted for.

Constitutive law

The aforementioned decisive advantage of 3D shell models with at least seven parameters is the application of complete constitutive laws without the need for modifications. Thus, every strain variable is related to an associated stress component via the material law. The application of only six parameters does not provide an asymptotically correct shell model due to an imbalance of energetically conjugate stress and strain components in transverse normal direction (BISCHOFF (1999), RÖSSLE ET AL. (1999)). Poisson thickness locking may show up, which results in artificial transverse normal stresses. Unlike other locking effects, this phenomenon is a defect in the mathematical shell formulation and does not diminish in the discrete model with mesh refinement.

Internal virtual work

The internal virtual work of the standard 7-parameter Reissner-Mindlin shell model can be derived on the basis of the strain tensor of Equation (4.32) and a 3D material tensor $\mathbb{C}^{7p}$

$$
\delta\Pi_{\text{Pvw}}^{\text{7p-stand., int}} = \int_{\Omega} \delta \left(\boldsymbol{\varepsilon}^{\text{7p-stand.}} \right)^{\text{T}} : \mathbb{C}^{7p} : \boldsymbol{\varepsilon}^{\text{7p-stand.}} \, \mathrm{d}\Omega \,.
\tag{4.34}
$$

4.5.2 Hierarchic parametrization (7p-hier.)

Kinematics

The hierarchic 7-parameter shell formulation represents an extension of the hierarchic 5-parameter Reissner-Mindlin shell model (5p-hier.) from Section 4.4.2. In order to describe the extension or shortening of the director and linear transverse normal strains, the kinematics of "5p-hier." is enriched with a 6th and 7th displacement parameter $\mathring{w}^{6p}$ and $\overline{w}^{7p}$ in terms of the covariant basis $\mathbf{A}_i$ as for the "7p-stand." model, which ultimately yields linear and quadratic displacement contributions in θ^3-direction. The hierarchic parametrization allows for nicely switching on or off the extensibility property of the shell by activating or deactivating the 6th displacement component, which is desirable for model-adaptivity. In Figure 4.4, the current configuration of the director for 3D shell is displayed, however, not accounting for the entire displacement field. Quadratic contributions through the thickness are not included in the sketch.

Figure 4.4: Deformed director configuration – 7-parameter models.

The position vector $\mathbf{x}^{7p\text{-hier.}}$ of the deformed configuration for the hierarchic 3D shell model with pure displacement ansatz is defined as

$$
\mathbf{x}^{7p\text{-hier.}} = \underbrace{\underbrace{\underbrace{\underbrace{\mathbf{r} + \theta^3 \left(\mathbf{A}_3 + \mathbf{\Phi} \times \mathbf{A}_3 \right)}_{3p} + \theta^3\, \mathbf{w}^{5p\text{-hier.}}}_{5p-\text{hier.}} + \theta^3\, \mathbf{w}^{6p}}_{6p-\text{hier.}} + \left(\theta^3 \right)^2 \mathbf{w}^{7p}}_{7p-\text{hier.}}
$$

$$
= \mathbf{r} + \theta^3 \mathbf{a}_3^{3p} + \theta^3\, \mathbf{w}^{5p\text{-hier.}} + \theta^3 \left(\mathring{w}^{6p}\, \mathbf{A}_3 \right) + \left(\theta^3 \right)^2 \left(\overline{w}^{7p} \mathbf{A}_3 \right).
$$

$$(4.35)$$

For the sake of brevity, the dependencies of the variables on the convective coordinates θ^i are omitted.

Clearly, the hierarchic parametrization of the shell models "5p-hier." and "7p-hier." can be ascertained which are based on the 3-parameter Kirchhoff-Love formulation.

The director $\mathbf{a}_3^{\text{7p-hier.}}$ of the deformed configuration may consequently be derived from Equation (4.35) and reads

$$\mathbf{a}_3^{\text{7p-hier.}} = \underbrace{\mathbf{a}_3^{\text{3p}}}_{\substack{\text{membrane+} \\ \text{bending}}} + \underbrace{\mathbf{w}^{\text{5p-hier.}}}_{\substack{\text{transverse} \\ \text{shear}}} + \underbrace{\mathbf{w}^{\text{6p}}}_{\substack{\text{thickness} \\ \text{change}}} = \mathbf{a}_3^{\text{7p-stand.}} . \tag{4.36}$$

The deformed director in Equation (4.36) again represents a 6-parameter model, as for the "7p-stand." shell, as no quadratic displacements in transverse normal direction are included. For a uniform notation, though, the director of the current configuration is specified with the label "7p-hier.".

The entire displacement field $\mathbf{u}^{\text{7p-hier.}}$ of the hierarchic 3D Reissner-Mindlin shell consists of contributions from the Kirchhoff-Love model, the hierarchic difference vector $\mathbf{w}^{\text{5p-hier.}}$, the linear displacement field $\mathbf{w}^{\text{6p}}$ and the quadratic term in transverse normal direction $\mathbf{w}^{\text{7p}}$. $\mathbf{u}^{\text{7p-hier.}}$ can be obtained by the difference of the position vectors of the deformed and undeformed configuration $\mathbf{x}^{\text{7p-hier.}}$ and $\mathbf{X}$ in the same way, as described for the standard 7-parameter shell and will therefore not be reproduced herein.

The partial derivation of $\mathbf{u}^{\text{7p-hier.}}$ with respect to the convective coordinates θ^i is required for computing the coefficients of the Green-Lagrange strain tensor

$$\begin{aligned}
\mathbf{u}_{,\alpha}^{\text{7p-hier.}} &= \mathbf{u}_{,\alpha}^{\text{5p-hier.}} + \theta^3 \left(\mathring{w}_{,\alpha}^{\text{6p}} \mathbf{A}_3 + \mathring{w}^{\text{6p}} \mathbf{A}_{3,\alpha} \right) + \left(\theta^3 \right)^2 \left(\overline{w}_{,\alpha}^{\text{7p}} \mathbf{A}_3 + \overline{w}^{\text{7p}} \mathbf{A}_{3,\alpha} \right), \\
\mathbf{u}_{,3}^{\text{7p-hier.}} &= \mathbf{u}_{,3}^{\text{5p-hier.}} + \left(\mathring{w}^{\text{6p}} \mathbf{A}_3 \right) + 2\,\theta^3 \left(\overline{w}^{\text{7p}} \mathbf{A}_3 \right).
\end{aligned} \tag{4.37}$$

Consequently, the linearized Green-Lagrange strain tensor $\boldsymbol{\varepsilon}^{\text{7p-hier.}}$ of the hierarchic 7-parameter shell model can be established

$$\begin{aligned}
&\boldsymbol{\varepsilon}^{\text{7p-hier.}} = \varepsilon_{ij}^{\text{7p-hier.}} \mathbf{G}^i \otimes \mathbf{G}^j, \\
&\text{with} \\
&\varepsilon_{ij}^{\text{7p-hier.}} = \frac{1}{2} \left(\mathbf{u}_{,i}^{\text{7p-hier.}} \cdot \mathbf{G}_j + \mathbf{u}_{,j}^{\text{7p-hier.}} \cdot \mathbf{G}_i \right).
\end{aligned} \tag{4.38}$$

The strain tensor coefficients $\varepsilon_{ij}^{\text{7p-hier.}}$ follow directly from Equations (4.2), (4.37) and (4.38)

$$
\begin{aligned}
\varepsilon_{11}^{\text{7p-hier.}} &= \varepsilon_{11}^{\text{5p-hier.}} + \theta^3 \left(\mathbf{w}_{,1}^{\text{6p}} \cdot \mathbf{A}_1 \right), \\
2\varepsilon_{12}^{\text{7p-hier.}} &= 2\varepsilon_{12}^{\text{5p-hier.}} + \theta^3 \left(\mathbf{w}_{,1}^{\text{6p}} \cdot \mathbf{A}_2 + \mathbf{w}_{,2}^{\text{6p}} \cdot \mathbf{A}_1 \right), \\
\varepsilon_{22}^{\text{7p-hier.}} &= \varepsilon_{22}^{\text{5p-hier.}} + \theta^3 \left(\mathbf{w}_{,2}^{\text{6p}} \cdot \mathbf{A}_2 \right), \\
2\varepsilon_{13}^{\text{7p-hier.}} &= \mathbf{w}^{\text{5p-hier.}} \cdot \mathbf{A}_1 + \mathbf{w}^{\text{6p}} \cdot \mathbf{A}_1 + \theta^3 \left(\mathbf{w}_{,1}^{\text{6p}} \cdot \mathbf{A}_3 + \mathbf{w}^{\text{6p}} \cdot \mathbf{A}_{3,1} + 2\,\overline{w}^{\text{7p}} \underbrace{\mathbf{A}_3 \cdot \mathbf{A}_1}_{=0} \right) \\
2\varepsilon_{23}^{\text{7p-hier.}} &= \mathbf{w}^{\text{5p-hier.}} \cdot \mathbf{A}_2 + \mathbf{w}^{\text{6p}} \cdot \mathbf{A}_2 + \theta^3 \left(\mathbf{w}_{,2}^{\text{6p}} \cdot \mathbf{A}_3 + \mathbf{w}^{\text{6p}} \cdot \mathbf{A}_{3,2} + 2\,\overline{w}^{\text{7p}} \underbrace{\mathbf{A}_3 \cdot \mathbf{A}_2}_{=0} \right) \\
\varepsilon_{33}^{\text{7p-hier.}} &= \mathbf{w}^{\text{6p}} \cdot \mathbf{A}_3 + \theta^3 \left(2\,\mathbf{w}^{\text{7p}} \cdot \mathbf{A}_3 \right).
\end{aligned}
$$

$$(4.39)$$

The discrete model of the 3D hierarchic shell with pure displacement ansatz is free from transverse shear locking like the hierarchic 5-parameter Reissner-Mindlin formulation introduced in Section 4.4.2, as the constraint of vanishing transverse shear strains, in case of pure bending, can easily be satisfied by setting the hierarchic shear vector $\mathbf{w}^{\text{5p-hier.}} = 0$.

Investigations with regard to locking effects of the discrete 7-parameter models are performed in Chapter 5.

Constitutive law

The material tensor $\mathbb{C}^{\text{7p}}$ of the hierarchic 7-parameter shell model is identical to the standard formulation of Section 4.5.1 and will therefore not be repeated here. It relates the stress components $\sigma^{\text{7p-hier.},\, ij}$ to the strain components $\varepsilon_{ij}^{\text{7p-hier.}}$.

Internal virtual work

Finally, the internal virtual work of the hierarchic 7-parameter Reissner-Mindlin shell model can be derived on the basis of the strain tensor of Equation (4.38) and the 3D material tensor $\mathbb{C}^{\text{7p}}$

$$
\delta\Pi_{\text{Pvw}}^{\text{7p-hier.},\,\text{int}} = \int\limits_{\Omega} \delta\left(\boldsymbol{\varepsilon}^{\text{7p-hier.}}\right)^{\text{T}} : \mathbb{C}^{\text{7p}} : \boldsymbol{\varepsilon}^{\text{7p-hier.}} \; \mathrm{d}\Omega\,.
$$

$$(4.40)$$

5

Hierarchic Isogeometric Shell Finite Elements

In the previous chapter, 3-, 5- and 7-parameter shell models were developed. The parametrization of the displacements of the hierarchic shear-deformable formulations (5p-hier., 7p-hier.) defined in Sections 4.4.2 and 4.5.2 avoids transverse shear and curvature thickness locking in the shell finite elements without the need of further remedies, such as assumed natural strains (ANS), mixed formulations or reduced integration. This will be demonstrated in numerical experiments of this chapter.

NURBS, which were introduced in Chapter 3 as a standard tool of geometric modeling in CAD/ CAM, are used as basis functions in a continuous Galerkin finite element ansatz for the discretization of the weak shell equations according to the isogeometric analysis concept of HUGHES ET AL. (2005).

Section 5.1 gives a short introduction to the fundamentals of the finite element method to an extent required within this thesis. Subsequently, the isoparametric concept with NURBS functions is applied to the variational virtual work formulations specified for the shell models in Chapter 4 in order to derive the discrete algebraic shell equations in Section 5.2. Next, the effect of higher-continuity NURBS discretizations on the accuracy of the discrete solution functions will be investigated and analyzed in numerical examples. The results reveal that along with improved accuracy of higher-continuity NURBS discretizations, the membrane part of the hierarchic shell elements with pure displacement ansatz is considerably prone to locking. Therefore, in the last section of this chapter, geometric locking effects of the developed NURBS shell elements of this work are analyzed and quantified.

5.1 Finite element fundamentals

The finite element method can be classified as a special form of the Ritz-Galerkin method. It represents a numerical approach for the approximate solution of mathematical models for boundary value problems or initial boundary value problems that are mainly described by partial differential equations in variational form.

In order to derive the displacement-based shell finite elements with a Bubnov-Galerkin ansatz, appropriate finite dimensional function spaces for both the solution and test functions have to be defined. They are subspaces of the continuous function spaces of the variational formulation; in this case the principle of virtual work. The NURBS functions of Chapter 3 will be employed for both the ansatz and weighting functions.

The discrete function spaces are associated with a mesh, i.e. a partitioning of the spatial patch domain Ω_{pa} into a finite number n_{e} of non-overlapping elements Ω^{e}, which in Equation (5.1) is mathematically defined with the assembly operator $\mathbb{A}$. The subdivision of a NURBS patch was defined by knot spans of nonzero length in Chapter 3. This procedure carries over to the analysis framework. The superscript $(\bullet)^{\mathrm{e}}$ specifies an element quantity and the index "h" is related to the discretization of the domain. It represents a characteristic dimension of an element. For $\mathrm{h} \to 0$, the finite element formulation has to ensure convergence of the approximate solution to the exact one.

$$\Omega_{\mathrm{pa}} = \Omega_{\mathrm{pa}}^{\mathrm{h}} = \mathop{\mathbb{A}}_{i=1}^{n_{\mathrm{e}}} \Omega_i^{\mathrm{e}}, \quad \text{with} \quad \Omega_i^{\mathrm{e}} \cap \Omega_j^{\mathrm{e}} = \varnothing \quad \text{for} \quad i \neq j \tag{5.1}$$

The first equal sign in Equation (5.1) points out that the CAD geometry is exactly embedded in the analysis framework, which clearly differs from conventional FEA, where the CAD representation is, in general, replaced with an approximate and independent finite element mesh description.

Historical development

From a mathematical point of view, the origin of FEA is often associated with the work of Courant on the eigenvalue analysis of beams with piecewise linear hat functions (COURANT (1943)). Its popularity, however, is related to engineering approaches particularly in the field of structural mechanics in the late 1950s and 1960s in conjunction with the rapid development of computer technology at that time. Some prominent early contributions are, for instance, ARGYRIS (1955), TURNER ET AL. (1956), ARGYRIS (1957), CLOUGH (1960) and ZIENKIEWICZ AND CHEUNG (1964). Basic mathematical concepts and theoretical fundamentals on finite elements were first derived in the 1970s by ZIENKIEWICZ (1971), BABUŠKA AND AZIZ (1972) and STRANG AND FIX (1973).

Nowadays, some prominent textbooks on the finite element method are HUGHES (2000), WRIGGERS (2001), BRAESS (2003), ZIENKIEWICZ ET AL. (2005) and BELYTSCHKO ET AL. (2008) among numerous other valuable publications.

The idea of using splines as finite element shape functions dates back at least to the 1970s. In PRENTER (1975), variational methods and numerical solution strategies were presented with particular emphasis on the finite element method and collocation methods on the basis of spline spaces. Swartz and Wendroff studied the effectiveness of spline-based finite elements compared to finite difference methods for time dependent problems (SWARTZ AND WENDROFF (1974)). Chung-Tze utilized cubic B-splines as finite element basis for the numerical modeling of elastic composite plate structures (CHUNG-TZE (1979)) and determined improved accuracy compared to conventional finite element discretizations and savings in both memory requirements and computational costs. B-spline-based finite elements for the analysis of shells of revolution were developed in FAN AND LUAH (1990). In HÖLLIG (2002) and HÖLLIG (2003) different types of B-spline basis functions were presented which are suitable for the numerical solution of boundary value problems. The author also provides theoretical fundamentals on stability and error estimates for B-spline functions.

Hence, several scientific papers of spline-based finite elements were published, yet rarely considered before the first paper of Hughes and coworkers on isogeometric analysis appeared (HUGHES ET AL. (2005)). Hughes was probably the first to cast the idea of integrating popular methods of CAD and analysis into a uniform and consistent concept.

Isoparametric concept

The isoparametric finite element concept, which is attributed to TAIG (1961) and IRONS (1966), applies the element shape functions for the approximation of the field variables, such as the displacements $\mathbf{u}$, also to the geometry representation and thus utilizes the same parametrization for both quantities.

In the isoparametric approach, a parametric element domain is defined, which in two dimensions topologically represents a square. The application of natural coordinates (ξ, η) enables an efficient construction of the shape functions on the parametric element, which can be used for all elements of the spatial configuration. Both the element geometry and the displacement field are defined as a linear combination of the basis functions and the nodal coordinates or displacement components respectively. The parametric element is uniquely mapped from the natural coordinate system into the global Cartesian frame for every element, without the need to distinguish between straight or curved elements. Isoparametric elements consequently enable an elegant mapping of arbitrary geometries into a finite element mesh due to their transformation properties.

For the derivation of element stiffness or mass matrices, differentiation and integration of discrete quantities, which are functions of the global coordinates $\{x, y, z\}$ is likewise simplified by carrying out the procedures in natural coordinates $\{\xi, \eta, \zeta\}$: The Jacobian $\mathbf{J}$ of three-dimensional transformations connects the differentials of $\{x, y, z\}$ to those of $\{\xi, \eta, \zeta\}$ and vice-versa

$$\mathbf{X} = \mathbf{J}^{\mathrm{T}} \boldsymbol{\xi} \quad \text{with} \quad \mathbf{J} = \frac{\partial(x, y, z)}{\partial(\xi, \eta, \zeta)} \,. \tag{5.2}$$

In IGA, the isoparametric concept is applied accordingly; the initial order of the classical concept, however, is switched. The geometry parametrization in IGA is embedded into the analysis domain and the solution fields are subsequently approximated with the functions of the geometry parametrization. Additionally, the parametric NURBS domain does not correspond to one single element, but to a patch $\tilde{\Omega}_{\mathrm{pa}}$, which already contains the complete partition into elements defined by the knot vectors. The entire parameter space is then mapped with one global geometry function to the spatial configuration Ω_{pa}, as was illustrated for a spherical NURBS segment in Figure 3.12.

Important properties of the B-spline basis functions for isogeometric analysis, which carry over to NURBS, have already been defined in Section 3.3. Further requirements on the NURBS basis functions, in order to ensure convergence of the isoparametric finite element ansatz, are discussed in more detail in the subsequent section.

For additional information on the classical isoparametric concept and IGA ansatz, see, for instance, STEIN AND BARTHOLD (1996), HUGHES (2000), ZIENKIEWICZ ET AL. (2005) and COTTRELL ET AL. (2009).

Functional analysis requirements on NURBS basis

The internal virtual work contributions of all displacement-based shell models – see Equations (4.13), (4.20), (4.26), (4.34) and (4.40) – may be formally expressed by symmetric, bilinear forms in the same way as defined for three-dimensional continua in Section 2.5.1. In addition, the corresponding requirements on the function spaces for both the trial and test functions of the continuous weak formulation with variational index of one have been established.

In FEA, the continuous function spaces are restricted to finite dimensional subspaces. The conditions required to determine a unique solution for the minimization and stationary problems defined in Section 2.5 can be directly transferred to discrete formulations, as discretization mathematically implies the restriction of the function spaces in which the solution is to be found.

The discrete bilinear forms for the individual internal energy contributions of the shell

models of Chapter 4 are

$$
\begin{aligned}
b^{\text{3p, h}}\left(\mathbf{u}^{\text{h}}, \delta\mathbf{u}^{\text{h}}\right) &:= \int_{\Omega^{\text{h}}} \delta\left(\boldsymbol{\varepsilon}^{\text{3p, h}}\right)^{\text{T}} : \mathbb{C}^{\text{3p, h}} : \boldsymbol{\varepsilon}^{\text{3p, h}} \, \mathrm{d}\Omega^{\text{h}} \\
b^{\text{5p-stand., h}}\left(\mathbf{u}^{\text{h}}, \delta\mathbf{u}^{\text{h}}\right) &:= \int_{\Omega^{\text{h}}} \delta\left(\boldsymbol{\varepsilon}^{\text{5p-stand., h}}\right)^{\text{T}} : \mathbb{C}^{\text{5p, h}} : \boldsymbol{\varepsilon}^{\text{5p-stand., h}} \, \mathrm{d}\Omega^{\text{h}} \\
b^{\text{5p-hier., h}}\left(\mathbf{u}^{\text{h}}, \delta\mathbf{u}^{\text{h}}\right) &:= \int_{\Omega^{\text{h}}} \delta\left(\boldsymbol{\varepsilon}^{\text{5p-hier., h}}\right)^{\text{T}} : \mathbb{C}^{\text{5p, h}} : \boldsymbol{\varepsilon}^{\text{5p-hier., h}} \, \mathrm{d}\Omega^{\text{h}} \\
b^{\text{7p-stand., h}}\left(\mathbf{u}^{\text{h}}, \delta\mathbf{u}^{\text{h}}\right) &:= \int_{\Omega^{\text{h}}} \delta\left(\boldsymbol{\varepsilon}^{\text{7p-stand., h}}\right)^{\text{T}} : \mathbb{C}^{\text{7p, h}} : \boldsymbol{\varepsilon}^{\text{7p-stand., h}} \, \mathrm{d}\Omega^{\text{h}} \\
b^{\text{7p-hier., h}}\left(\mathbf{u}^{\text{h}}, \delta\mathbf{u}^{\text{h}}\right) &:= \int_{\Omega^{\text{h}}} \delta\left(\boldsymbol{\varepsilon}^{\text{7p-hier., h}}\right)^{\text{T}} : \mathbb{C}^{\text{7p, h}} : \boldsymbol{\varepsilon}^{\text{7p-hier., h}} \, \mathrm{d}\Omega^{\text{h}} .
\end{aligned}
\tag{5.3}
$$

Second derivatives of the transverse displacements in the discrete weak forms of the Kirchhoff-Love-type (3p) internal energy functional and the hierarchic shear deformable 5- and 7-parameter shell models (5p-hier., 7p-hier.) require discrete functions with square integrable partial derivatives of second-order to ensure convergence of the numerical scheme. Although the standard Reissner-Mindlin shells (5p-stand., 7p-stand.) only have first derivatives and thus reduced integrability requirements, the same higher-order and higher-continuity NURBS basis functions are applied, which enable a unique definition of the director field in the entire patch domain.

The application of at least biquadratic and C^1-continuous NURBS basis functions for the displacement-based shell formulations in this thesis satisfies the completeness requirements of the basis to exactly represent all functions up to the order induced by the variational index of the underlying weak problem, which is two. Secondly, the compatibility of the NURBS basis, which is defined to be at least C^1-continuous at inter-element boundaries and infinitely continuous within element domains, is satisfied, which, together with completeness, finally ensures the consistency of the formulation. The requirements with regard to stability have already been defined in Section 2.5.1 and can be transferred to the discrete shell models.

Mathematical theorems and proofs on the convergence properties of isogeometric NURBS-based FEA and suitable error estimates were derived, for instance, in BAZILEVS (2006), BAZILEVS ET AL. (2006) and EVANS ET AL. (2009). These take into account the rational property of NURBS, the concept of support extension of the basis, which in general is not confined to one single element, and the reduced regularity of the basis functions at inter-element boundaries. The local approximation properties of NURBS finite element discretizations are consequently in between those of standard Sobolev spaces and discontinuous Galerkin methods. In the aforementioned references, the authors additionally identify identical rates of convergence for both the discrete solutions with NURBS and

standard finite element formulations of identical polynomial order, independent of their continuity.

5.2 Displacement-based, discrete element equations

5.2.1 Discrete shell quantities

The requirements on the finite-dimensional NURBS function spaces for the discrete weak forms of the shell models have been established in Section 2.5.1 by means of the Lax-Milgram-Theorem and further specified in Section 5.1 in order to ensure the existence, uniqueness and stability of the discrete solution function.

Throughout all numerical shell examples of this chapter and the following, at least biquadratic, bivariate NURBS with inter-element continuity of minimum C^1 for both the displacement field and the geometry are utilized, due to the base shell model with Kirchhoff-Love kinematics, although this is possibly not necessary with regard to the geometry representation. A cylindrical shell, for example, only requires second-order NURBS functions in one parametric direction, whereas the other direction is sufficiently accurately modeled with linear functions.

For the formulation of the discrete shell quantities, the convective coordinates θ^i of Figure 4.1 are associated with the natural coordinates $\boldsymbol{\xi} = \{\xi, \eta, \zeta\}$.

In order to compute the shell element stiffness matrices, the strain tensors of the five shell models defined in Equations (4.11), (4.18), (4.24), (4.32) and (4.38) and the corresponding material tensors $\mathbb{C}^{3\mathrm{p}}$, $\mathbb{C}^{5\mathrm{p}}$ and $\mathbb{C}^{7\mathrm{p}}$ have to be discretized, which in detail requires the discrete formulation of the mid-surface base vectors $\mathbf{A}_i^{\mathrm{h}}$ of the reference configuration, the rotation vector $\boldsymbol{\Phi}^{\mathrm{h}}$, the mid-surface displacements $\mathbf{v}^{\mathrm{h}}$, the difference displacement vectors $\mathbf{w}^{5\mathrm{p\text{-}stand.,\,h}}$, $\mathbf{w}^{5\mathrm{p\text{-}hier.,\,h}}$ of the Reissner-Mindlin shell formulations and finally $\mathbf{w}^{6\mathrm{p,\,h}}$ and $\mathbf{w}^{7\mathrm{p,\,h}}$, which introduce the linear and quadratic displacement distributions of the 7-parameter models in transverse normal direction.

According to the isoparametric concept, the discrete covariant base vectors $\mathbf{A}_\alpha^{\mathrm{h}}$, which are identical for all shell models of this work, are defined as the sum of the NURBS element basis function derivatives and the associated control point coordinates

$$
\begin{aligned}
\mathbf{A}_1^{\mathrm{h}}(\xi, \eta) &= \sum_{i=1}^{n_{\mathrm{cp}}} \left(N_i^{\mathrm{p,\,q}}(\xi, \eta)\right)_{,\xi} \mathbf{P}^i, \\
\mathbf{A}_2^{\mathrm{h}}(\xi, \eta) &= \sum_{i=1}^{n_{\mathrm{cp}}} \left(N_i^{\mathrm{p,\,q}}(\xi, \eta)\right)_{,\eta} \mathbf{P}^i.
\end{aligned}
\tag{5.4}
$$

The number of element basis functions and control points (n_{cp}) depends on the polynomial order p and q of the bivariate NURBS basis defined in Equation (3.9). For biquadratic NURBS ($p = q = 2$), the number of element basis functions and control points is equal to nine, for example.

The unique and pointwise exact definition of the discrete shell director $\mathbf{A}_3^{\mathrm{h}}$ in the entire NURBS patch domain, due to the higher-continuity basis functions, naturally avoids difficulties which arise from standard C^0-continuous discretizations. Different modeling strategies of C^0-continuous director fields and consequences are discussed, for instance, in Bischoff (1999) and Bischoff et al. (2004).

The CAD-exact NURBS director field $\mathbf{A}_3^{\mathrm{h}}$ is derived from the normalized cross product of the discrete in-plane covariant base vectors $\mathbf{A}_\alpha^{\mathrm{h}}$ of Equation (5.4) in the same way as for the continuous model

$$\mathbf{A}_3^{\mathrm{h}} (\xi, \eta) = \frac{\mathbf{A}_1^{\mathrm{h}} \times \mathbf{A}_2^{\mathrm{h}}}{\| \mathbf{A}_1^{\mathrm{h}} \times \mathbf{A}_2^{\mathrm{h}} \|} \,. \tag{5.5}$$

The discrete displacement field of the mid-surface $\mathbf{v}^{\mathrm{h}}$ is determined from the sum of NURBS element basis functions and the associated displacements $\mathbf{v}^i = \left\{ v_x^i, v_y^i, v_z^i \right\}$ of the control points as follows

$$\mathbf{v}^{\mathrm{h}} (\xi, \eta) = \sum_{i=1}^{n_{cp}} N_i^{\mathrm{p,q}} (\xi, \eta) \, \mathbf{v}^i \,. \tag{5.6}$$

Consequently, the discrete rotation vector $\mathbf{\Phi}^{\mathrm{h}}$ can be established, which rotates the undeformed director $\mathbf{A}_3^{\mathrm{h}}$ of the Kirchhoff-Love shell model into the current configuration $\mathbf{a}_3^{\mathrm{h}}$

$$\mathbf{\Phi}^{\mathrm{h}} (\xi, \eta) = \left(\frac{1}{\| \mathbf{A}_1^{\mathrm{h}} \times \mathbf{A}_2^{\mathrm{h}} \|} \, \mathbf{v}_{,\eta}^{\mathrm{h}} \cdot \mathbf{A}_3^{\mathrm{h}} \right) \mathbf{A}_1^{\mathrm{h}} - \left(\frac{1}{\| \mathbf{A}_1^{\mathrm{h}} \times \mathbf{A}_2^{\mathrm{h}} \|} \, \mathbf{v}_{,\xi}^{\mathrm{h}} \cdot \mathbf{A}_3^{\mathrm{h}} \right) \mathbf{A}_2^{\mathrm{h}} \,. \tag{5.7}$$

So far, all discrete quantities have been established for the 3-parameter Kirchhoff-Love shell element to compute its stiffness matrix.

The shear-deformable 5-parameter shell formulations additionally require the discretization of their difference vectors, which have to account for the inextensibility of the director in thickness direction. The principal structure for both $\mathbf{w}^{\mathrm{5p\text{-}stand.,h}}$ and $\mathbf{w}^{\mathrm{5p\text{-}hier.,h}}$ is identical and can be modeled with functions of the in-plane natural coordinates ξ and η only. The different mechanical meaning of both vectors in the shell kinematics has been explained in detail in Chapter 4; see, for instance Figure 4.3. Inextensibility in the geometrically linear case is constructed by expressing the components of the discrete difference vectors with regard to $\mathbf{A}_\alpha^{\mathrm{h}}$ as follows

$$\mathbf{w}^{\text{5p-stand., h}}(\xi, \eta) = \breve{w}^{\alpha, \text{h}}(\xi, \eta) \cdot \mathbf{A}_\alpha^{\text{h}} \quad \text{with} \quad \breve{w}^{\alpha, \text{h}}(\xi, \eta) = \sum_{i=1}^{n_{\text{cp}}} N_i^{\text{p, q}}(\xi, \eta) \, \breve{w}_\alpha^i,$$

$$\mathbf{w}^{\text{5p-hier., h}}(\xi, \eta) = \tilde{w}^{\alpha, \text{h}}(\xi, \eta) \cdot \mathbf{A}_\alpha^{\text{h}} \quad \text{with} \quad \tilde{w}^{\alpha, \text{h}}(\xi, \eta) = \sum_{i=1}^{n_{\text{cp}}} N_i^{\text{p, q}}(\xi, \eta) \, \tilde{w}_\alpha^i.$$

$$(5.8)$$

The discrete linear transverse displacements in θ^3-direction of both the standard and hierarchic 3D shell elements (7p-stand., 7p-hier.), which accounts for extensibility in thickness direction is equal to

$$\mathbf{w}^{\text{6p, h}}(\xi, \eta) = \mathring{w}^{\text{6p, h}}(\xi, \eta) \cdot \mathbf{A}_3^{\text{h}} \quad \text{with} \quad \mathring{w}^{\text{6p, h}}(\xi, \eta) = \sum_{i=1}^{n_{\text{cp}}} N_i^{\text{p, q}}(\xi, \eta) \, \mathring{w}^i. \tag{5.9}$$

Finally, the quadratic discrete displacement contributions $\mathbf{w}^{\text{7p, h}}$ of both 7-parameter shell elements (7p-stand., 7p-hier.) have to be defined. Their control point degrees of freedom $\overline{w}^i$ are interpolated within the element domain like the degrees of freedom $\mathring{w}^i$ of the linear transverse displacements $\mathbf{w}^{\text{6p, h}}$

$$\mathbf{w}^{\text{7p, h}}(\xi, \eta) = \overline{w}^{\text{7p, h}}(\xi, \eta) \cdot \mathbf{A}_3^{\text{h}} \quad \text{with} \quad \overline{w}^{\text{7p, h}}(\xi, \eta) = \sum_{i=1}^{n_{\text{cp}}} N_i^{\text{p, q}}(\xi, \eta) \, \overline{w}^i. \tag{5.10}$$

5.2.2 Stiffness matrix, numerical integration

With the expressions of Section 5.2.1 at hand, the discrete form of the principle of virtual work can now be written as a coupled system of linear algebraic equations in matrix-vector notation, i.e. $\mathbf{K} \cdot \mathbf{d} = \mathbf{f}$ for all shell models defined in Chapter 4. With regard to the applied linear elastostatics in this thesis, the matrix $\mathbf{K}$ is referred to as the stiffness matrix, the vector $\mathbf{d}$ is the vector of discrete control point displacements and $\mathbf{f}$ represents the force vector.

Due to the local support of NURBS basis functions, the structure of the global stiffness matrix is sparse. The evaluation of stiffness matrices and force vectors is performed on element level and then assembled into the system stiffness matrix and system force vector according to the direct stiffness method in the same way as for conventional finite elements, by accounting for both compatibility of the displacements and force equilibrium.

For numerical integration, element-based Gauss quadrature is used throughout all computations, although this is not optimal for higher-continuity basis functions, such as B-splines or NURBS (HUGHES ET AL. (2010)). For biquadratic NURBS basis func-

tions, 3×3 Gauss points are applied in-plane, whereas 2 Gauss points are used for numerical integration in thickness direction.

As mentioned in Chapter 4, no pre-integration of the material law in θ^3-direction of the shells is performed. The kinematic and static variables are defined on strain and stress basis, rather than their resultant form. Consequently, numerical integration of the element stiffness matrices consists of three nested loops: two for the in-plane directions (ξ, η) and one through the thickness (ζ).

5.2.3 Kinematic boundary conditions

The Kirchhoff-Love shell (3p) represents the basic mechanical shell model in this thesis with three independent parameters defining its kinematics, which correspond to the mid-surface displacement components v_i of a material point. No additional dependent rotational degrees of freedom have been established in the formulation. The imposition of homogeneous displacement boundary conditions on the control points of $\partial\Omega_u^{\mathrm{h}}$ consequently yields at most a hinged support. The definition of symmetry boundary conditions or clamped supports, therefore, follows the approach of KIENDL ET AL. (2009). Therein, the displacement degrees of freedom of the "second" row of control points, which are perpendicular to the tangent plane of the NURBS object at the support boundary are additionally fixed to preserve the original orientation of the tangent during deformation.

The 5-parameter standard formulation (5p-stand.) with difference vector to be imposed on the director of the undeformed configuration has two additional displacement degrees of freedom per material point, which are, however, defined in the local coordinate system and thus do not coincide with the global Cartesian reference frame in general. For the special case of a rectangular plate with the local coordinates $\{\theta^i\}$ having the same orientation as the global ones $\{x, y, z\}$, fixing the degrees of freedom $\breve{w}_1$ of all control points along the boundary edges in y-direction and simultaneously setting the degrees of freedom $\breve{w}_2$ of all control points along the edges in x-direction to zero, yields a clamping of the entire plate with soft support conditions, meaning that twisting along the edges is not constrained.

Clamping of the hierarchic 5- and 7-parameter shells (5p-hier., 7p-hier.) is performed analogously to the 3-parameter Kirchhoff-Love formulation by fixing the tangents of the NURBS object during deformation along the prescribed displacement boundary. Important to notice, however, is that the degrees of freedom $\tilde{w}_\alpha$ related to the hierarchic difference vector only account for transverse shear deformations. Fixing these variables in the same way as described for the standard Reissner-Mindlin shell (5p-stand.), consequently enforces the condition of setting the transverse shear forces to zero along the homogeneous displacement boundary, which may lead to wrong results.

The sixth degree of freedom, $\mathring{w}$ of the 7-parameter shells, is related to the extensibility in thickness direction. Setting them to zero enforces the inextensibility of the shell along the support boundary, which may, however, not be constrained if symmetry boundary conditions are to be modeled. Finally, the seventh degree of freedom $\overline{w}$, which for the 3D shells defines the quadratic displacement contribution in thickness direction, may be constrained. If $\overline{w} = 0$, the linear part of the transverse normal strains is set to zero along the prescribed displacement boundary.

For further details on the physical significance of the kinematic and static variables of shell formulations and the imposition of kinematic and static boundary conditions, the reader is referred to BISCHOFF (1999), BISCHOFF AND RAMM (2000), BISCHOFF ET AL. (2004), COTTRELL ET AL. (2009) and KIENDL ET AL. (2009), among others.

5.2.4 Numerical examples

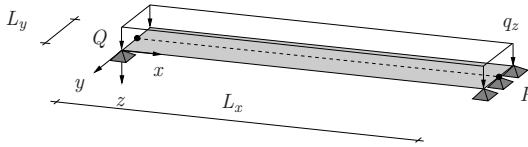**Example 1: Plate strip with uniaxial bending**

Figure 5.1: Simply supported plate strip with uniform transverse load.

The first example to be investigated is a rectangular simply supported plate strip as shown in Figure 5.1, which is subjected to a constant transverse area load of $q_z = 1.0$. A Young's modulus and Poisson's ratio of 1000.0 and 0.0 are chosen for the definition of the linear-elastic isotropic material. The sensitivity of the displacement-based shell element formulations (3p, 5p-stand., 5p-hier., 7p-stand., 7p-hier.) to transverse shear locking is analyzed. Due to the simple problem setup with uniaxial bending, the numerical shell results are compared to the analytical Bernoulli beam solution, which for a thickness of 1.0 yields a center deflection of $v_z = 1.5625$. The corresponding analytic displacement result with Timoshenko beam kinematics is $v_z = 1.5875$.

The plate strip has the dimensions $L_x = 10.0$, $L_y = 1.0$ and a uniform thickness of t, which will be varied in order to investigate the dependency of the numerical displacement results on the critical parameter, i.e. the slenderness $\frac{L_x}{t}$. The natural coordinates $\{\xi, \eta, \zeta\}$ have the same orientation as the global coordinates $\{x, y, z\}$. The metric of the shell is therefore constant in the entire patch domain. Consequently, derivatives of the base vectors, with respect to the natural coordinates, vanish. The area load is scaled with t^3, proportional to the bending stiffness, such that the computed deflection

becomes independent of t in the thin limit.

The spatial domain is discretized with a structured mesh of 10 elements in x-direction and one element in y-direction using biquadratic NURBS functions with maximum continuity of C^1.

For all shell models, homogeneous displacement boundary conditions are applied to the mid-surface displacement components v_i of all control points along the edges in y-direction at $x = 0.0$ and $x = L_x$.
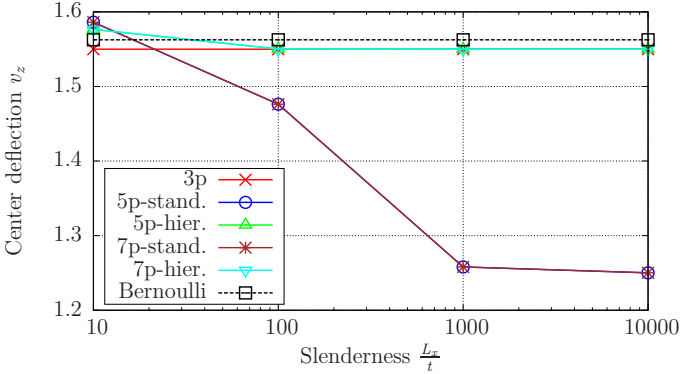

Figure 5.2: Plate strip – displacement convergence (transverse shear locking).

The chart of Figure 5.2 clearly illustrates that the displacement results of the Kirchhoff-Love-type (3p) and the hierarchic shell formulations (5p-hier., 7p-hier.) are independent of the slenderness and asymptotically converge to the analytic Bernoulli reference solution. Due to the relative coarse mesh, the numerical shell results slightly underestimate the beam reference solution. In the thick regime, the Reissner-Mindlin and 7-parameter elements match the analytic Timoshenko beam solution due to the influence of transverse shear. Whereas the Kirchhoff-Love shell element is free from spurious transverse shear strains by definition, the hierarchic 5-parameter and 3D shell elements do not suffer from this locking effect based on the independent parametrization of both bending and shear deformation; see Sections 4.4.2 and 4.5.2. The standard 5- and 7-parameter shell elements (5p-stand., 7p-stand.), on the other hand, clearly exhibit sensitivity to transverse shear locking. Equal order interpolation of both the mid-surface displacement field and the difference vector yields an imbalance of the NURBS function spaces in the kinematic equations of $\varepsilon_{\alpha3}^{\mathrm{h}}$; see Equations (4.19) and (4.33).

Next, the quality of the discrete transverse shear forces V_z will be investigated along the path P-Q of Figure 5.1 for the 5- and 7-parameter shell element formulations. Additionally, a NURBS-based Timoshenko beam model with hierarchic difference vector

(Timo.-hier.) and the analytic Timoshenko reference solution (Timo.-Ref.) are analyzed for a fixed slenderness of $\frac{L_x}{t} = 10$.
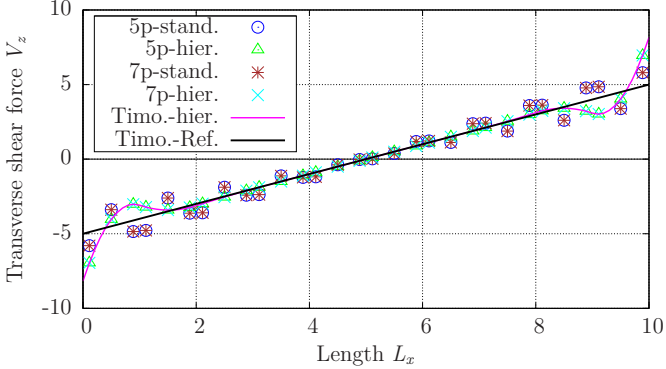

Figure 5.3: Plate strip and Timoshenko beam – transverse shear forces.

For computing the stress resultant transverse shear forces of the shell models in the global Cartesian basis $\mathbf{e}_i$, the stress components σ^{kl}, which are defined in curvilinear convective coordinates θ^i, first have to be transformed into a Cartesian frame according to Equation (5.11)

$$\overline{\sigma}^{ij} = \sigma^{kl} \left(\mathbf{G}_k \cdot \mathbf{e}_i \right) \left(\mathbf{G}_l \cdot \mathbf{e}_j \right). \tag{5.11}$$

The transverse shear stresses for the 5-parameter shell elements are constant across the thickness. For the given problem setup, the 7-parameter shell elements also have a constant distribution of transverse shear stresses in θ^3-direction. Due to the unit area of the rectangular cross section of the plate strip, the values of the transverse shear forces coincide with the values of the transverse shear stresses.

The evaluations along the path P-Q reveal an interesting result. Although the parametrization with hierarchic difference vector is insensitive to transverse shear locking, see Figure 5.2, oscillations in the transverse shear forces show up both for the hierarchic shell and the hierarchic Timoshenko beam elements. For the given problem setup with uniaxial bending, the transverse shear forces of the discrete hierarchic shell and hierarchic beam formulations are identical. The reason for this oscillation phenomenon, however, is not yet found. The oscillations are very pronounced near the supports and diminish towards the homogeneous interior of the structure. With progressive mesh refinement, they become more and more confined to the displacement boundary at $x = 0.0$ and $x = L_x$, with decreasing maximum amplitudes.

Example 2: Plate with biaxial bending

In this second example, a simply supported square plate subjected to constant transverse loading q_z is investigated, which, compared to the previous example, however, yields biaxial bending. The plate edges have a length of $L = 10.0$. The Young's modulus is equal to 1000.0 and a nonzero Poisson's ratio of 0.3 is chosen. Again, the sensitivity of the shell element formulations (3p, 5p-stand., 5p-hier., 7p-stand., 7p-hier.) to transverse shear locking is analyzed by evaluating the dependency of the center deflection of the plate on the critical parameter, i.e. the plate thickness t. The transverse unit load $q_z = 1.0$ is again scaled with the t^3, such that the displacement evaluations become independent of t in the thin limit.
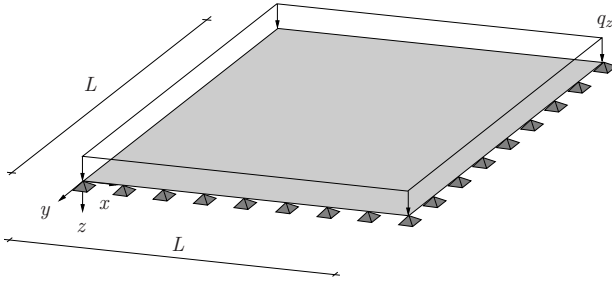

Figure 5.4: Simply supported plate with uniform transverse load.

A spatial discretization with 10 biquadratic NURBS elements in both x- and y-directions with maximum C^1-continuity is employed. The displacement values at the center of the plate are computed for all discrete shell models and compared to an analytical Kirchhoff plate solution $v_{z,\,\text{max}}^{\text{ref.}}$ of TIMOSHENKO AND WOINOWSKY-KRIEGER (2007). Only the first two terms of the series solution to $v_{z,\,\text{max}}^{\text{ref.}}$ are considered for a sufficiently accurate result, which finally yields

$$v_{z,\,\text{max}}^{\text{ref.}} = 0.442892\,. \tag{5.12}$$

The displacement results in Table 5.1 confirm the observations and results of the plate strip of the previous example. Both the Kirchhoff-Love-type (3p) and the hierarchic shell element formulations (5p-hier., 7p-hier.) match the analytic center deflection of the Kirchhoff plate model very well in the thin limit, independent of the slenderness of the structure. In the thick regime, the expected differences due to transverse shear effects are observed. The standard 5- and 7-parameter elements (5p-stand., 7p-stand.) again clearly underestimate the center deflection in the thin limit because of transverse

Slenderness $\frac{L}{t}$	10	100	1000	10000
Shell formulation (2nd order NURBS)				
3p	0.4423	0.4423	0.4423	0.4423
5p-stand.	0.4947	0.4367	0.3905	0.3878
5p-hier.	0.4938	0.4431	0.4423	0.4423
7p-stand.	0.4947	0.4367	0.3905	0.3878
7p-hier.	0.4936	0.4429	0.4421	0.4420

Table 5.1: Square plate – center deflection $v_{z,\,\max}$.

shear locking. The results, however, do not converge to zero with increasing slenderness, as they do in the case of linear elements due to the application of second-order NURBS discretizations.

In the thin limit, the results of the hierarchic 7-parameter shell do not exactly match the Kirchhoff solution. Whereas the 3- and 5-parameter formulations satisfy the condition of zero transverse normal stress, i.e. $\sigma^{33} = 0$ in a strong sense via static condensation of the corresponding constitutive equations, in the 7-parameter model, the zero transverse normal stress condition is only satisfied approximately. The quality of the approximation depends on the discretization ansatz in thickness direction of the shell. With mesh refinement, the deviation in the displacements fades away, which consequently yields a locking-free formulation.

In Figure 5.5, the vertical displacement v_z of the plate, which is discretized with Kirchhoff-Love shell elements, is displayed for a slenderness of $\frac{L}{t} = 100$.
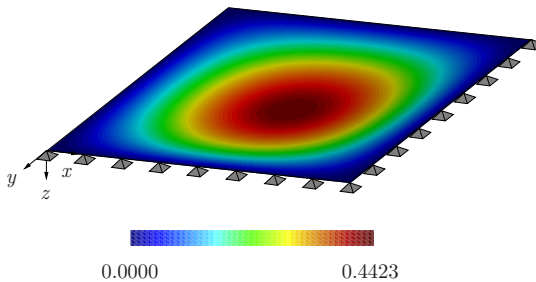

0.0000   0.4423

Figure 5.5: Kirchhoff-Love shell – deformation plot v_z.

The examples of this section show that standard formulations of displacement-based NURBS finite elements are not necessarily locking-free. For problems with constraints, the solution may depend on a critical parameter, which due to the mismatch of discrete NURBS function spaces may result in a significant underestimation of displacements. Although NURBS finite element methods are fundamentally of higher-order, locking does not vanish, but will only be alleviated. Therefore, the topic of locking of displacement-based NURBS finite elements is investigated in more detail in Section 5.4.

5.3 Higher-continuity NURBS discretizations

In Section 3.5, three different mesh refinement methods have been presented which enable enriching the NURBS basis and controlling inter-element continuity: knot insertion, order elevation and k-refinement. Whereas for CAD-based geometry representation, refinement of the function bases is used particularly for visual design, for numerical analysis, the modification of the NURBS basis is essential to ensure satisfactory approximation and convergence properties of the discrete solution functions.

Compared to classical C^0-continuous p- and h-refinement, the higher-continuity property of NURBS represents a significant novum in FEA. It allows for the straightforward formulation of problems with higher-continuous derivatives, such as the Kirchhoff-Love shell of Section 4.3, and in addition, provides improved accuracy of discrete solutions, which was first documented for smooth structural and fluid mechanics problems in HUGHES ET AL. (2005), COTTRELL ET AL. (2006) and COTTRELL ET AL. (2007).

K-refined NURBS, moreover, provide a homogeneous and repeating pattern of function coefficients and thus a regular distribution of nodal stiffness, which is in clear contrast to higher-order Lagrangian polynomials with an increasingly heterogeneous structure.
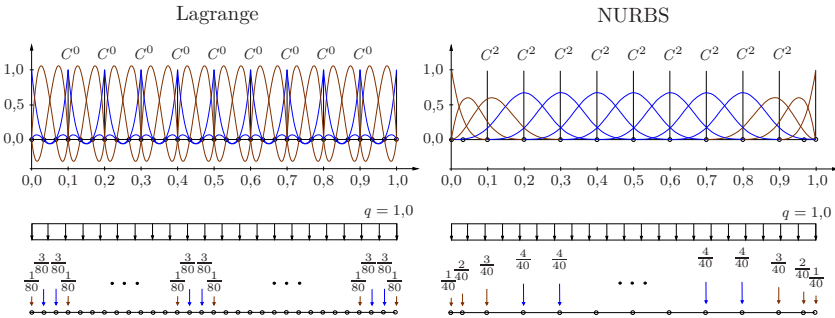

Figure 5.6: Consistent nodal forces – cubic Lagrange (C^0) vs. NURBS (C^2).

This difference is illustrated in Figure 5.6 for the distribution of consistent nodal forces of a 1D problem subjected to constant transverse loading. The spatial domain of unit length is discretized uniformly with ten elements and basis functions of cubic order for both cases. The nodal locations are displayed with black circles and element boundaries are highlighted with black vertical lines. Except for small regions at the patch boundary, the NURBS discretization yields uniform nodal forces of $\frac{4}{40}$ in the interior of the domain, whereas the Lagrange discretization shows the aforementioned heterogeneity within elements. Additionally, the difference in inter-element continuity of both discretizations is clearly demonstrated. Whereas the Lagrange model provides a C^0-continuous inter-

polation across element boundaries independent of the polynomial order, C^2-continuity is achieved with the k-refined cubic NURBS in the entire patch.

On the other hand, the higher continuity and smoothness of the NURBS basis may lead to unphysical phenomena, particularly for coarse mesh discretizations and non-smooth problems, such as contact, boundary layers, singularities or material interfaces. Local physical effects are consequently smeared over larger parts of the domain in the discrete model, and spurious deformations and oscillations of stresses may show up, as analyzed for NURBS contact problems in MATZEN ET AL. (2013), for instance. With regard to finite element technology, the continuity of derived quantities, such as stresses and strains, precludes the direct application of conventional approaches for C^0-continuous discretizations, such as the enhanced assumed strain (EAS), assumed natural strain (ANS) or reduced integration methods to improve the behavior of pure displacement formulations, which will be discussed in Chapter 6.

5.3.1 Effect of continuity on accuracy

In this section, the effect of higher-continuity NURBS on the approximation quality of discrete solutions compared to higher-order C^0-continuous element formulations will be investigated for a pinched cylindrical ring with fixed slenderness of $\frac{R}{t} = 100$.
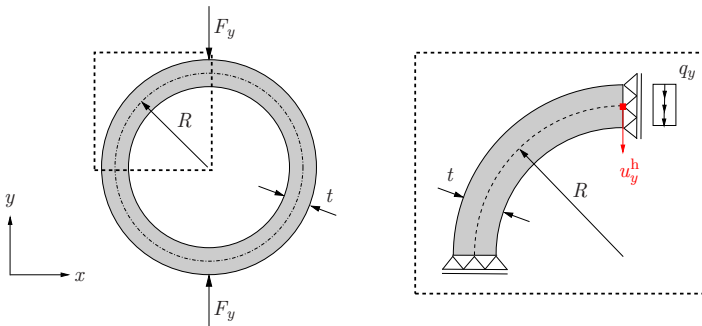
Problem setup

Figure 5.7: Pinched ring – problem setup.

The entire geometry can be modeled with four patches. For numerical analysis, however, only one quarter of the domain is discretized with one NURBS patch Ω_{pa} and appropriate symmetry boundary conditions. To avoid singularities due to the concentrated

loading F_y, an equivalent distributed shear force q_y is applied along the cross-section of the ring.

The discretization of the ring is performed with 2D NURBS continuum elements, which allow for a reduction of inter-element continuity up to C^0, in contrast to the hierarchic NURBS shell elements of this thesis, which require at least C^1-continuity of the NURBS basis. For the 2D problem setup, a state of plane stress is assumed.

In circumferential direction of the ring, 2nd and 3rd order NURBS functions are used along with mesh refinement. In radial direction, only one element with quadratic NURBS is applied to all computations, which is required for an asymptotically correct model. Consequently, five finite element models with different polynomial order and continuity are examined. The polynomial degree of the NURBS basis in circumferential direction of the ring is denoted with p; in radial direction, the variable q is used. The Young's modulus and the Poisson's ratio are equal to $E = 1000.0$ and $\nu = 0.0$ for all computations. For numerical integration, an element-based standard Gauss quadrature is employed in the same way, as defined previously for the NURBS shell element formulations.
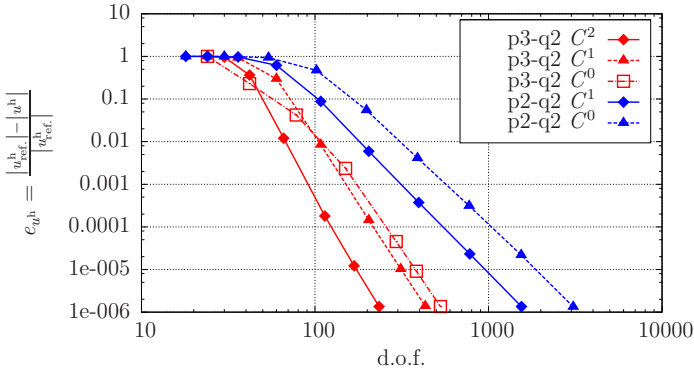
Numerical results

Figure 5.8: Pinched ring – relative error e_{u^h} (effect of continuity).

In Figure 5.8, the relative error in the displacements e_{u^h} is computed with respect to a numerical reference solution $u_{\mathrm{ref.}}^h$ and plotted versus the number of degrees of freedom (d.o.f.) in a double logarithmic scale. The evaluations refer to the discrete displacement u_y^h of the control point highlighted with a red box in Figure 5.7 in y-direction. The results of the biquadratic discretizations are displayed in blue; the cubic-quadratic models

are shown in red.

Several conclusions can be drawn from Figure 5.8: By comparing the red to the blue curves, it turns out that increasing the polynomial order of the NURBS basis reduces the relative error in the displacement results for the same number of degrees of freedom. Additionally, higher-order NURBS discretizations possess higher rates of convergence in the limit of an infinite number of degrees of freedom, which is revealed by the steeper slopes of the cubic NURBS discretizations. These observations are not fundamentally new for NURBS FEA, and they conform with the results known for traditional finite element formulations.

When looking at the class of red and blue curves in Figure 5.8 individually, their asymptotic rates of convergence are identical in the limit. The absolute errors, however, significantly differ from each other. With decreasing continuity of the basis in circumferential direction of the ring, the relative error increases. In the coarse mesh regime, the C^0-continuous approach with cubic basis appears to be superior to the one with maximum continuity. This phenomenon may, however, be due to the fact that for very coarse discretizations, the C^0-continuous shape functions happen to better approximate the discrete displacement result. In the asymptotic range, the maximum-continuity models provide significantly superior results.

This first example of a curved 2D thin-walled structure predominantly subjected to bending reveals that the higher continuity of the NURBS basis significantly improves the computational results compared to C^0-continuous shape functions for smooth problems.

5.3.2 In-plane behavior of NURBS shell elements

In Section 5.2.4, the two examples of plates subjected to transverse loading revealed that the hierarchic family of NURBS shell elements with pure displacement ansatz avoids transverse shear locking completely, whereas the standard shear-flexible formulations (5p-stand., 7p-stand.) tend to lock.

The curves of the relative error in the displacements for the pinched ring problem of Section 5.3.1, on the other hand, demonstrate that the rates of convergence of the displacement-based 2D continuum elements are not uniform and show slow convergence, particularly in the coarse mesh regime, which indicates locking. With increasing polynomial order, the relative error in fact becomes smaller; nevertheless, even the cubic NURBS discretizations tend to lock for the given bending dominated problem setup.

Therefore, the pinched ring of Figure 5.7 now is discretized with biquadratic Kirchhoff-Love shell elements with pure displacement formulation in order to investigate in-plane behavior of NURBS shell elements in the same way as for the 2D continuum elements, by analyzing the relative error in displacements. The circumferential and radial direc-

tions of the ring coincide with θ^1 and θ^2 and thus the in-plane directions of the shell elements. The Reissner-Mindlin and 3D shell formulations of Sections 4.4 and 4.5 are not considered herein. For the given model problem, no contributions of the difference vectors to the in-plane strain components $\varepsilon_{\alpha\beta}^{\mathrm{h}}$ will show up.

In circumferential direction, the number of elements is varied; in radial direction, again only one element is utilized. Three models with different slenderness $\frac{R}{t}$ are evaluated and compared among each other.
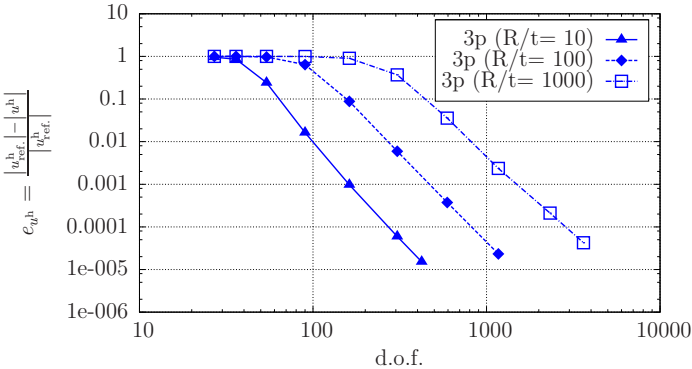

Figure 5.9: Pinched ring – relative error $e_{u^{\mathrm{h}}}$ (effect of slenderness).

In Figure 5.9, the relative error in the displacements for the control point highlighted in red in Figure 5.7 is plotted versus the number of degrees of freedom in a log-log scale. All three models have identical asymptotic convergence rates in the limit due to having the same polynomial order. The absolute errors, however, increase significantly with an increase in slenderness of the structure and are not uniform, particularly in the coarse mesh regime.

These observations, together with the results obtained from Figure 5.8, clearly indicate that NURBS finite elements and, with regard to this thesis, the in-plane part of the NURBS shells elements with pure displacement ansatz, is not locking-free for problems with constraints. The locking effects of this example are purely geometric.

So far, no detailed investigations have been performed to determine exactly which type of geometric locking effect deteriorates the approximation properties of the discrete solutions. It can be observed that higher-order and higher-continuity NURBS discretizations have improved accuracy properties compared to C^0-continuous discretizations for smooth problems, but they are not necessarily locking-free.

Therefore, in Section 5.4 a detailed investigation of the respective locking phenomena

showing up for the displacement-based NURBS shell finite elements in constraint problems is carried out.

5.4 Locking phenomena for NURBS shell elements

The most important locking phenomena in the context of numerical shell analysis are related to geometric constraints, which deteriorate the accuracy and slow down the convergence as thickness approaches zero. For the most general case of three-dimensional shells, these effects are transverse shear locking, curvature thickness locking and membrane locking. A detailed treatment of the different locking effects for shell finite elements in general can be found, for instance, in HAUSSER (1996), BISCHOFF (1999), KLINKEL (2000), BISCHOFF ET AL. (2004) and KOSCHNICK (2004).

Standard polynomial or NURBS-based shape functions in a Galerkin ansatz are often too inaccurate for a sufficiently precise approximation of the exact solution, if either kinematic or material-based constraints, such as fulfillment of the Kirchhoff condition for thin computational domains or incompressible material behavior are present.

Mathematically, locking is associated with an ill-conditioning of the respective physical problem or the set of partial differential equations, which depends on the existence of a small critical parameter. This parameter may be associated with some physical quantity, as for example the thickness of a structure or the bulk modulus. If the parameter approaches a limiting value, a large quotient of coefficients in the internal energy functional evolves, which inhibits uniform and optimal convergence of the discrete model with regard to this parameter, as the mesh parameter $h \to 0$.

A robust formulation, on the other hand, is characterized by uniform and optimal convergence of the discrete solution with respect to some norm for all values of the critical parameter, as h tends to zero (BABUŠKA AND SURI (1992), ARNOLD AND BREZZI (1997), BRAESS (2003)).

5.4.1 Constraint count method

In the following, the "constraint count" approach of HUGHES (2000) is briefly summarized and used in the subsequent sections to numerically analyze the sensitivity of the NURBS shell elements with regard to locking, without requiring in-depth mathematical fundamentals of mixed methods and proofs of stability conditions.

For a discrete model, the scalar constraint ratio cn is computed as the quotient of the number of displacement degrees of freedom and the amount of constraint conditions. Only those degrees of freedom are considered which contribute to the deformation mode under consideration. For computing the constraint ratio of a specific element type, the

existence of an infinitely large and structured mesh is assumed. In the discrete model, the number of relevant degrees of freedom $N_{\mathrm{d.o.f.}}$ is computed by the ratio of finite element nodes to elements, which is denoted with n_{node} times the number of nodal degrees of freedom $n_{\mathrm{d.o.f.}}$. The amount of constraints $N_{\mathrm{cons.}}$ is related to the number of quadrature points n_{q}, where the constraints are to be evaluated.

The optimal constraint number of the continuous problem $cn^{\mathrm{cont.}}$ is equal to the ratio of degrees of freedom per material point $N_{\mathrm{d.o.f.}}^{\mathrm{cont.}}$ and number of constraint conditions $N_{\mathrm{cons.}}$. A numerical estimate, with regard to the element performance, is obtained by comparing the discrete constraint number to the optimal one. If the constraint ratio cn is smaller than the optimal $cn^{\mathrm{cont.}}$, too many constraints exist and the element formulation tends to lock. Values of $cn \leq 1$ indicate severe locking, as more constraint conditions than displacement degrees of freedom are available. If $cn > 2$, the number of constraints is too small, which may lead to a poor approximation quality, oscillations of the solution or even instability of the element formulation.

Further details of this numerical approach with regard to the assessment of locking and existing shortcomings are provided, for instance, in Hughes (2000), Bischoff (1999) and Bischoff (2005).

The derivation of the optimal and discrete constraint number is illustrated in the following for a 2D continuum element subjected to pure bending. The optimal constraint number is equal to the ratio of displacement degrees of freedom, which is two, and the number of constraints, i.e. zero shear strains

$$cn^{\mathrm{cont.}} = \frac{N_{\mathrm{d.o.f.}}^{\mathrm{cont.}}}{N_{\mathrm{cons.}}} = \frac{2}{1} = 2 \,. \tag{5.13}$$

The four node bilinear displacement quadrilateral with 2×2 quadrature points, according to the course of action described before, yields

$$cn = \frac{N_{\mathrm{d.o.f.}}}{N_{\mathrm{cons.}}} = \frac{n_{\mathrm{d.o.f.}} \cdot n_{\mathrm{node}}}{n_{\mathrm{cons.}} \cdot n_{\mathrm{q}}} = \frac{2 \cdot 1}{1 \cdot 4} = \frac{1}{2} \,. \tag{5.14}$$

The discrete constraint number is significantly smaller than one, which reveals that the element formulation is strongly overconstrained and thus exhibits severe shear locking. An application of reduced one-point integration for example results in a constraint ratio $cn = 2$, which is optimal with regard to $cn^{\mathrm{cont.}}$; but it is known from literature (Zienkiewicz et al. (1971), Hughes et al. (1977)) that this approach will lead to zero energy deformation modes without the use of selective reduction or stabilization techniques. Methods to avoid locking for the NURBS shell finite elements of this thesis are discussed in Chapter 6.

5.4.2 Transverse shear locking

Transverse shear locking may show up in isoparametric displacement-based shear deformable beam, plate and shell finite element formulations that are applied to problems with constraints. Particularly for shell structures, which due to their efficient load carrying behavior can be built very slender, this locking effect may become very severe in computational structural analysis.

The Bernoulli or Kirchhoff constraint of zero transverse shear strains cannot be enforced accurately, especially for low-order displacement approximation functions, which are not able to represent the continuous deformation modes correctly and consequently lead to unphysical parasitic transverse shear strains and stresses that do not show up in the continuous formulation.

Timoshenko beam – analytical investigation of transverse shear locking

The straight Timoshenko beam model, although a fairly simple problem setup, allows for an analytical investigation of transverse shear locking and the computation of exact solutions for arbitrary load cases. The reasons and phenomena for shear locking can be carried over to plates and shells, which makes it sensible to investigate the shear-deformable beam problem first.

For a Timoshenko beam element with a rectangular cross section, the ratio of bending to shear stiffness is proportional to the square of the thickness t, which for $t \to 0$ converges quadratically to zero. If unphysical parasitic transverse shear is present, the major part of the deformation energy will be absorbed, which finally results in a significant underestimation of the displacements. This effect is in clear opposition to the continuous model, where with $t \to 0$, the influence of transverse shear vanishes, such that the continuous solution converges to the shear-rigid Bernoulli displacement solution.

The linear kinematic equations for the curvature κ and shear angle γ of a straight and plane Timoshenko beam are defined in Equation (5.15), where the transverse displacements u_y and the cross sectional rotations φ are the independent displacement parameters

$$
\begin{aligned}
\kappa &= \varphi' \,, \\
\gamma &= u_y' + \varphi \,.
\end{aligned}
\tag{5.15}
$$

First derivatives with respect to the coordinate of the beam center line are indicated with $(\bullet)'$. Equation (5.15) clearly reveals the different orders of functions in the equation for the shear angle γ, which for equal-order interpolation of both the displacements and rotations in the discrete model results in higher-order contributions of φ that cannot be balanced by the transverse displacements u_y' with the existence of derivatives.

The Timoshenko beam model of Figure 5.10, which is discretized with a pure displacement NURBS ansatz, will be analyzed with respect to transverse shear locking in the following.
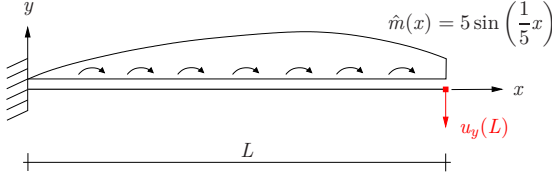

Figure 5.10: Timoshenko beam with sinusoidal moment loading.

The beam has a length of $L = 10.0$ and unit width $b = 1.0$. The Young's modulus and Poisson's ratio are equal to $E = 10000.0$ and $\nu = 0.0$, respectively. To analytically investigate locking, the thickness t stays symbolic, such that the computational results remain functions of the thickness.

The exact solutions for the displacements $u_y^{\text{ex}}(x)$ and rotations $\varphi^{\text{ex}}(x)$ are

$$
\begin{aligned}
u_y^{\text{ex}}(x) &= \frac{3}{200} x^2 \cos(2) + \frac{3}{4} \cos\left(\frac{1}{5}x\right) - \frac{3}{4}, \\
\varphi^{\text{ex}}(x) &= -\frac{3}{100} x \cos(2) + \frac{3}{20} \sin\left(\frac{1}{5}x\right).
\end{aligned}
\tag{5.16}
$$

For the continuous model, the pure moment loading $\hat{m}(x)$ results in pure bending deformations without transverse shear effects. The load is scaled with the 3rd power of the beam thickness t, such that the displacements are independent of the thickness parameter.

For simplicity, single element NURBS discretizations are used, as the investigated locking effect results from the mismatch of discrete function spaces in the kinematic equation for the transverse shear, rather than the number of elements.

In (5.17), the element displacement vector $\mathbf{d}_{p=1}$ is shown, which accounts for only the nonzero control point displacements for a discretization with linear ($p = 1$) NURBS functions. The tip displacements $u_y^{\text{h}}(x = L)$ of all displacement vectors $\mathbf{d}_{p=1}$ to $\mathbf{d}_{p=4}$ are highlighted in green; the discrete rotations at the tip of the beam in blue color. Only nonzero degrees of freedom are displayed

$$
\mathbf{d}_{p=1} = \begin{bmatrix} -3.92\, \frac{t^2}{125+3t^2} \\ 0.783\, \frac{t^2}{125+3t^2} \end{bmatrix}.
\tag{5.17}
$$

The results of $\mathbf{d}_{p=1}$ clearly reveal the dependency of the discrete solution on the beam thickness t, in contrast to the analytical model. The displacements even tend to zero with

$t \to 0$, which leads to a complete divergence and confirms conventional finite element results

$$\mathbf{d}_{p=2} = \begin{bmatrix} -0.568 \frac{t^2}{25+3t^2} \\ 0.075 \frac{43.5+9.75t^2}{25+3t^2} \\ -0.75 \frac{43.5+6.74t^2}{25+3t^2} \\ 0.261 \end{bmatrix}, \ \mathbf{d}_{p=3} = \begin{bmatrix} -0.122 \frac{t^2}{25+7t^2} \\ 0.05 \frac{81.6+20t^2}{25+7t^2} \\ -0.25 \frac{81.6+22.4t^2}{25+7t^2} \\ 0.05 \frac{125+37t^2}{25+7t^2} \\ -1.69 \\ 0.261, \end{bmatrix}, \ \mathbf{d}_{p=4} = \begin{bmatrix} -0.179 \frac{t^2}{125+63t^2} \\ 0.0375 \frac{365.9+177.7t^2}{125+63t^2} \\ -0.366 \\ 0.075 \frac{344.4+180.3t^2}{125+63t^2} \\ -0.1875 \frac{688.8+348.1t^2}{125+63t^2} \\ 0.0375 \frac{885.1+439.4t^2}{125+63t^2} \\ -1.69 \\ 0.261 \end{bmatrix}.$$

$$(5.18)$$

Additionally, higher-order NURBS discretizations with $p = 2, 3$ and 4 are investigated. For the 2nd order model, the rotation at the free end of the beam is now independent of t. For the cubic and quartic NURBS discretizations, both the tip displacements and the rotations match the exact solution. Nevertheless, even for cubic and quartic NURBS functions, the control point degrees of freedom in the interior of the patch still depend on the thickness t and thus indicate sensitivity to locking. The situation, however, becomes less dramatic as the polynomial order is increased. The displacement at the free end of the beam no longer tends to zero for $t \to 0$, as it was the case for the linear NURBS discretization.

In Figure 5.11, the exact error $\|e_u\|_{L^2}$ in the displacements is computed with respect to the L^2-norm for all four NURBS discretizations. L^2 represents the Sobolev space of square-integrable functions. The definition of the error is provided by Equation (5.19), where u_y^{h} denotes the NURBS finite element solution (HUGHES (2000), ZIENKIEWICZ ET AL. (2005))

$$\|e_u\|_{L^2} := \frac{\|u_y^{\mathrm{ex}} - u_y^{\mathrm{h}}\|_{L^2}}{\|u_y^{\mathrm{ex}}\|_{L^2}} . \tag{5.19}$$

The relative error for the linear NURBS discretization is almost one, even for a comparatively small slenderness of $\frac{L}{t} = 10$. For quadratic NURBS functions, $\|e_u\|_{L^2}$ already becomes significantly smaller with a value of approximately 0.25 for a slenderness of $\frac{L}{t} = 100$. The error curves of the cubic and quartic case are nearly horizontal and possess very small absolute values, which, from a practical point of view, become almost insignificant.

An application of the constraint count method of Section 5.4.1 for a linear Timoshenko
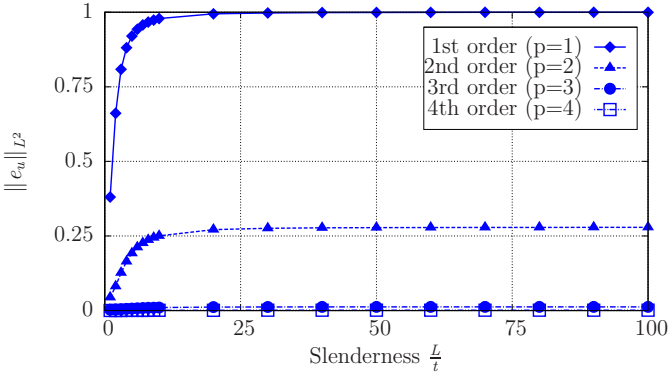
Figure 5.11: Timoshenko beam – exact L^2-norm error.

beam element yields the following results. The number of continuous constraints to be satisfied at a material point is one, i.e. $\gamma = 0$. The number of relevant degrees of freedom per material point is two, which are the transverse displacements and cross sectional rotations. Consequently, the optimal constraint ratio is equal to $cn^{\text{cont.}} = \frac{2}{1} = 2$. For an infinite mesh, the ratio of number of nodes to elements becomes one. Standard Gauss quadrature requires two integration points per element. The constraint number for the linear Timoshenko beam element yields $cn = \frac{1 \cdot 2}{2 \cdot 1} = 1$, which reveals that the element formulation is overconstrained and will exhibit locking.

Transverse shear locking for standard 5- and 7-parameter isogeometric shells

The 5- and 7-parameter shell models with standard difference vector to be imposed on the director of the undeformed configuration (5p-stand., 7p-stand.) have been introduced in Sections 4.4.1 and 4.5.1. As already assessed for the Timoshenko beam model, the constraint of vanishing transverse shear in the thin limit cannot be achieved for the standard shear deformable isogeometric shell elements if an equal-order NURBS interpolation is applied to both the mid-surface and difference vector displacement field. The highest polynomial order of the difference vectors cannot be balanced by the mid-surface displacements, which possess first derivatives in the strain tensor coefficients $\varepsilon_{\alpha 3}$, see Equations (4.19) and (4.33).

The shell elements consequently tend to transverse shear locking and principally show the same behavior as described for the discrete NURBS Timoshenko beam models before.

The effect of transverse shear locking for the shear deformable 5- and 7-parameter shell

elements with standard difference vector show up in exactly the same way, if, instead of a difference vector formulation, a parametrization with rotation tensors is applied. The same holds true for the Timoshenko beam model, if, instead of rotations, a difference vector is imposed on the undeformed director.

5.4.3 Membrane locking

The ability to carry loads in a state of pure bending, i.e. inextensional deformation without any membrane action is limited to developable shell structures, for example cylinders and cones. Membrane locking for curved, thin-walled beam and shell finite elements is related to the inability of describing inextensional pure bending deformation modes without additional unphysical parasitic membrane contributions. For flat structures with zero curvature, this phenomenon does not show up, as bending and membrane action are not coupled a priori.

In STOLARSKI AND BELYTSCHKO (1982), this phenomenon of undesired membrane-bending-coupling was denoted as membrane locking for the first time while the kinematics of a curved shallow beam was investigated, accounting for Marguerre's shallow shell theory (MARGUERRE (1938), LI AND SHYY (1997)).
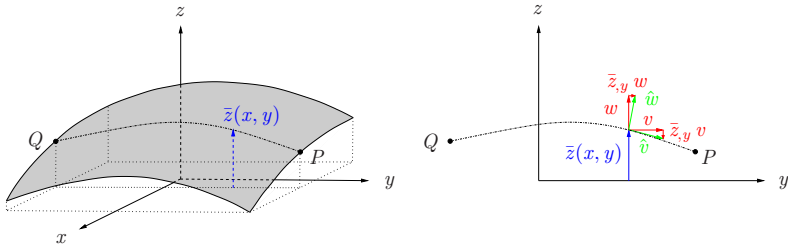

Figure 5.12: Marguerre shallow shell.

In the left sketch of Figure 5.12, the reference configuration of a shallow shell is displayed. By assuming linear kinematics and taking the x-y-plane as the reference plane of a three-dimensional Cartesian coordinate system, the mid-surface of the shell may be defined by

$$\bar{z} = z(x, y). \tag{5.20}$$

The displacement field $\mathbf{u} = \{u, v, w\}$ is again described in Cartesian coordinates. It yields for the cutting plane through the points P and Q, which is parallel to the y-z-

plane, as shown on the right of Figure 5.12

$$
\begin{aligned}
\tilde{v} &= v + \bar{z}_{,y}\, w\,, \\
\tilde{w} &= w - \bar{z}_{,y}\, v\,.
\end{aligned}
\tag{5.21}
$$

By accounting for the approximations $v \approx \hat{v}$, $w \approx \hat{w}$ and $\bar{z}_{,y}\, v \ll 1$, the entire displacement field, which is composed of mid-surface displacements and curvature contributions, is equal to

$$
\begin{aligned}
\tilde{u}(x, y, z) &= u(x, y) + \bar{z}_{,x}\, w(x, y)\,, \\
\tilde{v}(x, y, z) &= v(x, y) + \bar{z}_{,v}\, w(x, y)\,, \\
\tilde{w}(x, y, z) &= w(x, y)\,,
\end{aligned}
\tag{5.22}
$$

from which the linearized membrane strain components of the shallow shell can be derived

$$
\begin{aligned}
\varepsilon_{xx} &= \frac{\partial \tilde{u}}{\partial x} &&= \underbrace{u_{,x}}_{\text{lin.}} + \underbrace{\bar{z}_{,x}\, w_{,x}}_{\text{const.}}\,, \\
2\varepsilon_{xy} &= \frac{\partial \tilde{u}}{\partial y} + \frac{\partial \tilde{v}}{\partial x} &&= \underbrace{u_{,y} + v_{,x}}_{\text{lin.}} + \underbrace{\bar{z}_{,x}\, w_{,y} + \bar{z}_{,y}\, w_{,x}}_{\text{const.}}\,, \\
\varepsilon_{yy} &= \frac{\partial \tilde{v}}{\partial y} &&= \underbrace{v_{,y}}_{\text{lin.}} + \underbrace{\bar{z}_{,y}\, w_{,y}}_{\text{const.}}\,.
\end{aligned}
\tag{5.23}
$$

Equation (5.23) reveals that nonzero curvature, i.e. $\bar{z} \neq$ const., leads to contributions of different order in the membrane strain components. An isoparametric interpolation of both the geometry and displacement field therefore leads to unbalanced terms in the kinematics, which are the reason for membrane locking.

The critical parameter for membrane locking is again the thickness of the structure, as for transverse shear locking. The ratio of bending to membrane stiffness is proportional to the square of the thickness. With increasing slenderness of the discrete model, large parts of the internal energy are due to unphysical membrane action, which consequently results in a significant underestimation of the displacements and prevents a uniform convergence to the exact solution.

The application of the constraint count approach of Section 5.4.1 to numerically investigate the tendency of displacement-based shell finite elements to membrane locking will be examined in the following.

The number of continuous constraints to be satisfied if shear deformations are accounted for is three, which are the membrane normal forces and shear forces to vanish for the case of pure bending. The number of relevant degrees of freedom per material point consists of three mid-surface displacements and two rotations or difference vector displacements,

respectively. The optimal constraint ratio is therefore equal to $cn^{\text{cont.}} = \frac{5}{3} \approx 1.667$.
A four node bilinear shell element with standard 2×2 Gauss integration points gives $cn = \frac{5 \cdot 1}{3 \cdot 4} \approx 0.417$. The biquadratic nine node shell element with standard 3×3 Gauss points yields a discrete constraint number of $cn = \frac{5 \cdot 4}{3 \cdot 9} \approx 0.741$. Both values are significantly smaller than one, which indicates strongly overconstrained formulations that are sensitive to locking.

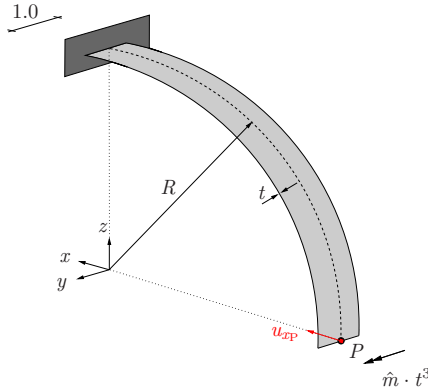**Analytical investigation of membrane locking – cylindrical shell strip**

Figure 5.13: Cylindrical shell – problem setup.

In this numerical example of a curved cylindrical shell subjected to bending, the behavior of the 3-parameter (3p) and hierarchic 5-parameter (5p-hier.) NURBS shell formulations with pure displacement ansatz is analyzed with regard to membrane locking. The 7-parameter shell formulation (7p-hier.) is not considered herein in order to exclude possible curvature-thickness locking effects from the investigations. Transverse shear locking will not show up due to the hierarchic difference vector formulation.

The required material constants for the linear elastic computations are Young's modulus $E = 1000.0$ and Poisson's ratio $\nu = 0.0$. Thus, material-based locking effects, which are discussed in Section 5.4.5, are excluded a priori.

The only remaining defect in the discrete kinematic equations of the curved shell finite elements may therefore originate from unphysical membrane-bending-coupling.

The shell segment has a radius of $R = 10.0$ and a width of 1.0 in y-direction. For the numerical simulations, the domain is discretized with a structured mesh of ten biquadratic NURBS shell elements with a maximum continuity of C^1 along the circumferential direction of the cylindrical strip. Along the edge $x = 0$ the structure is clamped. Clamping

of the rotation-free NURBS shell elements is performed according to Section 5.2.3 by setting all mid-surface displacement degrees of freedom v^i at $x = 0$ equal to zero and additionally applying homogeneous displacement boundary conditions in z-direction on the adjacent row of control points in order to fix the horizontal tangent at $x = 0$.

At the free edge, $x = R$, a moment loading of $\hat{m} = 1.0 \cdot t^3$ is applied to the discrete model. Due to the lack of rotational degrees of freedom, the moment is modeled with force couples, which are applied to the last two rows of control points. Based on the shape of the cylindrical segment, these rows of control points are both located at $x = R$ and thus the corresponding force couples have an orientation exactly in $\pm x$-direction.

An analytical reference solution is based on Bernoulli beam theory and yields the following stress resultants for the statically determinate structure

$$M = -1.0 \cdot t^3, \quad V = 0.0, \quad N = 0.0. \tag{5.24}$$

The exact radial displacement u_{x_P} at the free edge is equal to 1.20, independent of the slenderness $\frac{R}{t}$.
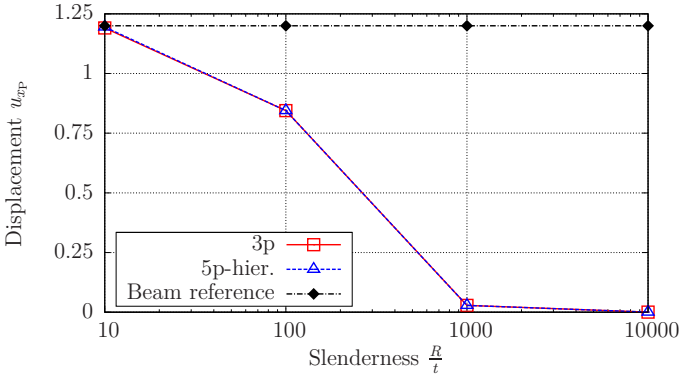

Figure 5.14: Cylindrical shell – displacement convergence (membrane locking).

Figure 5.14 clearly demonstrates the sensitivity of both the displacement-based Kirchhoff-Love (3p) and the hierarchic Reissner-Mindlin (5p-hier.) shell elements to membrane locking due to parasitic membrane strains in ε_{11}. Whereas for a comparatively thick structure the numerical results conform very well with the analytical reference solution, with increasing slenderness $\frac{R}{t}$, the discrete radial displacement of point P tends to zero. A moderate slenderness of $\frac{R}{t} = 100$ already reveals significant unphysical membrane strains, which lead to an underestimation of the reference displacement by almost 30%. The numerical displacement results are displayed in Table 5.2.

Slenderness $\frac{R}{t}$	10	100	1000	10000
Shell formulation (2nd order NURBS)				
3p	1.1909	0.8446	0.0285	0.0003
5p-hier.	1.1948	0.8446	0.0285	0.0003
Analytic result				
Beam reference	1.2000	1.2000	1.2000	1.2000

Table 5.2: Cylindrical shell – displacements u_{x_P} (membrane locking).

As mentioned before, the investigated displacement-based NURBS shell formulations may only exhibit membrane locking in the ε_{11} strain component. All other locking effects are excluded a priori due to the setup of this model problem. Additionally, no changes in thickness direction will show up during deformation, such that the results for the membrane strain component ε_{11} can also be carried over to the hierarchic 7-parameter shell element, in principle.

This numerical experiment illustrates that the isogeometric displacement-based NURBS shell element formulations require additional techniques for improving the behavior of the membrane part, which will be dealt with in detail in Chapter 6.

A comprehensive treatment and mathematical analysis of membrane locking for curved beam and shell structures can be found, for instance, in PITKÄRANTA (1992), ARNOLD AND BREZZI (1997), CHOI ET AL. (1998), BISCHOFF ET AL. (2004) or WISNIEWSKI (2010).

5.4.4 Curvature thickness locking

For the 3D NURBS shell elements with extensible director, which have been derived in Section 4.5, curvature thickness locking also has to be considered, which was identified first in RAMM ET AL. (1994) and BETSCH ET AL. (1995). This locking effect occurs for curved beam and shell elements with difference vector formulation and the application of averaged extensible directors. It may lead to artificial contributions in the transverse normal strains ε_{33}.

In order to explain this phenomenon more clearly, a curved shell structure with bilinear discretization subjected to pure bending in the $\theta^1 - \theta^3$-plane is investigated, as shown in Figure 5.15. For a state of pure bending, the length of the nodal directors has to remain unchanged during deformation. Additionally, the difference vector $\mathbf{w}$ is orthogonal to the director $\mathbf{A}_3$, i.e. $\mathbf{A}_3 \cdot \mathbf{w} = 0$ for zero Poisson's ratio and linear kinematics. Thus, no transverse normal strains ε_{33} will occur. The interpolation of even exact nodal directors with conventional C^0-continuous low-order Lagrangian shape functions in the element, however, results in an unphysical elongation or shortening of the director and thus artificial transverse normal strains.
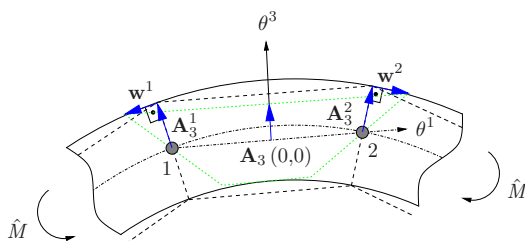
Figure 5.15: Pure bending deformation – curvature thickness locking.

The 7-parameter isogeometric shell formulations of Section 4.5 neither use averaged nodal directors, nor interpolate the discrete nodal director components in the element. They pointwise exactly define a smooth and extensible director field within the entire, at least biquadratic and C^1-continuous NURBS patch. Whereas for the 3D shell element "7p-stand." the difference vector is added on the undeformed director $\mathbf{A}_3$, "7p-hier." imposes the difference vector on the rotated shell normal.
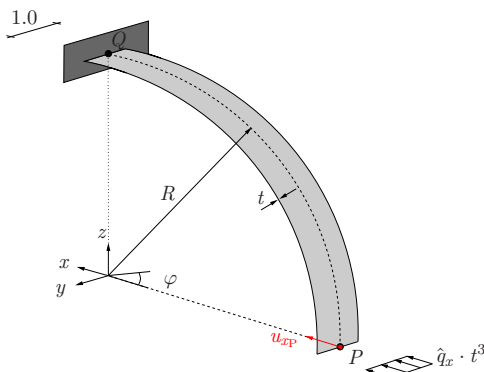
Figure 5.16: Cylindrical shell with transverse loading $\hat{q}_x$.

A cylindrical shell strip, which is subjected to a constant line load $\hat{q}_x$, as shown in Figure 5.16, will be investigated in order to examine if the hierarchic difference vector concept is able to intrinsically avoid curvature thickness locking. The geometric dimensions of the structure, the material properties and the kinematic boundary conditions coincide with the shell model of Section 5.4.3. This type of loading, however, does not only create a state of pure bending, but also results in transverse shear and membrane

normal forces. The analytical reference solution for a curved beam structure is obtained from equilibrium and is displayed in Figure 5.17.

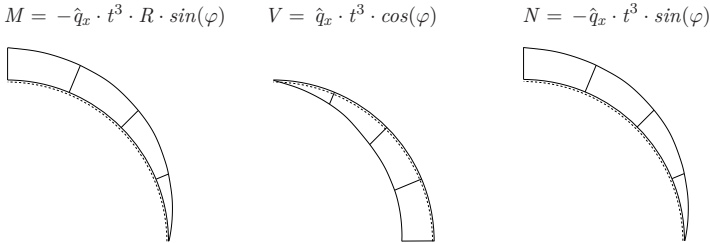$$M = -\hat{q}_x \cdot t^3 \cdot R \cdot sin(\varphi) \qquad V = \hat{q}_x \cdot t^3 \cdot cos(\varphi) \qquad N = -\hat{q}_x \cdot t^3 \cdot sin(\varphi)$$

Figure 5.17: Stress resultants M, V, N – beam reference solution.

For the bending dominated problem setup, the magnitude of the load $\hat{q}_x = 0.1$ is scaled with t^3. The beam reference solution for the radial displacement $u_{x_\mathrm{P}}^{\mathrm{ref.}}$ yields

$$u_{x_\mathrm{P}}^{\mathrm{ref.}} = \tfrac{3}{10}\,\pi + \tfrac{17}{20.000}\,\pi \cdot t^2 \approx 0.942478 + 0.002670 \cdot t^2\,. \tag{5.25}$$

Three NURBS shell finite element models are compared to the reference solution and among each other, which are all discretized with biquadratic C^1-continuous NURBS functions. First, a 7-parameter shell with standard difference vector (7p-stand.) according to Section 4.5.1 is analyzed. This model is sensitive to transverse shear locking, membrane locking and possibly curvature thickness locking for the given problem setup. Secondly, the hierarchic 7-parameter shell element of Section 4.5.2 is modified with a mixed ansatz for the in-plane part based on the two-field Hellinger-Reissner principle of Section 2.5.2 in order to remove membrane locking (7p-hier.-mixed). Parasitic transverse shear effects are intrinsically avoided, as described in Section 4.5.2, and verified in the numerical examples of Section 5.2.4. This mixed approach is explained in detail in Section 6.2 and will be used herein to concentrate on the problem of curvature thickness locking. Finally, the standard 7-parameter model is modified with the aforementioned mixed ansatz to remove membrane locking. Additionally, the Discrete Strain Gap (DSG) method, which will be discussed in detail in Section 6.1, is utilized to remove transverse shear locking. The resulting model is denoted with "7p-stand.-mixed-DSG" and may consequently only be prone to curvature thickness locking. As in the previous examples, the discrete radial displacement $u_{x_\mathrm{P}}^{\mathrm{h}}$ at the free edge, see Figure 5.16, is computed for a varying slenderness and compared to the analytical beam solution.

Figure 5.18 numerically confirms the previous explanations. The hierarchic 7-parameter NURBS shell element with mixed ansatz for the membrane part (7p-hier.-mixed) is completely free from geometric locking and matches the reference beam solution very well, independent of the slenderness $\frac{R}{t}$. The differences between "7p-hier.-mixed" and
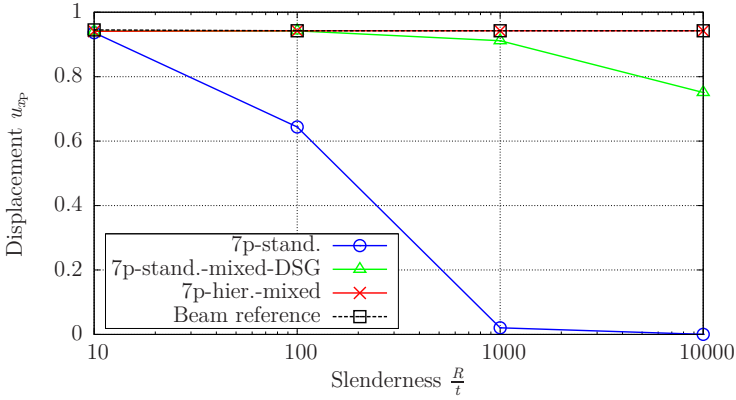
Figure 5.18: Cylindrical shell – displacement convergence (curvature thickness locking).

"7p-stand.-mixed-DSG" only result from curvature thickness locking. All other effects have been avoided or do not show up for the given problem definition. The hierarchic concept, therefore, not only removes the parasitic transverse shear effects, but also successfully eliminates curvature thickness locking for the NURBS shell finite elements of this thesis with extensible director. The standard difference vector shell element (7p-stand.) shows the worst behavior, as all aforementioned locking effects deteriorate its accuracy. Even for a comparatively small slenderness, the discrete radial displacements $u_{x_{\mathrm{P}}}^{\mathrm{h}}$ are strongly underestimated.

Slenderness $\frac{R}{t}$	10	100	1000	10000
Shell formulation (2nd order NURBS)				
7p-stand.	0.9364	0.6438	0.0205	0.0002
7p-stand.-mixed-DSG	0.9409	0.9421	0.9116	0.7509
7p-hier.-mixed	0.9409	0.9424	0.9425	0.9425
Analytic result				
Beam reference	0.9451	0.9425	0.9425	0.9425

Table 5.3: Cylindrical shell – displacements $u_{x_{\mathrm{P}}}$ (curvature thickness locking).

5.4.5 Material-based locking

Volumetric locking, in contrast to the aforementioned locking effects, depends on a material parameter, i.e. the Poisson's ratio ν. For incompressible or nearly incompressible material behavior, i.e. $\nu \to \frac{1}{2}$, the bulk modulus K tends to infinity and therefore repre-

sents the critical parameter. Typical examples are, for instance, rubbers, the von Mises plastic behavior of metals in the nonlinear regime or undrained soil. The corresponding constraint for the displacement field **u** is its divergence to be zero

$$\operatorname{div} \mathbf{u} = u_{j,j} = 0 \,. \tag{5.26}$$

If the applied finite element function spaces are not able to satisfy this constraint of a volume preserving strain field, unphysical membrane strains and stresses show up. They result in parasitic internal energy contributions, avoid uniform convergence and may even result in divergence, i.e. a complete locking of the element. With mesh refinement, volumetric locking may be alleviated.

The focus in this thesis is centered on the geometric locking effects of the NURBS-based shell finite elements formulations. For more detailed information on volumetric locking, the reader is referred to Hughes (2000), Braess (2003), Brenner and Scott (2008) and Belytschko et al. (2008).

The most prominent methods to eliminate or alleviate volumetric locking are reduced and selective reduced integration (Zienkiewicz et al. (1971), Hughes et al. (1977), Zienkiewicz and Taylor (2005)) and the EAS method (Simo and Rifai (1990), Andelfinger and Ramm (1993), Bischoff et al. (1999)), which are explained in more detail in Section 6.3. Numerical analysis of incompressible material behavior and volumetric locking in the context of isogeometric analysis has been performed in Auricchio et al. (2007), Elguedj et al. (2008), Auricchio et al. (2010), Taylor (2011) and Mathisen et al. (2011), among others.

Poisson thickness locking in shell element formulations has the same causes as volumetric locking. Parasitic linear strains and stresses may arise in transverse normal direction, which are based on nonzero membrane strains and lateral contraction due to nonzero Poisson's ratio. The 3- and 5-parameter shell formulations do not suffer from this phenomenon in thickness direction due to the modification of the material law as described in Sections 4.3 and 4.4. A displacement-based 6-parameter model, however, exactly shows this locking-effect for nonzero Poisson's ratio. Therefore 7-parameter shells with either quadratic displacement ansatz in thickness direction or the application of enhanced linear strain components according to the aforementioned EAS method are most frequently applied to avoid Poisson thickness locking.

5.4.6 Summary locking

In Section 5.4, the most prominent locking effects that may show up for the displacement-based isogeometric shell finite elements of this thesis have been investigated separately,

focusing on geometric locking in particular.

The numerical experiments revealed that transverse shear locking for the hierarchic shell elements of this thesis (5p-hier., 7p-hier.) is avoided by construction, which is, however, not the case for isogeometric structural finite element formulations in general. Investigations of the Timoshenko beam problem subjected to bending in Section 5.4.2 demonstrated that higher-order NURBS discretizations alleviate locking, such that, from a practical point of view, its influence becomes negligible; the phenomena are, however, not removed.

The pinched ring example of Section 5.3.1 demonstrated for the 3-parameter shell elements that the in-plane part of the hierarchic family of isogeometric shell elements with pure displacement ansatz is, in general, sensitive to locking in situations with constraints.

The behavior with regard to membrane locking was investigated separately for the model problem of a cylindrical shell strip subjected to pure bending. Significant locking of the hierarchic isogeometric shells could be determined. Even for a comparatively small slenderness, the displacement results were underestimated considerably; see Section 5.4.3.

The problem of curvature thickness locking was analyzed for the same problem setup, however, with a different type of loading for several 7-parameter NURBS shell elements. It turned out that the hierarchic 7-parameter shell model does not show any curvature thickness locking due to the hierarchic imposition of the difference vector. The comparison to a standard difference vector model exactly demonstrated this effect, as shown in Section 5.4.4.

In the subsequent chapter, therefore, two methods are presented to remove these locking effects for the higher-order and higher-continuity isogeometric shell elements of this thesis.

<div style="text-align: right; font-size: 3em; font-weight: bold">6</div>

Locking-free Hierarchic Shell Element Formulations

The numerical investigations of the isogeometric shell finite elements with pure displacement formulation in Chapter 5 revealed that the in-plane part of all elements is significantly prone to locking. Whereas for the hierarchic parametrizations (5p-hier., 7p-hier.) no additional geometric locking effects show up, the non-hierarchic shell elements (5p-stand., 7p-stand.) are sensitive to both transverse shear locking and curvature thickness locking. In this chapter, two methods are derived to remove the in-plane locking effects for the higher-order and higher-continuity NURBS shell elements: a NURBS-DSG ansatz and a mixed displacement-stress ($\mathbf{u}$-$\boldsymbol{\sigma}$) formulation, which is based on the Hellinger-Reissner variational principle of Section 2.5.2. Additionally, alternative strategies, which are frequently used in standard C^0-continuous FEA to avoid locking, are briefly discussed. Their practicability for higher-order and higher-continuity NURBS discretizations are investigated.

6.1 NURBS-DSG method

Originally, the "Discrete Shear Gap" (DSG) method was developed by Bletzinger and coworkers to remove transverse shear locking in beam, triangular and quadrilateral plate and shell finite elements with C^0-continuous Lagrange discretizations (BLETZINGER ET AL. (2000)). In KOSCHNICK ET AL. (2005) a generalization to solid finite elements was presented, which is able to avoid all geometric locking effects, rephrasing DSG as the "Discrete Strain Gap" method.

Therein, the strain distributions from a pure displacement formulation are modified to

explicitly satisfy the kinematic equations at discrete locations in the element. Thus, the DSG procedure has similarities to assumed natural strain (ANS) approaches (HUGHES AND TEZDUYAR (1981), BATHE AND DVORKIN (1985)). Both formulations evaluate discrete quantities at predefined collocation points that are subsequently interpolated within the element domain to remove parasitic contributions. No additional internal parameters or degrees of freedom are used. As both the DSG and the ANS method only modify the strain-displacement matrix $\mathbf{B}$, they are frequently denoted as "B-bar" methods (HUGHES (2000)) in literature.

The variational basis of the ANS approach was first derived in SIMO AND HUGHES (1986) based on the three-field Hu-Washizu functional (HU (1955), WASHIZU (1955)). A complete and consistent variational foundation of the DSG method, however, is still missing, to the author's best knowledge.

The conceptional simplicity and special quality of the DSG procedure, compared to ANS-type methods, is the unique location of the collocation points for the evaluation of the discrete strain values, which are always the nodes of an element independent of its shape and polynomial order. For ANS elements, on the contrary, the choice of sampling point locations and interpolation functions depends on the element type, the polynomial order and the strain components to be modified.

6.1.1 Effect of continuity on 1D NURBS-DSG approach

In this section, the influence of the continuity of NURBS functions on the derivation of locking-free NURBS-DSG element formulations will be investigated, which, for demonstration purpose, is defined for one-dimensional, straight Timoshenko beam problems.

NURBS C^0-continuous DSG procedure

First, the Timoshenko beam of Figure 5.10 which is subjected to a sinusoidal moment loading is investigated. By using higher-order, but C^0-continuous NURBS discretizations, the principle outline of the DSG method according to BLETZINGER ET AL. (2000) will be demonstrated. The problem data coincides with the example of Section 5.4.2. For the subsequent evaluations, a constant thickness of $t = 1.0$ is assumed.

The beam is discretized with three elements and quadratic, C^0-continuous B-spline basis functions, which are built from the knot vector $\mathbf{\Xi} = \left\{0, 0, 0, \frac{1}{3}, \frac{1}{3}, \frac{2}{3}, \frac{2}{3}, 1, 1, 1\right\}$ as displayed in Figure 6.1.

The linear kinematic equations for the continuous Timoshenko beam in terms of the cross sectional rotations φ and the slope of the beam axis u'_y are defined in Equation (5.15). Equal-order interpolation of both the displacements and rotations in the discrete model yields the mismatch of function spaces in the kinematic equation for the transverse
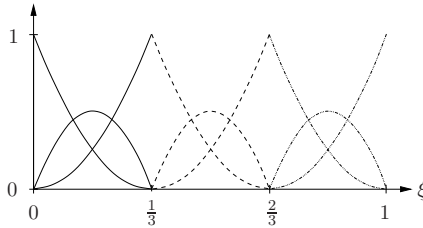
Figure 6.1: C^0-continuous B-spline basis $\mathbf{B}_2$, three elements.

shear. In this example, this results in higher-order (quadratic) terms of the rotations that cannot be balanced by the displacements due to the existence of first derivatives. Figure 6.2 shows the distribution of the parasitic, second-order transverse shear strains $\gamma_{\mathrm{par.}}^{\mathrm{h}}$ in the parametric domain $\tilde{\Omega}_{\mathrm{pa}}$, which, for the C^0 B-spline basis, are obviously discontinuous across element boundaries. The roots of the parasitic shear strains, which are marked with red boxes, are exactly at the Barlow points (BARLOW (1976)) of every element independent of the external load. This fact is known from standard FEA with C^0-continuity Lagrange shape functions.
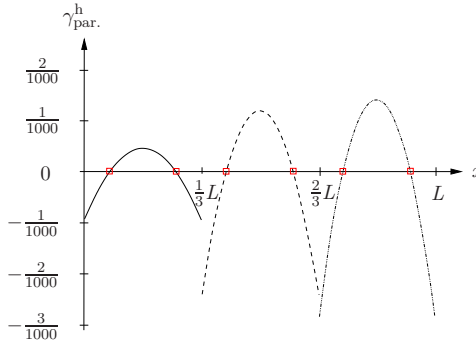
Figure 6.2: Timoshenko beam – parasitic transverse shear strains $\gamma_{\mathrm{par.}}^{\mathrm{h}}$.

By reordering Equation $(5.15)_2$ and subsequent integration, the displacement field u_y can be obtained as the sum of shear and bending deformations. In Equation (6.1), the displacements related to transverse shear are defined as

$$u_y^\gamma(x) = \int\limits_0^x \gamma(x)\,\mathrm{d}x\,. \tag{6.1}$$

115

The shear gap functions $u_y^{\gamma^{\mathrm{h}}}(x)$ for the beam model with quadratic NURBS discretization are displayed in Figure 6.3. They are, in general, nonzero within the element domain, but possess several roots, which are displayed with blue dots.
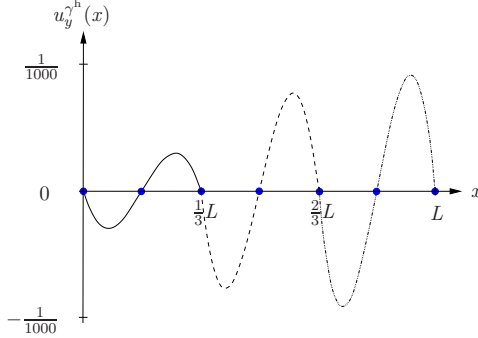

Figure 6.3: Timoshenko beam – shear gap functions $u_y^{\gamma^{\mathrm{h}}}(x)$.

Whereas for the Lagrange-DSG approach, the collocation points for computing the discrete shear gap values as the integral of the shear gap functions are always the nodes of an element, for the NURBS-DSG method, the Greville points (Gp) of the parametric domain have to be used. The Greville points (SCHOENBERG (1967)), which are also called Marsden-Schoenberg points (MARSDEN AND SCHOENBERG (1966)), are computed from the knot vector data according to Equation (6.2) for the one-dimensional case, with p denoting the polynomial degree of the NURBS basis functions

$$\xi_i^{\mathrm{Gp}} = \frac{\sum_{k=1}^{p} \xi_{i+k}}{p} \, . \tag{6.2}$$

With the discrete shear gap values at hand, the Lagrange-DSG procedure enables a direct computation of a modified shear gap function $\overline{u}_y^{\gamma^{\mathrm{h}}}(x)$, which is free from any parasitic shear by linearly interpolating the discrete nodal shear gaps with the standard element shape functions. Subsequent partial differentiation yields the new, locking-free transverse shear strains $\gamma^{\mathrm{h,\,DSG}}(x)$. Finally, a modified DSG strain-displacement matrix can be derived that is identical for all elements of the discrete domain. It may, therefore, be computed analytically in advance and thus would not negatively affect the computational runtime efficiency.

The application of C^0-continuous NURBS functions for the discretization of the displacement field results in discontinuous transverse shear strain distributions. Therefore, an element-by-element DSG approach can be carried out in the same way as for the Lagrange discretizations. The non-interpolatory property of NURBS basis functions

requires the determination of those coefficients that interpolate the discrete shear gaps at the collocation points. Therefore, in addition, a linear system of equations has to be solved which takes into account all nonzero NURBS basis functions at sampling points before the modified shear gap function can be defined (ECHTER AND BISCHOFF (2010)). The Lagrange-DSG method for plates and shells follows the same principal procedure of integration, collocation, interpolation and differentiation. The tensorial strain components are usually formulated in the parametric coordinates θ^α or ξ and η respectively, and the DSG values are computed for each coordinate direction separately.

More detailed information about applying the DSG method to structural and solid finite elements with Lagrange discretizations is provided, among others, in BISCHOFF (1999), BLETZINGER ET AL. (2000), BISCHOFF AND BLETZINGER (2001), KOSCHNICK (2004) and KOSCHNICK ET AL. (2005).

Higher-continuous NURBS-DSG ansatz

The procedure of deriving NURBS-based DSG finite elements with C^0-continuous basis, with the exception of solving an additional linear system of equations to obtain the interpolatory shear gaps, follows the conventional method known from Lagrange discretizations and can be performed on element level. Computational efficiency can therefore be preserved and the fill-in of the global stiffness matrix $\mathbf{K}^g_{\mathrm{DSG}}$ remains sparse. As shown in Figures 3.4, 3.6 or 3.8, higher-continuity NURBS may have different coefficients of element basis functions on every knot span and additionally varying inter-element continuity, which depend on the regularity of the associated knot vectors. This may lead to derived quantities, such as strains and stresses, that are again continuous within a patch. Their shapes may be different for every element, which is in clear contrast to the conventional C^0-continuous discretizations.

The strain integration procedure for computing the discrete shear gaps of the DSG approach consequently has to be carried out on patch level, rather than on element level (ECHTER AND BISCHOFF (2010)). The application of an element-by-element DSG method completely fails for higher-continuous NURBS basis functions. In addition, the roots of the parasitic shear strains are no longer the Barlow points.

The formal framework of integration, collocation, solution of a linear system of equations, interpolation and differentiation as described for C^0-continuous NURBS remains identical for higher-continuity NURBS. Due to continuous strain distributions across inter-element boundaries, however, the element DSG solution may depend on degrees of freedom of the entire patch domain and therefore compromise computational efficiency. Propagation of information throughout the patch is primarily related to the higher continuity of the NURBS shape functions, rather than the structure of the DSG method.

This effect has already been reported in ELGUEDJ ET AL. (2008) in the context of projection methods for material incompressibility with higher-order and higher-continuity NURBS discretizations in IGA.

An improved accuracy of discrete solutions with higher-continuous NURBS functions was described in Section 5.3.1. This can again be determined for the NURBS-DSG method. Whereas the C^0-continuous NURBS-DSG procedure with shape functions of order p represents an interpolation of $p + 1$ exact solution, higher-continuity NURBS-DSG formulations yield a least square fit of the $p + 1$ exact solution and thus ensure optimal convergence properties (ECHTER AND BISCHOFF (2010)).

An explanation of the coupling phenomenon can be provided by the kinematic linked interpolation method, which was originally developed in the context of shear deformable Reissner-Mindlin plate elements. The main idea consists of introducing additional "linked" shape functions, which are used to enrich the transverse displacement field by means of rotational degrees of freedom (ZIENKIEWICZ ET AL. (1993), TAYLOR AND AURICCHIO (1993), AURICCHIO AND LOVADINA (2001)).

The derivation of the aforementioned linked shape functions $\hat{\mathbf{B}}_3(\xi)$ will be demonstrated for a straight Timoshenko beam that is discretized with four elements of second order and C^1-continuity. The corresponding knot vector is $\mathbf{\Xi} = \left\{ 0, 0, 0, \frac{1}{4}, \frac{2}{4}, \frac{3}{4}, 1, 1, 1 \right\}$ and ultimately yields in six basis functions.

Starting from the locking-free NURBS-DSG transverse shear strains

$$\gamma^{\mathrm{h, DSG}}(x) = u_{y,\,x}^{\mathrm{h, DSG}}(x) + \varphi^{\mathrm{h}}(x) \tag{6.3}$$

the modified displacement field can be recovered by integration and reordering of the kinematic equation.

$$u_y^{\mathrm{h, DSG}}(x) = \int\limits_x \left(\gamma^{\mathrm{h, DSG}}(x) - \varphi^{\mathrm{h}}(x) \right) \, \mathrm{d}x + C_1 \,. \tag{6.4}$$

The integration constant C_1 can be determined by the condition $u_y^{\mathrm{h, DSG}}(0) = u_y^1$ and consequently gives $C_1 = u_y^1$.

The linked shape functions, which are related to the rotational degrees of freedom φ^i, can be ultimately obtained from the DSG displacement field $u_y^{\mathrm{h, DSG}}(x)$. They are of cubic order due to the integration of the rotation field according to Equation (6.4). The displacement distribution $u_y^{\mathrm{h, DSG}}(x)$ reads

$$u_y^{\mathrm{h, DSG}}(x) = \sum_{i=1}^{6} \left(B_{i,2}(\xi) \, u_y^i + \hat{B}_{i,3}(\xi) \, \varphi^i \right), \tag{6.5}$$

where $\mathbf{B}_2(\xi)$ are the standard six quadratic NURBS shape functions with *local* support and $\hat{\mathbf{B}}_3(\xi)$ represent the six linked shape functions, which possess *global* support in the entire patch domain, as shown in Figure 6.4.
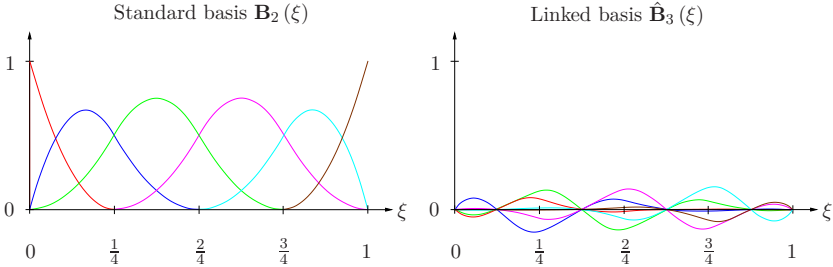
Figure 6.4: Timoshenko beam – standard and linked shape functions.
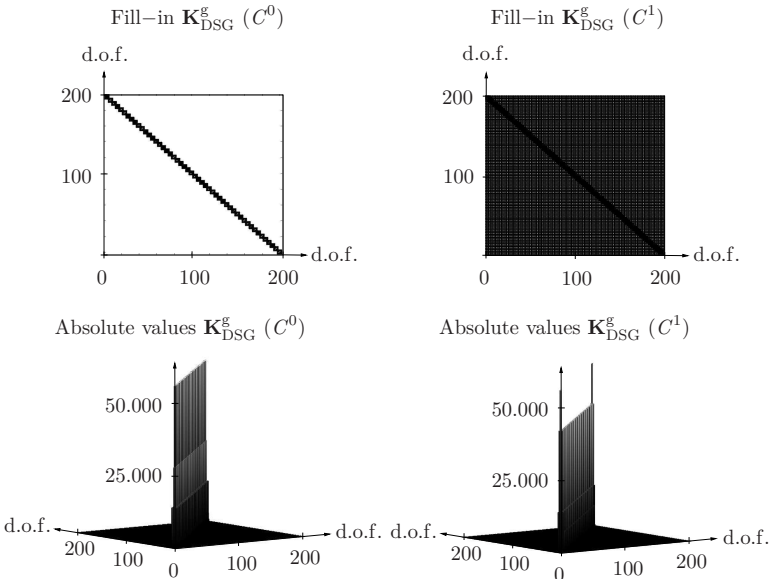

Figure 6.5: Timoshenko beam – $\mathbf{K}_{\mathrm{DSG}}^{\mathrm{g}}$, C^0- vs. C^1-continuity.

Figure 6.5 compares the fill-in and the absolute values of the DSG system stiffness matrices on a degree of freedom basis for a straight Timoshenko beam problem with both a C^0- and C^1-continuous NURBS discretization of second order. Both discrete models

consist of 202 degrees of freedom. Nonzero values are displayed in black and zero stiffness values in white color.

The two pictures on the left side refer to the C^0-model. On the right, the results of the C^1-DSG approach are illustrated. With respect to the fill-in, clearly the aforementioned difference of both NURBS-DSG versions can be ascertained. The band width on the main diagonal, with stiffness values significantly larger than zero, is of identical size for both models. Whereas the off-diagonal terms of the C^0-approach are exactly zero, the ones of the continuous DSG stiffness matrix are small but nonzero.

The element stiffness matrix $\mathbf{K}^e_{\mathrm{DSG}}$ consequently becomes a dense matrix with dimensions being equal to the global stiffness matrix $\mathbf{K}^g_{\mathrm{DSG}}$. Simple, and at first sight intuitive, engineering approaches to recover the band structure with zero off-diagonals of the fully populated C^1-DSG stiffness matrix completely failed. Neither the ansatz of performing some kind of "stiffness lumping" of the off-diagonal terms on the main diagonal, accounting for momentum balance nor the neglection of the almost zero off-diagonal values were successful. So far, no consistent procedure is known to the author to resolve this issue.

In order to cope with the extensive memory requirements of higher-continuity NURBS-DSG approaches, an iterative solution procedure with the conjugate gradient (CG) method has been successfully implemented. It is, however, restricted to beam problems up to now. Details of the CG method will not be explained herein. For more information, the reader is referred to DEUFLHARD AND HOHMANN (2008), for instance. Instead of computing the entire element stiffness matrix $\mathbf{K}^e_{\mathrm{DSG}}$ with both row and column dimensions being equal to $\mathbf{K}^g_{\mathrm{DSG}}$, only the material matrix and element strain-displacement matrix $\mathbf{B}^e_{\mathrm{DSG}}$ are computed. The row dimension of $\mathbf{B}^e_{\mathrm{DSG}}$ is equal to the number of strain components and thus significantly smaller than the one of $\mathbf{K}^e_{\mathrm{DSG}}$. By reversing the order of multiplications, an internal force vector is computed instead of a stiffness matrix expression. Therefore, $\mathbf{B}^e_{\mathrm{DSG}}$ is first multiplied with an initial guess of the solution vector $\mathbf{x}_0$. Afterwards, this intermediate result is multiplied with the material matrix and finally the outcome is multiplied with the transpose of $\mathbf{B}^e_{\mathrm{DSG}}$. The displacements and stress resultants obtained with the conjugate gradient DSG approach are identical to the higher-continuous NURBS-DSG ansatz with computation of an element stiffness matrix $\mathbf{K}^e_{\mathrm{DSG}}$.

For very slender beam structures, however, the convergence properties of the iterative solution procedure are badly influenced by the very large condition number of the system stiffness matrix. This phenomenon will also be of significant importance for thin shell analysis (GEE (2004)). The topic of preconditioning and the application of the iterative CG procedure to higher-continuity NURBS-DSG shell problems have not been investigated so far, but may significantly improve the performance of the method.

6.1.2 Isogeometric NURBS-DSG shell elements

The results of Section 6.1.1 revealed both positive and negative aspects of the higher-continuity NURBS-DSG approach for one-dimensional beam problems. The positive effect of locking-free finite elements with optimal convergence properties independent of the structure of the knot vector, i.e. continuity and polynomial order of the shape functions, is compromised by coupling of degrees of freedom, which may result in fully populated stiffness matrices and thus badly affect computational efficiency.

In this section, the equations for modifying the in-plane part of the shell models of Sections 4.3 to 4.5 with the NURBS-DSG method are defined. They are used to remove both membrane and in-plane shear locking, which were observed for the pure displacement formulations in Chapter 5. Therefore, the conclusions obtained from the higher-continuity NURBS-DSG ansatz of Section 6.1.1 are adapted to the original version presented in KOSCHNICK ET AL. (2002), BISCHOFF ET AL. (2003) and KOSCHNICK ET AL. (2005), which was derived to remove all geometric locking effects in standard C^0-continuous structural and continuum finite elements.

The computation of the modified DSG in-plane strain components $\varepsilon_{\alpha\beta}^{\mathrm{h,DSG}}$ from the displacement-based strain components $\varepsilon_{\alpha\beta}^{\mathrm{h}}$ is performed in the parametric domain and is valid for all isogeometric higher-order and higher-continuity shell elements of this thesis. The index n in Equation (6.6) represents the number of element shape functions

$$
\begin{aligned}
\varepsilon_{11}^{\mathrm{h,DSG}} &= \sum_{i=1}^{n} N_{,\xi}^{i} \int_{\xi_0}^{\xi_i^{\mathrm{Gp}}} \varepsilon_{11}^{\mathrm{h}} \,\mathrm{d}\xi\,, \\
\varepsilon_{22}^{\mathrm{h,DSG}} &= \sum_{i=1}^{n} N_{,\eta}^{i} \int_{\eta_0}^{\eta_i^{\mathrm{Gp}}} \varepsilon_{22}^{\mathrm{h}} \,\mathrm{d}\eta\,, \\
\varepsilon_{12}^{\mathrm{h,DSG}} &= \sum_{i=1}^{n} N_{,\xi}^{i} \int_{\xi_0}^{\xi_i^{\mathrm{Gp}}} \left(\sum_{j=1}^{n} N_{,\eta}^{j} \int_{\eta_0}^{\eta_j^{\mathrm{Gp}}} \varepsilon_{12}^{\mathrm{h}} \,\mathrm{d}\eta \right) \,\mathrm{d}\xi\,.
\end{aligned}
\tag{6.6}
$$

The formal procedure of Equation (6.6) consists of individually integrating and collocating the strain components $\varepsilon_{\alpha\beta}^{\mathrm{h}}$ at the Greville points, followed by interpolation and differentiation in order to obtain the modified locking-free strain distributions $\varepsilon_{\alpha\beta}^{\mathrm{h,DSG}}$.

Continuous strains within the patch domain require an integration over several knot spans. Therefore, the entire strain integral to a specific Greville point location ξ_i^{Gp} or η_i^{Gp} is composed of the sum of several element strain integrals up to the respective Greville point position. For the in-plane shear part, the aforementioned calculation steps have to be performed in both parametric directions, which ultimately yields a nested

ansatz.

For further details on the computation of the modified DSG strain components of two-dimensional continuum elements or the membrane part of the isogeometric shells of this thesis, the reader is referred to the diploma theses of MAIER (2009) and OESTERLE (2011) in addition to the literature mentioned before.

6.1.3 Numerical example – cylindrical shell strip (DSG)

In this section, the quality of the modified isogeometric NURBS shell formulations will be investigated for the cylindrical shell strip with a constant transverse line load $\hat{q}_x$ analyzed before in Section 5.4.4.

In Figure 6.6, the effect of varying slenderness $\frac{R}{t}$ on the discrete displacement results $u_{x_\mathrm{P}}^\mathrm{h}$ of shear-rigid Kirchhoff-Love shell models is analyzed. The analytical beam solution is compared to the results of both a pure displacement formulation (3p) and the DSG ansatz (3p-DSG) with modified membrane strain components $\varepsilon_{\alpha\beta}^{\mathrm{3p,\,h,\,DSG}}$. Whereas the "3p" NURBS model shows significant membrane locking as already determined in Section 5.4.3, the results of the "3p-DSG" shell element are completely free from spurious membrane strains, independent of the slenderness, and thus represent a locking-free shell formulation.
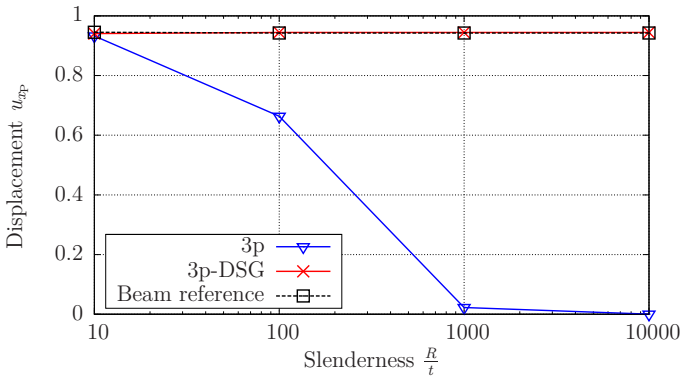
Figure 6.6: Cylindrical shell – displacement convergence, 3p shells, DSG.

In addition to the Kirchhoff-Love shell formulations, in Figure 6.7, several shear deformable 5-parameter Reissner-Mindlin shell elements are compared to the reference solution and among each other for the given problem setup. For the standard shell formulation (5p-stand.) of Section 4.4.1 with a difference vector imposed on the undeformed normal, both transverse shear and membrane locking effects are assumed. The

hierarchic difference vector model (5p-hier.) of Section 4.4.2 is free from parasitic transverse shear effects, but is prone to membrane locking in the same way as determined for the Kirchhoff-Love (3p) model in Figure 6.6. In addition, the DSG versions of the two aforementioned 5-parameter shell models are examined, which are denoted as "5p-stand.-DSG" and "5p-hier.-DSG".

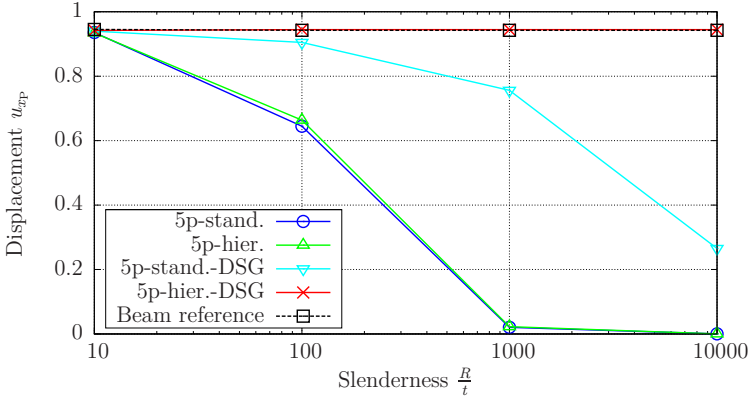**Figure 6.7:** Cylindrical shell – displacement convergence, 5p shells, DSG.

Figure 6.7 numerically confirms the previous assumptions. The shell element with standard difference vector (5p-stand.) shows the worst behavior as both unphysical transverse shear and membrane normal stresses deteriorate the accuracy. Looking at the DSG version of the standard model (5p-stand.-DSG), it turns out that for this example, removal of unphysical membrane contributions produces significantly better results than removal of transverse shear locking with the "5p-hier." shell. Nonetheless, "5p-stand.-DSG" still exhibits transverse shear locking, which becomes particularly pronounced for a slenderness of $\frac{R}{t} > 1000$. The small difference between "5p-stand." and "5p-hier." results from the predominant influence of membrane locking so that the additional effect of transverse shear does not become as obvious if both locking effects show up simultaneously. Finally, the performance of the hierarchic isogeometric NURBS shell element with DSG modification (5p-hier.-DSG) is evaluated. The formulation is completely free from geometric locking and matches the reference beam solution very well, independent of the chosen slenderness. The DSG approach of Section 6.1.2, therefore, successfully removes the undesired parasitic strain contributions for the case of higher-order and higher-continuity NURBS shell discretizations.

In Table 6.1, the numerical displacement results of the entire family of NURBS shell element formulations with DSG modification of the in-plane strain components are dis-

played. In addition to the 3- and 5-parameter models, the three-dimensional 7-parameter shells with DSG ansatz (7p-stand.-DSG, 7p-hier.-DSG) are also shown. Whereas "7p-hier.-DSG" is again completely locking-free, the "7p-stand.-DSG" shell element is prone to both transverse shear and curvature thickness locking, which was already investigated in Section 5.4.4. The effect of curvature thickness locking on the standard difference vector formulation can also be determined in Table 6.1 if the results of the "5p-stand.-DSG" shell element are compared to the "7p-stand.-DSG" version particularly for a large slenderness $\frac{R}{t}$.

Slenderness $\frac{R}{t}$	10	100	1000	10000
Shell formulation (2nd order NURBS)				
3p-DSG	0.9406	0.9444	0.9445	0.9445
5p-stand.-DSG	0.9396	0.9048	0.7560	0.2652
5p-hier.-DSG	0.9422	0.9445	0.9445	0.9445
7p-stand.-DSG	0.9403	0.9031	0.7158	0.0895
7p-hier.-DSG	0.9445	0.9445	0.9445	0.9445
Analytic result				
Beam reference	0.9451	0.9425	0.9425	0.9425

Table 6.1: Cylindrical shell – displacements u_{x_P}, overview of shell formulations, DSG.

So far, only the dependency of the discrete radial displacement $u_{x_\mathrm{P}}^\mathrm{h}$ on the slenderness of the structure $\frac{R}{t}$ has been analyzed for the cylindrical shell example. Therefore, in the following, the quality of the stress resultant bending moment $m_{\overline{xx}}$ will also be investigated for the 5-parameter Reissner-Mindlin shell element formulations studied before in Figure 6.7.

A fixed slenderness of $\frac{R}{t} = 1000$ is selected, for which several shell models, according to Figure 6.7, already exhibit significant locking in the investigated discrete displacements. For the computation of the bending moment $m_{\overline{xx}}$, a local Cartesian coordinate system is defined along the path P-Q as displayed in Figure 5.16, with the $\overline{x}$- and $\overline{z}$-axes to be tangential to the parametric θ^1- and θ^3-directions, respectively. The curvilinear stress components σ^{kl} are transformed into the local Cartesian basis $\overline{\mathbf{e}}_i$ according to Equation (5.11).

With the local Cartesian stress components $\sigma^{\overline{xx}}$ at the two Gauss points in ζ-direction, a linearly varying distribution of in-plane normal stresses through the thickness of the shell body is defined, which is subsequently multiplied with the thickness coordinate and then integrated in θ^3-direction of the shell.

In Figure 6.8, the bending moment $m_{\overline{xx}}$, which was computed from the linear part of the in-plane normal stresses, is plotted along the path P-Q. The results confirm the observations and conclusions made for the numerical displacement evaluations.

Both the standard and the hierarchic pure displacement models are very sensitive to locking for the defined slenderness. The bending moments $m_{\overline{xx}}$ are approximately zero along
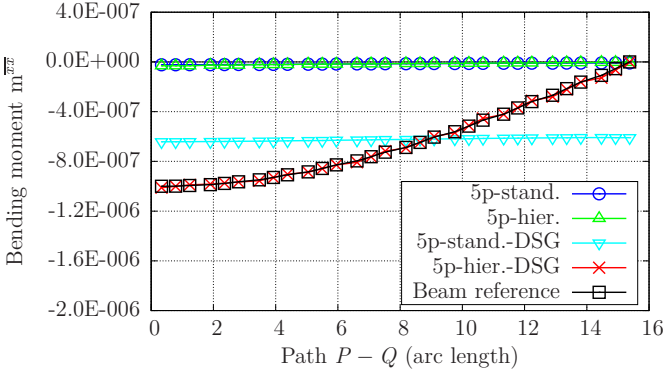
Figure 6.8: Cylindrical shell – bending moments $m_{\overline{xx}}$, 5p shells, DSG.

the entire path P-Q. A modification of the membrane strains with the DSG method generates significantly better results in the standard model (5p-stand.-DSG), which again reveals that the dominant locking phenomenon in this numerical test example is membrane locking. Still, however, transverse shear locking compromises the solution quality. As for the discrete displacement tests, the bending moment of "5p-hier.-DSG" again conforms very well with the beam reference solution derived in Figure 5.17.

In this section, the DSG approach of BLETZINGER ET AL. (2000) was successfully transferred to higher-order and higher-continuity NURBS discretizations in order to remove membrane and in-plane shear locking. The higher continuity of the NURBS basis functions may, however, result in a coupling of degrees of freedom, which compromises the computational efficiency. For the 3-parameter and the hierarchic isogeometric shell elements of this thesis, only the membrane part of the strains has to be modified to provide element formulations, which are completely free from geometric locking.

6.2 Displacement-stress (u-σ) mixed approach

Herein, an alternative to the NURBS-DSG method of Section 6.1 for higher-continuity NURBS is introduced, which is based on the two-field Hellinger-Reissner variational principle of Section 2.5.2 with an independent displacement field **u** and stress field **σ**. This mixed approach was first applied to the hierarchic family of NURBS-based shell finite elements in ECHTER ET AL. (2013) to remove all geometric locking effects from the in-plane strain components.

The first improvements of pure displacement-based finite elements with assumed stress

fields date back to the mid-sixties of the last century with the pioneering work of PIAN (1964) based on the principle of minimum complementary energy. Early hybrid stress element formulations on the basis of the Hellinger-Reissner principle are mainly associated with the works of PIAN AND CHEN (1982) and PIAN AND SUMIHARA (1984). The main idea therein consists of introducing optimal stress patterns on the element level, which, together with the strain modes from a pure displacement ansatz, avoid undesired energy contributions.

The class of hybrid-mixed methods with C^0-continuous discretizations of the primary variables utilize additional internal degrees of freedom, which, for a displacement-stress mixed approach, are the stress parameters that do not have to satisfy the continuity requirements on element boundaries. These parameters may therefore be eliminated on element level by static condensation such that the structure of the element stiffness matrix does not differ from a pure displacement formulation and consequently enables the application of conventional solution procedures.

As already determined for the higher-continuity NURBS-DSG approach of Section 6.1, continuous stress and strain fields do not allow for a direct use of unlocking methods designed for C^0-continuous discretizations to functions with higher continuity, but require a treatment on patch level.

6.2.1 Discrete weak form of Hellinger-Reissner principle

In order to obtain a discrete weak form of the Hellinger-Reissner variational principle, which was introduced in Section 2.5.2, rational bivariate NURBS functions for approximating both the unknown displacement and stress fields are used.

The discretization of the free variables $\mathbf{u}$ and $\boldsymbol{\sigma}$ and their variations $\delta\mathbf{u}$ and $\delta\boldsymbol{\sigma}$, respectively, is defined in Equation (6.7). The index $(\bullet)^{\mathrm{h}}$ in the subsequent derivations is again related to the discrete representation of the continuous fields

$$
\begin{aligned}
\mathbf{u} &\approx \mathbf{u}^{\mathrm{h}} &&= \mathbf{N}_{p,q} \cdot \mathbf{d}\,, \\
\delta\mathbf{u} &\approx \delta\mathbf{u}^{\mathrm{h}} &&= \mathbf{N}_{p,q} \cdot \delta\mathbf{d}\,, \\
\boldsymbol{\sigma} &\approx \boldsymbol{\sigma}^{\mathrm{h}} &&= \mathbf{M}_{r,s} \cdot \boldsymbol{\omega}\,, \\
\delta\boldsymbol{\sigma} &\approx \delta\boldsymbol{\sigma}^{\mathrm{h}} &&= \mathbf{M}_{r,s} \cdot \delta\boldsymbol{\omega}\,.
\end{aligned}
\tag{6.7}
$$

$\mathbf{N}_{p,q}$ are the bivariate NURBS basis functions according to Equation (3.9) with polynomial orders p and q in the parametric directions ξ and η. They are used to approximate the displacement field. $\mathbf{M}_{r,s}$ represent the NURBS basis functions for the discretization of the membrane stress fields. They are specified in Section 6.2.3. The vector $\mathbf{d}$ contains the control point displacement degrees of freedom and $\boldsymbol{\omega}$ comprises the discrete stress parameters. In order to transform the stress components between the natural coordi-

nate system and global Cartesian reference system, the transformation matrix $\mathbf{T}$ is used. Additionally, the displacement gradient grad $\mathbf{u}$ and its variation grad $\delta\mathbf{u}$ are replaced by the strain-displacement matrix $\mathbf{B}$ and the vector of control point displacements $\mathbf{d}$ and its variation $\delta\mathbf{d}$ in the discrete weak form, according to Equation (6.8)

$$
\begin{aligned}
\delta\Pi_{\mathrm{HR}}^{\mathrm{h}} = \ & -\int_{\Omega^{\mathrm{h}}} \delta\mathbf{d}^{\mathrm{T}} \cdot \mathbf{B}^{\mathrm{T}} \cdot \mathbf{T}^{\mathrm{T}} \cdot \mathbf{M}_{r,s} \cdot \boldsymbol{\omega}\,\mathrm{d}\Omega^{\mathrm{h}} + \int_{\Omega^{\mathrm{h}}} \delta\mathbf{d}^{\mathrm{T}} \cdot \mathbf{N}_{p,q}^{\mathrm{T}} \cdot \overline{\mathbf{b}}\,\mathrm{d}\Omega^{\mathrm{h}} \\
& + \int_{\Omega^{\mathrm{h}}} \delta\boldsymbol{\omega}^{\mathrm{T}} \cdot \mathbf{M}_{r,s}^{\mathrm{T}} \cdot \mathbb{C}^{-1} \cdot \mathbf{T}^{\mathrm{T}} \cdot \mathbf{M}_{r,s} \cdot \boldsymbol{\omega}\,\mathrm{d}\Omega^{\mathrm{h}} - \int_{\Omega^{\mathrm{h}}} \delta\boldsymbol{\omega}^{\mathrm{T}} \cdot \mathbf{M}_{r,s}^{\mathrm{T}} \cdot \mathbf{T} \cdot \mathbf{B} \cdot \mathbf{d}\,\mathrm{d}\Omega^{\mathrm{h}} \\
& + \int_{\partial\Omega_\sigma^{\mathrm{h}}} \delta\mathbf{d}^{\mathrm{T}} \cdot \mathbf{N}_{p,q}^{\mathrm{T}} \cdot \overline{\mathbf{t}}\,\partial\Omega_\sigma^{\mathrm{h}} = 0\,.
\end{aligned}
$$

(6.8)

The displacement boundary term of the continuous form vanishes in Equation (6.8) as the NURBS basis functions of the displacement field interpolation are at least C^1-continuous.

6.2.2 Stress fields for C^0-continuous function spaces

The choice of appropriate function spaces for the stresses dependent on the applied displacement functions follows the principal approach of PIAN AND SUMIHARA (1984), EISELE (1989) and ANDELFINGER (1991) for standard hybrid stress formulations with C^0-continuous displacement functions and discontinuous stress fields.
First, the procedure of deriving adequate stress functions for a standard four node two-dimensional continuum finite element on basis of eigenmode investigations is briefly presented. The associated element displacement modes of ANDELFINGER (1991) are repeated in Figure 6.9.
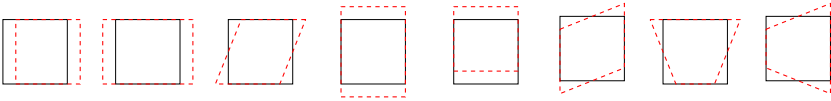
Figure 6.9: Displacement modes of a four node quadrilateral element.

An eigenvalue analysis of the 2D continuum element reveals that the formulation with bilinear ($p = q = 1$) shape functions is capable of exactly representing the three rigid body modes, the shear modes and the constant strain deformations. The two bending modes, rightmost in Figure 6.9, cannot be modeled correctly, which results in unphysical stresses that are the source of volumetric and shear locking.

The number of nonzero deformation modes for the bilinear element according to Figure 6.9 is equal to five. Consequently, the number of linearly independent stress modes also has to be equal to five. An optimal ansatz space for the stress matrix $\mathbf{M}_{1,1}(\xi, \eta)$ is provided in Equation (6.9). The rows of $\mathbf{M}_{1,1}(\xi, \eta)$ represent the trial functions for the contravariant in-plane stress components $\sigma^{\xi\xi,\,\mathrm{h}}$, $\sigma^{\eta\eta,\,\mathrm{h}}$ and $\sigma^{\xi\eta,\,\mathrm{h}}$. The vector $\boldsymbol{\omega}$ contains the stress parameters $\{\omega_1, ..., \omega_5\}$.

Compared to the complete stress space of a standard bilinear element, the highest order (linear) functions in ξ are removed from the normal stresses $\sigma^{\xi\xi,\,\mathrm{h}}$ and the linear contributions in η are eliminated from $\sigma^{\eta\eta,\,\mathrm{h}}$ in $\mathbf{M}_{1,1}(\xi, \eta)$. For the in-plane shear stresses $\sigma^{\xi\eta,\,\mathrm{h}}$, both linear terms in ξ and η are removed to get rid of locking. The element is still able to reproduce exactly the three constant stress modes and, in addition, correctly represents the two linear bending deformations without unphysical linear shear stresses or normal stresses. The invariance of $\mathbf{M}_{1,1}(\xi, \eta)$ with regard to ξ and η is satisfied, as every constant and linear strain mode has an associated work conjugate in the stresses. Increasing the number of stress parameters in Equation (6.9) reintroduces spurious parasitic stresses and thus again results in locking, whereas a reduction of stress parameters yields an unstable element formulation, which may exhibit zero energy modes.

$$
\begin{bmatrix} \sigma^{\xi\xi,\,\mathrm{h}} \\ \sigma^{\eta\eta,\,\mathrm{h}} \\ \sigma^{\xi\eta,\,\mathrm{h}} \end{bmatrix} = \underbrace{\begin{bmatrix} 1 & 0 & 0 & \eta & 0 \\ 0 & 1 & 0 & 0 & \xi \\ 0 & 0 & 1 & 0 & 0 \end{bmatrix}}_{\mathbf{M}_{1,1}(\xi,\eta)} \cdot \begin{bmatrix} \omega_1 \\ \omega_2 \\ \omega_3 \\ \omega_4 \\ \omega_5 \end{bmatrix}
\tag{6.9}
$$

With regard to the higher-order NURBS discretizations to be used in this thesis, the definition of optimal stress functions for a standard nine node two-dimensional solid element with biquadratic $(p = q = 2)$ C^0-continuous displacement field interpolation is briefly investigated. The deformation modes of this element type are given, for instance, in ANDELFINGER (1991). The stress matrix $\mathbf{M}_{2,2}(\xi, \eta)$ for the contravariant in-plane stress components reads

$$
\mathbf{M}_{2,2}(\xi, \eta) = \begin{bmatrix} 1 & 0 & 0 & \xi & \eta & \xi\eta & \eta^2 & \xi\eta^2 & 0 & 0 & 0 & 0 & 0 & 0 & 0 \\ 0 & 1 & 0 & 0 & 0 & 0 & 0 & 0 & \xi & \eta & \xi\eta & \xi^2 & \xi^2\eta & 0 & 0 \\ 0 & 0 & 1 & 0 & 0 & 0 & 0 & 0 & 0 & 0 & 0 & 0 & 0 & \xi & \eta \end{bmatrix}.
\tag{6.10}
$$

According to the procedure described for the bilinear element, the number of nonzero deformation modes for the biquadratic element is equal to fifteen, which consequently

yields the number of required linearly independent stress modes. For the stress components $\sigma^{\xi\xi,\mathrm{h}}$ and $\sigma^{\eta\eta,\mathrm{h}}$, again the highest order, i.e. the quadratic terms in ξ and η are omitted. For the in-plane stresses $\sigma^{\xi\eta,\mathrm{h}}$, a linear ansatz is established to avoid locking. Optimal stress matrices for both continuum and shell finite elements with C^0-continuous basis functions as well as further details on hybrid mixed methods are provided by the references cited throughout this section.

6.2.3 Stress fields for higher-continuous NURBS function spaces

The geometry and displacement field interpolations of the shell models of Sections 4.3 to 4.5 are based on at least C^1-continuous NURBS and thus yield continuous strain and stress distributions within the patch domain. The element-by-element approach of Section 6.2.2 can therefore not be pursued without additional considerations.

The choice of appropriate NURBS function spaces for the in-plane stress components of the isogeometric shell elements of this thesis, which depend on the functions to be used for the displacements, shows up, among others, in ELGUEDJ ET AL. (2008). Therein, strain projection methods are applied to incompressible or nearly incompressible material elasticity and plasticity by using higher-order and higher-continuity NURBS discretizations defined on patch level. ELGUEDJ ET AL. (2008) suggest that the projected, possibly continuous volumetric strain fields be one order and one level of continuity lower than the spaces of the displacements, except in cases of C^0-continuity, which remain C^0-continuous. C^0-continuity is, however, not allowed for the displacement field approximation of the hierarchic shell formulations in this thesis. According to Elguedj et al., the accurate and robust numerical results legitimate their procedure, which does not satisfy the LBB-condition (Equation (2.38)) required for proving stability and optimal convergence of the mixed finite element formulation.

In the following example, the definition of adequate NURBS displacement and stress function spaces for the mixed $\mathbf{u}$-$\boldsymbol{\sigma}$ approach defined on patch level is explained for the spherical shell segment of Figure 3.14 with three elements in both circumferential and meridian direction.

The curved structure requires at least quadratic NURBS functions for both the ξ- and η-direction, which, according to the isogeometric concept, are also used for the displacement field. The knot vectors are therefore $\boldsymbol{\Xi}^{p=2} = \left\{0,0,0,\frac{1}{3},\frac{2}{3},1,1,1\right\}$ and $\mathbf{H}^{q=2} = \left\{0,0,0,\frac{1}{3},\frac{2}{3},1,1,1\right\}$. The second order univariate basis functions of both parametric directions $\{B_{i,2}(\xi)\}$ and $\{C_{j,2}(\eta)\}$ are displayed in Figure 6.10. The functions for the stress components are defined to be one order and one continuity level lower than the displacement functions and thus correspond to linear univariate NURBS derived from the knot vectors $\boldsymbol{\Xi}^{p=1} = \left\{0,0,\frac{1}{3},\frac{2}{3},1,1\right\}$ and $\mathbf{H}^{q=1} = \left\{0,0,\frac{1}{3},\frac{2}{3},1,1\right\}$. The linear basis functions are also plotted in Figure 6.10.

Univariate quadratic C^1 NURBS basis $\{B_{i,2}(\xi)\}$ and $\{C_{j,2}(\eta)\}$:

Univariate linear C^0 NURBS basis $\{B_{i,1}(\xi)\}$ and $\{C_{j,1}(\eta)\}$:
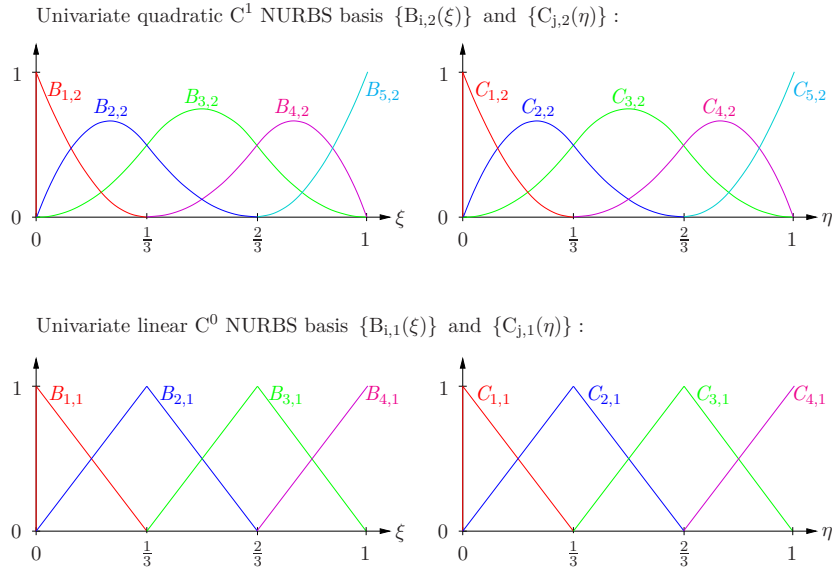

Figure 6.10: Basis functions for displacement and in-plane stress fields.

In Table 6.2, the appropriate knot vectors and univariate basis functions for the definition of the bivariate NURBS displacement and in-plane stress fields of the isogeometric shell elements are illustrated.

$\mathbf{u}^{\mathrm{h}}(\xi,\eta)$	$\mathbf{\Xi}^{p=2} \otimes \mathbf{H}^{q=2}$	$\{B_{i,2}(\xi)\} \otimes \{C_{j,2}(\eta)\}$
$\sigma^{11,\mathrm{h}}(\xi,\eta)$	$\mathbf{\Xi}^{p=1} \otimes \mathbf{H}^{q=2}$	$\{B_{i,1}(\xi)\} \otimes \{C_{j,2}(\eta)\}$
$\sigma^{22,\mathrm{h}}(\xi,\eta)$	$\mathbf{\Xi}^{p=2} \otimes \mathbf{H}^{q=1}$	$\{B_{i,2}(\xi)\} \otimes \{C_{j,1}(\eta)\}$
$\sigma^{12,\mathrm{h}}(\xi,\eta)$	$\mathbf{\Xi}^{p=1} \otimes \mathbf{H}^{q=1}$	$\{B_{i,1}(\xi)\} \otimes \{C_{j,1}(\eta)\}$

Table 6.2: Order of NURBS displacement and stress basis.

The displacement field $\mathbf{u}^{\mathrm{h}}$ adopts the biquadratic C^1-continuous NURBS functions of the geometry representation. The stress component $\sigma^{11,\mathrm{h}}$ omits the highest order, i.e. the quadratic terms in ξ-direction, which consequently yields a linear ansatz of $\sigma^{11,\mathrm{h}}$ in ξ and quadratic functions to be used for the η-direction, from which the bivariate tensor product NURBS stress functions are computed according to Equation (3.9). For $\sigma^{22,\mathrm{h}}$, the stresses are quadratic in ξ- and linear in η-direction. Finally, the contravariant in-plane stress components $\sigma^{12,\mathrm{h}}$ are defined to be linear in each direction and thus yield

a bilinear stress field in the patch domain.

Important to notice is the fact that the applied discretizations of both the displacement and in-plane stress fields utilize the same number of elements, whereas the spatial location of the control points and thus the degrees of freedom for the displacements and the individual stress fields do not coincide in general. Alternatively, a discretization with coincident location of both the displacement and stress degrees of freedom may be defined; this, however, yields different meshes for the displacement and stress fields.

6.2.4 Numerical example – cylindrical shell strip (mixed method)

The cylindrical shell with transverse line load $\hat{q}_x$, which was investigated first in Section 5.4.4, is again analyzed for the NURBS shell elements of this thesis, however, with modification of the membrane part according to the mixed ansatz of Section 6.2.3.

The problem setup additionally coincides with Section 6.1.3 and thus enables a comparison to the NURBS-DSG results. For the interpolation of the displacement and stress fields, the NURBS function definitions of Table 6.2 are applied.
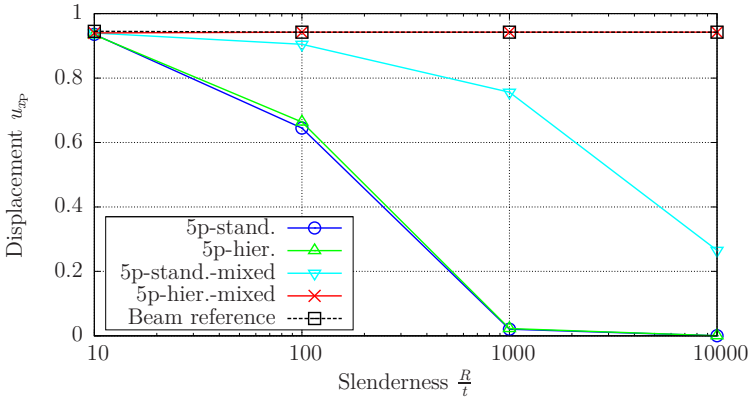

Figure 6.11: Cylindrical shell – displacement convergence, 5p shells, mixed $\mathbf{u}$-$\boldsymbol{\sigma}$.

In Figure 6.11, the sensitivity to locking is analyzed for the 5-parameter Reissner-Mindlin NURBS shell elements. The numerical displacement results $u_{x_\mathrm{P}}^\mathrm{h}$ of the mixed $\mathbf{u}$-$\boldsymbol{\sigma}$ ansatz are identical to the results of the DSG shell formulations of Section 6.1.3, as displayed in Table 6.3 for the entire family of isogeometric shell finite elements of this thesis. As the mixed formulation only improves the in-plane behavior of the shell elements to be investigated, transverse shear locking is still present for the standard 5- and 7-parameter NURBS shell models. The 7-parameter standard models additionally exhibit curvature

thickness locking, which was already identified in Section 5.4.4 and the numerical results with the NURBS-DSG-ansatz in Section 6.1.3. The mixed hierarchic shell formulations completely remove membrane locking and thus yield discrete displacement results $u_{x_\mathrm{P}}^\mathrm{h}$, which are independent of the slenderness $\frac{R}{t}$.

Slenderness $\frac{R}{t}$	10	100	1000	10000
Shell formulation (2nd order NURBS)				
3p-DSG	0.9406	0.9444	0.9445	0.9445
3p-mixed	0.9385	0.9424	0.9425	0.9425
5p-stand.-DSG	0.9396	0.9048	0.7560	0.2652
5p-stand.-mixed	0.9396	0.9048	0.7560	0.2652
5p-hier.-DSG	0.9422	0.9445	0.9445	0.9445
5p-hier.-mixed	0.9401	0.9424	0.9425	0.9425
7p-stand.-DSG	0.9403	0.9031	0.7158	0.0895
7p-stand.-mixed	0.9403	0.9031	0.7158	0.0895
7p-hier.-DSG	0.9445	0.9445	0.9445	0.9445
7p-hier.-mixed	0.9409	0.9424	0.9425	0.9425
Analytic result				
Beam reference	0.9451	0.9425	0.9425	0.9425

Table 6.3: Cylindrical shell – displacements u_{x_P}, overview of shell formulations, DSG vs. mixed method.

The results obtained with the mixed approach reveal that this formulation is capable of successfully removing in-plane locking effects of the isogeometric pure displacement-based shell elements of this thesis. No in-depth mathematical analysis of this method, however, has been performed so far. Up to now, the knowledge of standard C^0-continuous discretizations with mixed **u**-$\boldsymbol{\sigma}$ formulation that are carried out on element level has been adopted for higher-continuous NURBS discretizations on patch level.

6.3 Alternative methods to avoid geometric locking

In this section, alternative strategies to avoid particularly geometric locking, which are frequently used in standard C^0-continuous FEA are briefly discussed. Their practicability with regard to higher-order and higher-continuity NURBS discretizations is investigated. Additionally, the most prominent approaches developed so far to remove locking in the context of isogeometric analysis are described.

Assumed Natural Strain Method (ANS)

The ANS method (HUGHES AND TEZDUYAR (1981), BATHE AND DVORKIN (1985)), which was briefly discussed in Section 6.1, is widely used in conventional C^0-continuous

FEA in order to remove particularly transverse shear locking. The main idea consists of evaluating discrete shear strain values at appropriate collocation points in the element, which are subsequently interpolated with specific assumed strain shape functions, instead of deriving the transverse shear strains directly from the displacement field derivatives. The collocation points are located at positions in the element, where the parasitic transverse shear strains are equal to zero.

As the numerical implementation only requires a modification of the strain-displacement operator $\mathbf{B}$, the ANS approach is frequently denoted as "B-bar" method (HUGHES (2000)). In addition to the removal of transverse shear locking, the ANS method may also be used to eliminate membrane and curvature thickness locking effects. The main drawback of the ANS ansatz is related to the definition of sampling point locations and assumed strain shape functions, which depend on both the type of element and the polynomial order of the basis functions.

For higher-continuous NURBS discretizations, this method appears to be inappropriate due to the complexity of defining adequate collocation points. This will be explained in the following for the Timoshenko beam problem of Figure 5.10: A discretization of the structure with C^0-continuous NURBS and pure displacement formulation always yields the Barlow points as roots of the parasitic shear strains $\gamma_{\text{par.}}^{\text{h}}$ independent of the type of loading or the polynomial order of the NURBS basis, which is well-known from standard FEA. If, however, higher-continuity NURBS functions are used, the zeros of $\gamma_{\text{par.}}^{\text{h}}$ no longer coincide with the Barlow point locations and, even more problematic, change their position in dependence of the type of loading. These facts tremendously complicate or might even prevent the correct definition of sampling point positions for the ANS approach in the context of higher-continuity NURBS-based IGA.

Reduced integration

Reduced or selective reduced integration utilizes fewer integration points than required for the evaluation of quantities, such as stiffness or mass matrices, which may lead to undesired zero energy modes and consequently numerical instabilities, without the application of stabilization techniques. First applications of reduced and selective reduced integration to continuum and structural finite elements are related to DOHERTY ET AL. (1969), ZIENKIEWICZ ET AL. (1971) and HUGHES ET AL. (1977).

In BOUCLIER ET AL. (2012), selective reduced integration on element level with Gauss quadrature is investigated for curved thick Timoshenko beams in the context of IGA. Although this approach removes the geometric locking effects of a pure displacement formulation, it will become comparatively complex and laborious for higher-dimensional NURBS structures with arbitrary polynomial order and continuity, as is explained for the example of one quadratic 1D B-spline element of an entire patch domain. Due

to the quadratic basis functions, the element may have three different levels of continuity at its two ends, i.e. $C^0 - C^0$, $C^1 - C^0$ and $C^1 - C^1$. This ultimately requires three different reduced integration schemes. For higher-order and higher-dimensional NURBS discretizations, the number of possible inter-element continuity combinations significantly increases, which confines the general practicability of this approach.

HUGHES ET AL. (2010) study the use of efficient integration rules for higher-continuity NURBS in isogeometric analysis; these, however, are not intended to remove locking, but improve the computational efficiency of numerical integration. Rather than evaluating the integrals element-by-element, the authors suggest using integration rules on macro-elements, which require significantly less quadrature points by taking into account the smoothness of the basis functions. Their ansatz necessitates the numerical computation of the quadrature points and associated weights by solving nonlinear equation systems for higher-order and higher-continuity basis functions, which may compromise computational efficiency. Exact numbers, which compare the time savings due to less quadrature points and the effort of numerically computing the quadrature points and weights are not presented in this paper, however.

Enhanced Assumed Strain Method (EAS)

The method of enhanced assumed strains (EAS) was first developed in SIMO AND RIFAI (1990) on the basis of the three-field Hu-Washizu variational principle (HU (1955), WASHIZU (1955)). Instead of skipping undesired contributions in the strain quantities, the compatible displacement-based strains are enhanced by additional incompatible terms, in order to balance the parasitic strain part and thus avoid locking. This approach is closely related to the method of incompatible modes (TAYLOR ET AL. (1976)), as both formulations add additional degrees of freedom not globally, but on element level.

Compared to the methods to avoid locking described so far in this chapter, the EAS approach is also capable of removing material-based locking effects, i.e. volumetric and Poisson thickness locking, in addition to transverse shear and membrane locking.

A stable element formulation requires the enhanced strains to be linearly independent from the compatible displacement-based strains. Otherwise, identical strain modes show up in an element, which leads to a singular stiffness matrix. A further requirement in the EAS method is the orthogonality of the stress functions to the enhanced strains, such that associated energy expressions become zero. The incompatibility of the enhanced strain field additionally enables an elimination of the corresponding degrees of freedom on element level via static condensation, as for hybrid stress elements. The modified element stiffness consequently has the same structure as a pure displacement-based element and thus enables the application of standard assembly and solution methods. Details on the derivation of element stiffness matrices and the definition of adequate enhanced

strain functions are not provided herein. Further information in addition to the afore-mentioned references is provided, for instance, in ANDELFINGER (1991), ANDELFINGER AND RAMM (1993), BÜCHTER ET AL. (1994) and BISCHOFF ET AL. (1999).

First applications of the EAS method to higher-order and higher-continuity NURBS by the author of this thesis have not been successful so far. The unsolved problems are, for instance, continuous strain distributions in the entire patch domain and the dependency of the strains on the applied load, while simultaneously accounting for the linear independence of the enhanced and compatible strain fields as well as the orthogonality to the stresses.

Isogeometric mixed method for Reissner-Mindlin plates

In BEIRÃO DA VEIGA ET AL. (2012), isogeometric finite elements for plates with Reissner-Mindlin kinematics are derived which do not suffer from transverse shear locking. The authors adopt the procedures that were originally developed to smoothly approximate the differential forms of Maxwell equations or the Stokes problem (BUFFA ET AL. (2010), BUFFA ET AL. (2011)) by taking advantage of the regularity of spline functions for the discretization of Reissner-Mindlin plate problems.

This mixed approach utilizes smooth discrete function spaces for both the transverse displacements and the rotations, which enables the satisfaction of the Kirchhoff condition in the thin limit and thus yields isogeometric plate elements that are free from parasitic transverse shear effects by construction. Mathematical proof of stability and optimal convergence properties of the formulation are provided by the authors.

$\overline{\mathrm{B}}$ strain projection ansatz

In the original paper ELGUEDJ ET AL. (2008) the $\overline{B}$ strain projection approach was applied to higher-order and higher-continuity NURBS discretizations of incompressible or nearly incompressible material elasticity and plasticity problems to remove volumetric locking. The authors therein suggest that the projected, possibly continuous volumetric strain fields are one order and one level of continuity lower than the spaces of the displacements except for cases of C^0-continuity which remain C^0-continuous. BOUCLIER ET AL. (2012) adopt this procedure to remove both membrane and transverse shear locking in NURBS-based curved Timoshenko beam elements. Linear projection operators are defined to project both the membrane and transverse shear strain components onto a lower-dimensional basis in order to remove locking. For the Timoshenko beam problem additionally the equivalence of the $\overline{B}$ formulation and mixed methods is determined.

7

Numerical Examples

In the previous two chapters the accuracy of the hierarchic family of isogeometric shell element formulations of this thesis with both pure displacement ansatz and additional modification of the membrane strain components was tested in basic problem setups. This approach enabled the detailed and separate investigation of individual shell element properties and, moreover, a comparison of the finite element results to analytic reference solutions.

In this chapter, these isogeometric shell elements are tested in popular and more complex benchmark examples for the analysis of shell structures including multipatch NURBS domains. All numerical evaluations account for both geometric and material linear behavior. In addition to the pure displacement shell elements derived in Chapter 5, the formulations with modification of the membrane part by means of the mixed displacement-stress approach of Section 6.2 are investigated. The NURBS-DSG ansatz of Section 6.1, which is also capable to remove geometric locking effects of higher-order and higher-continuity NURBS elements and which was analyzed in detail in the previous chapter is not evaluated herein to confine the number of applied element formulations. These are summarized in the following for clarity:

- **3p**: 3-parameter formulation (Kirchhoff-Love), pure displacement ansatz, cf. Section 4.3,
- **3p-mixed**: 3-parameter formulation with mixed displacement-stress ansatz for modification of membrane part, cf. Sections 4.3 and 6.2

- **5p-stand.**: standard 5-parameter formulation (Reissner-Mindlin), pure displacement ansatz, update of director with difference vector added to the *undeformed* normal, cf. Section 4.4.1,
- **5p-stand.-mixed**: standard 5-parameter formulation (Reissner-Mindlin), mixed displacement-stress ansatz for modification of membrane part, cf. Sections 4.4.1 and 6.2,
- **5p-hier.**: hierarchic 5-parameter formulation (Reissner-Mindlin), pure displacement ansatz, update of the director with difference vector added to the *rotated* normal, cf. Section 4.4.2,
- **5p-hier.-mixed**: hierarchic 5-parameter formulation (Reissner-Mindlin), mixed displacement-stress ansatz for modification of membrane part, cf. Sections 4.4.2 and 6.2

- **7p-stand.**: standard 7-parameter formulation (Reissner-Mindlin), pure displacement ansatz, update of director with difference vector added to the *undeformed* normal, cf. Section 4.5.1,
- **7p-stand.-mixed**: standard 7-parameter formulation (Reissner-Mindlin), mixed displacement-stress ansatz for modification of membrane part, cf. Sections 4.5.1 and 6.2,
- **7p-hier.**: hierarchic 7-parameter formulation (Reissner-Mindlin), pure displacement ansatz, update of the director with difference vector added to the *rotated* normal, cf. Section 4.5.2,
- **7p-hier.-mixed**: hierarchic 7-parameter formulation (Reissner-Mindlin), mixed displacement-stress ansatz for modification of membrane part, cf. Sections 4.5.2 and 6.2

7.1 Scordelis-Lo roof

The first example to be investigated is the Scordelis-Lo roof according to MacNeal and Harder (1985), which represents a famous benchmark problem for the analysis of shell structures. The cylindrical singly-curved shell is supported with rigid diaphragms at either end ($y = -50, y = 0$) and is subjected to uniform gravity load of $q = 90$ per unit area, as shown in Figure 7.1. The system response of this numerical example is dominated by both membrane and bending action. At the supports, the structure allows for a motion in longitudinal direction and additionally for rotations. In the discrete model homogeneous displacement boundary conditions of $v_x = v_z = 0$ are applied to the control point degrees of freedom of the associated edges. The roof has a fixed slenderness of $\frac{R}{t} = 100$ and for FEA no symmetry conditions are imposed on the discrete models
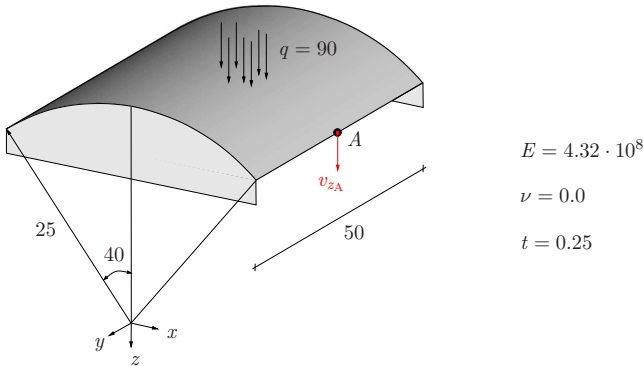
Figure 7.1: Scordelis-Lo roof – problem setup.

in this thesis. The structure is therefore calculated as a whole. Due to the rectangular topology of the shell domain single patch calculations are performed.

For the discretization of the geometry and the displacement field NURBS basis functions of at least second-order and C^1-continuity are used in both parametric directions ξ and η throughout all computations. The investigated quantity is the vertical deflection v_{z_A} of point "A" at the midspan of the free edge which is calculated for various discretizations. The results are compared to the reference solution of MacNeal and Harder (1985), which is 0.3024, and to the isogeometric Kirchhoff-Love shell of Kiendl et al. (2009).

Pure displacement formulation

In Figure 7.2 the displacement convergence of the hierarchic shell elements (5p-hier., 7p-hier.) and the basic Kirchhoff-Love shell (3p) with pure displacement formulations is analyzed for biquadratic to biquartic NURBS discretizations.

It turns out that with increasing polynomial order the numerical displacement results converge more rapidly towards the reference solution of MacNeal and Harder (1985). These observations conform with the experience from conventional FEA and the NURBS results of Sections 5.3 and 5.4. Whereas the second-order discretizations are significantly prone to locking and for convergence to the reference solution require a mesh with at least 20 control points per edge, the cubic and quartic NURBS approaches already provide the same accuracy with less than ten control points in each direction of the patch. The charts in Figure 7.2 moreover illustrate that for this problem setup the displacement results of the thin shell (3p), the Reissner-Mindlin formulation (5p-hier.) and the 3D shell (7p-hier.) are practically identical. This fact can be explained first by the
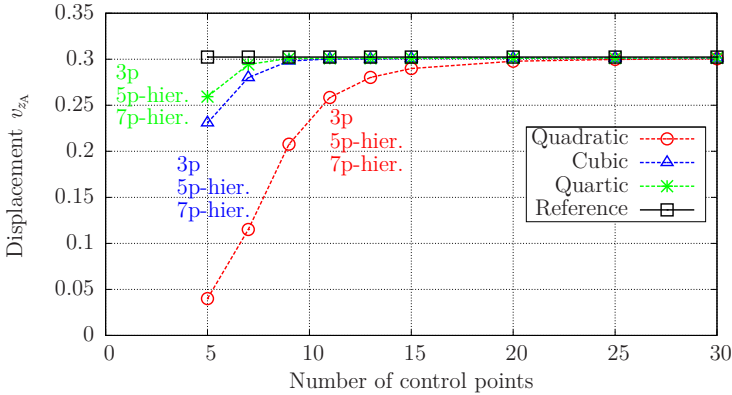
Figure 7.2: Scordelis-Lo roof. Displacement convergence of "3p", "5p-hier.", "7p-hier." displacement models.

homogeneous shape of the structure and the homogeneous type of loading, which yields a membrane dominated load-carrying behavior of the shell except edge disturbances at the supports. Secondly, the slenderness of $\frac{R}{t} = 100$ significantly reduces the influence of transverse shear and higher-order mechanical effects on the system response, which became already evident in the numerical examples of Chapters 5 and 6.

In Figure 7.3 the displacements u_z of the hierarchic 5-parameter shell (5p-hier.) are visualized for the 2nd to 4th order NURBS discretizations in contour plots for a mesh size of nine control points per edge. The plots are scaled with a factor of ten.
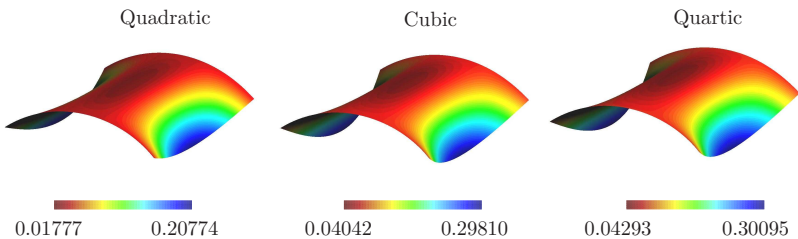

Figure 7.3: Scordelis-Lo roof. Displacement plots v_z of "5p-hier." shell – quadratic to quartic NURBS.

In order to analyze in more detail, which type of locking significantly affects the convergence properties of the displacement-based NURBS shell elements, the results of the

hierarchic and the standard formulations with second-order shape functions are compared to each other and to the 3-parameter Kirchhoff-Love shell element of KIENDL ET AL. (2009) in Table 7.1.

Control points per edge	7	11	19	35
Shell formulation (2nd order NURBS)				
3p	0.1151	0.2584	0.2967	0.3003
5p-stand.	0.1101	0.2480	0.2956	0.3008
5p-hier.	0.1151	0.2585	0.2970	0.3008
7p-stand.	0.1101	0.2480	0.2956	0.3008
7p-hier.	0.1151	0.2585	0.2970	0.3008
KIENDL ET AL. (2009)				
3p	0.0764	0.2480	0.2966	0.3003

Table 7.1: Scordelis-Lo roof. Displacements v_{z_A} of 2nd order NURBS shells – hierarchic vs. standard.

The results in Table 7.1 clearly reveal that for the given problem setup both transverse shear locking and curvature thickness locking have no significant influence on the discrete displacements v_{z_A}. Both approaches yield almost identical values for all mechanical shell models. The displacement results of Kiendl et al. conform well with the family of displacement-based isogeometric shell elements developed in this work for fine discretizations but differ clearly in the coarse mesh regime. In KIENDL ET AL. (2009) symmetry boundary conditions were applied to the Scordelis-Lo roof and only one quarter of the entire shell structure was computed. This fact is accounted for in the number of "control points per edge". Differences in modeling the roof as a whole or by the coupling of four patches, however, show up in the spatial location of the control points. The application of open uniform knot vectors results in a nonuniform distribution of control points at the ends of a patch domain in order to obtain a uniform parametrization. See, for instance, Figure 5.6. The coupling of patches based on open uniform knot vectors therefore yields different control point locations in the vicinity of the patch interface than a discretization of the same domain with one single patch with the same number of control points. A second possible reason for the differences in the coarse mesh regime may result from the definition of the symmetry boundary conditions along curved NURBS edges in KIENDL ET AL. (2009) whose influence diminishes with mesh refinement.

The cubic and quartic NURBS shell discretizations perform analogously and will therefore not be reproduced in the table.

Mixed u-σ formulation

The Scordelis-Lo roof is now investigated by using the hierarchic family of NURBS shell elements with modification of the membrane part by means of the mixed **u-σ** approach

of Section 6.2. Apart from this difference, the problem setup is identical to the pure displacement model.

Figure 7.4 displays the displacement convergence of the hierarchic shell elements with mixed formulation (5p-hier.-mixed, 7p-hier.-mixed) and the Kirchhoff-Love shell (3p-mixed) again for biquadratic to biquartic NURBS discretizations.
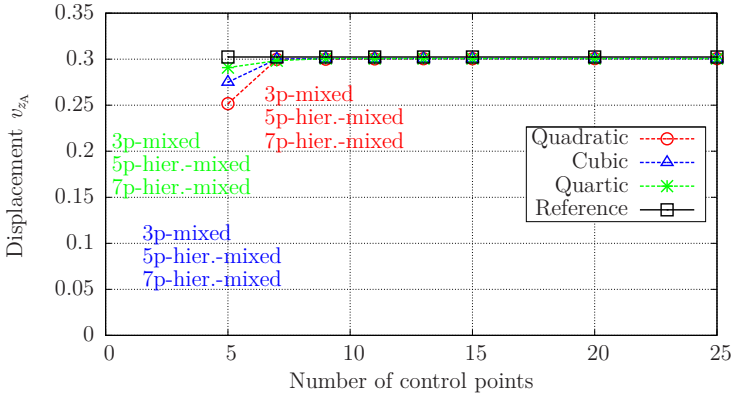

Figure 7.4: Scordelis-Lo roof. Displacement convergence of "3p-mixed", "5p-hier.-mixed", "7p-hier.-mixed" shell formulations.

As for the displacement-based shell elements increasing the polynomial order of the NURBS functions leads to improved convergence properties of the mixed isogeometric shells to the reference solution of MACNEAL AND HARDER (1985). The displacement results of the thin shell (3p-mixed), the Reissner-Mindlin formulation (5p-hier.-mixed) and the 3D shell (7p-hier.-mixed) are again identical. The removal of geometric locking effects from the in-plane part of the shell elements moves the convergence curves significantly closer to the reference solution for the same number of control points. Whereas the second-order displacement model required a mesh of at least 25 control points per edge to match the reference solution, the mixed model has the same accuracy with only seven control points per edge and thus needs less than ten percent of the number of degrees of freedom. Furthermore, the differences in the results due to the application of different polynomial orders (2nd to 4th order) are significantly smaller among the mixed than among the displacement formulations. The improved convergence properties of the mixed isogeometric shell elements that were already determined in the numerical example of Section 6.2.4, carry over to the Scordelis-Lo roof benchmark problem. For clarity, the displacement results v_{z_A} of the pure displacement models and the mixed approaches are displayed for the family of 3-, 5- and 7-parameter shells with both standard and hierarchic parametrization of the difference vector for 2nd order NURBS discretizations

in Table 7.2. The behavior among the shell formulations with cubic and quartic NURBS is analogous to the second-order shells and is therefore not included in the table.

Control points per edge	5	9	13	20	25	30
Shell formulation (2nd order NURBS)						
3p	0.04400	0.20768	0.28013	0.29751	0.29940	0.30004
3p-mixed	0.25169	0.29999	0.30050	0.30060	0.30061	0.30061
5p-hier.	0.03998	0.20774	0.28030	0.29781	0.29978	0.30049
5p-stand.	0.04014	0.19586	0.27362	0.29672	0.29942	0.30035
5p-hier.-mixed	0.25173	0.30013	0.30070	0.30090	0.30099	0.30107
5p-stand.-mixed	0.22912	0.27528	0.29241	0.29756	0.30050	0.29993
7p-hier.	0.03998	0.20774	0.28030	0.29781	0.29978	0.30049
7p-stand.	0.04014	0.19586	0.27362	0.29672	0.29942	0.30035
7p-hier.-mixed	0.25173	0.30013	0.30070	0.30090	0.30099	0.30107
7p-stand.-mixed	0.22913	0.27527	0.29241	0.29756	0.30050	0.29993

Table 7.2: Scordelis-Lo roof. Displacements v_{z_A} of 2nd order NURBS shells (standard, hierarchic, mixed).

7.2 Pinched hemisphere

The next example to be investigated in this chapter is a pinched hemispherical shell. This structure is doubly-curved and subjected to four radial point loads $F = \pm 2$ at its bottom ($z = 0$) at $90°$ intervals, which yields a bending dominated deformation.

$$E = 6.825 \cdot 10^7$$
$$\nu = 0.3$$
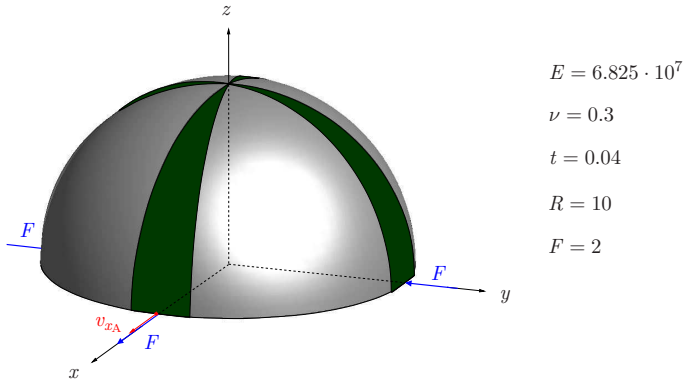$$t = 0.04$$
$$R = 10$$
$$F = 2$$

Figure 7.5: Pinched hemisphere (gray) and bending strips (green) – problem setup.

The pinched hemisphere benchmark problem follows BELYTSCHKO ET AL. (1985) and compared to the setup of MACNEAL AND HARDER (1985) no hole is introduced at

the top of the shell. The circumferential edge of the hemisphere at $z = 0$ is free. The entire structure is fixed at its top at $x = y = 0, z = 10$, which conforms with the setup of KIENDL ET AL. (2009) to which the displacement results are also compared. Again, no symmetry boundary conditions are imposed on the model as for the example of Section 7.1. The discrete structure consists of four NURBS patches with compatible discretizations along common edges. In order to ensure slope continuity the bending strip method described in Section 3.6 is applied to the analysis models at the patch interfaces as shown in green in Figure 7.5. The radius of the shell is ten and the thickness $t = 0.04$, which yields a slenderness of $\frac{R}{t} = 250$. The doubly-curved geometry and the displacement field require a discretization with NURBS functions of at least second-order and C^1-continuity for both parametric directions ξ and η. The quantity to be monitored is the radial displacement at the loaded point "A", which according to BELYTSCHKO ET AL. (1985) is equal to 0.0924.

Pure displacement formulation

For the pinched hemisphere the displacement convergence of the hierarchic shell elements (5p-hier., 7p-hier.) and the Kirchhoff-Love shell (3p) with pure displacement ansatz is analyzed for 2nd order to 4th order NURBS discretizations in Figure 7.6. The "number of control points per edge" refers to the number of control points to be used for one patch. For the entire shell problem spatially coincident control points along patch interfaces share the same degrees of freedom in the analysis models.
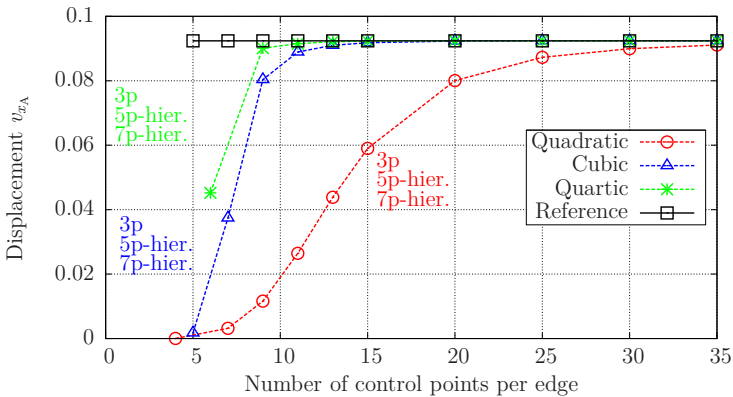

Figure 7.6: Hemisphere. Displacement convergence of "3p", "5p-hier.", "7p-hier." displacement models.

Several results from the Scordelis-Lo roof benchmark problem carry over to the pinched hemisphere. With increasing polynomial order of the NURBS basis the numerical displacement results converge more rapidly towards the reference solution as displayed in Figure 7.6. The ability of the displacement-based shell elements to correctly model the almost pure bending deformation of the shell for the applied load, however, is worse than determined in the numerical example of Section 7.1. The 2nd order NURBS discretizations require more than 35 control points per edge for each of the four patches to match the reference solution of BELYTSCHKO ET AL. (1985) and therefore exhibit significant locking sensitivity. Also for the cubic and quartic shell elements satisfactory displacement results do not show up if less than 15 control points are defined per edge. The choice of a reliable bending strip stiffness follows the investigations of KIENDL (2011) for this problem setup. It is defined such that it ensures the smooth coupling of the four surface patches during deformation on the one hand and to avoid numerical instabilities based on very large stiffness values of the strip on the other.

Differences in the displacement results of the shear-rigid 3-parameter shell and the shear-deformable 5- and 7-parameter formulations are again negligibly small as for the previous example of this chapter. Singularities in the displacements due to concentrated point loads showing up in shear-deformable theories of elasticity problems are neither pronounced nor evident for the investigated mesh sizes. For the thin hemispherical shell with a slenderness of $\frac{R}{t} = 250$ also the influence of transverse shear and higher-order mechanical effects on the overall system response is not apparent.

Mixed u-σ ansatz

As for the Scordelis-Lo roof, the multipatch hemisphere is now investigated by using the mixed **u-σ** ansatz of Section 6.2 for the membrane part of the hierarchic family of NURBS shell elements. Apart from that, the problem setup coincides with the pure displacement model.

In Figure 7.7 the displacement convergence of the mixed hierarchic shell elements (5p-hier.-mixed, 7p-hier.-mixed) and the shear-rigid Kirchhoff-Love model (3p-mixed) is displayed again for 2nd order to 4th order NURBS discretizations.

The conclusions drawn from Figure 7.7 for the pinched hemisphere coincide with those of the mixed models of Section 7.1: Improved convergence properties of the mixed isogeometric shells to the reference solution with increasing order of the NURBS basis can be ascertained. Additionally, the displacement results of all three shell formulations are practically identical. The locking-free shell elements, moreover, converge significantly faster to the reference solution for the same number of control points than the displacement models of Figure 7.6. Furthermore, the differences in the results due to
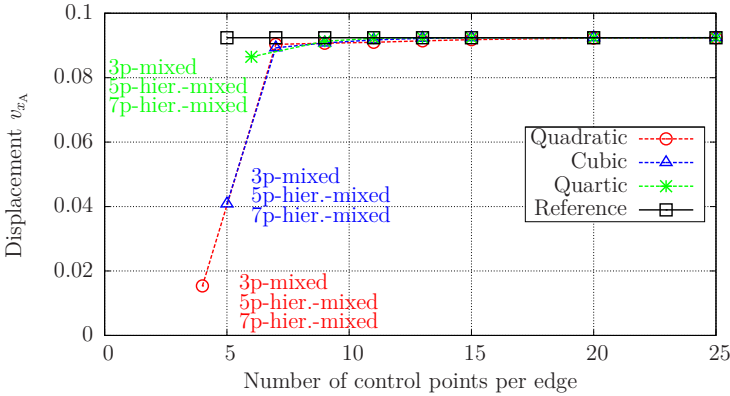
Figure 7.7: Hemisphere. Displacement convergence of "3p-mixed", "5p-hier.-mixed", "7p-hier.-mixed" shells.

the application of different polynomial orders (2nd to 4th order) is significantly smaller among the mixed than for the displacement formulations.

7.3 Highly-curved shell, model adaptivity

For the shell obstacle course examples Scordelis-Lo roof (Section 7.1) and hemispherical shell (Section 7.2) no evident differences showed up for the discrete displacement results among the different mechanical models (Kirchhoff-Love, Reissner-Mindlin, 3D shell). As concluded, slenderness values of $\frac{R}{t} \geq 100$ significantly reduced the influence of transverse shear and higher-order mechanical effects on the system response, which was also determined in the examples of Chapters 5 and 6.
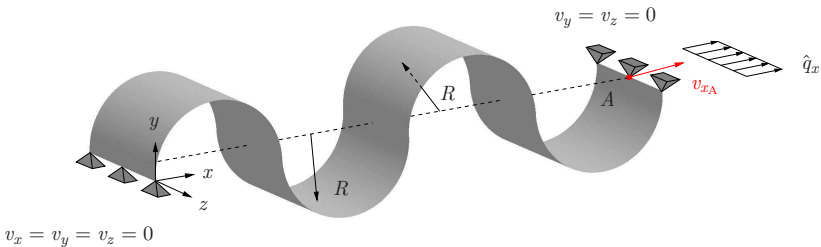

Figure 7.8: Curved shell – problem setup.

In Figure 7.8 a structure which is composed of eight 90° NURBS surface segments is depicted. To enforce slope continuity bending strips are used along patch interfaces. Both the geometry and displacement fields are discretized with second-order NURBS and C^1-continuity for both parametric directions ξ and η throughout all calculations.

Influence of shell models on displacement results

In the numerical example of this section the mechanical behavior of the three different models (Kirchhoff-Love, Reissner-Mindlin, 3D shell) of this thesis is analyzed for the cylindrical shell with high curvature by varying the slenderness from $\frac{R}{t} = 1$ to $\frac{R}{t} = 1000$. The radius to the mid-surface of the shell $R = 0.5$ is fixed, whereas the thickness is varied from $t = 0.5$ to $t = 0.0005$. In z-direction the structure has unit length. The shell is simply supported at both ends and subjected to a constant line load of $\hat{q}_x = 10$ which is scaled with the 3rd power of the thickness to keep the displacement results in the same range. In addition to bending also contributions from both transverse shear and in-plane normal forces contribute to the overall deformation for this particular model problem. The material constants for the linear elastic computations are Young's modulus $E = 1000$ and Poisson's ratio $\nu = 0$.

To avoid locking and to focus on the mechanical performance of the shell models, only the hierarchic shell elements with mixed formulation (5p-hier.-mixed, 7p-hier.-mixed) and the Kirchhoff-Love shell (3p-mixed) are employed. Additionally, a fine mesh with 50 elements in circumferential direction for every half cylinder and one element in z-direction of the structure is used. A numerical reference solution to the NURBS shell element "5p-hier.-mixed" is provided with the commercial software ANSYS by using the four node Reissner-Mindlin-type "SHELL181" (ANSYS (2011)). The number of isogeometric shell elements coincides with the mesh size defined in ANSYS.
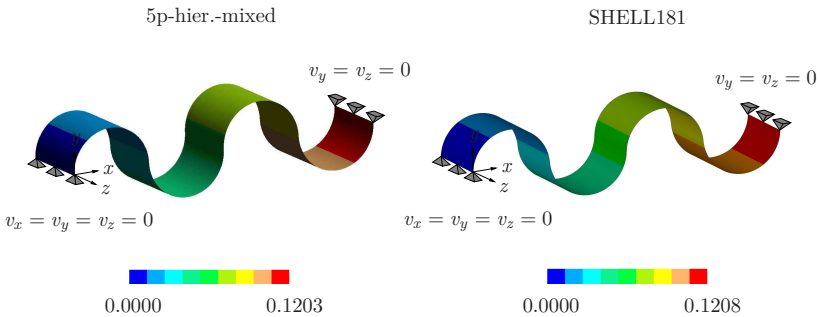

Figure 7.9: Curved shell – displacement plots v_x (5p-hier.-mixed, SHELL181).

In Figure 7.9 the identical mechanical behavior of both shell formulations is demonstrated in the displacement contour plots v_x for $\frac{R}{t} = 1$. The small deviations in the displacement results in the fourth decimal place are based on numerical effects such as for example implementation and applied finite element technology rather than due to the employed shell mechanics.

Next, the displacement results v_{x_A} as displayed in Figure 7.8 are evaluated and compared among the aforementioned shell element formulations in Table 7.3 for a varying slenderness $\frac{R}{t}$.

Slenderness $\frac{R}{t}$	1	10	100	1000
Shell formulation (2nd order NURBS)				
3p-mixed	0.1059	0.0946	0.0943	0.0943
5p-hier.-mixed	0.1203	0.0948	0.0943	0.0943
7p-hier.-mixed	0.1280	0.0949	0.0943	0.0943
ANSYS reference				
SHELL181 (5p)	0.1208	0.0944	0.0941	0.0941

Table 7.3: Curved shell – displacements v_{x_A}, overview of shell formulations.

Table 7.3 confirms that independent of the slenderness the shell elements "SHELL181" and "5p-hier.-mixed" which discretize the same shell model (Reissner-Mindlin) yield approximately the same results. Locking effects on the displacement results are considered to be insignificant for the fine mesh and the mixed element formulations applied for discretization.

For very thick shells obvious differences in the displacements of point "A" show up among the Kirchhoff-Love (3p), the Reissner-Mindlin (5p) and the 3D shell (7p) models due to significant contributions of bending, transverse shear and higher-order effects. The difference in v_{x_A} between the "3p-mixed" and "5p-hier.-mixed" shells amount to 12% based on the influence of transverse shear for $\frac{R}{t} = 1$. Between "5p-hier.-mixed" and "7p-hier.-mixed" three-dimensional mechanical effects yield a discrepancy of 6% for the same ratio of $\frac{R}{t}$. With increasing slenderness up to $\frac{R}{t} = 1000$ further insight can be derived from the results of Table 7.3: Thin shells are predominantly affected by membrane and bending action. Whereas the displacement values v_{x_A} of the NURBS-based shell elements (3p-mixed, 5p-hier.-mixed, 7p-hier.-mixed) clearly differ from each other in the very thick regime they convergence very fast to the same value as the slenderness increases. Even for the slenderness ratio of $\frac{R}{t} = 10$, which can be still considered as thick, the differences between the Kirchhoff-Love and the Reissner-Mindlin model are only in a range of 0.2%. Also the deviation of "5p-hier.-mixed" to "7p-hier.-mixed" amounts to 0.1% only which underlines the fast reduction of transverse shear action and effects in thickness direction on the evaluated deformation results.

Model adaptivity – Reissner-Mindlin to Kirchhoff-Love

In Chapter 1, the "blended" isogeometric shell of BENSON ET AL. (2013) was briefly presented. This ansatz links the shell theories of Kirchhoff-Love and Reissner-Mindlin by a linear combination of the kinematics of both models. The main intention is to apply the Kirchhoff-Love model in regions which are dominated by membrane and bending action, whereas Reissner-Mindlin kinematics is applied in areas where transverse shear has a significant influence, i.e. in non-smooth domains of low continuity, such as folds, intersections or boundaries.

With regard to model adaptivity this approach can be adopted straightforward to the hierarchic Reissner-Mindlin-type (5p-hier.) and Kirchhoff-Love-type (3p) shell formulations developed in this thesis. By imposing zero displacements on the degrees of freedom related to the difference vector $\mathbf{w}^{\text{5p-hier.}}$ the strain tensor coefficients $\varepsilon_{\alpha i}^{\text{5p-hier.}}$ of the Reissner-Mindlin shell become equal to the shear-rigid Kirchhoff-Love formulation; see Equations (4.12) and (4.25). As both mechanical shell models apply the stress assumption $\sigma^{33} = 0$ for asymptotic correctness no further action with respect to the material law has to be carried out. In Table 7.4 the displacement values v_{x_A} of the 3-parameter Kirchhoff-Love shell (3p-mixed), the hierarchic 5-parameter Reissner-Mindlin model (5p-hier.-mixed) and the constrained hierarchic 5-parameter Reissner-Mindlin formulation (5p-hier.-mixed-constr.) with mixed ansatz of the in-plane strain components are compared among each other. The mesh size coincides with the setup of the previous section. The discrete displacement results exactly confirm the aforementioned explanations. The constrained hierarchic Reissner-Mindlin shell (5p-hier.-mixed-constr.) yields exactly the same results as the shear-rigid Kirchhoff-Love model (3p-mixed) by simply fixing the displacement parameters related to the shear vector.

Slenderness $\frac{R}{t}$	1	10	100	1000
Shell formulation (2nd order NURBS)				
3p-mixed	0.1059	0.0946	0.0943	0.0943
5p-hier.-mixed	0.1203	0.0948	0.0943	0.0943
5p-hier.-mixed-constr.	0.1059	0.0946	0.0943	0.0943

Table 7.4: Curved shell – displacements v_{x_A}, model adaptivity.

For the hierarchic 3D shell (7p-hier.) in addition to transverse shear also the degrees of freedom of the linear and quadratic transverse normal displacement fields $\mathbf{w}^{\text{6p}}$ and $\mathbf{w}^{\text{7p}}$ can be set to zero such that the strain tensor coefficients $\varepsilon_{ij}^{\text{7p-hier.}}$ (see Equation (4.39)) again coincide with the 3-parameter Kirchhoff-Love shell. The material equations of the 7-parameter formulation, however, do not account for the stress assumption $\sigma^{33} = 0$. In order to switch from the 3D shell to the Kirchhoff-Love (3p) or Reissner-Mindlin (5p-hier.) model the constitutive law has to be modified accordingly.

8

Summary and Conclusions

8.1 Summary

This work is concerned with the isogeometric analysis of shells. A new hierarchic family of NURBS-based shell finite elements was developed.

Besides a shear-rigid 3-parameter shell element formulation with Kirchhoff-Love kinematics, both a shear flexible 5-parameter Reissner-Mindlin-type and a 7-parameter 3D shell element which accounts for thickness change were derived.

Compared to existing isogeometric shell elements the hierarchy showing up in the shell mechanics (3p, 5p, 7p) is transferred to the parametrization of the kinematic shell equations. This represents the key innovation of this thesis. The minimalistic 3-parameter shell model can be gradually enhanced with additional degrees of freedom in order to systematically increase the approximation quality of the shell formulation. The enhancement of the extra displacement parameters is performed such that a complete reformulation of the 5- and 7-parameter shell kinematic equations is not required. With regard to model adaptivity, the hierarchic construction also allows for a straightforward coupling of the different shell element formulations of the hierarchy.

The continuity requirements on the displacement functions for the proposed hierarchic shell models are identical to those of the 3-parameter formulation, i.e. C^1, which can, however, be naturally satisfied with the applied higher-continuity NURBS discretizations. All shell models of the hierarchy utilize a pure displacement ansatz. For the hierarchic shell models the concept of a difference vector is used to account for transverse shear deformations. In contrast to existing isogeometric Reissner-Mindlin-type shell formulations, the vector is added to the *rotated* director of the deformed configuration and thus effectively splits the displacement field into contributions due to bending and transverse shear which naturally avoids transverse shear locking. For the 3D shell

the hierarchic concept in addition avoids curvature thickness locking by default which was demonstrated in several numerical experiments.

Second, new strategies to remove geometric locking effects from higher-order and higher-continuity NURBS discretizations were developed and applied to the in-plane part of the family of isogeometric shell finite elements to remove membrane locking. Therefore a NURBS-based Discrete Strain Gap method and a mixed displacement-stress formulation were derived which ultimately lead to isogeometric shell finite elements that are completely free from geometric locking. The higher-continuity of the NURBS shape functions to be used for the discretization of the displacement fields may result in continuous strain and stress distributions which consequently do not allow for the application of finite element technology on element level but require considerations on patch level and may additionally lead to coupling of degrees of freedom.

For more complex geometries which require the definition of several patches and adequate coupling techniques the bending strip method of KIENDL ET AL. (2010) was adopted. This penalty-type method weakly imposes the constraint of connecting surface patches with slope continuity. The choice of appropriate stiffness parameters for the bending strips follows the analyses and recommendations of KIENDL (2011). The shell obstacle course examples evaluated in this thesis conform well with the results from literature; see, for instance, KIENDL ET AL. (2009).

Numerical analyses of a very thick and highly-curved shell with a ratio of radius to thickness equal to one revealed significant differences in the displacement response of the structure for the three different shell models (3p, 5p, 7p). With increasing slenderness a fast diminution of the influence of both transverse shear and higher-order mechanical effects on the investigated displacement results could be observed even for a moderately slender structure. For the same problem setup systematic deactivation of degrees of freedom was tested for the 5-parameter Reissner-Mindlin shell by imposing zero displacements on the shear vector degrees of freedom. The results obtained, perfectly match the 3-parameter Kirchhoff-Love solution and thus provide an ideal basis for a model adaptive approach.

8.2 Prospect

The kinematics of all shell elements of this thesis were developed and tested for the geometrically linear case. Therefore a first upcoming task will cover the extension of the element formulations to geometric and material non-linearity. For the shear-rigid Kirchhoff-Love shell the procedure is straightforward by formulating the non-linear rotation of the undeformed director $\mathbf{A}_3$ to the current configuration $\mathbf{a}_3$. The extension to large deformations for the 5-parameter Reissner-Mindlin shell model may be based on

either a difference vector ansatz or alternatively resort to hierarchic rotations. Attention, however, has to be paid to the satisfaction of the inextensibility condition for both approaches. For information on the theory of large rotations and the classification of different algorithmic concepts, the reader is referred to ARGYRIS (1982) and BETSCH ET AL. (1998), for instance. By all means, the principal concept of a hierarchic update of the shell director can be applied to all shell models (3p, 5p, 7p) developed in this work also in the geometrically non-linear regime.

The hierarchic parametrization applied to the shell models in this thesis enabled an elegant and effective split into bending and shear deformations and thus avoids transverse shear locking in a pure displacement formulation. A desirable extension of this concept might be the respective hierarchic split of bending and membrane deformations in order to avoid membrane locking and thus derive shell element models that are purely displacement-based and at once completely free from geometric locking.

The NURBS-based shell finite elements derived in this work possess several promising properties and advantages compared to standard Lagrange discretizations. Further studies will demonstrate the competitiveness of the isogeometric analysis and in particular isogeometric shell analysis to Lagrange-based finite element methods.

A

Appendix

A.1 Vector and tensor algebra fundamentals

- Vectors (first-order tensors) in co- and contravariant form:

$$\mathbf{a} = a_l \, \mathbf{g}^l = a^l \, \mathbf{g}_l \,. \tag{A.1}$$

- Scalar product (simple contraction) of two vectors:

$$\mathbf{a} \cdot \mathbf{b} = \mathbf{b} \cdot \mathbf{a} = (a_l \, \mathbf{g}^l) \cdot (b^m \, \mathbf{g}_m) = a_l \, b^m = a^l \, b_m \,. \tag{A.2}$$

- Vector (cross) product of two vectors (permutation symbol ε^{lmn}):

$$\mathbf{c} = \mathbf{a} \times \mathbf{b} = -\mathbf{b} \times \mathbf{a} = \varepsilon_{lmn} \, a^l \, b^m \, \mathbf{g}^n = \varepsilon^{lmn} \, a_l \, b_m \, \mathbf{g}_n \,. \tag{A.3}$$

- Mixed product of three vectors:

$$\mathbf{a} \cdot (\mathbf{b} \times \mathbf{c}) = \varepsilon_{lmn} \, a^l \, b^m \, c^n = \varepsilon^{lmn} \, a_l \, b_m \, c_n \,. \tag{A.4}$$

- Tensorial (dyadic) product of two vectors yields second-order tensor:

$$
\begin{aligned}
\mathbf{a} \otimes \mathbf{b} \;&= \mathbf{C} \\
\mathbf{C} \quad &= a^l \, b^m \, \mathbf{g}_l \otimes \mathbf{g}_m = a_l \, b_m \, \mathbf{g}^l \otimes \mathbf{g}^m = a^l \, b_m \, \mathbf{g}_l \otimes \mathbf{g}^m = a_l \, b^m \, \mathbf{g}^l \otimes \mathbf{g}_m \\
&= C^{lm} \, \mathbf{g}_l \otimes \mathbf{g}_m = C_{lm} \, \mathbf{g}^l \otimes \mathbf{g}^m = C^l_{\;m} \, \mathbf{g}_l \otimes \mathbf{g}^m = C_l^{\;m} \, \mathbf{g}^l \otimes \mathbf{g}_m \,.
\end{aligned} \tag{A.5}
$$

- Scalar product (double contraction) of two *second-order* tensors:

$$\mathbf{C} : \mathbf{D} = C^{lm} D_{lm} = \mathbf{D} : \mathbf{C} \, . \tag{A.6}$$

- Tensorial (dyadic) product of four vectors yields fourth-order tensor:

$$
\begin{aligned}
\mathbf{a} \otimes \mathbf{b} \otimes \mathbf{c} \otimes \mathbf{d} \ &= \mathbf{C} \\
\mathbf{C} \ &= a^l \, b^m \, c^n \, d^o \mathbf{g}_l \otimes \mathbf{g}_m \otimes \mathbf{g}_n \otimes \mathbf{g}_o \\
&= C^{lmno} \mathbf{g}_l \otimes \mathbf{g}_m \otimes \mathbf{g}_n \otimes \mathbf{g}_o \, .
\end{aligned}
\tag{A.7}
$$

- Product rule (divergence operator):

$$\mathrm{div} \left(\mathbf{C} \cdot \mathbf{a} \right) = \mathbf{C}^{\mathrm{T}} : \mathrm{grad} \, \mathbf{a} + \left(\mathrm{div} \, \mathbf{C}^{\mathrm{T}} \right) \cdot \mathbf{a} \, . \tag{A.8}$$

- Divergence theorem:

$$
\begin{aligned}
\int_{\Omega} \mathrm{div} \, \mathbf{C} \, \mathrm{d}\Omega \ &= \int_{\partial\Omega} \mathbf{C} \cdot \mathbf{n} \, \partial\Omega \\
\int_{\Omega} \mathrm{div} \, \mathbf{a} \, \mathrm{d}\Omega \ &= \int_{\partial\Omega} \mathbf{a} \cdot \mathbf{n} \, \partial\Omega \, .
\end{aligned}
\tag{A.9}
$$

- Partial integration (combination of product rule and divergence theorem) with substitutions $\boldsymbol{\sigma}^{\mathrm{lin}} = \mathbf{C}^{\mathrm{T}}, \delta\mathbf{u} = \mathbf{a}$):

$$\int_{\Omega} \boldsymbol{\sigma}^{\mathrm{lin}} : \, \mathrm{grad} \, \delta\mathbf{u} \, \mathrm{d}\Omega = \int_{\partial\Omega} \delta\mathbf{u} \cdot \boldsymbol{\sigma}^{\mathrm{lin}} \cdot \mathbf{n} \, \partial\Omega - \int_{\Omega} \delta\mathbf{u} : \mathrm{div} \, \boldsymbol{\sigma}^{\mathrm{lin}} \, \mathrm{d}\Omega \, . \tag{A.10}$$

Bibliography

Ahmad, D., Irons, B., and Zienkiewicz, O. (1968). Curved thick shell and membrane elements with particular reference to axi-symmetric problems. *Proceedings of the 2nd Conference on Matrix Methods in Structural Mechanics, Berke, L., Bader, R. M., Mykytow, W. J., Przemieniecki, J. S. and Shirk, M. H. (eds)*.

Altenbach, J. and Altenbach, H. (1994). *Einführung in die Kontinuumsmechanik*. Teubner, Stuttgart.

Andelfinger, E. (1991). *Untersuchungen zur Zuverlässigkeit hybrid-gemischter finiter Elemente für Flächentragwerke*. PhD thesis, Bericht Nr. 13, Institut für Baustatik, Universität Stuttgart.

Andelfinger, E. and Ramm, E. (1993). EAS elements for two-dimensional, three-dimensional, plate and shell structures and their equivalence to HR-elements. *International Journal for Numerical Methods in Engineering*, 36:1311–1337.

ANSYS, I. (2011). Ansys Inc, Release 11.0 Documentation for Ansys.

Antman, S. (2005). *Nonlinear problems of elasticity*. Springer, New York, 2nd edition.

Argyris, J. (1955). Energy theorems and structural analysis: A generalized discourse with applications on energy principles of structural analysis including the effects of temperature and non–linear stress–strain relations, Part I. General theory. *Aircraft Engineering and Aerospace Technology*, 27:125–134.

Argyris, J. (1957). Die Matrizentheorie der Statik. *Ingenieur-Archiv*, 25:174–194.

Argyris, J. (1982). An excursion into large rotations. *Computer Methods in Applied Mechanics and Engineering*, 32:85–155.

Argyris, J. and Scharpf, D. (1968). The SHEBA family of shell elements for the matrix displacement method. *Aeronautical Journal of the Royal Aeronautical Society*, 71:873–883.

Arnold, D. and Brezzi, F. (1997). Locking-free finite element methods for shells. *Mathematics of Computation*, 66:1–14.

Arnold, D. and Falk, R. (1996). Asymptotic analysis of the boundary layer for the Reissner-Mindlin plate model. *SIAM Journal of Mathematical Analysis*, 27:486–514.

Auricchio, F., Beirão da Veiga, L., Buffa, A., Lovadina, C., Reali, A., and Sangalli, G. (2007). A fully "locking-free" isogeometric approach for plane linear elasticity problems: A stream function formulation. *Computer Methods in Applied Mechanics and Engineering*, 197:160–172.

Auricchio, F., Beirão da Veiga, L., Lovadina, C., and Reali, A. (2010). The importance of the exact satisfaction of the incompressibility constraint in nonlinear elasticity: mixed FEMs versus NURBS-based approximations. *Computer Methods in Applied Mechanics and Engineering*, 199:314–323.

Auricchio, F. and Lovadina, C. (2001). Analysis of kinematic linked interpolation methods for Reissner-Mindlin plate problems. *Computer Methods in Applied Mechanics and Engineering*, 190:2465–2482.

Babuška, I. and Aziz, A. (1972). Survey lectures on the mathematical foundations of the finite element method. In Aziz, A., editor, *The mathematical foundations of the finite element method with applications to partial differential equations*, pages 3–363. Academic Press, New York.

Babuška, I. and Suri, M. (1992). On locking and robustness in the finite element method. *SIAM Journal on Numerical Analysis*, 29:1261–1293.

Başar, Y. and Krätzig, W. (1985). *Mechanik der Flächentragwerke*. Vieweg & Sohn, Braunschweig.

Başar, Y. and Weichert, D. (2000). *Nonlinear continuum mechanics of solids: Fundamental mathematical and physical concepts*. Springer, Berlin.

Barlow, J. (1976). Optimal stress locations in finite element models. *International Journal for Numerical Methods in Engineering*, 10:243–251.

Bathe, K.-J. and Dvorkin, E. (1985). A four-node plate bending element based on Mindlin/ Reissner plate theory and a mixed interpolation. *International Journal for Numerical Methods in Engineering*, 21:367–383.

Bazilevs, Y. (2006). *Isogeometric Analysis of Turbulence and Fluid-Structure Interaction*. PhD thesis, Faculty of the Graduate School of the University of Texas at Austin, USA.

Bazilevs, Y., Beirão da Veiga, L., Cottrell, J., Hughes, T., and Sangalli, G. (2006). Isogeometric analysis: approximation, stability and error estimates for h-refined meshes. *Mathematical models and methods in applied sciences*, 16:1031–1090.

Bazilevs, Y., Calo, V., Cottrell, J., Evans, J., Hughes, T., Lipton, S., Scott, M., and Sederberg, T. (2010). Isogeometric analysis using T-splines. *Computer Methods in Applied Mechanics and Engineering*, 199:229–263.

Beirão da Veiga, L., Buffa, A., Lovadina, C., Martinelli, M., and Sangalli, G. (2012). An isogeometric method for the Reissner-Mindlin plate bending problem. *Computer Methods in Applied Mechanics and Engineering*, 209–212:45–53.

Belytschko, T., Liu, W., and Moran, B. (2008). *Nonlinear finite elements for continua and structures*. Wiley, Chichester.

Belytschko, T., Stolarski, H., Liu, W., Carpenter, N., and Ong, J.-J. (1985). Stress projection for membrane and shear locking in shell finite elements. *Computer Methods in Applied Mechanics and Engineering*, 51:221–258.

Benson, D., Bazilevs, Y., Hsu, M., and Hughes, T. (2010). Isogeometric shell analysis: The Reissner–Mindlin shell. *Computer Methods in Applied Mechanics and Engineering*, 199:276–289.

Benson, D., Bazilevs, Y., Hsu, M., and Hughes, T. (2011). A large deformation, rotation-free, isogeometric shell. *Computer Methods in Applied Mechanics and Engineering*, 200:1367–1378.

Benson, D., Hartmann, S., Bazilevs, Y., Hsu, M., and Hughes, T. (2013). Blended isogeometric shells. *Computer Methods in Applied Mechanics and Engineering*, 255:133–146.

Betsch, P., Gruttmann, F., and Stein, E. (1995). A 4-node finite shell element for the implementation of general hyperelastic 3D-elasticity at finite strains. *Computer Methods in Applied Mechanics and Engineering*, 130:57–79.

Betsch, P., Menzel, A., and Stein, E. (1998). On the parameterization of finite rotations in computational mechanics. *Computer Methods in Applied Mechanics and Engineering*, 155:273–305.

Bézier, P. (1968). How Renault uses numerical control for car body design and tooling. SAE paper 680010, Soc. Automotive Engineers' Congress, Detroit, MI, USA.

Bischoff, M. (1999). *Theorie und Numerik einer dreidimensionalen Schalenformulierung*. PhD thesis, Bericht Nr. 30, Institut für Baustatik, Universität Stuttgart.

Bischoff, M. (2005). Advanced finite element methods. Unterlagen zur Vorlesung, Sommersemester 2005, Technische Universität München.

Bischoff, M. (2011a). Computational methods for shell analysis. Unterlagen zur Vorlesung, Wintersemester 2011/ 12, Universität Stuttgart.

Bischoff, M. (2011b). Finite Elemente für Tragwerksberechnungen. Unterlagen zur Vorlesung, Sommersemester 2011, Universität Stuttgart.

Bischoff, M. and Bletzinger, K.-U. (2001). Stabilized DSG plate and shell elements. *in: W.A. Wall et al. (Eds.), Trends in Computational Structural Mechanics, CIMNE, Barcelona*, pages 253–263.

Bischoff, M., Koschnick, F., and Bletzinger, K.-U. (2003). Stabilized DSG elements: A new paradigm in finite element technology. In: Proc. of the 4th European LS-DYNA Conference, Ulm, Germany.

Bischoff, M. and Ramm, E. (1997). Shear deformable shell elements for large strains and rotations. *International Journal for Numerical Methods in Engineering*, 40:4427–4449.

Bischoff, M. and Ramm, E. (2000). On the physical significance of higher order kinematic and static variables in a three-dimensional shell formulation. *International Journal of Solids and Structures*, 37:6933–6960.

Bischoff, M., Ramm, E., and Braess, D. (1999). A class of equivalent enhanced assumed strain and hybrid stress finite elements. *Computational Mechanics*, 22:443–449.

Bischoff, M., Wall, W., Bletzinger, K.-U., and Ramm, E. (2004). *Models and finite elements for thin-walled structures*. in: Encyclopedia of Computational Mechanics, Solids, Structures and Coupled Problems, Vol. 2, Wiley, New York.

Bletzinger, K.-U., Bischoff, M., and Ramm, E. (2000). A unified approach for shear-locking-free triangular and rectangular shell finite elements. *Computers and Structures*, 75:321–334.

Bogner, F., Fox, R., and Schmit, L. (1960). The generation of interelement-compatible stiffness and mass matrices by the use of interpolation formulae. In *Proceedings 1st Conference on Matrix Methods in Structural Mechanics, Wright Patterson Air Force Base, Ohio, AFFDL-TR-66-80*, pages 397–443.

Bonet, J. and Wood, R. (2008). *Nonlinear continuum mechanics for finite element analysis*. Cambridge University Press.

Bornemann, P. and Cirak, F. (2013). A subdivision-based implementation of the hierarchical b-spline finite element method. *Computer Methods in Applied Mechanics and Engineering*, 253:584–598.

Bouclier, R., Elguedj, T., and Combescure, A. (2012). Locking free isogeometric formulations of curved thick beams. *Computer Methods in Applied Mechanics and Engineering*, 245–246:144–162.

Braess, D. (2003). *Finite Elemente: Theorie, schnelle Löser und Anwendungen in der Elastizitätstheorie*. Springer, Berlin.

Braun, M. (1995). *Nichtlineare Analysen von geschichteten, elastischen Flächentragwerken*. PhD thesis, Bericht Nr. 19, Institut für Baustatik, Universität Stuttgart.

Brenner, S. and Scott, L. (2008). *The mathematical theory of finite element methods.* Springer, Berlin.

Brezzi, F. (1974). On the existence, uniqueness and approximation of saddle-point problems arising from lagrangian multipliers. *RAIRO Analyse Numérique*, 8:129–151.

Büchter, N. (1992). *Zusammenführung von Degenerationskonzept und Schalentheorie bei endlichen Rotationen.* PhD thesis, Bericht Nr. 14, Institut für Baustatik, Universität Stuttgart.

Büchter, N. and Ramm, E. (1992). Shell theory versus degeneration – a comparison in large rotation finite element analysis. *International Journal for Numerical Methods in Engineering*, 34:39–59.

Büchter, N., Ramm, E., and Roehl, D. (1994). Three-dimensional extension of non-linear shell formulation based on the enhanced assumed strain concept. *International Journal for Numerical Methods in Engineering*, 37:2551–2568.

Buffa, A., de Falco, C., and Sangalli, G. (2011). Isogeometric analysis: Stable elements for the 2D Stokes equation. *International Journal for Numerical Methods in Fluids*, 65:1407–1422.

Buffa, A., Sangalli, G., and Vázquez, R. (2010). Isogeometric analysis in electromagnetics: B-splines approximation. *Computer Methods in Applied Mechanics and Engineering*, 199:1143–1152.

Choi, D., Palma, E., Sanchez-Palencia, E., and Vilarino, M. (1998). Membrane locking in the finite element computation of very thin elastic shells. *Modélisation mathématique et analyse numérique*, 32:131–152.

Chung-Tze, S. (1979). On spline finite element method. *Mathematic Numerica Sinica*, 01.

Ciarlet, P. (1988). *Mathematical elasticity: Volume I: Three-dimensional elasticity.* North-Holland, Amsterdam.

Ciarlet, P. (2006). *An introduction to differential geometry with applications to elasticity.* Springer Verlag, Berlin.

Cirak, F. and Ortiz, M. (2001). Fully C^1-conforming subdivision elements for finite deformation thin shell analysis. *International Journal for Numerical Methods in Engineering*, 51:813–833.

Cirak, F., Ortiz, M., and Schröder, P. (2000). Subdivision surfaces: a new paradigm for thin shell analysis. *International Journal for Numerical Methods in Engineering*, 47:2039–2072.

Clough, R. (1960). The finite element method in plane stress analysis. In *Papers of the 2nd Conference on Electronic Computation, Pittsburgh, USA, September 8–9, 1960.* American Society of Civil Engineers.

Bibliography

Cohen, E., Lyche, T., and Riesenfeld, R. (1980). Discrete B-splines and subdivision techniques in computer aided geometric design and computer graphics. *Computer Graphics and Image Processing*, 14:87–111.

Cosserat, E. and Cosserat, F. (1909). Théorie des corps déformables. *Librairie Scientifique, A. Hermann et Fils, Paris, France.*

Cottrell, J., Hughes, T., and Bazilevs, Y. (2009). *Isogeometric analysis: Toward integration of CAD and FEA.* Wiley, Chichester.

Cottrell, J., Hughes, T., and Reali, A. (2007). Studies of refinement and continuity in isogeometric structural analysis. *Computer Methods in Applied Mechanics and Engineering*, 196:4160–4183.

Cottrell, J., Reali, A., Bazilevs, Y., and Hughes, T. (2006). Isogeometric analysis of structural vibrations. *Computer Methods in Applied Mechanics and Engineering*, 195:5257–5296.

Courant, R. (1943). Variational methods for the solution of problems of equilibrium and vibrations. *Bulletin of the American Mathematical Society*, 49:1–23.

Cox, M. (1972). The numerical evaluation of B-splines. *IMA Journal of Applied Mathematics*, 10:134–149.

de Boor, C. (1972). On calculation with B-splines. *IMA Journal of Applied Mathematics*, 6:50–62.

de Casteljau, P. (1963). Courbes et surfaces à pôles. Technical report at Citroen, National Industrial Property Institute (INPI), France.

Deuflhard, P. and Hohmann, A. (2008). *Numerische Mathematik 1, 4. Auflage.* Walter de Gruyter, Berlin.

Doherty, W., Wilson, E., and Taylor, R. (1969). Stress analysis of axisymmetric solids utilizing higher order quadrilateral finite elements. UCB/SESM Report No. 69/03, University of California, Berkeley, USA.

Dörfel, M., Jüttler, B., and Simeon, B. (2010). Adaptive isogeometric analysis by local h-refinement with T-splines. *Computer Methods in Applied Mechanics and Engineering*, 199:264–275.

Dornisch, W., Klinkel, S., and Simeon, B. (2013). Isogeometric Reissner-Mindlin shell analysis with exactly calculated director vectors. *Computer Methods in Applied Mechanics and Engineering*, 253:491–504.

Duhem, P. (1893). Le potentiel thermodynamique et la pression hydrostatique. *Annales scientifiques de l'École Normale Supérieure*, 10:183–230.

Eberlein, R. and Wriggers, P. (1997). Finite element formulations of five and six parameter shell theories accounting for finite plasticity. *in: Proceedings of COMPLAS 5, eds. D. R. J. Owen, E. Hinton and E. Onate, CIMNE, Barcelona.*

Echter, R. and Bischoff, M. (2010). Numerical efficiency, locking and unlocking of NURBS finite elements. *Computer Methods in Applied Mechanics and Engineering*, 199:374–382.

Echter, R., Oesterle, B., and Bischoff, M. (2013). A hierarchic family of isogeometric shell finite elements. *Computer Methods in Applied Mechanics and Engineering*, 254:170–180.

Eisele, S. (1989). Eigenwertuntersuchungen von hybriden Finiten Elementen. Diplomarbeit, Institut für Baustatik, Universität Stuttgart.

Elguedj, T., Bazilevs, Y., Calo, V., and Hughes, T. (2008). $\overline{B}$ and $\overline{F}$ projection methods for nearly incompressible linear and non-linear elasticity and plasticity using higher-order NURBS elements. *Computer Methods in Applied Mechanics and Engineering*, 197:2732–2762.

Epstein, M. and Glockner, P. (1977). Nonlinear analysis of multilayered shells. *International Journal of Solids and Structures*, 13:1081–1089.

Ericksen, J. and Truesdell, C. (1958). Exact theory of stress and strain in rods and shells. *Archive for Rational Mechanics and Analysis*, 1:295–323.

Evans, J., Bazilevs, Y., Babuška, I., and Hughes, T. (2009). n-Widths, sup–infs, and optimality ratios for the k-version of the isogeometric finite element method. *Computer Methods in Applied Mechanics and Engineering*, 198:1726–1741.

Fan, S. and Luah, M. (1990). New spline finite element for analysis of shells of revolution. *Journal of engineering mechanics*, 116:709–726.

Farin, G. (1999). *Nurbs: From projective geometry to practical use.* A.K. Peters, Natick.

Farin, G. (2002). *Curves and surfaces for CAGD: A practical guide.* Academic Press, San Diego.

Farin, G., Hoschek, J., and Kim, M.-S. (2002). *Handbook of computer aided geometric design.* Elsevier, Amsterdam.

Flügge, W. (1962). *Statik und Dynamik der Schalen.* Springer, Berlin.

Forsey, D. and Bartels, R. (1988). Hierarchical B-Spline refinement. *ACM SIGGRAPH Computer Graphics*, 22:205–212.

Gee, M. (2004). *Effiziente Lösungsstrategien in der nichtlinearen Schalenmechanik.* PhD thesis, Bericht Nr. 43, Institut für Baustatik, Universität Stuttgart.

Green, A., Naghdi, P., and Wainwright, W. (1965). A general theory of a Cosserat surface. *Archive for Rational Mechanics and Analysis*, 20:287–308.

163

Green, A. and Zerna, W. (1954). *Theoretical elasticity*. Courier Dover Publications, New York.

Green, A. and Zerna, W. (1992). *Theoretical elasticity*. Dover Publications, New York.

Gruttmann, F. and Wagner, W. (1994). On the numerical analysis of local effects in composite structures. *Composite Structures*, 29:1–12.

Hartmann, S. (2007). *Kontaktanalyse dünnwandiger Strukturen bei großen Deformationen*. PhD thesis, Bericht Nr. 49, Institut für Baustatik, Universität Stuttgart.

Hauptmann, R. and Schweizerhof, K. (1998). A systematic development of solid-shell element formulations for linear and non-linear analyses employing only displacement degrees of freedom. *International Journal for Numerical Methods in Engineering*, 42:49–69.

Haußer, C. (1996). *Effiziente Dreieckselemente für Flächentragwerke*. PhD thesis, Bericht Nr. 21, Institut für Baustatik, Universität Stuttgart.

Hellinger, E. (1914). Die allgemeinen Ansätze der Mechanik der Kontinua. *Enzyklopädie der Mathematischen Wissenschaften*, 4/4:601–694.

Höllig, K. (2002). *Finite element approximation with splines*. in: Handbook of Computer Aided Geometric Design. G. Farin, J. Hoschek, and M.S. Kim (eds.), Elsevier.

Höllig, K. (2003). *Finite element methods with B-splines*. SIAM, Philadelpia.

Holzapfel, G. (2000). *Nonlinear solid mechanics: A continuum approach for engineering*. Wiley, Chichester.

Hörmann, M. (2002). *Nichtlineare Versagensanalysen von Faserverbundstrukturen*. PhD thesis, Bericht Nr. 39, Institut für Baustatik, Universität Stuttgart.

Hsiung, C. (1981). *A first course in differential geometry*. Wiley, Chichester.

Hu, H.-C. (1955). On some variational principles in the theory of elasticity and plasticity. *Scientia Sinica*, 4:33–54.

Hughes, T. (2000). *The finite element method: Linear static and dynamic finite element analysis*. Dover Publications, Mineola, New York.

Hughes, T., Cottrell, J., and Bazilevs, Y. (2005). Isogeometric analysis: CAD, finite elements, NURBS, exact geometry and mesh refinement. *Computer Methods in Applied Mechanics and Engineering*, 194:4135–4195.

Hughes, T., Reali, A., and Sangalli, G. (2008). Duality and unified analysis of discrete approximations in structural dynamics and wave propagation: comparison of p-method finite elements with k-method NURBS. *Computer Methods in Applied Mechanics and Engineering*, 197:4104–4124.

Hughes, T., Reali, A., and Sangalli, G. (2010). Efficient quadrature for NURBS-based isogeometric analysis. *Computer Methods in Applied Mechanics and Engineering*, 199:301–313.

Hughes, T., Taylor, R., and Kanoknukulchai, W. (1977). A simple and efficient finite element for plate bending. *International Journal for Numerical Methods in Engineering*, 11:1529–1543.

Hughes, T. and Tezduyar, T. (1981). Finite elements based upon Mindlin plate theory with particular reference to the four-node bilinear isoparametric element. *Journal of Applied Mechanics*, 48:587–596.

Irons, B. (1966). Engineering application of numerical integration in stiffness method. *Journal of the American Institute of Aeronautics and Astronautics*, 14:2035–2037.

Kiendl, J. (2011). *Isogeometric analysis and shape optimal design of shell structures*. Dissertation, Lehrstuhl für Statik, Technische Universität München.

Kiendl, J., Bazilevs, Y., Hsu, M., Wüchner, R., and Bletzinger, K.-U. (2010). The bending strip method for isogeometric analysis of Kirchhoff-Love shell structures comprised of multiple patches. *Computer Methods in Applied Mechanics and Engineering*, 199:2403–2416.

Kiendl, J., Bletzinger, K.-U., Linhard, J., and Wüchner, R. (2009). Isogeometric shell analysis with Kirchhoff–Love elements. *Computer Methods in Applied Mechanics and Engineering*, 198:3902–3914.

Kim, H.-J., Seo, Y.-D., and Youn, S.-K. (2009). Isogeometric analysis for trimmed CAD surfaces. *Computer Methods in Applied Mechanics and Engineering*, 198:2982–2995.

Kirchhoff, G. (1850). Über das Gleichgewicht und die Bewegung einer elastischen Scheibe. *Journal für reine angewandte Mathematik*, 40:51–58.

Klingbeil, E. (1966). *Tensorrechnung für Ingenieure*. Bibliographisches Institut AG, Mannheim.

Klinkel, S. (2000). *Theorie und Numerik eines Volumen-Schalen-Elementes bei finiten elastischen und plastischen Verzerrungen*. Dissertation, Institut für Baustatik, Karlsruher Institut für Technologie.

Klinkel, S., Gruttmann, F., and Wagner, W. (2006). A robust non-linear solid shell element based on a mixed variational formulation. *Computer Methods in Applied Mechanics and Engineering*, 195:179–201.

Koiter, W. (1960). A consistent first approximation in the general theory of thin elastic shells. *Proceedings of the IUTAM Symposium, North–Holland Publication Company, Amsterdam*, pages 12–33.

Koiter, W. (1961). A systematic simplification of the equations in the linear theory of thin shells. *Kon. Ned. Academie der Wetenschappen, Holland*, 64:612.

Koschnick, F. (2004). *Geometrische Locking-Effekte bei finiten Elementen und ein allgemeines Konzept zu ihrer Vermeidung*. Lehrstuhl für Statik, Technische Universität München.

Koschnick, F., Bischoff, M., and Bletzinger, K.-U. (2002). Avoiding membrane locking with the DSG method. In: H. A. Mang, F. G. Rammerstorfer und J. Eberhardsteiner (Herausgeber): Proceedings of the Fifth World Congress on Computational Mechanics (WCCM V), July 7-12, 2002, Vienna.

Koschnick, F., Bischoff, M., Camprubi, N., and Bletzinger, K.-U. (2005). The discrete strain gap method and membrane locking. *Computer Methods in Applied Mechanics and Engineering*, 194:2444–2463.

Kreyszig, E. (1991). *Differential geometry*. Dover Publications, Mineola, New York.

Kühhorn, A. and Schoop, H. (1992). A nonlinear theory for sandwich shells including the wrinkling phenomenon. *Archive of Applied Mechanics*, 64:413–427.

Ladyzhenskaya, O. and Ural'tseva, N. (1968). *Linear and quasilinear elliptic equations*. Mathematics in science and engineering, 46. Academic Press, New York.

Li, S. and Shyy, W. (1997). On invariant integrals in the Marguerre-von Karman shallow shell. *International Journal of Solids and Structures*, 34:2927–2944.

Li, X., Zheng, J., Sederberg, T., Hughes, T., and Scott, M. (2012). On linear independence of T-spline blending functions. *Computer Aided Geometric Design*, 29:63–76.

Long, Q., Bornemann, P., and Cirak, F. (2012). Shear-flexible subdivision shells. *International Journal for Numerical Methods in Engineering*, 90:1549–1577.

Loop, C. (1987). Smooth subdivision surfaces based on triangles. Master Thesis, University of Utah, Department of Mathematics.

Love, A. (1888). On the small vibrations and deformations of thin elastic shells. *Philosophical Transactions of the Royal Society*, 179:491ff.

MacNeal, R. and Harder, R. (1985). A proposed standard set of problems to test finite element accuracy. *Finite Elements in Analysis and Design*, 1:3–20.

Maier, D. (2009). Anwendung der DSG-Methode auf 2d Nurbs finite Elemente. Diplomarbeit, Institut für Baustatik, Universität Stuttgart.

Marguerre, K. (1938). Zur Theorie der gekrümmten Platten großer Formänderung. *Proceedings of Fifth International Congress for Applied Mechanics, Wiley, New York*, pages 93–101.

Marsden, J. and Hughes, T. (1983). *Mathematical foundations of elasticity*. Prentice-Hall, London.

Marsden, J. and Schoenberg, I. (1966). On variation diminishing spline approximation methods. *Mathematica*, 31:61–82.

Mathisen, K., Okstad, K., Kvamsdal, T., and Raknes, S. (2011). Isogeometric analysis of finite deformation nearly incompressible solids. *Rakenteiden Mekaniikka (Journal of Structural Mechanics)*, 44:260–278.

Matzen, M., Cichosz, T., and Bischoff, M. (2013). A point to segment contact formulation for isogeometric, NURBS based finite elements. *Computer Methods in Applied Mechanics and Engineering*, 255:27–39.

Mindlin, R. (1951). Influence of rotary inertia and shear on flexural motions of iotropic elastic plates. *Journal of Applied Mechanics*, 18:31–38.

Morgenstern, D. (1959). Herleitung der Plattentheorie aus der dreidimensionalen Elastizitätstheorie. *Archive of Rational Mechanics and Analysis*, 4:145–152.

Naghdi, P. (1963). A new derivation of the general equations of elastic shells. *International Journal of Engineering Science*, 1:509–522.

Naghdi, P. (1972). *The theory of shells and plates*. Handbuch der Physik, VI/2. Springer, Berlin.

Oden, J. and Reddy, J. (1976). *Variational methods in theoretical mechanics*. Springer, Berlin.

Oesterle, B. (2011). Vermeidung geometrischer Locking-Effekte bei isogeometrischen finiten Elementen. Diplomarbeit, Institut für Baustatik, Universität Stuttgart.

Parisch, H. (1995). A continuum-based shell theory for non-linear applications. *International Journal for Numerical Methods in Engineering*, 38:1855–1883.

Park, K. and Felippa, C. (1998). A variational framework for solution method developments in structural mechanics. *Journal of Applied Mechanics*, 65:242–249.

Park, K. and Felippa, C. (2000). A variational principle for the formulation of partitioned structural systems. *International Journal for Numerical Methods in Engineering*, 47:395–418.

Parvizian, J., Düster, A., and Rank, E. (2007). Finite cell method: h- and p- extension for embedded domain methods in solid mechanics. *Computational Mechanics*, 41:122–133.

Pian, T. (1964). Derivation of element stiffness matrices by assumed stress distributions. *American Institute of Aeronautics and Astronautics Journal*, 2:1333–1336.

Pian, T. and Chen, D. (1982). Alternative ways for formulation of hybrid stress elements. *International Journal for Numerical Methods in Engineering*, 18:1679–1684.

Pian, T. and Sumihara, K. (1984). Rational approach for assumed stress finite elements. *International Journal for Numerical Methods in Engineering*, 20:1685–1695.

Pian, T. and Wu, C.-C. (2006). *Hybrid and incompatible finite element methods (CRC Series– Modern Mechanics and Mathematics)*. Taylor & Francis Group, Boca Raton.

Piegl, L. and Tiller, W. (1997). *The NURBS book (Monographs in visual communication)*. Springer, Berlin.

Pitkäranta, J. (1992). The problem of membrane locking in finite element analysis of cylindrical shells. *Numerische Mathematik*, 61:523–542.

Prenter, P. (1975). *Splines and variational methods*. Dover Publications, Mineola, New York.

Ramm, E. (1976). Geometrisch nichtlineare Elastostatik und Finite Elemente. Habilitationsschrift, Institut für Baustatik, Universität Stuttgart.

Ramm, E., Bischoff, M., and Braun, M. (1994). Higher order nonlinear shell formulation – a step back into three dimensions. *in: (K. Bell, ed.) From Finite Elements to the Troll Platform, Ivar Holand 70th Anniversary, Norwegian Institute of Technology, Trondheim*, pages 65–88.

Reddy, B. (1998). *Introductory functional analysis : With applications to boundary value problems and finite elements*. Springer, Berlin.

Reddy, J. (1997). *Mechanics of Laminated Composite Plates: Theory and Analysis*. CRC Press, Boca Raton, Florida.

Reissner, E. (1942). Note on the expressions for the strains in a bent, thin shell. *American Journal of Mathematics*, 64:768–772.

Reissner, E. (1945). The effect of transverse shear deformation on the bending of elastic plates. *Journal of Applied Mechanics*, 12:69–76.

Reissner, E. (1950). On a variational theorem in elasticity. *Journal of Mathematics and Physics*, 29:90–95.

Riesenfeld, R. (1972). Application of B-spline approximation to geometric problems of computer aided design. Ph.D. dissertation, Syracuse University, Syracuse, NY.

Rogers, D. (2001). *An introduction to NURBS with historical perspective*. Academic Press, San Diego.

Rogers, D. and Adams, J. (1990). *Mathematical elements for computer graphics*. McGraw-Hill, New York.

Rössle, A., Bischoff, M., Wendland, W., and Ramm, E. (1999). On the mathematical foundation of the 1–1–2 plate model. *International Journal of Solids and Structures*, 36:2143–2168.

Sanchez-Palencia, E. and Vassiliev, D. (1992). Remarks on vibration of thin elastic shells and their numerical computation. *Comptes Rendus de l'Académie des Sciences*, 314:445–452.

Sansour, C. (1995). A theory and finite element formulation of shells at finite deformations involving thickness change: Circumventing the use of a rotation tensor. *Archive of Applied Mechanics*, 10:194–216.

Schillinger, D. (2012). *The p- and B-spline versions of the geometrically nonlinear finite cell method and hierarchical refinement strategies for adaptive isogeometric and embedded domain analysis*. PhD thesis, Technische Universität München.

Schillinger, D., Dede, L., Scott, M., Evans, J., Borden, M., Rank, E., and Hughes, T. (2012). An isogeometric design-through-analysis methodology based on adaptive hierarchical refinement of NURBS, immersed boundary methods, and T-spline CAD surfaces. *Computer Methods in Applied Mechanics and Engineering*, 249–252:116–150.

Schmidt, R., Wüchner, R., and Bletzinger, K.-U. (2012). Isogeometric analysis of trimmed NURBS geometries. *Computer Methods in Applied Mechanics and Engineering*, 241–244:93–111.

Schoenberg, I. (1967). On spline functions, with a supplement by T.N.E. Greville. *In: Inequalities (Proc. Symposium Wright-Patterson Air Force Base, August 1965, ed. by O. Shisha)*, pages 255–291.

Schoop, H. (1986). Oberflächenorientierte Schalentheorien endlicher Verschiebungen. *Ingenieur-Archiv*, 56:427–437.

Scott, M., Li, X., Sederberg, T., and Hughes, T. (2012). Local refinement of analysis-suitable T-splines. *Computer Methods in Applied Mechanics and Engineering*, 213–216:206–222.

Simo, J. and Fox, D. (1989). On a stress resultant geometrically exact shell model. Part I: Formulation and optimal parametrization. *Computer Methods in Applied Mechanics and Engineering*, 72:267–304.

Simo, J. and Hughes, T. (1986). On the variational foundations of assumed strain methods. *Journal of Applied Mechanics*, 53:51–54.

Simo, J. and Rifai, M. (1990). A class of mixed assumed strain methods and the method of incompatible modes. *International Journal for Numerical Methods in Engineering*, 29:1595–1638.

Stein, E. and Barthold, F.-J. (1996). *Elastizitätstheorie*. in: Der Ingenieurbau, Ernst & Sohn, Berlin.

Stolarski, H. and Belytschko, T. (1982). Membrane locking and reduced integration for curved elements. *Journal on Applied Mechanics*, 49:172–176.

Strang, G. and Fix, G. (1973). *An analysis of the finite element method*. Prentice-Hall, Englewood Cliffs.

Swartz, B. and Wendroff, B. (1974). The relative efficiency of finite difference and finite element methods. I: Hyperbolic problems and splines. *SIAM Journal on Numerical Analysis*, 11:979–993.

Szabó, B., Düster, A., and Rank, E. (2004). *The p-version of the finite element method*. in: Encyclopedia of Computational Mechanics, Fundamentals Vol.1, Wiley, New York.

Taig, I. (1961). Structural analysis by the matrix displacement method. English electric aviation report No. S017.

Taylor, R. (2011). Isogeometric analysis of nearly incompressible solids. *International Journal for Numerical Methods in Engineering*, 87:273–288.

Taylor, R. and Auricchio, F. (1993). Linked interpolation for Reissner-Mindlin plate elements: Part II- A simple triangle. *International Journal for Numerical Methods in Engineering*, 36:3057–3066.

Taylor, R., Beresford, P., and Wilson, E. (1976). A non-conforming element for stress analysis. *International Journal for Numerical Methods in Engineering*, 10:1211–1220.

Timoshenko, S. and Woinowsky-Krieger, S. (2007). *Theory of plates and shells*. McGraw-Hill, New York.

Turner, M., Clough, R., Martin, H., and Topp, L. (1956). Stiffness and deflection analysis of complex structures. *Journal of the Aeronautical Sciences*, 23:805–823.

Versprille, K. (1975). Computer-aided design applications of the rational B-spline approximation form. PhD thesis, Syracuse University.

Vuong, A., Giannelli, C., Jüttler, B., and Simeon, B. (2011). A hierarchical approach to adaptive local refinement in isogeometric analysis. *Computer Methods in Applied Mechanics and Engineering*, 200:3554–3567.

Washizu, K. (1955). On the variational principles of elasticity and plasticity. *Technical Report 25–18, Massachusetts Institute of Technolgy*.

Wikipedia (2013a). Airbus a380 — wikipedia, die freie enzyklopädie. [Online; Stand 4. April 2013].

Wikipedia (2013b). Kühlturm — wikipedia, die freie enzyklopädie. [Online; Stand 4. April 2013].

Wikipedia (2013c). Muscheln — wikipedia, die freie enzyklopädie. [Online; Stand 4. April 2013].

Wisniewski, K. (2010). *Finite rotation shells: Basic equations and finite elements for Reissner kinematics*. Springer, Berlin.

Wriggers, P. (2001). *Nichtlineare Finite-Element-Methoden*. Springer, Berlin.

Wunderlich, W. (1966). Differentialsystem und Übertragungsmatrizen der Biegetheorie allgemeiner Rotationsschalen. *Heft 4, Schriftenreihe des Lehrstuhls für Stahlbau, Technische Hochschule Hannover*.

Zienkiewicz, O. (1971). *The finite element method in structural and continuum mechanics*. McGraw-Hill, London.

Zienkiewicz, O. and Cheung, Y. (1964). The finite element method for analysis of elastic isotropic and orthotropic slabs. *ICE Proceedings*, 28:471–488.

Zienkiewicz, O. and Taylor, R. (2005). *The finite element method: For solid and structural mechanics*. Elsevier, Oxford, 6th edition.

Zienkiewicz, O., Taylor, R., and Too, J. (1971). Reduced integration technique in general analysis of plates and shells. *International Journal for Numerical Methods in Engineering*, 3:275–290.

Zienkiewicz, O., Taylor, R., and Zhu, J. (2005). *The finite element method: Its basis and fundamentals*. Elsevier, Oxford, 6th edition.

Zienkiewicz, O., Xu, Z., and Zeng, L. (1993). Linked interpolation for Reissner-Mindlin plate elements: Part I- A simple quadrilateral. *International Journal for Numerical Methods in Engineering*, 36:3043–3056.

Lebenslauf

Persönliche Angaben:

Name	Ralph Fritz Echter
Geburtsdatum	03. September 1977
Geburtsort	Aichach
Familienstand	Ledig

Schulische Ausbildung:

1983 - 1988	Grundschule, Affing
1988 - 1997	Deutschherren-Gymnasium, Aichach
Juni 1997	Allgemeine Hochschulreife

Zivildienst:

1997 - 1998	Lebenshilfe Aichach-Friedberg

Studium:

2000 - 2004	Diplomstudium Bauingenieurwesen, Hochschule München
August 2004	Diplomingenieur (FH)
2004 - 2006	Masterstudium Computational Mechanics, Technische Universität München
September 2006	Master of Science (MSc)

Beruflicher Werdegang:

1998 - 2000	Berufsausbildung zum Zimmerer, Aichach
2006 - 2007	Berechnungsingenieur bei der CADFEM GmbH, Grafing bei München
2007 - 2013	Wissenschaftlicher Mitarbeiter am Institut für Baustatik und Baudynamik der Universität Stuttgart
seit Juli 2013	Berechnungsingenieur bei der CADFEM GmbH, Grafing bei München

Berichte des Instituts für Baustatik und Baudynamik der Universität Stuttgart

1 (1983) P. Osterrieder:
Traglastberechnung von räumlichen Stabwerken bei großen Verformungen mit finiten Elementen.

2 (1983) T.A. Kompfner:
Ein finites Elementmodell für die geometrisch und physikalisch nichtlineare Berechnung von Stahlbetonschalen.

3 (1983) A. Diack:
Beitrag zur Stabilität längsversteifter Kreiszylinderschalen unter Axialdruck.

4 (1984) A. Burmeister, F.W. Bornscheuer, E. Ramm:
Traglasten von Kugelbehältern mit Stutzen und Formabweichungen unter Innendruck und Stützenlängskraft.

5 (1985) H. Stegmüller:
Grenzlastberechnungen flüssigkeitsgefüllter Schalen mit "degenerierten" Schalenelementen.

6 (1987) A. Burmeister:
Dynamische Stabilität nach der Methode der finiten Elemente mit Anwendung auf Kugelschalen.

7 (1987) G. Kammler:
Ein finites Elementmodell zur Berechnung von Trägern und Stützen mit offenem, dünnwandigem Querschnitt unter Berücksichtigung der Interaktion zwischen globalem und lokalem Versagen.

8 (1988) A. Matzenmiller:
Ein rationales Lösungskonzept für geometrisch und physikalisch nichtlineare Strukturberechnungen.

9 (1989) D. Tao:
Die Technik der reduzierten Basis bei nichtlinearen finiten Element-Berechnungen.

10 (1989) K. Weimar:
Ein nichtlineares Balkenelement mit Anwendung als Längssteifen axialbelasteter Kreiszylinder.

11 (1990) K.-U. Bletzinger:
Formoptimierung von Flächentragwerken.

12 (1990) S. Kimmich:
Strukturoptimierung und Sensibilitätsanalyse mit finiten Elementen.

13 (1991) U. Andelfinger:
Untersuchungen zur Zuverlässigkeit hybrid-gemischter finiter Elemente für Flächentragwerke.

14 (1992) N. Büchter:
Zusammenführung von Degenerationskonzept und Schalentheorie bei endlichen Rotationen.

15 (1992) T.J. Hofmann:
Beitrag zur verfeinerten Balkentheorie.

16 (1994) D. Roehl:
Zur Berechnung von großen elastoplastischen Deformationen bei Flächentragwerken und Kontinua.

17 (1994) R. Reitinger:
Stabilität und Optimierung imperfektionsempfindlicher Tragwerke.

18 (1995) R. Suanno:
Ein dreidimensionales Simulationsmodell für Stahlbeton mit Plastizität und Schädigung.

19 (1995) M. Braun:
Nichtlineare Analysen von geschichteten, elastischen Flächentragwerken.

20 (1996) N. Rehle:
Adaptive Finite Element Verfahren bei der Analyse von Flächentragwerken.

21 (1996) C. Haußer:
Effiziente Dreieckselemente für Flächentragwerke.

22 (1996) D. Kuhl:
Stabile Zeitintegrationsalgorithmen in der nichtlinearen Elastodynamik dünnwandiger Tragwerke.

23 (1998) H. Schmidts:
Zur effizienten Modellierung und Analyse von Hochhaustragwerken.

24 (1998) H. Wang:
Interaktion des lokalen und globalen Stabilitätsverhaltens dünnwandiger Stäbe.

25 (1998) K. Maute:
Topologie- und Formoptimierung von dünnwandigen Flächentragwerken.

26 (1998) B. Maurer:
Karl Culmann und die graphische Statik.

27 (1998) F. Cirak:
Adaptive Finite-Element-Methoden bei der nichtlinearen Analyse von Flächentragwerken.

28 (1998) M. Trautz:
Zur Entwicklung von Form und Struktur historischer Gewölbe aus der Sicht der Statik.

29 (1999) H. Menrath:
Numerische Simulation des nichtlinearen Tragverhaltens von Stahl-verbundträgern.

30 (1999) M. Bischoff:
Theorie und Numerik einer dreidimensionalen Schalenformulierung.

31 (1999) W.A. Wall:
Fluid-Struktur-Interaktion mit stabilisierten Finiten Elementen.

32 (2000) E. Kuhl:
Numerische Modelle für kohäsive Reibungsmaterialien.

33 (2001) A. Maute:
Adaptive Finite-Element-Methoden in der Strukturdynamik.

34 (2001) S. Schwarz:
Sensitivitätsanalyse und Optimierung bei nichtlinearem Struktur-
verhalten.

35 (2001) A. Haufe:
Dreidimensionale Simulation bewehrter Flächentragwerke aus Beton mit
der Plastizitätstheorie.

36 (2001) D.P. Mok:
Partitionierte Lösungsverfahren in der Strukturdynamik und der Fluid-
Struktur-Interaktion.

37 (2002) H. Steeb:
Fehlerschätzer für FE-Berechnungen bei entfestigenden Materialien.

38 (2002) K. Krausz:
Tragverhalten gemauerter Tonnengewölbe mit Stichkappen.

39 (2002) M. Hörmann:
Nichtlineare Versagensanalyse von Faserverbundstrukturen.

40 (2003) V. Gravemeier:
The Variational Multiscale Method for Laminar and Turbulent Incom-
pressible Flow.

41 (2004) R. Kemmler:
Stabilität und große Verschiebungen in der Topologie- und Form-
optimierung.

42 (2004) G.A. D'Addetta:
Discrete Models for Cohesive Frictional Materials.

43 (2004) M. Gee:
Effiziente Lösungsstrategien in der nichtlinearen Schalenmechanik.

44 (2004) T. Erhart:
Strategien zur numerischen Modellierung transienter Impaktvorgänge bei nichtlinearem Materialverhalten.

45 (2005) M. Leukart:
Kombinierte anisotrope Schädigung und Plastizität bei kohäsiven Reibungsmaterialien.

46 (2006) F. Huber:
Nichtlineare dreidimensionale Modellierung von Beton- und Stahlbetontragwerken.

47 (2007) A. Lipka:
Verbesserter Materialeinsatz innovativer Werkstoffe durch die Topologieoptimierung.

48 (2007) A.S. Hund:
Hierarchische Mehrskalenmodellierung des Versagens von Werkstoffen mit Mikrostruktur.

49 (2007) S. Hartmann:
Kontaktanalyse dünnwandiger Strukturen bei großen Deformationen.

50 (2007) T.M. Hettich:
Diskontinuierliche Modellierung zur Versagensanalyse von Verbundmaterialien.

51 (2007) Ch. Förster:
Robust methods for fluid-structure interaction with stabilised finite elements.

52 (2009) M. von Scheven:
Effiziente Algorithmen für die Fluid-Struktur-Wechselwirkung.

53 (2010) J. Kato:
Material Optimization for Fiber Reinforced Composites applying a Damage Formulation.

54 (2010) C.F. Hilchenbach:
Optimierung von Mehrphasenstrukturen mit lokalem Schädigungsverhalten.

55 (2011) I. Bruss:
Dreidimensionale Schädigungsmodellierung heterogener Materialien.

56 (2012) B.J. Schneider:
Polygonale diskrete Elemente zur Modellierung heterogener Materialien.

57 (2012) R. Etlender:
Modellierung und Simulation der Wellenausbreitung in flexiblen hydraulischen Leitungen.

58 (2012) T. Cichosz:
Stabile und konsistente Kontaktmodellierung in Raum und Zeit.

Ralph Echter

This work is concerned with the isogeometric analysis of shells. A new hierarchic family of NURBS-based shell finite elements is developed. Besides a shear-rigid 3-parameter shell element formulation with Kirchhoff-Love kinematics, both a shear flexible 5-parameter Reissner-Mindlin-type and a 7-parameter 3D shell element which accounts for thickness change are derived.

Compared to existing isogeometric shell elements the hierarchy showing up in the shell mechanics is transferred to the parameterization of the kinematic shell equations by gradually enhancing the minimalistic 3-parameter shell model with additional degrees of freedom in order to systematically increase the approximation quality of the shell formulation. This represents the key innovation of this thesis with significant benefits both with regard to finite element technology and model adaptivity.

The continuity requirements on the displacement functions for the proposed hierarchic shell models are C^1, which can be naturally satisfied with the applied higher-continuity NURBS discretizations. All shell models of the hierarchy utilize a pure displacement ansatz. Due to the concept of a hierarchic parameterization both transverse shear locking and curvature thickness locking are avoided by default for the Reissner-Mindlin-type and the 3D shell formulations. In order to remove membrane locking two new strategies for higher-order and higher-continuity discretizations – a NURBS-based Discrete Strain Gap method and a mixed displacement-stress formulation – are developed and applied to the in-plane part of the isogeometric shell finite elements, which ultimately lead to isogeometric shell element formulations that are completely free from geometric locking.